

ABSTRACT

NOORMAN, MARCELLA JO. Analysis of Fluid Flow Models with Biological Applications. (Under the direction of H.T. Banks and Lorena Bociu).

Mathematical models are a valuable tool to researchers, particularly in problems for which noninvasive techniques for experimentation are not currently available or are extremely costly. Such circumstances are common in biological problems and, in particular, in the study of human diseases. While mathematical modeling cannot replace experimentation, it does give us the ability to test hypotheses and study the dynamics and relationships between potentially crucial components *in silico* rather than *in vivo* or *in vitro*. The main advantages of studying such problems mathematically is the relatively low cost of computation along with the speed at which results can be obtained and used to inform further experimentation. Here, we look specifically at two different problems with applications in biology and medicine. First, we study a poro-visco-elastic model that can be applied to optical perfusion which plays a role in glaucoma. Second, we look at models of the liver microstructure that have been built specifically to study non-alcoholic fatty liver disease.

Poro-elastic and poro-visco-elastic models describe fluid flow through porous, deformable media. They are relevant in many applications in bioengineering and medicine, such as tissue perfusion and fluid flow inside cartilages and bones. In particular, we are interested in the application of these models specifically to optical perfusion and its relation to glaucoma, as well as confined compression tests for biological tissues. In both these applications, and many other biological applications, pressure loads on the tissue (represented in the model through boundary traction) play an extremely important role. The inclusion or absence of structural viscosity has also been seen to be a major determinant in the behavior of solutions to poro-elastic and poro-visco-elastic models [39]. The amount of structural viscosity included in the solid component plays a relevant role in many biological and medical applications as well as structural viscosity of biological tissues is known to decrease with age and disease. We investigate the effect of these pressure loads and structural viscosity through a sensitivity analysis of the system with respect to the boundary traction and compare the results obtained in the purely elastic case versus the visco-elastic case. We also consider sensitivity with respect to boundary flux conditions, however the results are much less consistent than those for the sensitivity with respect to boundary traction. Ultimately, this analysis will direct and inform the development of relevant control and optimization problems for the given poro-visco-elastic model which could be used to help develop novel strategies to improve experimental and clinical approaches in bioengineering and medicine.

Non-alcoholic fatty liver disease (NAFLD) is the most common cause of chronic liver disease and can lead to cirrhosis and liver cancer. Precipitated by the build up of extra fat in the liver not caused by alcohol, it is still not understood why steatosis occurs where it does in the liver microstructure in

NAFLD. It is likely, however, that the location of steatosis is due, at least in part, to metabolic zonation (heterogeneity among liver cells in function and enzyme expression). Recently, there has been an influx of computational and mathematical models in order to investigate the relationship between metabolic zonation and steatosis in NAFLD. Of interest among these models are “compartments-in-series” models. These compartmental models include the spatial distribution of metabolite concentrations via series of compartments that are connected through some representation of blood flow. Here, we analyze one such model, looking at how the number of compartments as well as inclusion of dispersion in the flow affect simulation results.

© Copyright 2018 by Marcella Jo Noorman

All Rights Reserved

Analysis of Fluid Flow Models with Biological Applications

by
Marcella Jo Noorman

A dissertation submitted to the Graduate Faculty of
North Carolina State University
in partial fulfillment of the
requirements for the Degree of
Doctor of Philosophy

Applied Mathematics

Raleigh, North Carolina

2018

APPROVED BY:

Hien Tran

Stephen Campbell

H.T. Banks
Co-chair of Advisory Committee

Lorena Bociu
Co-chair of Advisory Committee

DEDICATION

To my father who has always shared my love of math and to my late grandfather who I know still does, you both inspired me to be the mathematician I never knew I wanted to be.

I am proud to carry on your legacies.

BIOGRAPHY

Marcella Noorman was born and raised in Grand Rapids, Michigan where she was homeschooled by her parents. In May of 2013, she received a bachelor's degree with a math major and physics minor from Belmont University in Nashville, Tennessee. Noorman then moved to Raleigh, North Carolina where she began working with Dr. Lorena Bociu while completing a year-long post-baccalaureate program at North Carolina State University (NCSU). She remained at NCSU to work under doctors Lorena Bociu and H.T. Banks while pursuing her Ph.D. in Applied Mathematics.

ACKNOWLEDGEMENTS

First and foremost, I would like to thank my advisors, Lorena Bociu and H.T. Banks, without whom this work would not have been possible. Both of you have played a huge role in my life, not just academically and professionally, but personally. I cannot thank you enough for all the support and encouragement you've given me. Lorena, thank you for being an incredible role model for women in math and for me in particular. Dr. Banks, thank you for always pushing me forward and reminding me not to get too hung up on the little things. I feel extremely blessed to have had you both as mentors and friends.

Thank you to my collaborators who have all played major roles in the development of the research presented herein. To my friend Dr. Kidist Bekele-Maxwell, thank you for all the hours you spent working with me on coding and analyzing results. I truly owe a great debt of gratitude to you for helping me become the coder I am today. To Dr. Giovanna Guidoboni, thank you for your insights and for taking the time to help me understand our current knowledge of glaucoma. To Dr. Richard Allen and Dr. CJ Musante, my mentors during my Pfizer internship, thank you for introducing me to such an interesting problem and for your continued support and encouragement. Your guidance, then and now, has been of great value to me.

Thank you to my undergraduate math professors who encouraged me to pursue math when I was exploring other career options. In particular, Dr. Biles, Dr. Acree, and Dr. Miller, you gave me my first taste of research, set up independent studies for me to explore topics I was interested in, helped ignite my passion for math, and showed me that I could pursue that passion. If it weren't for you, I do not know if I would be getting my Ph.D. in applied math. For that, I can never thank you enough.

Thank you to my friends. While too many to name, there are some whom must be mentioned. To those who have been with me through graduate school, in particular, Meredith, Jamie, Mary, Sadie, Emma, and Richard, thank you for always being there for me, for being excited when I was excited, and for listening when I needed someone to talk to. To my lab friends, Neha, Nick, Amanda L., Rebecca, Kidist, Bekah, Amanda M., Annabel, thank you for being available when I needed to vent, for offering advice and support, and for so many great lunchtime conversations. Thank you to all my undergraduate friends who let me talk about math even when they didn't know what I was talking about (and the few who did). To my friend since childhood, Laura, thanks for always being there.

Thank you to my family who has always stood beside me and offered boundless support. To my parents, who knew long before I did that I was destined to be a mathematician. Your loving guidance has shaped me into the person I am today, and I am so grateful to have you as parents. Dad, thank you for always being excited about math and science with me. The way you think has always been an inspiration to me, and I constantly strive to intermingle creativity and logic the way you do. Mom,

thank you for always being just a phone call away and my editor for everything. Thank you to my sisters, who put up with me at my worst and will always be my best friends. Macia, thank you for always challenging me. Megan, thank you for always standing up for me. To my brother-in-law, Brad, thank you for truly being my big brother. Thank you to my grandparents, whose love and support has never wavered. In particular, to my late Grandpa Kearney, whose slide rule will always be among my most cherished items. To the rest of my large, amazing family, there are too many aunts, uncles, and cousins to name. I hope you all know how much you mean to me and how thankful I am to have you in my life.

And lastly, to my nephews, Phineas and Dorian, thank you for bringing joy and curiosity to my life. I hope I can always be an inspiration to you to proudly follow your dreams.

TABLE OF CONTENTS

LIST OF TABLES	viii
LIST OF FIGURES	ix
Chapter 1 SENSITIVITY OF PORO-ELASTIC AND PORO-VISCO-ELASTIC MODELS WITH APPLICATIONS IN OPTICAL AND TISSUE PERFUSION	1
1.1 Optical Perfusion and Glaucoma	2
1.1.1 Basic biology	3
1.1.2 Intraocular pressure (IOP)	5
1.1.3 Lamina cribrosa	6
1.2 Poro-Elastic and Poro-Visco-Elastic Models	7
1.2.1 Model Derivation	9
1.2.2 Well-posedness results	15
1.2.3 Discretization	18
1.3 Sensitivity Analysis	27
1.3.1 Functional Sensitivities	28
1.3.2 Numerical Methods	30
1.3.3 Complex Step Method	31
1.4 Selected Results	34
1.4.1 Sensitivity with Respect to Boundary Conditions	35
1.4.2 Varying Structural Viscosity	71
1.5 Dimensional Analysis	76
1.5.1 Confined Compression	76
1.5.2 Dimensionless Model	78
1.5.3 Numerical Procedure	80
1.5.4 Selected Results	80
1.6 Conclusions and Future Work	85
Chapter 2 ZONATED MODELS FOR THE LIVER MICROSTRUCTURE WITH APPLICATIONS IN NON-ALCOHOLIC FATTY LIVER DISEASE	89
2.1 Non-alcoholic Fatty Liver Disease	90
2.2 Liver Biology	90
2.2.1 Zonation	91
2.2.2 Zonated steatosis	91
2.3 Mathematical models	92
2.3.1 Compartments-in-series model	96
2.3.2 Advection-Reaction (AR) Version	105
2.3.3 Advection-Reaction-Dispersion (ADR) Version	108
2.4 Results	110
2.4.1 Mesh Refinement	110
2.4.2 Comparison of AR and ADR	113
2.5 Conclusions and Future Work	114

BIBLIOGRAPHY	118
APPENDICES	133
Appendix A RATES OF METABOLIC PROCESSES FOR LIVER MODELS	134
A.1 Glucose Metabolism	135
A.2 Lipid Metabolism	143
A.3 Energy Metabolism	150
Appendix B EQUATIONS FOR LIVER METABOLISM MODELS	155
B.1 Compartments-in-series model	155
B.1.1 Hepatic equations	156
B.1.2 Systemic blood equations	157
B.1.3 Hepatic blood equations	159
B.2 PDE models	159
B.2.1 Hepatic equations	160
B.2.2 Systemic blood equations	161
B.2.3 Hepatic blood equations	161

LIST OF TABLES

Table 2.1	All molecules represented in the model with their abbreviated variable name. H denotes hepatic, HB denotes hepatic blood, SB denotes systemic blood. . . .	95
Table 2.2	Transports between hepatocytes (<i>H</i>) and hepatic blood (<i>HB</i>) in AR and ADR systems.	106
Table 2.3	Change of metabolite levels in over x from refining the mesh from $n = 5$ to $n = 500$ (relative to overall range of metabolite level).	111
Table 2.4	Change of metabolite levels over x from refining the mesh from $n = 50$ to $n = 500$ (relative to overall range of metabolite level).	113
Table 2.5	Change of metabolite levels over x between AR and ADR simulation (relative to overall range of AR simulation metabolite level).	114
Table A.1	Roles of molecules in Glucokinase (<i>GK</i>).	136
Table A.2	Roles of molecules in Glucose-6-phosphatase (<i>G6Pase</i>).	137
Table A.3	Roles of molecules in Glycogen Synthase (<i>GS</i>).	138
Table A.4	Roles of molecules in Glycogen Phosphorylase (<i>GP</i>).	139
Table A.5	Roles of molecules in Glucogenesis part 1 (<i>PEPCK</i>).	140
Table A.6	Roles of molecules in Glucogenesis part 2 (<i>FBP</i>).	141
Table A.7	Roles of molecules in Glycolysis part 1 (<i>PFK</i>).	142
Table A.8	Roles of molecules in Glycolysis part 2 (<i>PK</i>).	143
Table A.9	Roles of molecules in pyruvate oxidation (<i>PDH</i>).	144
Table A.10	Roles of molecules in β -Oxidation (<i>βoxi</i>).	145
Table A.11	Roles of molecules in Lipogenesis (<i>Lgen</i>).	147
Table A.12	Roles of molecules in Lipolysis (<i>Lip</i>).	148
Table A.13	Roles of molecules in Triglyceride Synthesis (<i>TSyn</i>).	149
Table A.14	Roles of molecules in Glycerol Kinase (<i>GlyK</i>).	150
Table A.15	Roles of molecules in Adenosine Tri-phosphate Synthesis (<i>ATPS</i>).	151
Table A.16	Roles of molecules in Uridine Diphosphate Kinase (<i>NDKU</i>).	152
Table A.17	Roles of molecules in Guanosine Diphosphate Kinase (<i>NDKG</i>).	152
Table A.18	Roles of molecules in Adenosine Kinase (<i>AK</i>). Note: this is a bidirectional process.	153
Table A.19	Roles of molecules in Additional Adenosine Triphosphate Use (<i>ATPu</i>).	154
Table B.1	Parameter values for rate of glucose uptake in the body excluding the liver. . . .	158
Table B.2	Parameter values for rate of adipose lipolysis.	158
Table B.3	Parameter values for rate of meal inputs.	158

LIST OF FIGURES

Figure 1.1	A normal optic cup (left) vs. a glaucomatous optic cup (right). The arrow from the bottom of the figures indicates the visible portion of the optic nerve head which is the circular structure through which the blood vessels pass. The arrow inside the visible portion of the optic nerve head indicates the optic cup. Figure from WikEM: http://medbox.iab.me/modules/en-wikem/wiki/File_Glaucoma-cupping-1024x414.html	2
Figure 1.2	Anatomy and vascular supply of the optic nerve head as presented in [149]. . .	4
Figure 1.3	Sensitivity of u (left panel), p (center panel), and v (right panel) with respect to g_1 at $g_1 = .3$	36
Figure 1.4	Sensitivity of u (left panel), p (center panel), and v (right panel) with respect to ψ_1 at $\psi_1 = 3$	36
Figure 1.5	Sensitivity of u (left panel), p (center panel), and v (right panel) with respect to g_2	38
Figure 1.6	Sensitivity of u (left panel), p (center panel), and v (right panel) with respect to ψ_2	39
Figure 1.7	Linear spline approximations of g_3 and ψ_3	41
Figure 1.8	Sensitivity function of solid displacement u with respect to boundary stress g_{3h} in the direction ϕ_4 , when $\delta = 1$. Note, the two figures give different angles of view of the sensitivity.	41
Figure 1.9	Sensitivity function of solid displacement u with respect to boundary stress g_{3h} in the direction ϕ_4 , when $\delta = 0$. Note, the two figures give different angles of view of the sensitivity.	42
Figure 1.10	Sensitivity functions of solid displacement u with respect to boundary stress g_{3h} in the direction $\bar{g} = \sum_{i=0}^{10} \phi_i$ when $\delta = 1$ (left) and $\delta = 0$ (right).	42
Figure 1.11	Sensitivity function of solid displacement u with respect to boundary source ψ_{3h} in the direction ϕ_0 when $\delta = 1$ (left) and $\delta = 0$ (right).	43
Figure 1.12	Sensitivity function of solid displacement u with respect to boundary source ψ_{3h} in the direction ϕ_3 when $\delta = 1$ (left) and $\delta = 0$ (right).	43
Figure 1.13	Sensitivity functions of solid displacement u with respect to boundary stress ψ_{3h} in the direction $\bar{\psi} = \sum_{i=0}^{10} \phi_i$ when $\delta = 1$ (left) and $\delta = 0$ (right).	44
Figure 1.14	Sensitivity function of fluid pressure p with respect to boundary stress g_{3h} in the direction ϕ_4 when $\delta = 1$. Note, the two figures give different angles of view of the sensitivity.	44
Figure 1.15	Sensitivity function of fluid pressure p with respect to boundary stress g_{3h} in the direction ϕ_4 when $\delta = 0$. Note, the two figures give different angles of view of the sensitivity.	45
Figure 1.16	Sensitivity functions of fluid pressure p with respect to boundary stress g_{3h} in the direction $\bar{g} = \sum_{i=0}^{10} \phi_i$ when $\delta = 1$ (left) and $\delta = 0$ (right).	45
Figure 1.17	Sensitivity functions of fluid pressure p with respect to boundary source ψ_{3h} in the direction ϕ_0 when $\delta = 1$ (left) and $\delta = 0$ (right).	46
Figure 1.18	Sensitivity functions of fluid pressure p with respect to boundary source ψ_{3h} in the direction ϕ_3 when $\delta = 1$ (left) and $\delta = 0$ (right).	46

Figure 1.19	Sensitivity functions of fluid pressure p with respect to boundary stress ψ_{3h} in the direction $\tilde{\psi} = \sum_{i=0}^{10} \phi_i$ when $\delta = 1$ (left) and $\delta = 0$ (right).	47
Figure 1.20	Sensitivity functions of discharge velocity v with respect to boundary stress g_{3h} in the direction ϕ_0 when $\delta = 1$ (left) and $\delta = 0$ (right).	47
Figure 1.21	Sensitivity functions of discharge velocity v with respect to boundary stress g_{3h} in the direction ϕ_3 when $\delta = 1$ (left) and $\delta = 0$ (right).	48
Figure 1.22	Sensitivity functions of discharge velocity v with respect to boundary stress g_{3h} in the direction $\tilde{g} = \sum_{i=0}^{10} \phi_i$ when $\delta = 1$ (left) and $\delta = 0$ (right).	48
Figure 1.23	Sensitivity functions of discharge velocity v with respect to boundary source ψ_{3h} in the direction ϕ_0 when $\delta = 1$ (left) and $\delta = 0$ (right).	49
Figure 1.24	Sensitivity functions of discharge velocity v with respect to boundary source ψ_{3h} in the direction ϕ_3 when $\delta = 1$ (left) and $\delta = 0$ (right).	49
Figure 1.25	Sensitivity functions of discharge velocity v with respect to boundary stress ψ_{3h} in the direction $\tilde{\psi} = \sum_{i=0}^{10} \phi_i$ when $\delta = 1$ (left) and $\delta = 0$ (right).	50
Figure 1.26	Linear spline approximations of g_4 and ψ_4	51
Figure 1.27	Sensitivity functions of solid displacement u with respect to boundary stress g_{4h} in the direction ϕ_0 when $\delta = 1$ (left) and $\delta = 0$ (right).	52
Figure 1.28	Sensitivity functions of solid displacement u with respect to boundary stress g_{4h} in the direction ϕ_3 when $\delta = 1$ (left) and $\delta = 0$ (right).	52
Figure 1.29	Sensitivity functions of solid displacement u with respect to boundary stress g_{4h} in the direction $\tilde{g} = \sum_{i=0}^{N_g} \phi_i$ when $\delta = 1$ (left) and $\delta = 0$ (right).	53
Figure 1.30	Sensitivity functions of solid displacement u with respect to boundary source ψ_{4h} in the direction $\tilde{\phi}_0$ when $\delta = 1$ (left) and $\delta = 0$ (right).	53
Figure 1.31	Sensitivity functions of solid displacement u with respect to boundary source ψ_{4h} in the direction $\tilde{\phi}_3$ when $\delta = 1$ (left) and $\delta = 0$ (right).	54
Figure 1.32	Sensitivity functions of solid displacement u with respect to boundary source ψ_{4h} in the direction $\tilde{\psi} = \sum_{i=0}^{N_\psi} \tilde{\phi}_i$ when $\delta = 1$ (left) and $\delta = 0$ (right).	54
Figure 1.33	Sensitivity functions of pressure p with respect to boundary stress g_{4h} in the direction ϕ_0 when $\delta = 1$ (left) and $\delta = 0$ (right).	55
Figure 1.34	Sensitivity functions of pressure p with respect to boundary stress g_{4h} in the direction ϕ_3 when $\delta = 1$ (left) and $\delta = 0$ (right).	55
Figure 1.35	Sensitivity functions of fluid pressure p with respect to boundary stress g_{4h} in the direction $\tilde{g} = \sum_{i=0}^{N_g} \phi_i$ when $\delta = 1$ (left) and $\delta = 0$ (right).	56
Figure 1.36	Sensitivity functions of fluid pressure p with respect to boundary source ψ_{4h} in the direction $\tilde{\phi}_0$ when $\delta = 1$ (left) and $\delta = 0$ (right).	56
Figure 1.37	Sensitivity functions of fluid pressure p with respect to boundary source ψ_{4h} in the direction $\tilde{\phi}_3$ when $\delta = 1$ (left) and $\delta = 0$ (right).	57
Figure 1.38	Sensitivity functions of fluid pressure p with respect to boundary source ψ_{4h} in the direction $\tilde{\psi} = \sum_{i=0}^{N_\psi} \tilde{\phi}_i$ when $\delta = 1$ (left) and $\delta = 0$ (right).	57
Figure 1.39	Sensitivity functions of discharge velocity v with respect to boundary stress g_{4h} in the direction ϕ_0 when $\delta = 1$ (left) and $\delta = 0$ (right).	58
Figure 1.40	Sensitivity functions of discharge velocity v with respect to boundary stress g_{4h} in the direction ϕ_3 when $\delta = 1$ (left) and $\delta = 0$ (right).	58

Figure 1.41	Sensitivity functions of discharge velocity v with respect to boundary stress g_{4h} in the direction $\bar{g} = \sum_{i=0}^{N_g} \phi_i$ when $\delta = 1$ (left) and $\delta = 0$ (right).	59
Figure 1.42	Sensitivity functions of discharge velocity v with respect to boundary source ψ_{4h} in the direction $\tilde{\phi}_0$ when $\delta = 1$ (left) and $\delta = 0$ (right).	59
Figure 1.43	Sensitivity functions of discharge velocity v with respect to boundary source ψ_{4h} in the direction $\tilde{\phi}_3$ when $\delta = 1$ (left) and $\delta = 0$ (right).	60
Figure 1.44	Sensitivity functions of discharge velocity v with respect to boundary source ψ_{4h} in the direction $\tilde{\psi} = \sum_{i=0}^{N_\psi} \tilde{\phi}_i$ when $\delta = 1$ (left) and $\delta = 0$ (right).	60
Figure 1.45	Solution functions of solid displacement u when $\delta = 1$ (left) and $\delta = 0$ (right).	61
Figure 1.46	Solution functions of fluid pressure p when $\delta = 1$ (left) and $\delta = 0$ (right).	61
Figure 1.47	Solution functions of discharge velocity v when $\delta = 1$ (left) and $\delta = 0$ (right).	62
Figure 1.48	Linear spline approximations of g_5^q for $q = 100$ (left) and $q = \infty$ (right).	62
Figure 1.49	Sensitivity functions of solid displacement u with respect to boundary stress g_{5h}^{100} in the direction ϕ_0 when $\delta = 1$ (left) and $\delta = 0$ (right).	63
Figure 1.50	Sensitivity functions of solid displacement u with respect to boundary stress g_{5h}^{100} in the direction ϕ_5 when $\delta = 1$ (left) and $\delta = 0$ (right).	63
Figure 1.51	Sensitivity functions of solid displacement u with respect to boundary stress g_{5h}^∞ in the direction ϕ_0 when $\delta = 1$ (left) and $\delta = 0$ (right).	64
Figure 1.52	Sensitivity functions of solid displacement u with respect to boundary stress g_{5h}^∞ in the direction ϕ_5 when $\delta = 1$ (left) and $\delta = 0$ (right).	64
Figure 1.53	Sensitivity functions of solid displacement u with respect to boundary stress g_5^∞ in the direction $\bar{g} = \sum_{i=0}^{20} \phi_i$ when $\delta = 1$ (left) and $\delta = 0$ (right).	65
Figure 1.54	Sensitivity functions of fluid pressure p with respect to boundary stress g_{5h}^{100} in the direction ϕ_0 when $\delta = 1$ (left) and $\delta = 0$ (right).	65
Figure 1.55	Sensitivity functions of fluid pressure p with respect to boundary stress g_{5h}^{100} in the direction ϕ_5 when $\delta = 1$ (left) and $\delta = 0$ (right).	66
Figure 1.56	Sensitivity functions of fluid pressure p with respect to boundary stress g_{5h}^∞ in the direction ϕ_0 when $\delta = 1$ (left) and $\delta = 0$ (right).	66
Figure 1.57	Sensitivity functions of fluid pressure p with respect to boundary stress g_{5h}^∞ in the direction ϕ_5 when $\delta = 1$ (left) and $\delta = 0$ (right).	67
Figure 1.58	Sensitivity functions of fluid pressure p with respect to boundary stress g_5^∞ in the direction $\bar{g} = \sum_{i=0}^{20} \phi_i$ when $\delta = 1$ (left) and $\delta = 0$ (right).	67
Figure 1.59	Sensitivity functions of discharge velocity v with respect to boundary stress g_{5h}^{100} in the direction ϕ_0 when $\delta = 1$ (left) and $\delta = 0$ (right).	68
Figure 1.60	Sensitivity functions of discharge velocity v with respect to boundary stress g_{5h}^{100} in the direction ϕ_5 when $\delta = 1$ (left) and $\delta = 0$ (right).	68
Figure 1.61	Sensitivity functions of discharge velocity v with respect to boundary stress g_{5h}^∞ in the direction ϕ_0 when $\delta = 1$ (left) and $\delta = 0$ (right).	69
Figure 1.62	Sensitivity functions of discharge velocity v with respect to boundary stress g_{5h}^∞ in the direction ϕ_5 when $\delta = 1$ (left) and $\delta = 0$ (right).	69
Figure 1.63	Sensitivity functions of discharge velocity v with respect to boundary stress g_5^∞ in the direction $\bar{g} = \sum_{i=0}^{20} \phi_i$ when $\delta = 1$ (left) and $\delta = 0$ (right).	70
Figure 1.64	Sensitivity of u to boundary traction g for various values of $0 \leq \delta \leq 1$	71
Figure 1.65	Sensitivity of u to boundary traction g for various values of $1 \leq \delta \leq 2$	71

Figure 1.66	Sensitivity of p to boundary traction g for various values of $0 \leq \delta \leq 1$	72
Figure 1.67	Sensitivity of p to boundary traction g for various values of $1 \leq \delta \leq 2$	73
Figure 1.68	Sensitivity of ν to boundary traction g for various values of $0 \leq \delta \leq 1$	73
Figure 1.69	Sensitivity of ν to boundary traction g for various values of $1 \leq \delta \leq 2$	73
Figure 1.70	Sensitivity of u to ψ for various values of $0 \leq \delta \leq 1$	74
Figure 1.71	Sensitivity of u to ψ for various values of $1 \leq \delta \leq 2$	74
Figure 1.72	Sensitivity of p to ψ for various values of $0 \leq \delta \leq 1$	74
Figure 1.73	Sensitivity of p to ψ for various values of $1 \leq \delta \leq 2$	75
Figure 1.74	Sensitivity of ν to ψ for various values of $0 \leq \delta \leq 1$	75
Figure 1.75	Sensitivity of ν to ψ for various values of $1 \leq \delta \leq 2$	75
Figure 1.76	Schematic of confined compression as presented in [186].	77
Figure 1.77	Linear splines	81
Figure 1.78	Sensitivity of \hat{u} to \hat{P} in direction $s_2(t)$ for $0 \leq \eta \leq 1$	82
Figure 1.79	Maximum magnitude of sensitivities and the time at which it occurs for each value of $\hat{\eta}$ considered.	83
Figure 1.80	Sensitivity of \hat{p} to \hat{P} in direction $s_1(t)$ for $0 \leq \eta \leq 1$	84
Figure 1.81	Time derivative of sensitivity of \hat{p} (left panel) and \hat{v} (right panel) in direction s_1	84
Figure 1.82	Sensitivity of \hat{v} to \hat{P} in direction $s_1(t)$ for $0 \leq \eta \leq 1$	85
Figure 1.83	Sensitivity of \hat{p} (left panel) and log of sensitivity of \hat{v} (right panel) with respect to \hat{P} in direction s_1 at time $t = 0$	86
Figure 2.1	Portal axis of a liver sinusoid.	91
Figure 2.2	Schematic illustrating general structure of the models in consideration.	95
Figure 2.3	Schematic of compartments-in-series model.	96
Figure 2.4	Schematic of metabolite concentration in hepatic blood for compartments-in-series liver microstructure model.	100
Figure 2.5	Concentrations in systemic blood before and after model changes.	101
Figure 2.6	Data fit and model predictions for glucose uptake in rest of body.	102
Figure 2.7	Schematics of how adipose lipolysis is modeled.	103
Figure 2.8	Data fit to reduced fatty acid model with adipose lipolysis Eq. 2.13.	104
Figure 2.9	Schematic of meal input DE.	105
Figure 2.10	Metabolite levels for various mesh sizes across the sinusoid at time of largest difference between $h = 1/5$ and $h = 1/500$ (72 hour simulations).	112
Figure 2.11	Metabolite levels for AR and ADR versions of the model across the sinusoid at time of largest difference (24 hour simulations).	115
Figure 2.12	Computational times of ADR against AR with exponential fit.	116
Figure A.1	Variables and conversions included in each hepatic compartment as depicted in [11].	135
Figure A.2	Schematic of glucose metabolism.	136
Figure A.3	Schematic of lipid metabolism.	144

CHAPTER

1

SENSITIVITY OF PORO-ELASTIC AND PORO-VISCO-ELASTIC MODELS WITH APPLICATIONS IN OPTICAL AND TISSUE PERFUSION

Poro-elastic and poro-visco-elastic models describe fluid flow through porous, deformable media. They are relevant in many applications in bioengineering and medicine, such as tissue perfusion and fluid flow inside cartilages and bones. In particular, we are interested in the application of these models specifically to optical perfusion and its relation to glaucoma, as well as confined compression tests for biological tissues. In both these applications, and many other biological applications, pressure loads on the tissue (represented in the model through boundary traction) play an extremely important role. The inclusion or absence of structural viscosity has also been seen to be a major determinant in the behavior of solutions to poro-elastic and poro-visco-elastic models [39]. The amount of structural viscosity included in the solid component plays a relevant role in many biological and medical applications as well as structural viscosity of biological tissues is known to decrease with age and disease. We investigate the effect of these pressure loads and structural viscosity through a sensitivity analysis of the system with respect to the boundary traction

and compare the results obtained in the purely elastic case versus the visco-elastic case. We also consider sensitivity with respect to boundary flux conditions, however the results are much less consistent than those for the sensitivity with respect to boundary traction. Ultimately, this analysis will direct and inform the development of relevant control and optimization problems for the given poro-visco-elastic model which could be used to help develop novel strategies to improve experimental and clinical approaches in bioengineering and medicine.

1.1 Optical Perfusion and Glaucoma

Glaucoma is a heterogeneous group of eye diseases that cause vision loss and blindness. Approximately 64.3 million people between the ages of 40 and 80 were affected by glaucoma in 2013. That number is expected to rise to 76 million in 2020 and 112 million by 2040 [98]. Glaucoma is the leading cause of irreversible blindness worldwide [98]. Unfortunately, the biological basis of glaucoma is still poorly understood and the factors contributing to its progression have not been fully characterized [190]. Further, the diseases that fall under the category of glaucoma can have different causes. However, they are all characterized by cupping of the optic disc (see Fig. 1.1). This cupping occurs as a result of the degeneration of retinal ganglion cells and is a symptom unique to the glaucomas.

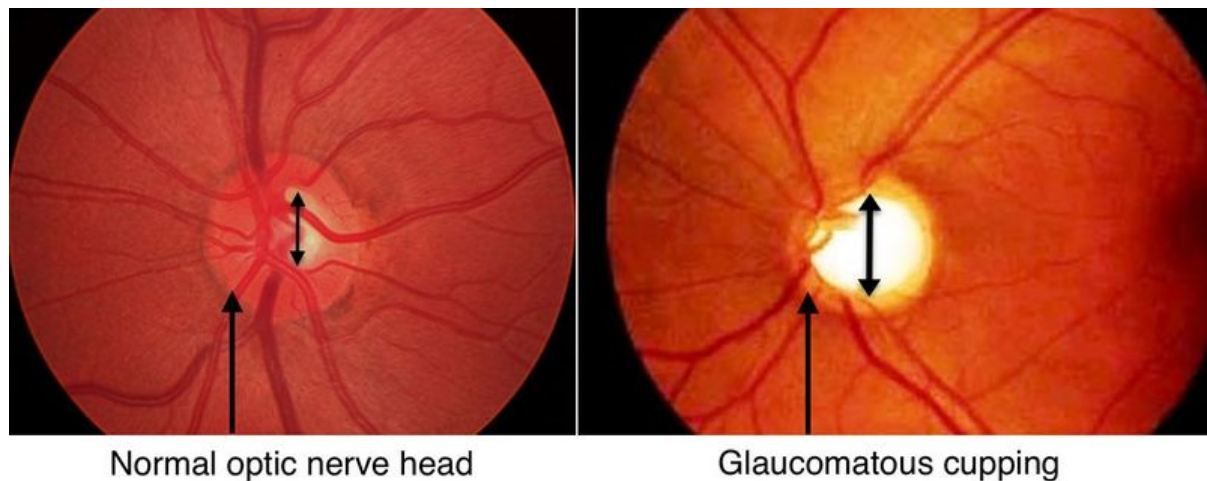


Figure 1.1 A normal optic cup (left) vs. a glaucomatous optic cup (right). The arrow from the bottom of the figures indicates the visible portion of the optic nerve head which is the circular structure through which the blood vessels pass. The arrow inside the visible portion of the optic nerve head indicates the optic cup. Figure from WikEM: http://medbox.iab.me/modules/en-wikem/wiki/File_Glaucoma-cupping-1024x414.html

The two main types of glaucoma are open-angle and angle-closure glaucoma. In angle-closure

glaucoma, the anterior chamber angle is blocked by the peripheral iris so that the aqueous humor (the clear fluid that supplies nutrients to and removes waste from the clear structures in the anterior eye) cannot access its main outflow system. This causes the intraocular pressure (IOP) to increase which can cause damage to the optic nerve. In open-angle glaucoma, the anterior chamber angle remain unblocked, however there is still typically an increased resistance of aqueous humor outflow again increasing the IOP. There are cases in open-angle glaucoma when optic nerve damage occurs despite having normal IOP levels (10-21mmHg). In fact, surveys have shown that 20-52% of patients with glaucoma have IOP within the normal range [114]. This is called normal pressure or low tension glaucoma and can occur despite normal or only slightly increased aqueous outflow resistance.

Glaucoma is largely asymptomatic until late stages of the disease, and as such its presence often goes unnoticed by patients until visual problems arise. Once diagnosed, treatment is focused on preventing further progression of the disease as the glaucomas are irreversible. The only risk factor of glaucoma that can currently be treated is intraocular pressure (IOP) levels. Upon diagnosis, the practitioner will determine a “target” IOP level, typically 30-50% lower than the patients baseline IOP, and prescribe any number of methods in an attempt to reach this target, including drug treatment, laser therapy, or surgery. Reducing IOP is currently the only treatment of proven benefit and does stop or significantly slow down the progression of glaucoma in most patients. There is, however, large variation in effectiveness between individuals with some having no change in the rate of disease progression.

Changes in the optic nerve head generally precede visual field loss and a significant amount of optic nerve and nerve fiber damage can occur before any changes occur in the visual field. In order to detect glaucoma, then, practitioners examine the patients optic disc and retinal nerve fibre layer. Indicators of glaucoma are the loss or degradation of the neuroretinal rim (which causes the optic cup to enlarge and deepen), thinning of the retinal nerve fiber layer, and optic disc hemorrhages. Note that, though elevated IOP is considered an important risk factor for glaucoma, it is not involved in diagnosis.

The hemodynamics in the optic nerve head may also play a role in glaucoma. Hemorrhages at the optic nerve head are fairly common and considered a risk factor of glaucoma [114]. Thus, optical perfusion and impaired blood flow in the central retinal artery and optic nerve head may cause damage to the retinal ganglion cells through a decrease in oxygen and nutrients [54].

1.1.1 Basic biology

The visible portion of the optic nerve is the superficial nerve fiber layer. Below this is the prelaminar layer which lines up with the choroid (the pigmented vascular layer of the eyeball between the retina and the sclera). These top two layers are comprised mostly of axons (about 95%) along with some astrocytes (about 5%). Below the prelaminar is the laminar region which includes the lamina

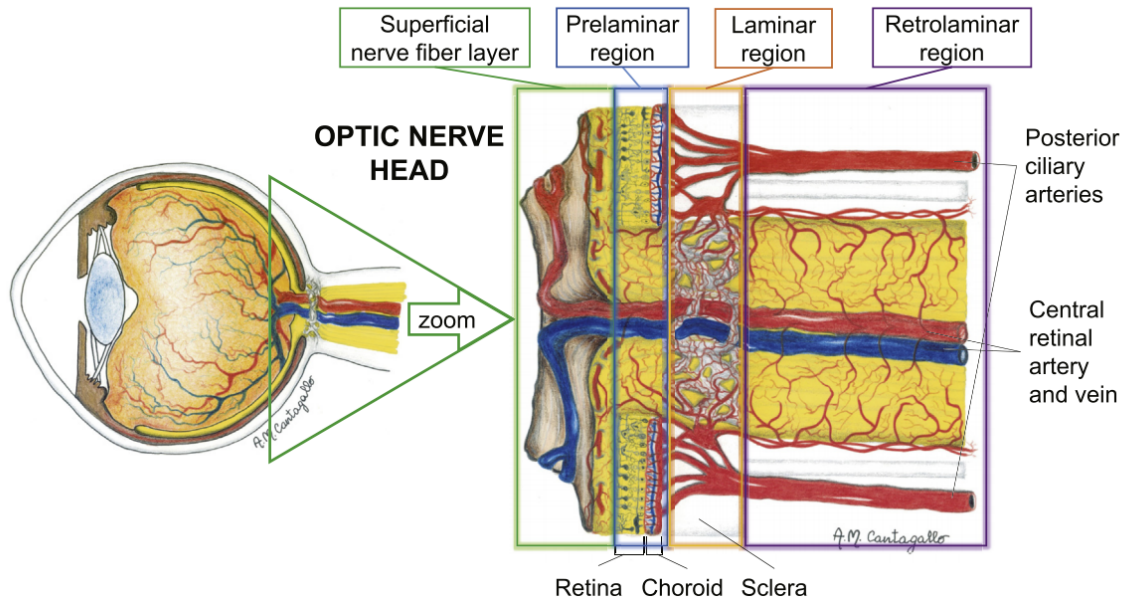


Figure 1.2 Anatomy and vascular supply of the optic nerve head as presented in [149].

cribrosa, a porous tissue through which the retinal ganglion cell axons and blood vessels pass through the optic nerve head. The lamina cribrosa is believed to be primarily where the damage occurs that causes the degeneration of retinal ganglion cells in glaucoma. Below the laminar region is the retrolaminar region where the nerve fibers (that is, the retinal ganglion cell axons) begin to take on myelination which causes the optic nerve to double in diameter.

There are 1.2 million retinal ganglion cell axons in the optic nerve. Retinal ganglion cells are neurons located in the inner retina that receive visual information from photoreceptors. They have long axons that go through the optic nerve and extend into the brain. It is the degeneration of these nerves that causes the cupping seen in the optic disc. When this cupping occurs, we also may see thinning of the retinal nerve fiber layer and ganglion cell layer as well as posterior bowing of the lamina cribrosa.

The blood supply for the optic nerve head comes from the ophthalmic artery and reaches the various regions of the optic nerve head through the central retinal artery and the posterior ciliary arteries. Blood in the optic nerve head drains almost entirely through the central retinal vein. Both the central retinal artery and the central retinal vein pass through the lamina cribrosa in order to reach the upper regions of the optic nerve head. The central retinal artery supplies the surface nerve fiber layer and the retrolaminar region with blood. The posterior ciliary branches into short posterior ciliary arteries which enter the sclera around the optic nerve and supply the laminar and prelaminar regions with blood. Note that, though the central retinal artery goes through the lamina cribrosa, its blood supply comes entirely from the posterior ciliary branches, not the central retinal

artery.

1.1.2 Intraocular pressure (IOP)

IOP is the fluid pressure (specifically that of the aqueous humor) inside the eye. Aqueous humor is the clear fluid that fills the space in the front of the eyeball between the lens and the cornea. Its purpose is to supply nutrients to and remove waste from the cornea and lens as these structures don't have blood vessels going to them. The production of aqueous humor is, on average, $2\mu\text{l}/\text{min}$, though the rate of production decreases with age, during sleep, and as a result of inflammation. The outflow of aqueous humor is primarily pressure dependent and occurs through the trabecular meshwork into the episcleral venous system, though there is also some outflow that is independent of pressure. IOP is determined by the balance between aqueous production and outflow and can be given by

$$P_o = \frac{F}{C} + P_v, \quad (1.1)$$

where P_o is IOP, P_v is the episcleral venous pressure, F is the rate of aqueous humor production, and C is the facility of aqueous humor outflow.

Mean IOP is normally 15.5mmHg and 10–21mmHg is considered a “normal” range though some people naturally have higher than normal IOP levels without developing glaucoma. There is also considerable fluctuation of IOP throughout the day, with more fluctuation seen in glaucoma patients than in healthy patients [119]. The importance of these fluctuations in glaucoma progression is a debated topic, with studies on the role of IOP fluctuation as an independent risk factor of glaucoma producing controversial results [12, 73, 119, 178]. However, some have suggested that these fluctuations could explain normal-pressure glaucoma and glaucomas that are not receptive to treatment [131]. Many have suggested that 24 hour monitoring of IOP is needed to better understand the role of IOP in glaucoma and the importance of IOP fluctuations [116, 132, 152, 178] and a number of studies with 24 hour IOP monitoring confirms this [3, 29, 93, 122]. While devices for monitoring IOP continuously and semi-continuously exist and are continuing to be further developed, they are rather costly and are not typically feasible in routine practice [13, 152, 178]. Without accessibility to 24 hour IOP monitoring devices, other strategies have been suggested in order to attempt to determine the range of fluctuation in IOP over 24 hours. Such tactics include taking IOP measurements when the patient is in different body positions (in particular, in a supine position) [73, 100, 137].

Many different activities are known to elevate IOP, including playing loud, high pitched notes on wind and brass instruments, certain positions in yoga, weight lifting, wearing a tight necktie, rubbing ones eyes, and sleeping [30, 86, 97, 131, 187]. The amount of IOP elevation varies depending upon activity, being only 2–4mmHg when wearing a tight necktie, up to elevations of 300mmHg and 400mmHg from eye compression like rubbing or massaging the eyes [131]. IOP elevation has even been found to occur in situations of psychological stress [40, 185].

1.1.3 Lamina cribrosa

The lamina cribrosa is believed to be the primary location of injury in glaucoma. A thin, collagenous tissue at the base of the optic nerve head that is believed to be an extension of the sclera, the lamina is covered in fenestrations of varying sizes that allow the optic nerve fibers to exit the eye. Mesh-like webs of astrocyte processes extend across each fenestration, while the fibrous trabeculae are composed of interlacing skeins of fine collagen fibers [70]. The lamina cribrosa also has a single canal in the center through which the central retinal artery and vein pass.

Providing structural and functional support to the retinal ganglion cell axons, the lamina cribrosa also acts as a barrier between the high pressure intraocular space and the low pressure retrolaminar space thus causing a pressure gradient across the lamina. The pressure difference between the IOP and retrolaminar tissue pressure (which is strongly correlated with cerebrospinal fluid pressure [136]) can cause stress and strain on the lamina cribrosa. When this pressure difference becomes too large, compression, deformation, and remodelling of the lamina cribrosa can occur [98, 190]. It is conjectured that these structural changes in the lamina could cause decreased rates of optic nerve axonal transport and mechanical damage to the nerve fibers [54, 98, 190].

This remodeling of the lamina cribrosa in glaucomatous eyes can result in posterior displacement [54, 99] from loss of collagen fibers in the top-centre of the lamina and recruitment of new collagen at the lower surface, resulting in cupping [50]. Changes in collagen in the optic nerve head has been suggested as a possible cause of glaucoma [91]. The content and composition of collagen molecules in the lamina cribrosa have been observed to be different in glaucoma and glaucoma suspected eyes in comparison to normal eyes [180]. Variation of collagen structure may affect the flexibility and resilience required by the lamina cribrosa in order to support the optic nerve fibers [91, 164]. Further, changes in tissue viscoelasticity have been found to be associated with glaucoma [68].

Studies have also found the lamina cribrosa to be significantly thinner in glaucoma patients in comparison to healthy patients [99]. A thin lamina cribrosa can't offer as much biomechanical support to the optic nerve fibers [91]. Also, the thinner the lamina cribrosa, the steeper the pressure gradient across it which may increase the lamina cribrosas susceptibility to glaucomatous optic neuropathy [91, 99]. If the steepness of the pressure gradient is the parameter of interest in susceptibility to glaucomatous damage, rather than the level of IOP, this would suggest that normal-pressure glaucoma may be glaucoma in patients with an abnormally thin lamina cribrosa [99]. Another explanation for normal-pressure glaucoma would be abnormally low retrolaminar tissue pressure [99, 190].

1.2 Poro-Elastic and Poro-Visco-Elastic Models

Poro-elastic models describe fluid flow through porous, deformable media. The mathematical theory for these models began in 1925 with Terzaghi's one-dimensional analysis [181]. Terzaghi, known as the father of soil mechanics, used this model to describe soil consolidation in one dimension with remarkable success. In 1941, Biot generalized the mathematical theory of consolidation to three dimensions, laying out the mathematical foundation for coupling deformation to flow in porous media and hence starting the mathematical development of poro-elasticity [36]. Currently, there are many mathematical results in the literature regarding their well-posedness [47, 141, 171, 176, 196] and associated numerical simulations [57, 146–148].

Terzaghi and Biot were interested in problems concerning soil consolidation in which the soil plays the role of the porous media. Since then, media such as clay and rock have also been modeled via poro-elasticity with many applications in problems in geophysics and petroleum engineering, along with soil consolidation [33, 41, 62, 69, 79, 92, 113, 118, 123, 154, 163, 167, 188, 189]. Other examples of poro-elastic structures include biological tissues, such as cartilage, bone, and vascularized tissues. As such, poro-elastic models have also found a variety of applications in bioengineering and medicine [50, 53, 58, 96, 117, 138, 162, 172, 179]. Specifically of interest to us has been their use in the study of tissue perfusion in the optic nerve head with a focus on the lamina cribrosa [50]. Unlike materials like soil and rock, most biological tissue exhibit both elastic and visco-elastic behavior resulting from the combined action of various components, including elastin, collagen, and extracellular matrix [186]. For this reason, one may want to account for the structural viscosity of the material as well, giving rise to a poro-visco-elastic system. As such, poro-visco-elastic models have also been applied to many problems in bioengineering and medicine [65, 109, 127, 153, 168, 177, 191, 194].

For both poro-elastic and poro-visco-elastic models, the equations of linear momentum (for the fluid-solid mixture) and mass balance (of the fluid) are strongly coupled through the permeability tensor which describes the ability of fluid to flow within the porous material. In general, permeability is a nonlinear function of porosity, with the structure of the nonlinearity being dependent on the geometrical architecture of the pores inside the solid matrix and on the physical properties of the fluid. Biological tissues have a mass density similar to that of water, so the assumption is made that the solid and fluid are incompressible components in the mixture. This leads to a simplified constitutive equation for fluid content, in comparison to Biot's model, resulting in it being equal to volumetric solid strain. Through the dependence of porosity on fluid content, the permeability becomes, implicitly, a nonlinear function of the volumetric solid strain. Due to their biological and medical applications, the fluid-solid mixture systems are considered on bounded domains, with appropriate, inhomogeneous, mixed boundary conditions for both the solid displacement and the fluid pressure. In most of these applications, the boundary conditions are the primary

drivers of the dynamics of the system. Their influence over and ability to control the solution is an important open question with beneficial implications in the development of novel strategies to improve experimental and clinical approaches in bio-engineering and medicine.

In [39], a theoretical and numerical analysis on nonlinearly coupled poro-elastic and poro-visco-elastic models with mixed boundary conditions was done. The focus of the analysis was on the role of visco-elasticity in the fluid-solid mixture and the regularity of the boundary data. An interesting interplay was found between the time regularity of the boundary traction and the presence or lack of structural viscosity (as well as the time regularity of the source of linear momentum) in guaranteeing boundedness of the solution of the coupled system. Specifically, in the case of purely poro-elastic models (i.e., no structural viscosity included), the boundary traction and linear momentum source needed to be H^1 in time in order to obtain a bounded solution (both solid displacement and fluid pressure) that is L^2 in time and H^1 in space. In contrast, the boundary traction and linear momentum only needed to be L^2 in time in order to get a bounded solution to the poro-visco-elastic system which is, for solid displacement, H^1 in space and time, and for fluid pressure, L^2 in time and H^1 in space. In addition, numerical simulations performed on a one dimensional version of the model (which retain the nonlinearity of the coupling) hinted at blow up in the fluid energy (which depends on the discharge velocity) as the boundary traction and the source of linear momentum lost H^1 smoothness in time when structural viscosity is not present in the system. These results can have tremendous implications in biological applications where sources present in the system can, physiologically, have sudden changes in time. For example, IOP is known to physiologically change suddenly. This potential blow up in the discharge velocity then indicates that physiological changes in sources can induce pathological changes in the dynamics of the coupling if visco-elasticity is not present in the structure. For the lamina cribrosa, this implies that physiological changes in the IOP can induce pathological changes in the hemodynamics of the lamina if the viscoelasticity provided by the collagen fibers is not intact.

The work presented here extends the analysis done in [39]. Our goal is to further investigate the interplay between boundary conditions and structural viscosity through a numerical sensitivity analysis on the poro-elastic and poro-visco-elastic models introduced in [39] with respect to the imposed boundary data. Though the theoretical analysis in [39] does not indicate any differences in regularity requirements on the boundary flux condition, we still consider the sensitivities of the solution to this condition and compare these sensitivities to sensitivities with respect to the boundary traction. Results obtained in the purely elastic case are compared to results obtained in the visco-elastic case and we also look at how varying the amount of structural viscosity in the system affects the results. Sensitivity analysis can provide valuable information on how the fluid-mechanical responses are affected by changes in boundary data. It can also reveal which parameters are most important in the system and can effectively be used as controls. This work is intended as a precursor to relevant control and optimization problems for the poro-visco-elastic models which

can inform novel strategies to improve experimental and clinical approaches in bioengineering and medicine.

1.2.1 Model Derivation

We will describe here the derivation of the poro-visco-elastic model in question. We note that the theoretical work on well-posedness in [39] was done in the general three dimensions, however for computational sake, we consider only the one dimensional model. For these reasons, we will first present the model in three dimensions before briefly describing its one dimensional analog. Throughout this section, symbols which are not bold denote scalar quantities or functions.

1.2.1.1 Three Dimensional Model

Let $\Omega \subset \mathbb{R}^3$ be an open domain occupied by the fluid-solid mixture with boundary $\Gamma = \partial\Omega$. Taking \mathbf{x} to be the position vector of each point in the body with respect to the Cartesian reference frame, let $V(\mathbf{x}, t) \subset \Omega$ be an arbitrary representative elementary volume (that is, the smallest volume one can take a measurement of that will yield a value representative of the whole) centered at \mathbf{x} at time t and $V_f(\mathbf{x}, t) \subset V(\mathbf{x}, t)$ be the portion of the elementary volume occupied by the fluid component. Then, assuming the solid is fully saturated by the fluid, the porosity ϕ is given by the volumetric fraction of the fluid component,

$$\phi(\mathbf{x}, t) = \frac{V_f(\mathbf{x}, t)}{V(\mathbf{x}, t)}. \quad (1.2)$$

We can then define the fluid content ζ to be

$$\zeta = \phi(\mathbf{x}, t) - \phi_0(\mathbf{x}), \quad (1.3)$$

where $\phi_0(\mathbf{x})$ is the baseline porosity. Under the assumptions of negligible inertia, small deformations, and incompressible mixture components [9, 77, 115, 120, 150], the following balance equations describe the motion of the poro-visco-elastic material:

$$\zeta_t + \nabla \cdot \mathbf{v} = S(\mathbf{x}, t) \quad (1.4)$$

and

$$\nabla \cdot \boldsymbol{\sigma} + \mathbf{F} = \mathbf{0}, \quad (1.5)$$

where \mathbf{v} is the discharge velocity (or Darcy velocity), $\boldsymbol{\sigma}$ is the total stress tensor of the mixture, S is the net volumetric fluid production rate, and \mathbf{F} is a body force per unit of volume. Note that Eq. 1.4 describes the balance of mass of the fluid component while Eq. 1.5 describes the the balance of linear momentum for the fluid-solid mixture.

1.2.1.1.1 Constitutive equations

We complete the balance equations with the following constitutive equations.

Total stress The total stress $\boldsymbol{\sigma}$ is comprised of both the elastic and the visco-elastic stresses ($\boldsymbol{\sigma}_e$ and $\boldsymbol{\sigma}_v$ respectively), which are given by

$$\boldsymbol{\sigma}_e = 2\mu_e \boldsymbol{\epsilon}(\mathbf{u}) + \lambda_e (\nabla \cdot \mathbf{u}) \mathbf{I} \quad (1.6)$$

and

$$\boldsymbol{\sigma}_v = \frac{\partial}{\partial t} [2\mu_v \boldsymbol{\epsilon}(\mathbf{u}) + \lambda_v (\nabla \cdot \mathbf{u}) \mathbf{I}], \quad (1.7)$$

where \mathbf{u} is the solid displacement, $\mu_e, \lambda_e, \mu_v, \lambda_v$ are the Lamé elastic and visco-elastic parameters (respectively), \mathbf{I} is the identity tensor, and $\boldsymbol{\epsilon}(\mathbf{u}) = \frac{1}{2}(\nabla \mathbf{u} + (\nabla \mathbf{u})^T)$ is the symmetric part of the gradient. The total stress is then given by

$$\boldsymbol{\sigma} = \boldsymbol{\sigma}_e + \delta \boldsymbol{\sigma}_v - p \mathbf{I}, \quad (1.8)$$

where p is the fluid pressure (or Darcy pressure) and $\delta \geq 0$ is a parameter indicating the extent to which the model includes structural viscosity. Note that, if $\delta = 0$, we are looking at the purely elastic problem.

Discharge velocity The discharge velocity \mathbf{v} is given by Darcy's law and takes the form

$$\mathbf{v} = -\mathbf{K}(\phi) \nabla p, \quad (1.9)$$

where \mathbf{K} is the permeability tensor. We assume the permeability is a function of porosity ϕ and a multiple of the identity tensor. That is,

$$\mathbf{K} = k(\phi) \mathbf{I}, \quad (1.10)$$

where

$$k(\phi) = k_{ref} f_k(\phi). \quad (1.11)$$

Here, k_{ref} is a reference value for the permeability of the mixture and f_k is a function (often times nonlinear) that depends upon the geometrical architecture of the pores inside the deformable matrix and the physical properties of the fluid. In the following analysis, we will consider f_k to either be constant (in which case we take $k = k_{ref}$) or given by the Carman-Kozeny formula for Newtonian fluid flow through spherical particles [90]:

$$f_k(\phi) = \frac{\phi^3}{(1-\phi)^2}. \quad (1.12)$$

Note that the form of f_k determines the type of coupling occurring between the balance of mass and balance of linear momentum equations. That is, if f_k is linear, it is a linear coupling, and, similarly, if f_k is nonlinear, it is a nonlinear coupling. An important point of distinction is that a linear coupling does not necessarily mean the system itself is linear. Only if f_k is constant do we get a fully linear system. Otherwise, the system itself is nonlinear regardless of whether or not the coupling between the balance equations is.

Fluid content The fluid content, given above by Eq. 1.3, can also be written in the form given by Biot in his 1941 work [36],

$$\zeta = c_0 p + \alpha \nabla \cdot \mathbf{u}, \quad (1.13)$$

where c_0 is the constrained specific storage coefficient and α is the Biot-Willis coefficient. However, from our assumption of incompressibility of the fluid and solid components of the mixture we have $c_0 = 0$ and $\alpha = 1$ [62] so that the fluid content becomes

$$\zeta = \nabla \cdot \mathbf{u}. \quad (1.14)$$

Since fluid content is also defined to be the difference between porosity and a baseline value for that porosity (see Eq. 1.3), we can now write porosity as a function of dilation $\nabla \cdot \mathbf{u}$:

$$\phi(\nabla \cdot \mathbf{u}) = \nabla \cdot \mathbf{u} - \phi_0. \quad (1.15)$$

Thus, we can consider permeability \mathbf{K} to be a function of the solid dilation:

$$\mathbf{K}(\phi(\nabla \cdot \mathbf{u})) = \mathbf{K}(\nabla \cdot \mathbf{u}). \quad (1.16)$$

1.2.1.1.2 Boundary and initial conditions

We finish the model description with the following initial and boundary conditions.

Boundary conditions For the boundary, we take $\Gamma = \Gamma_N \cup \Gamma_D$ where $\Gamma_D = \Gamma_{D,p} \cup \Gamma_{D,v}$. Note here that we do allow $\bar{\Gamma}_N \cap \bar{\Gamma}_D$ to possibly be nonempty [39]. The subscripts N and D denote the portions of the boundary for which we impose conditions on the stress and displacement, respectively. The subscripts p and v indicate conditions imposed on the fluid pressure and discharge velocity, respectively. The boundary conditions then are given by

$$\boldsymbol{\sigma} \mathbf{n} = \mathbf{g}, \quad \mathbf{v} \cdot \mathbf{n} = 0, \quad \text{on } \Gamma_N, \quad (1.17)$$

$$\mathbf{u} = \mathbf{0}, \quad p = 0, \quad \text{on } \Gamma_{D,p}, \quad (1.18)$$

$$\mathbf{u} = \mathbf{0}, \quad \mathbf{v} \cdot \mathbf{n} = \psi, \quad \text{on } \Gamma_{D,v}, \quad (1.19)$$

where \mathbf{n} is the outward unit normal and \mathbf{g} and ψ are given functions of space and time that denote the boundary traction and flux condition, respectively.

Initial conditions The choice for initial condition will depend upon the value of δ . That is, if $\delta > 0$ we assume

$$\mathbf{u}(\mathbf{x}, 0) = \mathbf{u}^0 \quad (1.20)$$

in Ω .

If $\delta = 0$, then only the fluid content $\zeta = \nabla \cdot \mathbf{u}$ undergoes time differentiation. As a result, we only need a condition on $\nabla \cdot \mathbf{u}$. So, we assume

$$\nabla \cdot \mathbf{u} = d_0, \quad (1.21)$$

where d_0 is such that there exists some \mathbf{u}^0 for which $\nabla \cdot \mathbf{u}^0 = d_0$.

1.2.1.1.3 Full system

The entire system together is given by

$$\left\{ \begin{array}{ll} \nabla \cdot \boldsymbol{\sigma} = -\mathbf{F}, & \text{in } \Omega \times (0, T), \\ \zeta_t + \nabla \cdot \mathbf{v} = S(\mathbf{x}, t), & \text{in } \Omega \times (0, T), \\ \boldsymbol{\sigma} \mathbf{n} = \mathbf{g}, \quad \mathbf{v} \cdot \mathbf{n} = 0, & \text{on } \Gamma_N \times (0, T), \\ \mathbf{u} = \mathbf{0}, \quad p = 0, & \text{on } \Gamma_{D,p} \times (0, T), \\ \mathbf{u} = \mathbf{0}, \quad \mathbf{v} \cdot \mathbf{n} = \psi, & \text{on } \Gamma_{D,v} \times (0, T), \\ IC(\delta) & \text{for } t = 0, \text{ in } \Omega, \end{array} \right. \quad (1.22)$$

where $IC(\delta)$ is given by Eq. 1.20 when $\delta > 0$ and by Eq. 1.21 when $\delta = 0$.

1.2.1.2 One Dimensional Model

Though the theoretical analysis referenced in Section 1.2.2 and throughout this chapter was done for the general three dimensional system, the computations are done on a one dimensional version of the model. Physically, one can interpret the one dimensional poro-visco-elastic model as being a slice of a porous, deformable media. We here briefly describe that one dimensional system. Unless otherwise specified, everything here is defined the same as it is in Section 1.2.1.1.

We take the open interval (x_0, x_f) to be our spatial domain with boundary $\{x_0, x_f\}$ and length

$L = x_f - x_0$. The balance equations take the form

$$\frac{\partial \zeta}{\partial t} + \frac{\partial v}{\partial x} = S(x, t) \quad (1.23)$$

and

$$\frac{\partial \sigma}{\partial x} + F = 0, \quad (1.24)$$

where S is the fluid production rate and F is the body force. We note that this is the one-dimensional equivalence to Eq. 1.4 and Eq. 1.5.

1.2.1.2.1 Constitutive equations

The different appearance of the constitutive equations mainly comes from the fact that the spatial derivative of u now represents two physically different quantities, the strain and the dilation of the solid. This is due to the fact that, mathematically, the divergence and the gradient of a “one dimensional vector” are the same.

Total stress In one dimension, the elastic (respectively visco-elastic) stress is merely a multiple of one spatial derivative (respectively one mixed derivative) of u . That is,

$$\sigma_e = (2\mu_e + \lambda_e) \frac{\partial u}{\partial x} \quad (1.25)$$

and

$$\sigma_v = (2\mu_v + \lambda_v) \frac{\partial^2 u}{\partial t \partial x}. \quad (1.26)$$

The total stress is then given by

$$\sigma = \sigma_e + \delta \sigma_v - p. \quad (1.27)$$

Discharge velocity The discharge velocity is given by

$$v = -k(\phi) \frac{\partial p}{\partial x}, \quad (1.28)$$

where $k(\phi) = k_{ref} f_k(\phi)$ is the permeability.

Fluid content The fluid content is given by both

$$\zeta = \phi(x, t) - \phi_0(x) \quad (1.29)$$

and

$$\zeta = \frac{\partial u}{\partial x}. \quad (1.30)$$

This gives us that porosity (and thus permeability) are now dependent upon $\frac{\partial u}{\partial x}$ as well. That is,

$$\phi = \frac{\partial u}{\partial x} + \phi_0 \quad (1.31)$$

and

$$k\left(\phi\left(\frac{\partial u}{\partial x}\right)\right) = k\left(\frac{\partial u}{\partial x}\right). \quad (1.32)$$

1.2.1.2.2 Boundary and initial conditions

Boundary conditions We still allow $\Gamma = \Gamma_D \cup \Gamma_N$ and $\Gamma_D = \Gamma_{D,p} \cup \Gamma_{D,v}$. However, we note that in this case $\Gamma = \{x_0, x_f\}$ so we must allow $\Gamma_N, \Gamma_{D,p}, \Gamma_{D,v}$ to be empty, but not all of them simultaneously. The boundary conditions are then given by

$$\sigma n = g, \quad v n = 0, \quad \text{for } x \in \Gamma_N, \quad t \in (0, T), \quad (1.33)$$

$$u = 0, \quad p = 0, \quad \text{for } x \in \Gamma_{D,p}, \quad t \in (0, T), \quad (1.34)$$

$$u = 0, \quad v n = \psi, \quad \text{for } x \in \Gamma_{D,v}, \quad t \in (0, T), \quad (1.35)$$

where n is the outward unit normal. That is, $n(x_0) = -1$ and $n(x_f) = 1$. In this case, g and ψ are given functions of time that represent the boundary traction and flux condition respectively.

Initial conditions The choice for initial condition again depends upon the value of δ . If $\delta > 0$, we assume

$$u(x, 0) = u_0(x) \quad (1.36)$$

in (x_0, x_f) , and if $\delta = 0$

$$\frac{\partial u}{\partial x}(x, 0) = d_0(x), \quad (1.37)$$

where d_0 is such that there exists some u_0 for which $\frac{\partial u_0}{\partial x} = d_0$.

1.2.1.2.3 Full system

The entire one-dimensional system is given by

$$\begin{cases} \frac{\partial \sigma}{\partial x} = -F, & \text{in } (x_0, x_f) \times (0, T), \\ \frac{\partial \zeta}{\partial t} + \frac{\partial v}{\partial x} = S(x, t), & \text{in } (x_0, x_f) \times (0, T), \\ \sigma n = g, \quad v n = 0, & \text{for } x \in \Gamma_N, \quad t \in (0, T), \\ u = 0, \quad p = 0, & \text{for } x \in \Gamma_{D,p}, \quad t \in (0, T), \\ u = 0, \quad v n = \psi, & \text{for } x \in \Gamma_{D,v}, \quad t \in (0, T), \\ IC(\delta) & \text{for } t = 0, \quad x \in (x_0, x_f), \end{cases} \quad (1.38)$$

where $IC(\delta)$ is given by Eq. 1.36 when $\delta > 0$ and by Eq. 1.37 when $\delta = 0$.

1.2.2 Well-posedness results

The existence of solutions to Eq. 1.22 was studied in [39] along with the derivation of some energy estimates. Those results are presented here as they support, inform, and add further meaning to our numerical study. The following notation will be used for the functional framework:

$$H_{\Gamma_*}^1(\Omega) = \{f \in H^1(\Omega) : \gamma[f]|_{\Gamma_*} = 0\},$$

where $\gamma[f]$ is the trace map of f from $H^1(\Omega)$ to $H^{1/2}(\Gamma)$. Let

$$V = H_{\Gamma_{D,p}}^1(\Omega), \quad \mathbf{V} = (H_{\Gamma_D}^1(\Omega))^3.$$

For inner products and norms, we will denote

$$(\cdot, \cdot) = (\cdot, \cdot)_{L^2(\Omega)}, \quad \langle \cdot, \cdot \rangle_{\Gamma} = \langle \cdot, \cdot \rangle_{L^2(\Gamma)}, \quad \|\cdot\| = \|\cdot\|_{L^2(\Omega)}.$$

Then, the elastic bilinear form can be given by

$$a(\mathbf{u}, \mathbf{w}) = (\nabla \cdot \mathbf{u}, \nabla \cdot \mathbf{w}) + (\nabla \mathbf{u}, \nabla \mathbf{w}) + (\nabla \mathbf{u}, (\nabla \mathbf{w})^T).$$

The definition of weak solution to the three dimensional system Eq. 1.22 for both $\delta > 0$ and $\delta = 0$ are given below.

Definition 1.2.1 (Visco-elastic solution) *A solution to Eq. 1.22 (with $\delta > 0$) is represented by the pair of functions $\mathbf{u} \in H^1(0, T; \mathbf{V})$ and $p \in L^2(0, T; V)$ such that:*

(a) the following relations are satisfied for any $\mathbf{w} \in \mathbf{V}$, $q \in V$, and $f \in C^\infty((0, T))$

$$\begin{aligned} \delta \int_0^T a(\mathbf{u}_t, \mathbf{w}) f \, dt + \int_0^T a(\mathbf{u}, \mathbf{w}) f \, dt - \int_0^T (p, \nabla \cdot \mathbf{w}) f \, dt &= \int_0^T \langle \mathbf{g}, \mathbf{w} \rangle_{\Gamma_N} f \, dt - \int_0^T (\mathbf{F}, \mathbf{w}) f \, dt, \\ \int_0^T (k(\nabla \cdot \mathbf{u}) \nabla p, \nabla q) f \, dt + \int_0^T (\nabla \cdot \mathbf{u}_t, q) f \, dt &= - \int_0^T \langle \psi, q \rangle_{\Gamma_{D,v}} f \, dt + \int_0^T (S, p) f \, dt. \end{aligned}$$

(b) the initial conditions $\mathbf{u}(\mathbf{x}, 0) = \mathbf{u}^0 \in \mathbf{V}$ and $\nabla \cdot \mathbf{u}(\mathbf{x}, 0) = d_0 \in L^2(\Omega)$ are given, and it is required that $\nabla \cdot \mathbf{u}^0 = d_0$ (in the $L^2(\Omega)$ sense).

Definition 1.2.2 (Elastic solution) A solution to Eq. 1.22 (with $\delta = 0$) is represented by the pair of functions $\mathbf{u} \in L^2(0, T; \mathbf{V})$ and $p \in L^2(0, T; V)$ such that:

(a) the following relations are satisfied for any $\mathbf{w} \in \mathbf{V}$, $q \in V$, and $f \in C_0^\infty((0, T))$:

$$\begin{aligned} \int_0^T a(\mathbf{u}, \mathbf{w}) f \, dt - \int_0^T (p, \nabla \cdot \mathbf{w}) f \, dt &= \int_0^T \langle \mathbf{g}, \mathbf{w} \rangle_{\Gamma_N} f \, dt - \int_0^T (\mathbf{F}, \mathbf{w}) f \, dt, \\ \int_0^T (k(\nabla \cdot \mathbf{u}) \nabla p, \nabla q) f \, dt - \int_0^T (\nabla \cdot \mathbf{u}, q) f' \, dt &= - \int_0^T \langle \psi, q \rangle_{\Gamma_{D,v}} f \, dt + \int_0^T (S, p) f \, dt. \end{aligned}$$

(b) for every $q \in V$, the term $(\nabla \cdot \mathbf{u}(t), q)$ uniquely defines an absolutely continuous function on $[0, T]$ and the initial condition $(\nabla \cdot \mathbf{u}(0), q) = (d_0, q)$ is satisfied.

We also have the following definitions for energy and data:

Definition 1.2.3 (Energy and data) Energy functionals for solutions and data are defined as follows

$$\begin{aligned} E(\mathbf{u}(t)) &\equiv \frac{1}{2} [\|\nabla \cdot \mathbf{u}(t)\|^2 + \|\nabla \mathbf{u}\|^2 + (\nabla \mathbf{u}, \nabla \mathbf{u}^T)], \\ E(p(t)) &= E_{\mathbf{u}}(p(t)) \equiv (k(\nabla \cdot \mathbf{u}) \nabla p, \nabla p), \\ DATA_0 \Big|_0^T &\equiv \int_0^T [\|\mathbf{g}(t)\|_{L^2(\Gamma_N)}^2 + \|\psi(t)\|_{L^2(\Gamma_{D,v})}^2 + \|S(t)\|_{L^2(\Omega)}^2 + \|\mathbf{F}(t)\|_{L^2(\Omega)}^2 \\ &\quad + \|\mathbf{g}_t(t)\|_{L^2(\Gamma_N)}^2 + \|\mathbf{F}_t(t)\|_{L^2(\Omega)}^2] dt + \sup_{[0, T]} [\|\mathbf{F}(t)\|^2 + \|\mathbf{g}(t)\|_{L^2(\Gamma_N)}^2], \\ DATA_\delta \Big|_0^T &\equiv \int_0^T [\|\mathbf{g}(t)\|_{L^2(\Gamma_N)}^2 + \|\psi(t)\|_{L^2(\Gamma_{D,v})}^2 + \|S(t)\|_{L^2(\Omega)}^2 + \|\mathbf{F}(t)\|_{L^2(\Omega)}^2] dt. \end{aligned}$$

Note that, when $\delta > 0$, the notion of time differentiability for the solution is stronger than in the case $\delta = 0$. As a consequence, time regularity requirements of the data (i.e., $DATA_*|_0^T$) are significantly weaker in the case $\delta > 0$ than in the case $\delta = 0$.

With these definitions in place, we can present the existence results along with the energy estimates obtained in [39]. We note that these theorems do require some assumptions stated in [39], however, since proving existence is not the goal here, we will omit them.

Theorem 1.2.1 (Existence of visco-elastic solutions) *Consider Eq. 1.22 with $\delta > 0$. Suppose the assumptions stated in [39] hold, and consider data of the form:*

$$\mathbf{F} \in L^2(0, T; (L^2(\Omega))^3), \quad S \in L^2(0, T; L^2(\Omega)), \quad (1.39)$$

$$\mathbf{g} \in L^2(0, T; (H^{1/2}(\Gamma_N))^3), \quad \psi \in L^2(0, T; L^2(\Gamma_{D,v})). \quad (1.40)$$

Then, there exists a visco-elastic solution as defined in Definition 1.2.1 satisfying the a priori bound

$$\begin{aligned} \sup_{t \in [0, T]} E(\mathbf{u}(t)) + \int_0^T [E(p(t)) + E(\mathbf{u}(t)) + E(\mathbf{u}_t)] dt \\ \leq C_1 \left[E(\mathbf{u}(0)) + \left(\frac{1}{1 + \delta} \right) DATA_\delta|_0^T \right] \exp\left(\frac{C_2 T}{1 + \delta} \right). \end{aligned} \quad (1.41)$$

Theorem 1.2.2 (Existence of elastic solutions) *Consider Eq. 1.22 with $\delta = 0$. Suppose the assumptions stated in [39] hold, and consider data of the form:*

$$\mathbf{F} \in H^1(0, T; (L^2(\Omega))^3), \quad S \in L^2(0, T; L^2(\Omega)), \quad (1.42)$$

$$\mathbf{g} \in H^1(0, T; (H^{1/2}(\Gamma_N))^3), \quad \psi \in L^2(0, T; L^2(\Gamma_{D,v})). \quad (1.43)$$

Then, there exists an elastic solutions as defined in Definition 1.2.2 satisfying the a priori bound

$$\sup_{t \in [0, T]} E(\mathbf{u}(t)) + \int_0^T [E(p(t)) + E(\mathbf{u}(t))] dt \leq C_1 [E(\mathbf{u}(0)) + DATA_0|_0^T] e^{C_2 T}. \quad (1.44)$$

We note that these theorems require a higher level of time regularity for the body force \mathbf{F} and boundary traction \mathbf{g} when $\delta = 0$ as opposed to $\delta > 0$. However, these requirements for the existence of solution were only shown to be sufficient, not necessary. Thus, from these theorems alone we do not know if this higher time regularity of the data is actually a requirement for solutions to the elastic problem to exist. In order to investigate this further, some preliminary numerics were done in [39] to test how the solution to the elastic system reacts when the boundary traction loses this H^1 smoothness in time. These numerical experiments hinted at fluid energy E_p blow up when \mathbf{g} went from being H^1 in time to L^2 in time. This was seen through the appearance of peaks in the energy E_p at points where \mathbf{g} experienced discontinuities in time. Further, the fluid pressure and discharge velocity were much less smooth in the elastic case in comparison to the visco-elastic case.

1.2.3 Discretization

We present here the discretization used in order to solve the system numerically. Following the discretization in [39], we first discretize in time using the backward Euler (BE) method and then discretize in space using the dual mixed hybridized finite element method. A Picard iteration is used to handle the implicit nature of the the BE method due to the nonlinearity of the system as well as the nonlinear dependence of permeability on the dilation of the solid in the stationary case.

This algorithm was tested in a number of cases for which the analytic solution is known and a grid refinement study was done. Details on this study can be found in [39]. In the stationary case, $\mathcal{O}(h^2)$ convergence is found for the hybrid and dual variables and a linear convergence rate $\mathcal{O}(h)$ is found for the primal variables [39] (the different kinds of variables are described in Section 1.2.3.4). Interestingly, these are optimal convergence rates for second order elliptic problems [39]. In the time dependent case, however, these convergence rates are lowered to linear for all variables except the total stress due to the BE method only being first order accurate [39].

1.2.3.1 Elastic Pressure Parameter

Before performing the discretization, we introduce the elastic pressure parameter \wp which is introduced in order to avoid displacement differentiation in the evaluation of the permeability. This helps to prevent the degradation of computational accuracy from numerical differentiation. This parameter also acts as a Lagrange multiplier to enforce material incompressibility which means it allows one to avoid the occurrence of locking in finite element discretizations when $\lambda_e \rightarrow \infty$ [94].

We define \wp by the equation

$$\frac{\wp}{\lambda_e} + \frac{\partial u}{\partial x} = 0. \quad (1.45)$$

With this parameter then, we evaluate $k\left(\frac{-\wp}{\lambda_e}\right)$ instead of $k\left(\frac{\partial u}{\partial x}\right)$ in computation. Note that no boundary conditions need to be imposed on \wp since the total stress is already prescribed on Γ_N in (1.33). The main thing that changes in the system with the addition of the elastic pressure parameter is the total stress, which is now given by

$$\sigma = 2\mu_e \frac{\partial u}{\partial x} - \wp + \delta \frac{\partial}{\partial t} \left[2\mu_v \frac{\partial u}{\partial x} - \frac{\lambda_v}{\lambda_e} \wp \right] - p. \quad (1.46)$$

Note that we only replace dilation terms with \wp .

1.2.3.2 Backward Euler Time Discretization

For discretization in time, we partition the temporal domain into N_t subintervals of length $\Delta t = T/N_t$. Let the partition be given by

$$\mathcal{T}_{\Delta t} = \{t_0 = 0, t_1, \dots, t_{N_t-1}, t_{N_t} = T\}$$

and define for any time dependent functions $f(t)$, $f^i = f(t_i)$ for all $i = 0, \dots, N_t$. Taking u^0 to be given by Eq. 1.36, applying the BE method to our system gives us the following scheme.

Given u^i and \wp^i , $i = 0, \dots, N_t - 1$, solve:

$$\frac{\partial \sigma^{i+1}}{\partial x} = -F^{i+1}, \quad (1.47)$$

$$\begin{aligned} \sigma^{i+1} = & 2\mu_e \frac{\partial u^{i+1}}{\partial x} - \wp^{i+1} - p^{i+1} + \delta \frac{1}{\Delta t} \left[2\mu_v \frac{\partial u^{i+1}}{\partial x} - \frac{\lambda_v}{\lambda_e} \wp^{i+1} \right] \\ & - \delta \frac{1}{\Delta t} \left[2\mu_v \frac{\partial u^i}{\partial x} - \frac{\lambda_v}{\lambda_e} \wp^i \right], \end{aligned} \quad (1.48)$$

$$\frac{\wp^{i+1}}{\lambda_e} + \frac{\partial u^{i+1}}{\partial x} = 0, \quad (1.49)$$

$$-\frac{\wp^{i+1}}{\lambda_e \Delta t} + \frac{\partial v^{i+1}}{\partial x} = S^{i+1} - \frac{\wp^i}{\lambda_e \Delta t}, \quad (1.50)$$

$$v^{i+1} = -k \left(-\frac{\wp^{i+1}}{\lambda_e} \right) \frac{\partial p^{i+1}}{\partial x}, \quad (1.51)$$

for x in Ω , with

$$\sigma^{i+1} n = g^{i+1}, \quad v^{i+1} n = 0, \quad \text{on } \Gamma_N, \quad (1.52)$$

$$u^{i+1} = 0, \quad p^{i+1} = 0, \quad \text{on } \Gamma_{D,p}, \quad (1.53)$$

$$u^{i+1} = 0, \quad v^{i+1} n = \psi^{i+1}, \quad \text{on } \Gamma_{D,v}. \quad (1.54)$$

1.2.3.3 Picard Iteration

A Picard iteration is used in order to deal numerically with the permeabilities nonlinear dependence on \wp . The Picard iteration updates our numerical scheme as follows.

Given $u^{(0)} = u^i$ and $\wp^{(0)} = \wp^i$, for each $j \geq 0$ until convergence, solve:

$$\frac{\partial \sigma^{(j+1)}}{\partial x} = -F^{i+1}, \quad (1.55)$$

$$\begin{aligned} \sigma^{(j+1)} = & 2\mu_e \frac{\partial u^{(j+1)}}{\partial x} - \wp^{(j+1)} - p^{(j+1)} + \delta \frac{1}{\Delta t} \left[2\mu_v \frac{\partial u^{(j+1)}}{\partial x} - \frac{\lambda_v}{\lambda_e} \wp^{(j+1)} \right] \\ & - \delta \frac{1}{\Delta t} \left[2\mu_v \frac{\partial u^i}{\partial x} - \frac{\lambda_v}{\lambda_e} \wp^i \right], \end{aligned} \quad (1.56)$$

$$\frac{\wp^{(j+1)}}{\lambda_e} + \frac{\partial u^{(j+1)}}{\partial x} = 0, \quad (1.57)$$

$$-\frac{\wp^{(j+1)}}{\lambda_e \Delta t} + \frac{\partial v^{(j+1/2)}}{\partial x} = S^{i+1} - \frac{\wp^i}{\lambda_e \Delta t}, \quad (1.58)$$

$$v^{(j+1/2)} = -k \left(-\frac{\wp^{(j)}}{\lambda_e} \right) \frac{\partial p^{(j+1)}}{\partial x}, \quad (1.59)$$

for x in Ω , with

$$\sigma^{(j+1)} n = g^{i+1}, \quad v^{(j+1)} n = 0, \quad \text{on } \Gamma_N, \quad (1.60)$$

$$u^{(j+1)} = 0, \quad p^{(j+1)} = 0, \quad \text{on } \Gamma_{D,p}, \quad (1.61)$$

$$u^{(j+1)} = 0, \quad v^{(j+1)} n = \psi^{i+1}, \quad \text{on } \Gamma_{D,v}. \quad (1.62)$$

The Picard iteration is considered to have converged at the first value j^* such that

$$\frac{\|X^{(j^*)} - X^{(j^*-1)}\|}{\|X^{(j^*)}\|} < \varepsilon,$$

where ε is some prescribed tolerance and X is any variable in the set $\{u_h, p_h, \hat{u}_h, \hat{p}_h, \sigma_h, v_h\}$. These variables are defined below in Section 1.2.3.4. Note that the “half step” $j + 1/2$ indicates the variable is being computed using variables from both the next step (i.e., $j + 1$) and the previous step (i.e., j).

1.2.3.4 Dual Mixed Hybridized Finite Elements

The dual mixed hybridized (DMH) finite element method treats the dual variables σ and v as independent variables along with the primal variables u and p . The lowest order Raviart-Thomas mixed finite element pair is used for the dual and primal variables. This spatial discretization will only provide weak satisfaction of the Dirichlet boundary conditions. To address this, a hybridization technique which introduces the hybrid variables \hat{u} and \hat{p} (described in more detail below) and allows the Dirichlet boundary conditions to be satisfied in a strong sense [39].

We start by reformulating the system Eq. 1.55 - Eq. 1.62. For ease of notation, we drop all super-

scripts denoting both time steps in the BE method and iterations of the Picard iteration. The only superscripts that we will maintain are those indicating a variable from a previous time step and those indicating the time step of known functions such as F, S, g , and ψ . The exception to this will be the superscript on the permeability k , which will be left as a reminder that the permeability is evaluated one iteration behind everything else in the Picard iteration. Rearranging the equations, integrating Eq. 1.55 - Eq. 1.59 against test functions ξ, τ , and utilizing integration by parts gives us the following formulation of the system already discretized temporally:

$$\int_{\Omega} \xi \frac{\partial \sigma^{(j+1)}}{\partial x} dx = - \int_{\Omega} F^{i+1} \xi dx, \quad (1.63)$$

$$\begin{aligned} \int_{\Omega} m_u^{-1} \sigma \tau dx + \int_{\Omega} u \frac{\partial \tau}{\partial x} dx - \int_{\Gamma} u \tau n ds + \frac{m_p}{m_u} \int_{\Omega} \wp \tau dx + \frac{1}{m_u} \int_{\Omega} p \tau dx \\ = \frac{\delta}{\Delta t} \frac{2\mu_v + \lambda_v}{\lambda_e} \frac{1}{m_u} \int_{\Omega} \wp^i \tau dx, \end{aligned} \quad (1.64)$$

$$\frac{1}{\lambda_e} \int_{\Omega} \wp \xi + \int_{\Gamma} u \xi n ds - \int_{\Omega} u \frac{\partial \xi}{\partial x} dx = 0, \quad (1.65)$$

$$-\frac{1}{\lambda_e \Delta t} \int_{\Omega} \wp \xi dx + \int_{\Omega} \xi \frac{\partial v}{\partial x} dx = \int_{\Omega} S^{i+1} \xi dx - \frac{1}{\lambda_e \Delta t} \int_{\Omega} \wp^i \xi dx, \quad (1.66)$$

$$\int_{\Omega} k^{-1} v \tau dx - \int_{\Omega} p \frac{\partial \tau}{\partial x} dx + \int_{\Gamma} p \tau n ds = 0, \quad (1.67)$$

for $x \in \Omega$, where n is the unit outward normal, $m_u = 2\left(\mu_e + \frac{\delta\mu_v}{\Delta t}\right)$, and $m_p = 1 + \frac{\delta\lambda_v}{\Delta t\lambda_e}$. Note that the only terms from the previous time step before this formulation were $\frac{\partial u^i}{\partial x}$ and \wp^i . Here, we use Eq. 1.45 to reduce the number of terms from the previous time step to just one by substituting $-\frac{\wp^i}{\lambda_e}$ for $\frac{\partial u^i}{\partial x}$.

We now introduce the finite element framework. Let $\{\mathcal{K}_h\}$ be a partition of the domain Ω into subintervals $K_k = (x_{k-1}, x_k)$, $k = 1, \dots, N_h$ of length $h = L/N_h$ for some $N_h \in \mathbb{N}$. Denote the midpoint of K_k by \bar{x}_k and the boundary of K_k by $\partial K_k = \{x_{k-1}, x_k\}$. The associated unit normal vector is given by n_k , where $n_k = -1$ at $x = x_{k-1}$ and $n_k = 1$ at $x = x_k$. Now, let $\mathcal{P}_q(K_k)$ be the set of polynomials in

K_k of degree less than or equal to q . The finite element spaces are then given by

$$U_h = \{u_h \in L^2(\Omega) : u_h|_{K_k} \in \mathcal{P}_0(K_k), \forall K_k \in \mathcal{K}_h\}, \quad (1.68)$$

$$V_h = \{v_h \in L^2(\Omega) : v_h|_{K_k} \in \mathcal{P}_1(K_k), \forall K_k \in \mathcal{K}_h\}, \quad (1.69)$$

$$M_h = \{\mu_h : \{x_0, \dots, x_{N_h}\} \rightarrow \mathbb{R}^{N_h+1} : |\mu_h| < \infty, \forall x_k \in \{x_0, \dots, x_{N_h}\}\}, \quad (1.70)$$

$$M_{h,0}^u = \{\mu_h \in M_h : \mu_h = 0 \text{ on } \Gamma_D\}, \quad (1.71)$$

$$M_{h,0}^p = \{\mu_h \in M_h : \mu_h = 0 \text{ on } \Gamma_{D,p}\}. \quad (1.72)$$

In addition, we set $W_h^u = V_h \times U_h \times M_{h,0}^u$ and $W_h^p = V_h \times U_h \times M_{h,0}^p$. The spaces $M_h, M_{h,0}^u$ and $M_{h,0}^p$ are for the hybrid variables \hat{u}, \hat{p} which are the restrictions of u and p to the nodes of the FE mesh (i.e., to $\{x_0, \dots, x_{N_h}\}$). We denote by u_h, p_h, σ_h, v_h the approximations of u, p, σ, v , respectively, in the interior of each element $K_k \in \mathcal{K}_h$, and by \hat{u}_h, \hat{p}_h the approximations of \hat{u}, \hat{p} respectively. That is, \hat{u}_h, \hat{p}_h approximates u, p respectively, at each node of the FE mesh (i.e., $\{x_0, \dots, x_{N_h}\}$). Then, taking $\mathbf{U}_h := (\sigma_h, u_h, \hat{u}_h)^T$ and $\mathbf{P}_h := (v_h, p_h, \hat{p}_h)^T$, the finite element space for \mathbf{U}_h is W_h^u and for \mathbf{P}_h is W_h^p . Now, also letting \wp_h be the approximation of \wp in the interior of each element $K_k \in \mathcal{K}_h$, the finite element approximation of (1.55)-(1.62) is:

Find $(\mathbf{U}_h, \wp_h, \mathbf{P}_h) \in (W_h^u \times U_h \times W_h^p)$ such that, for all $(\tau_h, \xi_h, \mu_h^u, \mu_h^p) \in V_h \times U_h \times M_{h,0}^u \times M_{h,0}^p$,

$$B(\xi_h, \sigma_h) = -(F^{i+1}, \xi_h)_h, \quad (1.73)$$

$$\begin{aligned} A(m_u^{-1} \sigma_h, \tau_h) + B(u_h, \tau_h) - C(\hat{u}_h, \tau_h) \\ + \frac{m_p}{m_u} D(\wp_h, \tau_h) + \frac{1}{m_u} D(p_h, \tau_h) = \frac{\delta(\lambda_v + 2\mu_v)}{\Delta t \lambda_e m_u} D(\wp_h^i, \tau_h), \end{aligned} \quad (1.74)$$

$$\frac{1}{\lambda_e} (\wp_h, \xi_h)_h + G(\hat{u}_h, \xi_h) = 0, \quad (1.75)$$

$$-\frac{1}{\lambda_e \Delta t} (\wp_h, \xi_h)_h + B(\xi_h, v_h) = (S^{i+1}, \xi_h)_h - \frac{1}{\lambda_e \Delta t} (\wp_h^i, \xi_h)_h, \quad (1.76)$$

$$A(k^{-1} v_h, \tau_h) - B(p_h, \tau_h) + C(\hat{p}_h, \tau_h) = 0, \quad (1.77)$$

$$C(\mu_h^u, \sigma_h) = g^{i+1} \mu_h^u|_{\Gamma_N}, \quad (1.78)$$

$$C(\mu_h^p, v_h) = \psi^{i+1} \mu_h^p|_{\Gamma_{D,v}}, \quad (1.79)$$

where the bilinear forms A, B, C, D, G are given by

$$A(a^{-1}J_h, \tau_h) = \sum_{K_k \in \mathcal{K}_h} \int_{K_k} a^{-1} J_h \tau_h dx, \quad \forall (J_h, \tau_h) \in V_h \times V_h, \quad (1.80)$$

$$B(q_h, \tau_h) = \sum_{K_k \in \mathcal{K}_h} \int_{K_k} q_h \frac{\partial \tau_h}{\partial x} dx, \quad \forall (q_h, \tau_h) \in U_h \times V_h, \quad (1.81)$$

$$C(\mu_h, J_h) = \sum_{K_k \in \mathcal{K}_h} \int_{\partial K_k} \mu_h J_h n_k ds, \quad \forall (\mu_h, J_h) \in M_{h,0} \times V_h, \quad (1.82)$$

$$D(q_h, \tau_h) = \sum_{K_k \in \mathcal{K}_h} \int_{K_k} a q_h \tau_h dx, \quad \forall (q_h, \tau_h) \in U_h \times V_h, \quad (1.83)$$

$$G(\mu_h, \xi_h) = \sum_{K_k \in \mathcal{K}_h} \int_{\partial K_k} \mu_h \xi_h n_k ds, \quad \forall (\mu_h, \xi_h) \in M_{h,0} \times U_h, \quad (1.84)$$

along with

$$(f, g)_h = \sum_{K_k \in \mathcal{K}_h} \int_{K_k} f g dx.$$

Note that Eq. 1.78 and Eq. 1.79 are included to incorporate Neumann type boundary conditions. The system Eq. 1.73 - Eq. 1.79 constitutes a linear algebraic system for the seven scalar dependent variables in $\mathbf{U}_h, \wp_h, \mathbf{P}_h$. At first glance, this system appears to have an exceptional number of unknowns which may imply extremely large computational costs. However, almost all of these equations are local and, as such, the primal and dual variables (u_h, p_h and σ_h, v_h , respectively) can be rewritten in terms of the hybrid variables \hat{u}_h, \hat{p}_h and the problem data. This elimination procedure is called static condensation and effectively reduces the computational cost of solving this system so that it is competitive with standard displacement-based approaches [39].

1.2.3.5 Static condensation

Since static condensation is an elimination process that utilizes the local nature of the system Eq. 1.73 - Eq. 1.79, we will here restrict ourselves to a single arbitrary element $K_k \in \mathcal{K}_h$. On such an element, the bilinear forms Eq. 1.80 - Eq. 1.84 become small matrices corresponding to their action on the single element. Specifically, we let $\mathbf{A}, \mathbf{C} \in \mathbb{M}^{2 \times 2}$, $\mathbf{B}, \mathbf{G} \in \mathbb{M}^{1 \times 2}$, and $\mathbf{D} \in \mathbb{M}^{2 \times 1}$ represent the actions of $A(\cdot, \cdot), C(\cdot, \cdot), B(\cdot, \cdot), G(\cdot, \cdot), D(\cdot, \cdot)$, respectively, on the arbitrary element K_k . Further, we let $\boldsymbol{\sigma}, \mathbf{v}, \hat{\mathbf{u}}, \hat{\mathbf{p}} \in \mathbb{R}^{1 \times 2}$ and $\mathbf{u}, \mathbf{p}, \wp \in \mathbb{R}^{1 \times 1}$ represent the degrees of freedom for the restrictions of $\sigma_h, v_h, \hat{u}_h, \hat{p}_h$ and u_h, p_h, \wp_h , respectively, on arbitrary element K_k . Lastly, we will use the midpoint rule to approximate $(\cdot, \cdot)_h|_{K_k} = (\cdot, \cdot)_{L^2(K_k)}$.

We will start with the fluid phase. Noting that \mathbf{A} is invertible, from Eq. 1.76 we have

$$\mathbf{B}\mathbf{v} - \frac{h}{\lambda_e \Delta t} \wp = \mathcal{J}^{i+1}, \quad (1.85)$$

where

$$\mathcal{J}^{i+1} = hS^{i+1}(\bar{x}_k) - \frac{h}{\lambda_e \Delta t} \wp^i. \quad (1.86)$$

From Eq. 1.77 we get

$$\mathbf{v} = -k^{(j)} \mathbf{A}^{-1} [\mathbf{C}\hat{\mathbf{p}} - \mathbf{B}^T \mathbf{p}], \quad (1.87)$$

and from Eq. 1.75 we get

$$\wp = -\frac{\lambda_e}{h} \mathbf{G}\hat{\mathbf{u}}. \quad (1.88)$$

Now, substituting Eq. 1.87 and Eq. 1.88 into Eq. 1.85 we get

$$k^{(j)} \mathbf{B} \mathbf{A}^{-1} \mathbf{B}^T \mathbf{p} = k^{(j)} \mathbf{B} \mathbf{A}^{-1} \mathbf{C} \hat{\mathbf{p}} - \frac{h}{\Delta t} \mathbf{G} \hat{\mathbf{u}} + \mathcal{J}^{i+1}, \quad (1.89)$$

making \mathbf{p} a function of $\hat{\mathbf{p}}$ and $\hat{\mathbf{u}}$ as well as known values $S^{i+1}(\bar{x}_k)$ and \wp^i (note that \wp^i is a known quantity since it would have been found in the previous time step). To reflect this more clearly, we write

$$\boxed{\mathbf{p} = \mathcal{J} \hat{\mathbf{p}} + \mathcal{R} \hat{\mathbf{u}} + \mathcal{B}_p^{-1} \mathcal{J}^{i+1}}, \quad (1.90)$$

where

$$\mathcal{B}_p = k^{(j)} \mathbf{B} \mathbf{A}^{-1} \mathbf{B}^T, \quad (1.91)$$

$$\mathcal{J} = k^{(j)} \mathcal{B}_p^{-1} \mathbf{B} \mathbf{A}^{-1} \mathbf{C}, \quad (1.92)$$

$$\mathcal{R} = -\frac{h}{\Delta t} \mathcal{B}_p^{-1} \mathbf{G}. \quad (1.93)$$

Note, \mathcal{B}_p is symmetric positive definite so that its inverse is well-defined. Substituting Eq. 1.90 into Eq. 1.87 gives us

$$\boxed{\mathbf{v} = \mathcal{L}_{pp} \hat{\mathbf{p}} + \mathcal{L}_{pu} \hat{\mathbf{u}} + \mathbf{b}_p}, \quad (1.94)$$

where

$$\mathcal{L}_{pp} = -k^{(j)} \mathbf{A}^{-1} [\mathbf{C} - \mathbf{B}^T \mathcal{J}], \quad (1.95)$$

$$\mathcal{L}_{pu} = k^{(j)} \mathbf{A}^{-1} \mathbf{B}^T \mathcal{R}, \quad (1.96)$$

$$\mathbf{b}_p = k^{(j)} \mathbf{A}^{-1} \mathbf{B}^T \mathcal{B}_p^{-1} \mathcal{J}^{i+1}. \quad (1.97)$$

Thus, we see that \mathbf{v} can also be written as a function of $\hat{\mathbf{p}}, \hat{\mathbf{u}}$, and known quantities.

Continuing similarly with the solid phase, we have from Eq. 1.74

$$\frac{1}{m_u} \mathbf{A} \boldsymbol{\sigma} + \mathbf{B}^T \mathbf{u} - \mathbf{C}^T \hat{\mathbf{u}} + \frac{m_p}{m_u} \mathbf{D} \wp + \frac{1}{m_u} \mathbf{D} \mathbf{p} = \frac{\delta(\lambda_v + 2\mu_v)}{\Delta t \lambda_e m_u} \mathbf{D} \wp^i. \quad (1.98)$$

Rearranging this equation and substituting in Eq. 1.88 gives us

$$\boldsymbol{\sigma} = \mathcal{M} \hat{\mathbf{u}} - m_u \mathbf{A}^{-1} \mathbf{B}^T \mathbf{u} - \mathbf{A}^{-1} \mathbf{D} \mathbf{p} + r^i, \quad (1.99)$$

where

$$\mathcal{M} = \mathbf{A}^{-1} \left(m_u \mathbf{C} + \frac{\lambda_e m_p}{h} \mathbf{D} \mathbf{G} \right), \quad (1.100)$$

$$r^i = \frac{\delta(\lambda_v + 2\mu_v)}{\Delta t \lambda_e} \mathbf{A}^{-1} \mathbf{D} \wp^i. \quad (1.101)$$

Now, from Eq. 1.73, we have

$$\mathbf{B} \boldsymbol{\sigma} = -d^{i+1}, \quad (1.102)$$

where

$$d^{i+1} = h F^{i+1}(\bar{x}_k). \quad (1.103)$$

Substituting Eq. 1.90 and Eq. 1.99 into Eq. 1.102, we get

$$m_u \mathbf{B} \mathbf{A}^{-1} \mathbf{B}^T \mathbf{u} = \mathbf{B}(\mathcal{M} - \mathbf{A}^{-1} \mathbf{D} \mathcal{R}) \hat{\mathbf{u}} - \mathbf{B} \mathbf{A}^{-1} \mathbf{D} \mathcal{J} \hat{\mathbf{p}} + \mathbf{B}(r^i - \mathbf{A}^{-1} \mathbf{D} \mathcal{B}_p^{-1} \mathcal{J}^{i+1}) + a^{i+1}, \quad (1.104)$$

making \mathbf{u} a function of $\hat{\mathbf{p}}$ and $\hat{\mathbf{u}}$ as well as known values. To reflect this more clearly, we write

$$\boxed{\mathbf{u} = \tilde{\mathcal{R}} \hat{\mathbf{u}} + \tilde{\mathcal{J}} \hat{\mathbf{p}} + \mathcal{B}_u^{-1} f^{i+1}}, \quad (1.105)$$

where

$$\mathcal{B}_u = m_u \mathbf{B} \mathbf{A}^{-1} \mathbf{B}^T, \quad (1.106)$$

$$\tilde{\mathcal{J}} = -\mathcal{B}_u^{-1} \mathbf{B} \mathbf{A}^{-1} \mathbf{D} \mathcal{J}, \quad (1.107)$$

$$\tilde{\mathcal{R}} = \mathcal{B}_u^{-1} \mathbf{B}(\mathcal{M} - \mathbf{A}^{-1} \mathbf{D} \mathcal{R}), \quad (1.108)$$

$$f^{i+1} = \mathbf{B}(r^i - \mathbf{A}^{-1} \mathbf{D} \mathcal{B}_p^{-1} \mathcal{J}^{i+1}) + d^{i+1}. \quad (1.109)$$

Note, \mathcal{B}_u is symmetric positive definite so that its inverse is well-defined. Lastly, substituting Eq. 1.90 and Eq. 1.105 into Eq. 1.99, we get

$$\boxed{\boldsymbol{\sigma} = \mathcal{L}_{uu} \hat{\mathbf{u}} + \mathcal{L}_{up} \hat{\mathbf{p}} + \mathbf{b}_u}, \quad (1.110)$$

where

$$\mathcal{L}_{uu} = \mathcal{M} - \mathbf{A}^{-1}[m_u \mathbf{B}^T \tilde{\mathcal{R}} + \mathbf{D}\mathcal{R}], \quad (1.111)$$

$$\mathcal{L}_{up} = -\mathbf{A}^{-1}[m_u \mathbf{B}^T \tilde{\mathcal{J}} + \mathbf{D}\mathcal{J}], \quad (1.112)$$

$$\mathbf{b}_u = r^i - m_u \mathbf{A}^{-1} \mathbf{B}^T \mathcal{B}_u^{-1} f^{i+1} - \mathbf{A}^{-1} \mathbf{D} \mathcal{B}_p^{-1} \mathcal{J}^{i+1}. \quad (1.113)$$

Thus, we see that σ can also be written as a function of $\hat{\mathbf{p}}, \hat{\mathbf{u}}$, and known quantities.

1.2.3.6 Stiffness matrix

Having eliminated all variables except $\hat{\mathbf{p}}$ and $\hat{\mathbf{u}}$, we can now construct the stiffness matrix. This will follow from enforcing continuity on stress σ_h and discharge velocity v_h across elements. That is, if $\sigma_{K_k} = \begin{bmatrix} \sigma_{K_k}^1 \\ \sigma_{K_k}^2 \end{bmatrix}$ gives the degrees of freedom of the restriction of σ_h to K_k , then we must have $\sigma_{K_k}^2 = \sigma_{K_{k+1}}^1$ and similarly for v_h .

Using the notation $\mathcal{L}_{**}^{K_k} = \begin{bmatrix} L_{**}^{K_k,11} & L_{**}^{K_k,12} \\ L_{**}^{K_k,21} & L_{**}^{K_k,22} \end{bmatrix}$ and $\mathbf{b}_* = \begin{bmatrix} b_*^{K_k,1} \\ b_*^{K_k,2} \end{bmatrix}$ to denote the local matrices \mathcal{L}_{**} and \mathbf{b}_* , respectively, on element K_k , then from Eq. 1.110 we have

$$\sigma_{K_k}^2 = \mathcal{L}_{uu}^{K_k,21} \hat{u}_h^{k-1} + \mathcal{L}_{uu}^{K_k,22} \hat{u}_h^k + \mathcal{L}_{up}^{K_k,21} \hat{p}_h^{k-1} + \mathcal{L}_{up}^{K_k,22} \hat{p}_h^k + b_u^{K_k,2}, \quad (1.114)$$

where $\hat{u}_h(x_k) = \hat{u}_h^k$ and $\hat{p}_h(x_k) = \hat{p}_h^k$. Similarly,

$$\sigma_{K_{k+1}}^1 = \mathcal{L}_{uu}^{K_{k+1},11} \hat{u}_h^k + \mathcal{L}_{uu}^{K_{k+1},12} \hat{u}_h^{k+1} + \mathcal{L}_{up}^{K_{k+1},11} \hat{p}_h^k + \mathcal{L}_{up}^{K_{k+1},12} \hat{p}_h^{k+1} + b_u^{K_{k+1},1}. \quad (1.115)$$

Enforcing continuity on the stress then gives us

$$\begin{aligned} & -\mathcal{L}_{uu}^{K_k,21} \hat{u}_h^{k-1} + (\mathcal{L}_{uu}^{K_{k+1},11} - \mathcal{L}_{uu}^{K_k,22}) \hat{u}_h^k + \mathcal{L}_{uu}^{K_{k+1},12} \hat{u}_h^{k+1} \\ & - \mathcal{L}_{up}^{K_k,21} \hat{p}_h^{k-1} + (\mathcal{L}_{up}^{K_{k+1},11} - \mathcal{L}_{up}^{K_k,22}) \hat{p}_h^k + \mathcal{L}_{up}^{K_{k+1},12} \hat{p}_h^{k+1} = b_u^{K_k,2} - b_u^{K_{k+1},1}. \end{aligned} \quad (1.116)$$

This gives us the information need to create banded matrices \mathbf{M}_{uu} and \mathbf{M}_{up} as well as a vector $\underline{\mathbf{b}}_u$ such that

$$\begin{bmatrix} \mathbf{M}_{uu} & \mathbf{M}_{up} \end{bmatrix} \begin{bmatrix} \hat{\mathbf{u}} \\ \hat{\mathbf{p}} \end{bmatrix} = \underline{\mathbf{b}}_u,$$

where

$$\underline{\hat{\mathbf{u}}} = [\hat{u}_h^0, \hat{u}_h^1, \dots, \hat{u}_h^{N_h}]^T \quad \text{and} \quad \underline{\hat{\mathbf{p}}} = [\hat{p}_h^0, \hat{p}_h^1, \dots, \hat{p}_h^{N_h}]^T.$$

Following a similar process to enforce continuity on v_h , we get matrices \mathbf{M}_{pu} and \mathbf{M}_{pp} and vector $\underline{\mathbf{b}}_p$.

Putting it all together, we get the full system

$$\begin{bmatrix} \mathbf{M}_{uu} & \mathbf{M}_{up} \\ \mathbf{M}_{pu} & \mathbf{M}_{pp} \end{bmatrix} \begin{bmatrix} \underline{\hat{\mathbf{u}}} \\ \underline{\hat{\mathbf{p}}} \end{bmatrix} = \begin{bmatrix} \underline{\mathbf{b}_u} \\ \underline{\mathbf{b}_p} \end{bmatrix}. \quad (1.117)$$

The construction of the \mathbf{M}_{**} matrices and $\underline{\mathbf{b}}_*$ vectors comes almost entirely from the continuity condition of σ_h and v_h . The only exceptions are the first and last rows which may need to be adjusted to account for boundary conditions. For example, suppose $\Gamma_{D,p} = x_0$, $\Gamma_N = x_f$, and $\Gamma_{D,v} = \emptyset$. Then, to enforce the Dirichlet condition (i.e., the condition on $\Gamma_{D,p}$) we would set the first row of \mathbf{M}_{uu} and \mathbf{M}_{pp} to the first canonical vector (i.e., $[1, 0, \dots, 0]$), the first row of \mathbf{M}_{up} and \mathbf{M}_{pu} to all zeros, and the first entry of $\underline{\mathbf{b}}_u$ and $\underline{\mathbf{b}}_p$ to zero. To allow the Neumann condition (i.e., the condition on Γ_N), we would determine the last row of \mathbf{M}_{uu} and \mathbf{M}_{up} from the equation given by

$$\sigma_{K_{N_h}}^2 = g^{i+1}$$

and the last row of \mathbf{M}_{pu} and \mathbf{M}_{pp} from the equation given by

$$v_{K_{N_h}}^2 = 0.$$

1.3 Sensitivity Analysis

The purpose of a sensitivity analysis is to study what effect perturbations in system inputs has on the system output. Such analysis plays a critical role in many aspects of modeling and data analysis including in parameter selection and identifiability in inverse problem formulations [15, 21, 22], asymptotic theories for large sample size problems in statistics [25, 28, 60, 78, 166], studies on data set information content [24], and optimal experiment design [26, 27]. Here, we utilize a sensitivity analysis to inform potential control formulations in biomedical studies using poro-elastic and poro-visco-elastic models with the ultimate goal of informing novel strategies to improve experimental and clinical approaches in bioengineering and medicine. In particular, we look to perform a local sensitivity analysis on the poro-elastic and poro-visco-elastic models presented in Section 1.2.1 with respect to the two sources of boundary data: the boundary traction and flux.

A local sensitivity analysis seeks to determine the rate of change of solutions to a system with respect to varying inputs (such as parameters, boundary data, body forces, etc.). Mathematically, this boils down to computing the derivative of the solutions with respect to the input of interest. For illustrative purposes, supposed $f(x, t; \theta)$ is the solution to a system with parameters $\theta = [\theta_1, \dots, \theta_n]$ which can include initial condition, boundary condition, etc.. Then, supposing θ does not depend

upon x or t , the sensitivity of f with respect to θ is simply

$$\frac{\partial f}{\partial \theta} = \left[\frac{\partial f}{\partial \theta_1}, \dots, \frac{\partial f}{\partial \theta_n} \right]. \quad (1.118)$$

If θ does depend on space and/or time (i.e., $\theta = \theta(x, t)$), then functional derivatives are required. This is, in fact, the case that we find ourselves in since, regardless of being spatially one-dimensional and hence resulting in a boundary comprised of two single points, the boundary conditions themselves are still time dependent. Allowing this dependence on time is of particular importance in some applications, such as the lamina cribrosa and its role in glaucoma, as it has been suggested that transient changes in IOP (appearing in the model as boundary traction) may play a crucial role in the continuing development of glaucoma, particularly in patients with normal-pressure glaucoma [131].

1.3.1 Functional Sensitivities

Let C, D be Banach spaces with $\mathcal{C} \subset C$ open and $F : \mathcal{C} \rightarrow D$.

Definition 1.3.1 (Directional derivative and first variation) *Let $w \in \mathcal{C}$ and $h \in C$ be given. If the limit*

$$\delta F(w, h) := \lim_{s \searrow 0} \frac{1}{s} (F(w + sh) - F(w))$$

exists in D , then it is called the directional derivative of F at w in the direction h . If this limit exists for all $h \in C$, then the mapping $h \mapsto \delta F(w, h)$ is termed the first variation of F at w .

Note that the first variation is not necessarily a linear mapping.

Definition 1.3.2 (Gâteaux differentiability and derivative) *Suppose that the first variation $\delta F(w, h)$ at $w \in \mathcal{C}$ exists, and suppose there exists a continuous linear operator $A : C \rightarrow D$ such that*

$$\delta F(w, h) = Ah, \quad \forall h \in C.$$

Then, F is said to be Gâteaux differentiable at w , and A is referred to as the Gâteaux derivative of F at w . We write $A = F'(w)$.

For our problem, F would be a map taking the boundary conditions (g, ψ) to the corresponding solution (u, p) . We now define the Fréchet derivative:

Definition 1.3.3 (Fréchet differentiability and derivative) *F is said to be Fréchet differentiable at $w \in \mathcal{C}$ in there exists an operator $A \in \mathcal{L}(C, D)$ and a mapping $r(w, \cdot) : C \rightarrow D$ with the following properties: for all $h \in C$ such that $w + h \in \mathcal{C}$, we have*

$$F(w + h) = F(w) + Ah + r(w, h),$$

where the so-called remainder r satisfies the condition

$$\lim_{\|h\|_C \rightarrow 0} \frac{\|r(w, h)\|_D}{\|h\|_C} = 0.$$

The operator A is called the Fréchet derivative of F at w and we write $A = DF(w)$.

Now, let C, D , and Z be Banach spaces with $\mathcal{C} \subset C$ and $\mathcal{D} \subset D$ be open.

Theorem 1.3.1 (Chain rule) *Let $F : \mathcal{C} \rightarrow \mathcal{D}$ and $G : \mathcal{D} \rightarrow Z$ be Fréchet differentiable at $w \in \mathcal{C}$ and at $F(w) \in \mathcal{D}$, respectively. Then the composition $E = G \circ F : \mathcal{C} \rightarrow Z$, defined by $E(w) = G(F(w))$, is Fréchet differentiable at w , and*

$$DE(w) = DG(F(w))DF(w).$$

As the Fréchet derivative operator is an infinite dimensional object, we need a finite dimensional approximation in order to estimate it numerically. To do so, we will start by approximating the boundary conditions with linear splines. Numerically, we will compute the Fréchet derivative of (u, p, v) with respect to these linear spline approximations. For example, let \hat{g} be the linear spline approximation of g :

$$g \approx \hat{g} = \sum_{i=0}^n \alpha_i \phi_i(t), \quad (1.119)$$

where ϕ_i , $i = 0, 1, \dots, n$ are linear splines on $[0, T]$. That is, we partition the time interval $[0, T]$ into n subintervals of equal length $\Delta t = \frac{T}{n}$ and define

$$\phi_0(t) = \begin{cases} \frac{t_1 - t}{\Delta t}, & \text{for } t \in [t_0, t_1], \\ 0, & \text{otherwise,} \end{cases} \quad \phi_n(t) = \begin{cases} \frac{t - t_{n-1}}{\Delta t}, & \text{for } t \in [t_{n-1}, t_n], \\ 0, & \text{otherwise,} \end{cases}$$

$$\phi_i(t) = \begin{cases} \frac{t - t_{i-1}}{\Delta t}, & \text{for } t \in [t_{i-1}, t_i], \\ \frac{t_{i+1} - t}{\Delta t}, & \text{for } t \in [t_i, t_{i+1}], \\ 0, & \text{otherwise,} \end{cases} \quad \text{for } i = 1, \dots, n-1,$$

where $t_0 = 0$ and $t_n = T$. Then, we can consider \hat{g} to be a function of its coordinates $\alpha_0, \dots, \alpha_n$ in the linear spline space $S = \text{span}\{\phi_0, \dots, \phi_n\}$ so that we have $\hat{g} = \hat{g}(\alpha)$ where $\alpha = [\alpha_0, \dots, \alpha_n]^T$. Thus, we have $\hat{g}(\alpha) : \mathbb{R}^{n+1} \rightarrow S$. Now, let $u(g)$ be the map from the boundary condition g to the corresponding solid displacement u . Then, assuming Fréchet differentiability of u with respect to g and \hat{g} with

respect to α , we have from the chain rule

$$D u(\alpha) = D u(\hat{g}(\alpha)) D \hat{g}(\alpha). \quad (1.120)$$

Note that $D \hat{g}(\alpha)$ and $D u(\alpha)$ are Jacobian matrices with respect to α . Thus, we have

$$D \hat{g}(\alpha) = \begin{bmatrix} \frac{\partial \hat{g}}{\partial a_0} & \frac{\partial \hat{g}}{\partial a_1} & \dots & \frac{\partial \hat{g}}{\partial a_n} \end{bmatrix} = \begin{bmatrix} \phi_0 & \phi_1 & \dots & \phi_n \end{bmatrix} \quad (1.121)$$

and

$$D u(\alpha) = \begin{bmatrix} \frac{\partial u}{\partial a_0} & \frac{\partial u}{\partial a_1} & \dots & \frac{\partial u}{\partial a_n} \end{bmatrix}. \quad (1.122)$$

Taking $h = [h_0, \dots, h_n]^T \in \mathbb{R}^{n+1}$, we have

$$D \hat{g}(\alpha) h = \sum_{i=0}^n h_i \phi_i \quad (1.123)$$

so that $D \hat{g}(\alpha) h \in S$. Therefore, for any $\bar{g} \in S$, we have

$$D u(\hat{g}) \bar{g} = D u(\alpha) \begin{bmatrix} \bar{g}_0 \\ \bar{g}_1 \\ \vdots \\ \bar{g}_n \end{bmatrix}, \quad (1.124)$$

where $\bar{g} = \sum_{i=0}^n \bar{g}_i \phi_i(t)$. So, we can see the action of $D u(\hat{g})$ on elements in S through the Jacobian matrix of u with respect to α . In terms of sensitivity, this means that we can compute the sensitivity of u with respect to \hat{g} in the direction \bar{g} by computing the Jacobian matrix of u with respect to α and multiplying it by the coordinates of \bar{g} in the linear spline space S . Numerically, this amounts to computing the derivatives $\frac{\partial u}{\partial a_i}$ for $i = 0, \dots, n$ and calculating the appropriate linear combination of these partial derivatives. We can similarly compute the sensitivities of p and v with respect to g and the sensitivities of u, p , and v with respect to ψ .

1.3.2 Numerical Methods

There are a number of different techniques for approximating sensitivity derivatives, including finite difference approximations, sensitivity equations, and automatic differentiation (see [23, 25, 28] and the references therein). Sensitivity equations are accurate and computationally inexpensive for reasonably small systems. However, the complex nature of our problem, in particular attempting to compute functional sensitivities from a nonlinear fluid-solid mixture problem, does not lend itself easily to sensitivity equations. While the system of sensitivity equations will be linear in the sensitivities (as is always true for sensitivity equations), this system is coupled to the original

nonlinear system and the coupling occurs through derivatives of the solution to the nonlinear system which further complicates the numerics. The finite difference method, on the other hand, is relatively easy and efficient to implement. However, finite differences suffer from cancellation error for small step sizes.

Another method for calculating sensitivities is the complex-step method [128, 129]. The idea of using complex variables to estimate derivatives originated in [124, 125], and has become quite popular in aerodynamic optimization [5, 6, 128, 129, 175]. The complex-step estimate is second order accurate and extremely robust while retaining a reasonable computational cost. In [128], Martins et al. show the method to have implementation advantages over automatic differentiation and computational advantages over finite-differencing. In [19], we demonstrated the use of the complex-step method for computing sensitivities to biological models and compared our results with solutions of traditional sensitivity equations. We observed that (i) the method is easy to implement, (ii) the complexity of the algorithm is the same as the complexity of the algorithm evaluating the solution function (i.e., the algorithm solving the system of equations), (iii) less computation time is needed in comparison to using sensitivity equations if the number of parameters is not large compared to the dimension of the problem, and (iv) the method gives consistently second order accurate approximation of the derivative for a wide range of step size values which can be taken as small as machine precision. Moreover, we showed that, even though the complex-step formula is derived assuming analyticity of the solution function, the approximation provides accurate one-sided derivatives for functions with far less smoothness, implying that analyticity of the solution functions is sufficient but not necessary for the complex-step method to be effective.

1.3.3 Complex Step Method

We derive here the complex step method, following the process outlined in [128]. Let $z \in \mathbb{C}$ with $z = x + iy$ for $x, y \in \mathbb{R}$ and $f(z) = f(x, y) = u(x, y) + iv(x, y)$ be a function of a complex variable. If f is analytic, then the Cauchy-Riemann equations hold:

$$\frac{\partial u}{\partial x} = \frac{\partial v}{\partial y}, \quad \frac{\partial u}{\partial y} = -\frac{\partial v}{\partial x}. \quad (1.125)$$

Note that these equations establish a relationship between the real and imaginary parts of the function f . Applying the definition of partial derivative to the first equation in Eq. 1.125, we have

$$\frac{\partial u}{\partial x} = \lim_{h \rightarrow 0} \frac{v(x, y+h) - v(x, y)}{h} = \lim_{h \rightarrow 0} \frac{\text{Im}[f(x + i(y+h))] - \text{Im}[f(x + iy)]}{h}. \quad (1.126)$$

Now, if f is actually a real-valued function for real inputs (which is the case we're in), then we can take

$$y = 0, \quad f(x) = u(x, 0), \quad \text{and} \quad v(x, 0) = \text{Im}[f(x)] = 0.$$

Thus, Eq. 1.126 becomes

$$\frac{\partial f}{\partial x} = \lim_{h \rightarrow 0} \frac{\text{Im}[f(x + ih)]}{h}. \quad (1.127)$$

Therefore, for small h , we have the complex-step derivative approximation

$$\frac{\partial f}{\partial x} \approx \frac{\text{Im}[f(x + ih)]}{h}. \quad (1.128)$$

This formula can also be obtained through a Taylor series expansion of f about a small complex step:

$$f(x + ih) \approx f(x) + ihf'(x) - \frac{h^2}{2!}f''(x) - i\frac{h^3}{3!}f^{(3)}(x) + \frac{h^4}{4!}f^{(4)}(x) + \dots \quad (1.129)$$

Taking the imaginary parts of both sides of Eq. 1.129 and dividing by h gives

$$f'(x) \approx \frac{\text{Im}[f(x + ih)]}{h} + O(h^2),$$

with truncation error

$$E_t(h) = \frac{h^2}{6}f^{(3)}(x). \quad (1.130)$$

We note that, although a step size parameter is required, in most cases the numerical derivatives are not subject to subtractive cancellation errors as in the use of finite differences, (see [129] for exceptions and remedies). Therefore, the method exhibits true second-order accuracy as the step size is reduced. The accuracy of the complex-step estimate then is only limited by the numerical precision of the algorithm that evaluates the function f . In addition, the procedure is easily implemented into existing programs. The only requirements are that the floating point variables be declared as complex and that a complex perturbation be added to the variable of interest.

Note that the complex-step approximation formula (1.128) is derived based on the Cauchy-Riemann formula for analytic functions. Therefore, this derivation only applies to analytic functions f . However, we showed in [19] that, in the case where the functions have singularities or branch cuts where they are not analytic, the complex-step method provides a correct derivative approximation up to the point of discontinuity. In addition, it gives accurate approximations of one-side derivatives if the function is uniquely defined at that point. The method also provides an accurate first order derivative when a function has jumps in its higher order derivatives.

1.3.3.1 Implementation of the complex-step method

Since the derivation of the complex-step approximation formula Eq. 1.128 is based upon analyticity, and specifically the satisfaction of the Cauchy-Riemann equations, we must make sure the numerical algorithm also satisfies these equations. Thus, we need to extend functions of real variables to functions of complex variables in a such a way so as to guarantee that the Cauchy-Riemann equations

still hold. The discussion below describes implementation of the complex-step method in Matlab, however the same principles hold for other programming languages. For further discussion and Fortran implementation see [128, 129].

When we convert a ‘real’ algorithm to a ‘complex’ one, we are mainly concerned with two types of operations:

1. **Relational operators.** Relational logic operators like “greater than” and “less than” are defined in Matlab to compare only the real parts of a complex number. These operators are usually used in ‘if’ statements to redirect the execution thread. The original algorithm and its complex version must follow the same execution thread. Therefore, the Matlab definition for these types of operators is the correct one.
2. **Arithmetic functions and operators.** In Matlab, complex numbers are a standard data type and many functions have complex counterparts. Functions that choose one argument like *max* and *min* are based on relational operators. Therefore, one would assume that they are defined based on their real parts in Matlab. Unfortunately, that is not the case. In Matlab, *min* and *max* functions compare the moduli of two complex numbers. Hence, they need to be redefined to compare only the real parts.

Another function that needs to be given attention is the absolute value (*abs*) function. In Matlab, *abs* returns the modulus of a complex number. The modulus, however, is not an analytic function and does not satisfy the Cauchy-Riemann equations. So, we redefine this function using the Cauchy-Riemann equations in order to ensure that the complex-step method will give a correct derivative approximation. We know that we should have

$$\frac{\partial u}{\partial x} = \frac{\partial v}{\partial y} = \begin{cases} -1, & x < 0 \\ +1, & x > 0 \end{cases} . \quad (1.131)$$

Then, since $\frac{\partial v}{\partial x} = 0$ on the real axis, the Cauchy-Riemann equations (Eq. 1.125) tell us that we need $\frac{\partial u}{\partial y} = 0$ on the real axis. Thus, the real part of the result must be independent of the imaginary part of the variable. This means that the new sign of the imaginary part depends only on the sign of the real part of the complex number, and an analytic absolute value function can be defined as:

$$abs(x + iy) = \begin{cases} -x - iy & x < 0 \\ x + iy & x \geq 0 \end{cases} . \quad (1.132)$$

This function is not analytic at $x = 0$. However, as mentioned above, the complex-step approximation yields an accurate derivative up to the discontinuity. In addition, since we have defined the function at $x = 0$ in the same way as it is defined for $x > 0$, the method gives the

correct right-hand side derivative at $x = 0$.

Similarly, for every real valued function we can obtain a unique complex function definition by requiring that the complex extension satisfies the Cauchy-Riemann equations and that the real and complex parts have the same properties. If Matlab's complex analog function is not already correctly defined, we can adjust the definition using a custom function. Many of the arithmetic operators including addition, multiplication, and trigonometric function have standard complex definitions that are analytic almost everywhere. The transpose operator ($'$) in Matlab gives the complex conjugate of the matrix, however the non-conjugate transpose ($.'$) is appropriately defined for the complex-step method. Note that before implementing the complex-step method, one always needs to check whether the functions and operators in the algorithm need re-definition and do so accordingly.

The implementation procedure for using the complex-step method to approximate a first order derivative $\frac{df}{dx}$ is:

1. Define all functions and operators that are not defined for complex arguments such as, for example, *max*, *min* and *abs*.
2. Add a small complex step ih to the desired variable x and run the algorithm that evaluates f .
3. Compute $\frac{df}{dx}$ using Eq. 1.128.

1.4 Selected Results

Using insight from results in [19, 20], we compute the desired sensitivities using the complex-step derivative approach outlined in Section 1.3.3, in combination with the dual mixed hybridized (DMH) finite element discretization developed for the nonlinear coupling in [39] and presented in Section 1.2.3. First, we apply the method to four one-dimensional test cases discussed in [39], for which analytical solutions are available. We use the first test case (where the data and the permeability are constants) to validate our technique. In the other three cases, while the analytic solutions are provided in [39] (either for $\delta = 0$ or $\delta = 1$), there is no explicit dependence on the boundary data in the formulas. So there is no analytic information about how sensitive the solution is to the given data. Lastly, we perform sensitivity analysis on a one-dimensional, dynamical case with irregular (in time) boundary data. In this case, the numerical results in [39] predicted a finite time blow up for the fluid energy when viscoelasticity is not present in the system. Our goal in this case is to compute and compare the sensitivities of the states with respect to the boundary data for $\delta = 0$ and $\delta = 1$, as well as treat δ as a control parameter, and see how the sensitivities change while δ takes a variety of values in two important ranges: $0 \leq \delta \leq 1$ and $\delta \geq 1$.

1.4.1 Sensitivity with Respect to Boundary Conditions

1.4.1.1 Constant Data, Constant Permeability - Case 1 (Validation)

Let the domain be given by $(x_0, x_f) = (0, 1)$ of length $L = 1$. Consider the purely elastic ($\delta = 0$) system Eq. 1.38 with constant volumetric sources F_1 , S_1 , constant boundary data g_1 and ψ_1 , and with boundary conditions given by

$$\begin{cases} u = p = 0, & x_0 = 0, \\ \sigma n = g_1 \text{ and } v n = \psi_1, & x_f = 1. \end{cases} \quad (1.133)$$

This problem admits the following analytic solution, provided in [39]:

$$\begin{aligned} u(x) &= \frac{x}{H_A} \left[F_1 \left(L - \frac{x}{2} \right) + g_1 \right] - \frac{x^2}{2H_A k_{\text{ref}}} \left[\psi_1 - S_1 \left(L - \frac{x}{3} \right) \right], \\ p(x) &= \frac{x}{H_A} \left[S_1 \left(L - \frac{x}{2} \right) - \psi_1 \right], \\ \wp(x) &= -\frac{\lambda_e}{H_A} (\sigma(x) + p(x)), \\ \sigma(x) &= g_1 + F_1(L - x), \\ v(x) &= \psi_1 + S_1(x - L). \end{aligned}$$

If we treat the boundary data as constant parameters and thus assume that $g_1, \psi_1 \in \mathbb{R}$, and we consider the following specific values for the reference value of the permeability and the Lamé constants

$$k = k_{\text{ref}} = 1 \text{ cm}^3 \text{ s g}^{-1}, \quad H_A = \lambda_e + 2\mu_e = 3 \text{ dyne cm}^{-2}, \quad \lambda_e = \mu_e = 1 \text{ dyne cm}^{-2}, \quad \phi = 0.5,$$

we can simplify the formulas for the the solutions to

$$\begin{aligned} u(x, g_1, \psi_1) &= -\frac{S_1}{18} x^3 - \frac{1}{6} (F_1 + \psi_1 - S_1) x^2 + \frac{1}{3} (F_1 + g_1) x, \\ p(x, g_1, \psi_1) &= -\frac{S_1}{2} x^2 + (S_1 - \psi_1) x, \\ \sigma(x, g_1, \psi_1) &= g_1 + F_1(1 - x), \\ v(x, g_1, \psi_1) &= \psi_1 + S_1(x - 1). \end{aligned}$$

and find the partial derivatives with respect to g_1 and ψ_1 :

$$\frac{\partial u}{\partial g_1} = \frac{x}{3}, \quad \frac{\partial p}{\partial g_1} = 0, \quad \frac{\partial v}{\partial g_1} = 0, \quad (1.134)$$

$$\frac{\partial u}{\partial \psi_1} = -\frac{x^2}{6}, \quad \frac{\partial p}{\partial \psi_1} = -x, \quad \frac{\partial v}{\partial \psi_1} = 1. \quad (1.135)$$

For the numerical computations, we assume that the volumetric and boundary source terms are given by the following specific values:

$$F_1 = 0.3 \text{ dyne cm}^{-3}, \quad S_1 = 0.3 \text{ s}^{-1}, \quad g_1 = 0.3 \text{ dyne cm}^{-2}, \quad \psi_1 = 3 \text{ cm s}^{-1}.$$

The computed sensitivities of u , p , and v with respect to g_1 and ψ_1 at $(g_1, \psi_1) = (0.3, 3)$ are shown in Fig. 1.3 and Fig. 1.4.

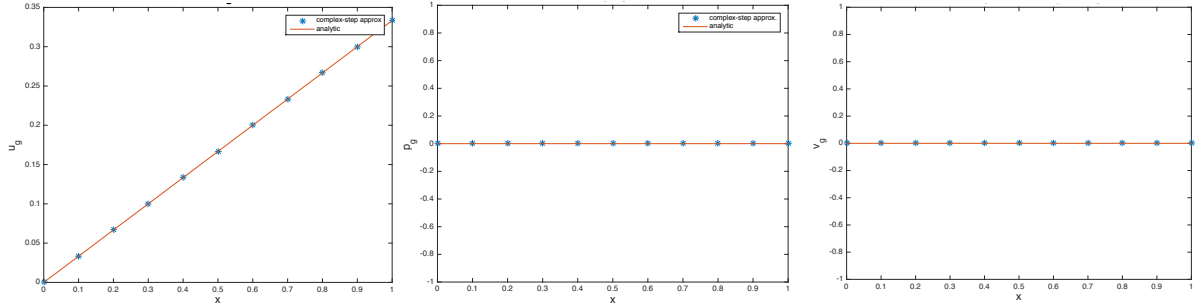


Figure 1.3 Sensitivity of u (left panel), p (center panel), and v (right panel) with respect to g_1 at $g_1 = .3$

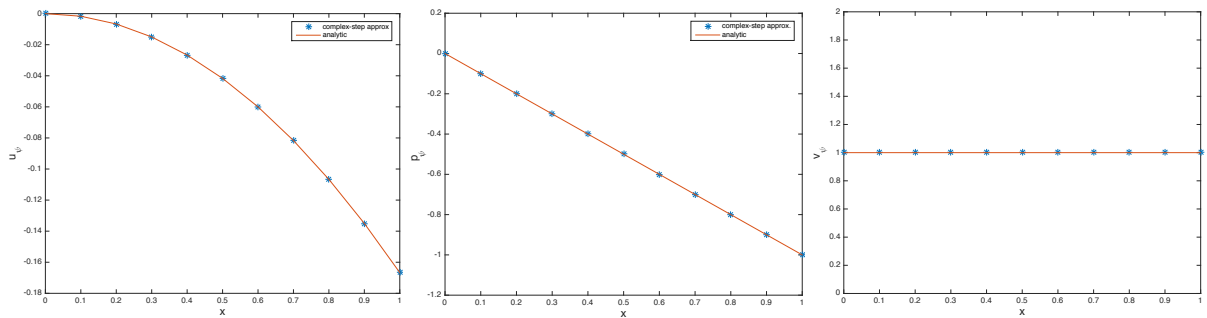


Figure 1.4 Sensitivity of u (left panel), p (center panel), and v (right panel) with respect to ψ_1 at $\psi_1 = 3$

Observations From Fig. 1.3 and Fig. 1.4, we can see that the sensitivity derivatives obtained via the complex-step method agree with the ones computed analytically (given in Eq. 1.134 and Eq. 1.135). Note that the sensitivities of the solid displacement u to the boundary data (g_1, ψ_1) at $g_1 = .3$ and $\psi_1 = 3$ increase in magnitude as we approach the right end point $x_f = 1$ at which the boundary conditions are applied, which is to be expected.

1.4.1.2 Constant Boundary Data, Variable Permeability - Validation Case 2

Let $(x_0, x_f) = (-1, 1)$ of length $L = 2$. Consider the fluid-solid mixture given by the system Eq. 1.38 with $\delta = 0$. For boundary conditions, we take homogeneous Dirichlet boundary conditions at $x_0 = -1$ and non-homogenous Neumann boundary conditions at $x_f = 1$ given by

$$\begin{cases} u = p = 0, & x_0 = -1, \\ \sigma n = g_2, \quad \psi n = \psi_2, & x_f = 1. \end{cases} \quad (1.136)$$

Volumetric and boundary source terms are given by

$$\begin{aligned} F_2(x) &= -[U_{\text{ref}} H_A \chi''(x) - P_{\text{ref}} \chi'(x)], \\ S_2(x) &= -k_{\text{ref}} P_{\text{ref}} \chi''(x) \Theta(x) - k_{\text{ref}} P_{\text{ref}} U_{\text{ref}} \chi'(x) \chi''(x) \Xi(x), \\ g_2 &= U_{\text{ref}} H_A \chi'(x_f) - P_{\text{ref}} \chi(x_f) = -0.9425, \\ \psi_2 &= -k_{\text{ref}} P_{\text{ref}} \chi'(x_f) \Theta(x_f) = 0.0304, \end{aligned}$$

where

$$\chi(x) = \sin(\omega_x x), \quad \Phi(x) = \phi_0 + U_{\text{ref}} \chi'(x), \quad \Theta(x) = \frac{\Phi^3(x)}{[1 - \Phi(x)]^2}, \quad \Xi(x) = \frac{\Phi^2(x)[3 - \Phi(x)]}{[1 - \Phi(x)]^3},$$

and

$$\omega_x = 2\pi/L, \quad U_{\text{ref}} = 0.1 \text{ cm}, \quad P_{\text{ref}} = 1 \text{ dyne cm}^{-2}, \quad H_A = 3 \text{ dyne cm}^{-2}, \quad \phi_0 = 0.5.$$

In comparison to the previous case, the porosity ϕ is now allowed to vary with the derivative of the displacement within the range $[\Phi_{\min}, \Phi_{\max}]$, where $0 < \Phi_{\min} < \Phi_{\max} < 1$, in such a way that the permeability k , expressed by the nonlinear relation of Carman-Kozeny Eq. 1.12, satisfies the following lower and upper bounds [48]:

$$0 < k_{\text{ref}} \frac{\Phi_{\min}^3}{(1 - \Phi_{\min})^2} \leq k(\phi) \leq k_{\text{ref}} \frac{\Phi_{\max}^3}{(1 - \Phi_{\max})^2}.$$

Here we set $\Phi_{\min} = 0.125$, $\Phi_{\max} = 0.875$ and $k_{\text{ref}} = 1 \text{ cm}^3 \text{ s g}^{-1}$. From [39], we know that the problem

admits the following exact stationary solution [39]:

$$\begin{aligned} u(x) &= U_{ref} \chi(x), \\ p(x) &= P_{ref} \chi(x), \\ \sigma(x) &= U_{ref} H_A \chi'(x) - P_{ref} \chi(x), \\ v(x) &= -k_{ref} P_{ref} \chi'(x) \Theta(x), \\ \wp(x) &= -\lambda_e U_{ref} \chi'(x). \end{aligned}$$

Due to the particular choice of data and implicitly, the structure of the solutions, we can see that the Darcy velocity is a function of ψ_2 , but it does not depend on g_2 , therefore v_2 is not sensitive to g_2 . However, solid displacement u and fluid pressure p depend nonlinearly and implicitly on both g_2 and ψ_2 , especially due to the permeability being nonlinearly dependent on porosity.

Similarly to case 1, we consider g_2 and ψ_2 as constant parameters and compute the sensitivities of the states with respect to g_2 and ψ_2 at $g_2 = -0.9425$ and $\psi_2 = 0.0304$. The numerical results agree with the analytical ones in the case of the discharge velocity. For u and p , we don't have explicit dependence on the boundary data and thus have no analytic results to compare our numerical results with.

Observations We can see in Fig. 1.5 and Fig. 1.6 that, in comparison to Case 1, the peaks in sensitivity for both u and p are in the interior of the domain, which could be explained by the nonlinearity of the permeability, but also by the fact that the volumetric source of momentum is also non-zero and thus the solution is not driven solely by the boundary data.

Remark 1.4.1 For further validation, we computed the sensitivities in this case also using the finite difference method and obtained similar results (not included here). There were small differences in the magnitudes of the sensitivities, which are due to the 1st order accuracy of the forward difference.

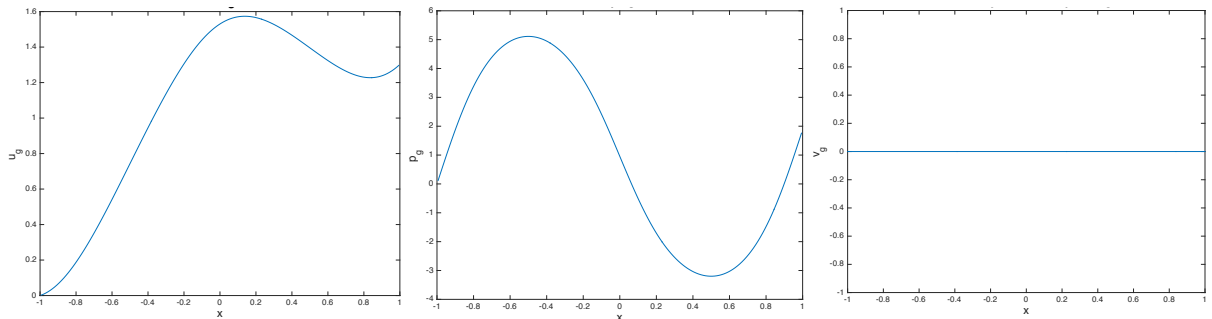


Figure 1.5 Sensitivity of u (left panel), p (center panel), and v (right panel) with respect to g_2 .

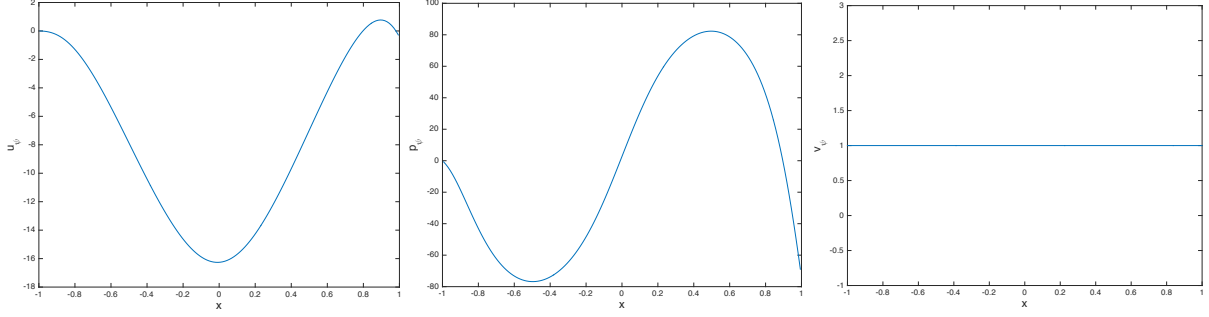


Figure 1.6 Sensitivity of u (left panel), p (center panel), and v (right panel) with respect to ψ_2 .

1.4.1.3 Dynamical Poro-Visco-Elastic Model, Constant Permeability - Case 3

In this example, we consider the system in Eq. 1.38 on $(x_0, x_f) \times (t_0, t_f) = (0, 1) \times (0, .1)$, with boundary conditions given by

$$\begin{cases} u = p = 0, & x = 0, \\ \sigma n = g_3(t), \quad v n = \psi_3(t), & x_f = 1. \end{cases} \quad (1.137)$$

We prescribe the following volumetric and boundary source terms

$$\begin{aligned} F_3(x, t) &= -U_{\text{ref}} \chi''(x) [H_A \tau(t) + \delta H_V \tau'(t)] - P_{\text{ref}} \tau(t) \chi'(x), \\ S_3(x, t) &= U_{\text{ref}} \tau'(t) \chi'(x) - k_{\text{ref}} P_{\text{ref}} \chi''(x) \tau(t), \\ g_3(t) &= U_{\text{ref}} \chi'(x_f) [H_A \tau(t) + \delta H_V \tau'(t)] - P_{\text{ref}} \tau(t) \chi(x_f), \\ \psi_3(t) &= -k_{\text{ref}} P_{\text{ref}} \tau(t) \chi'(x_f), \end{aligned}$$

where the spatial and temporal shape functions are given by

$$\begin{aligned} \chi(x) &= \sin(\omega_x x), \quad \text{with } \omega_x = 8/L, \\ \tau(t) &= \sin^2(\omega_t t), \quad \text{with } \omega_t = 8/t_f, \end{aligned}$$

respectively, and the parameters have the following values:

$$U_{\text{ref}} = 0.1 \text{ cm}, \quad P_{\text{ref}} = 0.3 \text{ dyne cm}^{-2},$$

$$H_A = \lambda_e + 2\mu_e = 3 \text{ dyne cm}^{-2}, \quad \lambda_e = \mu_e = 1 \text{ dyne cm}^{-2}, \quad H_V = \lambda_v + 2\mu_v = 0.5774 \text{ dynes cm}^{-2}.$$

As in Case 1, we assume that the porosity and permeability are constant and given by

$$\phi = \phi_0 = 0.5 \quad \text{and} \quad k = k_{\text{ref}} = 1 \text{ cm}^3 \text{ s g}^{-1},$$

respectively. For the purely elastic case $\delta = 0$, the problem admits the exact solution [39]

$$\begin{aligned} u(x, t) &= U_{\text{ref}} \chi(x) \tau(t), \\ p(x, t) &= P_{\text{ref}} \chi(x) \tau(t), \\ \sigma(x, t) &= U_{\text{ref}} \chi'(x) [H_A \tau(t) + \delta H_V \tau'(t)] - P_{\text{ref}} \chi(x) \tau(t), \\ v(x, t) &= -k_{\text{ref}} P_{\text{ref}} \chi'(x) \tau(t), \\ \wp(x, t) &= -\lambda_e U_{\text{ref}} \chi'(x) \tau(t), \end{aligned}$$

which now depends on both space and time, and implicitly on the boundary data.

Assuming that the data-to-state map is Fréchet differentiable, we follow the process outlined in Section 1.3.1 and approximate both the data and the directions using linear splines. Partitioning the time interval $[0, .1]$ into ten subintervals of equal length $\Delta t = .01$ and defining ϕ_i as in Section 1.3.1 for $i = 0, \dots, n$ with $n = 10$, we approximate the data by

$$g_3(t) \approx g_{3h} = \sum_{i=0}^{10} \alpha_i \phi_i(t), \quad \psi_3(t) \approx \psi_{3h} = \sum_{i=0}^{10} \beta_i \phi_i(t),$$

where $\alpha_i = g_3(t_i)$, and $\beta_i = \psi_3(t_i)$ (see Fig. 1.7). Moreover, we consider $\bar{g}, \bar{\psi} \in \text{span}\{\phi_i\}_0^{10}$, and write them as

$$\bar{g}(t) = \sum_{i=0}^{10} \bar{\alpha}_i \phi_i(t), \quad \bar{\psi}(t) = \sum_{i=0}^{10} \bar{\beta}_i \phi_i(t).$$

In the figures below, we display the graphs of the directional derivatives first in the case of directions taken as particular splines, like ϕ_1 and ϕ_2 , and then for specific linear combinations of the splines, like $w_h = \sum_{i=1}^{11} \phi_i$. Note that if the direction is taken to be a particular spline ϕ_i then the functional sensitivity in that direction is the partial derivative with respect to the corresponding coordinate of the boundary data. For example, the sensitivity of u with respect to g_{3h} in the direction ϕ_i is

$$(D_{g_{3h}} u) \phi_i = \frac{\partial u}{\partial \alpha_i}.$$

For all the sensitivities, we include both the visco-elastic and purely elastic cases and compare the results.

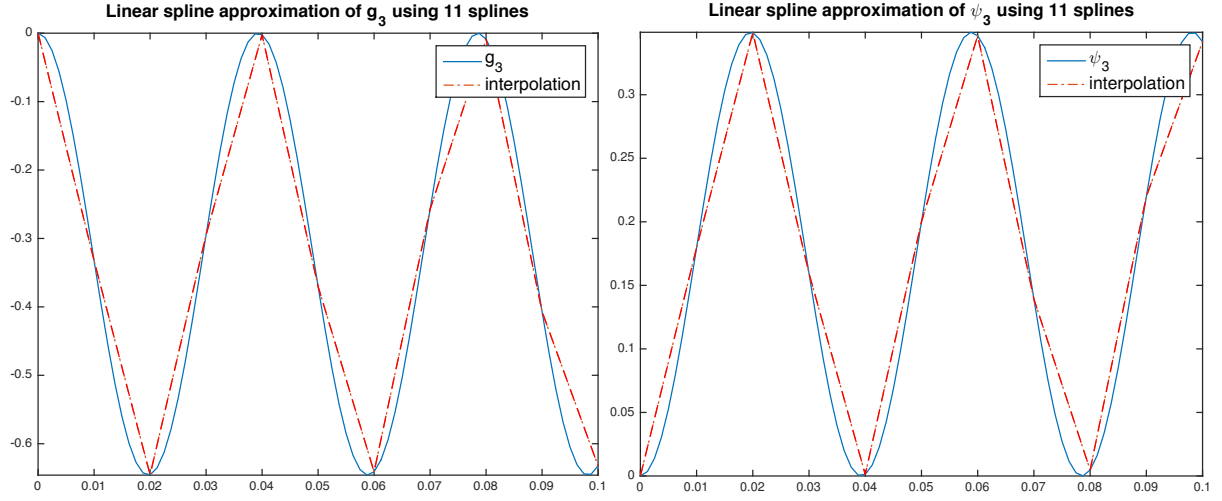


Figure 1.7 Linear spline approximations of g_3 and ψ_3 .

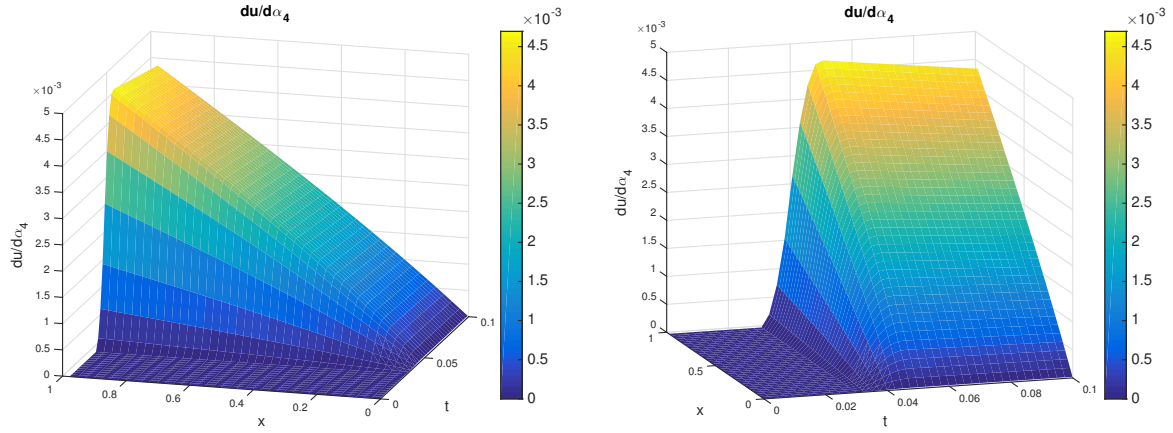


Figure 1.8 Sensitivity function of solid displacement u with respect to boundary stress g_{3h} in the direction ϕ_4 , when $\delta = 1$. Note, the two figures give different angles of view of the sensitivity.

Observations Comparing Fig. 1.8-Fig. 1.13 (note the different scales for $\delta = 0$ and $\delta = 1$), we see that u appears to be more sensitive to g_{3h} than it is to ψ_{3h} , regardless of the values of δ . We also note that both $\frac{\partial u}{\partial g_{3h}}$ and $\frac{\partial u}{\partial \psi_{3h}}$ are larger in magnitude when $\delta = 0$ than when $\delta = 1$. However, this difference in magnitude is more significant for $\frac{\partial u}{\partial g_{3h}}$ where we see a full order of magnitude difference.

Further, we notice that the sensitivity of u with respect to g_{3h} is more prevalent throughout the spatial domain than the sensitivity of u with respect ψ_{3h} , regardless of the value of δ (though, when $\delta = 1$, the sensitivity of u with respect to g_{3h} steadily decreases as we get farther away from the point where g_{3h} is applied. The sensitivity of u with respect to g_{3h} stays consistent throughout the spatial

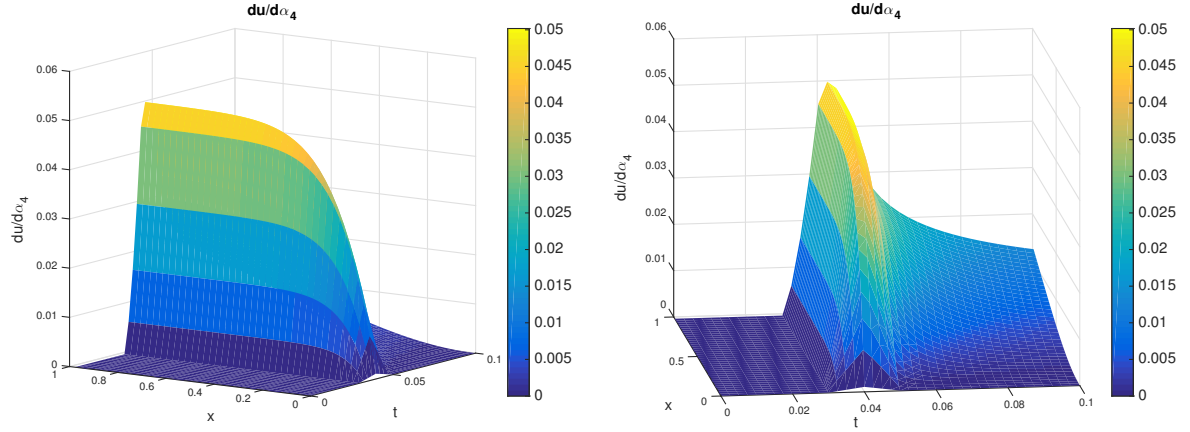


Figure 1.9 Sensitivity function of solid displacement u with respect to boundary stress g_{3h} in the direction ϕ_4 , when $\delta = 0$. Note, the two figures give different angles of view of the sensitivity.

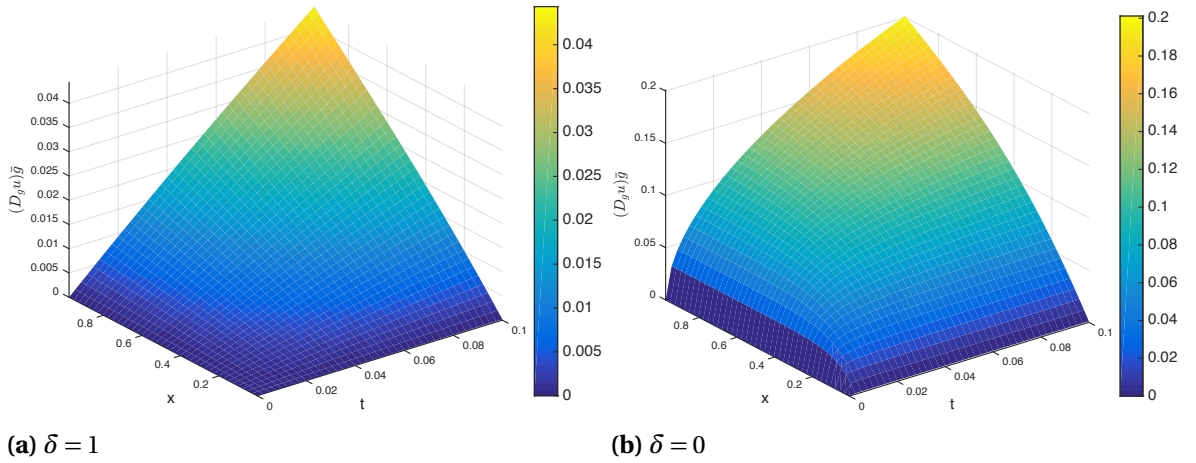


Figure 1.10 Sensitivity functions of solid displacement u with respect to boundary stress g_{3h} in the direction $\bar{g} = \sum_{i=0}^{10} \phi_i$ when $\delta = 1$ (left) and $\delta = 0$ (right).

domain when $\delta = 0$). In contrast, the sensitivity of u (to both g_{3h} and ψ_{3h}) throughout the temporal domain is most prevalent when $\delta = 1$. This could indicate that the effect of the term $\frac{\partial u}{\partial t}$ dominates the expression for the stress σ when $\delta = 1$.

Comparing Fig. 1.14-Fig. 1.19, we see that when $\delta = 1$, p appears to be more sensitive to ψ_{3h} than it is to g_{3h} . However, when $\delta = 0$, the opposite is true. Similar to the sensitivity of u with respect to g_{3h} , the sensitivity of p with respect to g_{3h} is about one order of magnitude larger when $\delta = 0$ than when $\delta = 1$. In contrast, the sensitivity of p with respect to ψ_{3h} reacts in the opposite manner; that is, p appears to be more sensitive to ψ_{3h} when $\delta = 1$ than when $\delta = 0$.

Similar to the sensitivities for u , we see that p is more sensitive to g_{3h} throughout the spatial

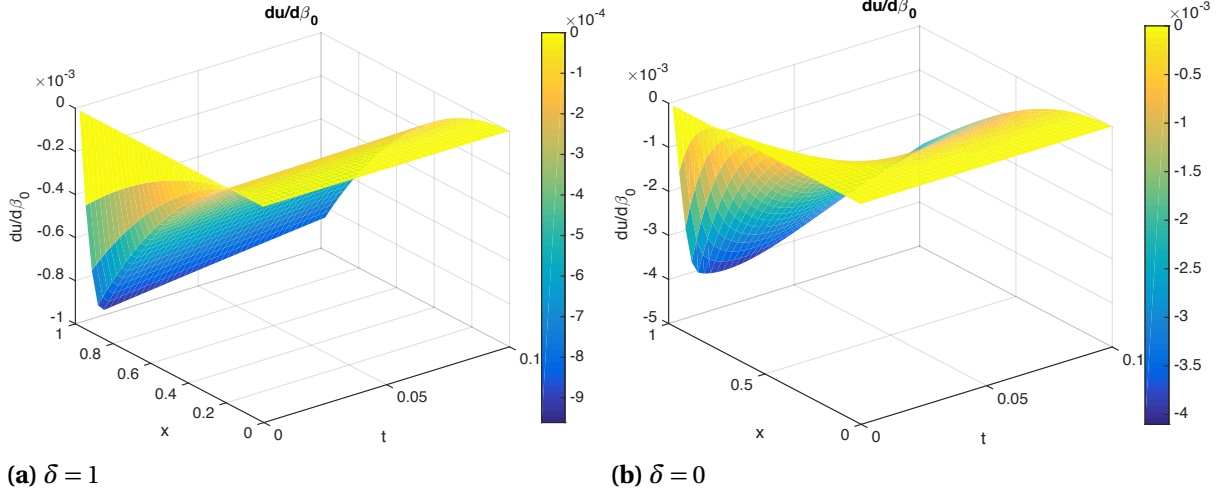


Figure 1.11 Sensitivity function of solid displacement u with respect to boundary source ψ_{3h} in the direction ϕ_0 when $\delta = 1$ (left) and $\delta = 0$ (right).

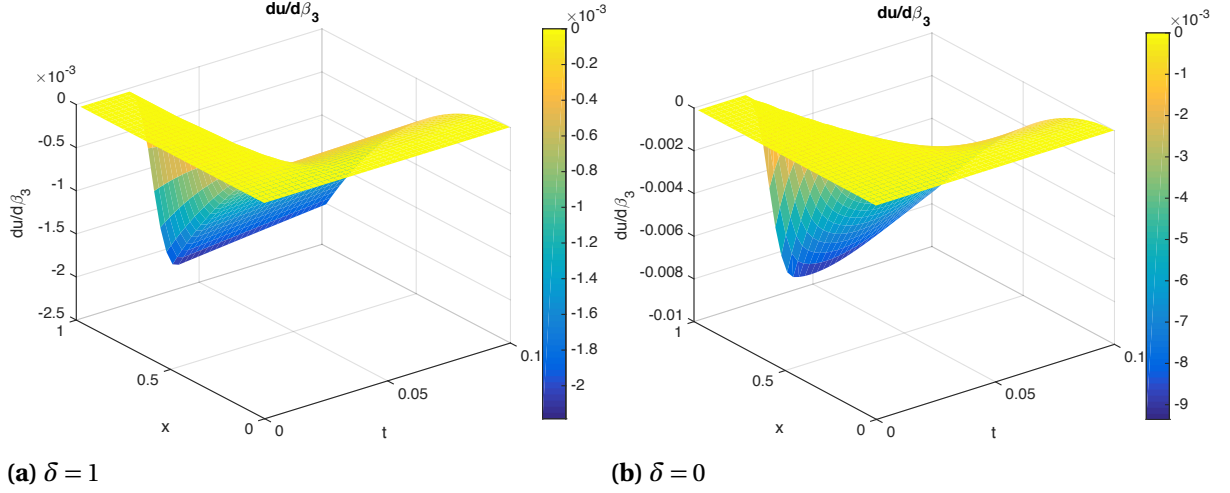


Figure 1.12 Sensitivity function of solid displacement u with respect to boundary source ψ_{3h} in the direction ϕ_3 when $\delta = 1$ (left) and $\delta = 0$ (right).

domain than to ψ_{3h} . However, we do not see much sensitivity throughout the temporal domain when looking in the direction of particular splines. This is most likely due to the lack of time derivatives on p .

Similar to the sensitivities of p , we see from Fig. 1.20-Fig. 1.25 that v is more sensitive to ψ_{3h} than it is to g_{3h} when $\delta = 1$, but it is more sensitive to g_{3h} than to ψ_{3h} when $\delta = 0$. We again see that, when $\delta = 0$, the sensitivity of v with respect to g_{3h} is one order of magnitude larger than when $\delta = 1$. On the other hand, the magnitude of the sensitivity of v with respect to ψ_{3h} is the same for $\delta = 0$

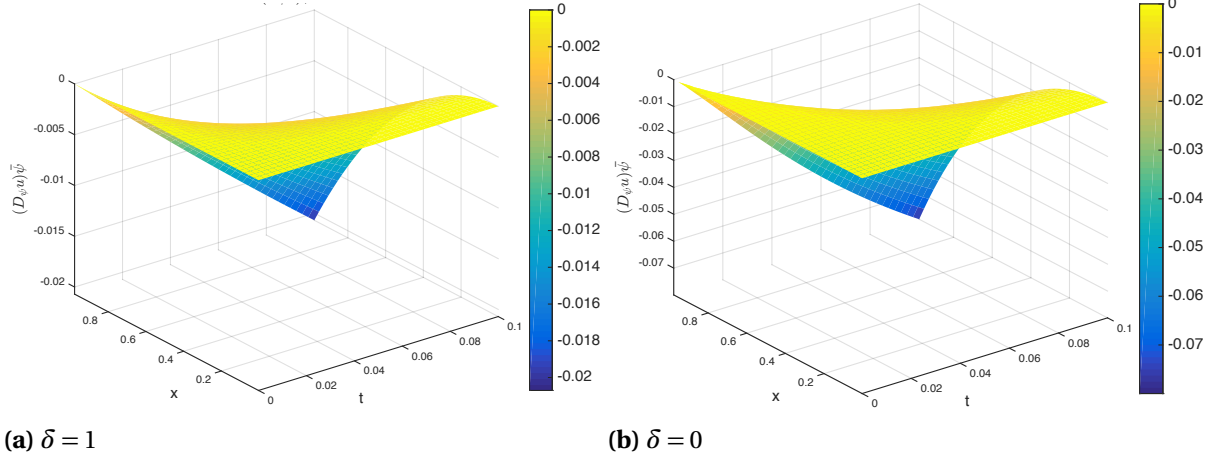


Figure 1.13 Sensitivity functions of solid displacement u with respect to boundary stress ψ_{3h} in the direction $\tilde{\psi} = \sum_{i=0}^{10} \phi_i$ when $\delta = 1$ (left) and $\delta = 0$ (right).

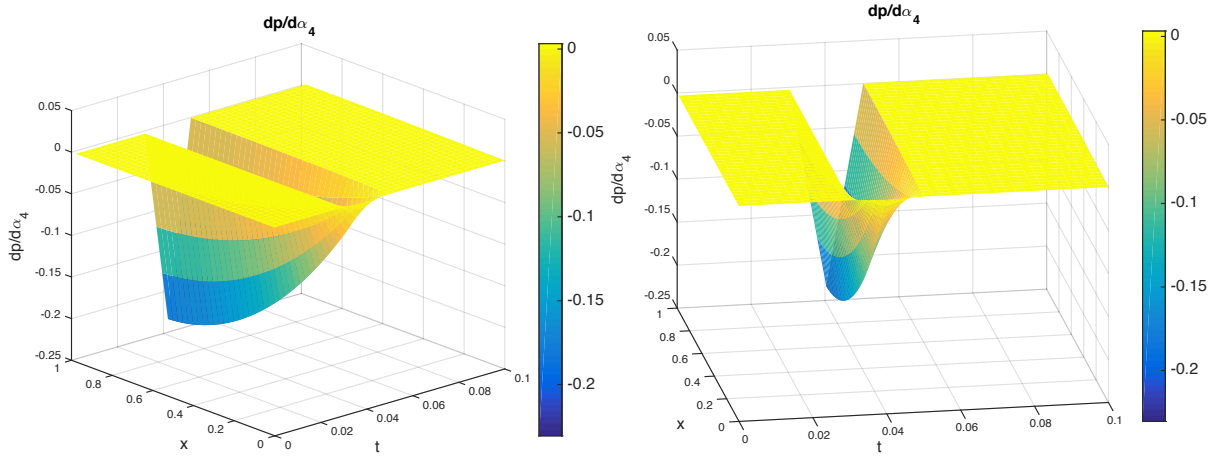


Figure 1.14 Sensitivity function of fluid pressure p with respect to boundary stress g_{3h} in the direction ϕ_4 when $\delta = 1$. Note, the two figures give different angles of view of the sensitivity.

and $\delta = 1$.

Moreover, these sensitivities are similar to the sensitivities for p in that we do not see the sensitivity continuing throughout the temporal domain when taken in the direction of particular splines. Unlike the sensitivities for u and p , however, the sensitivity of v (to both g_{3h} and ψ_{3h}) is more prevalent throughout the spatial domain when $\delta = 1$.

Looking specifically at the sensitivities with respect to g_{3h} (Fig. 1.8 - Fig. 1.10, Fig. 1.14 - Fig. 1.16, and Fig. 1.20 - Fig. 1.22) we can see that in the purely elastic case ($\delta = 0$), the sensitivities of all three states with respect to g_{3h} are larger than in the visco-elastic case ($\delta = 1$).

Moreover, for $\delta = 1$, the sensitivities of u and p with respect to g_{3h} decrease as we go farther

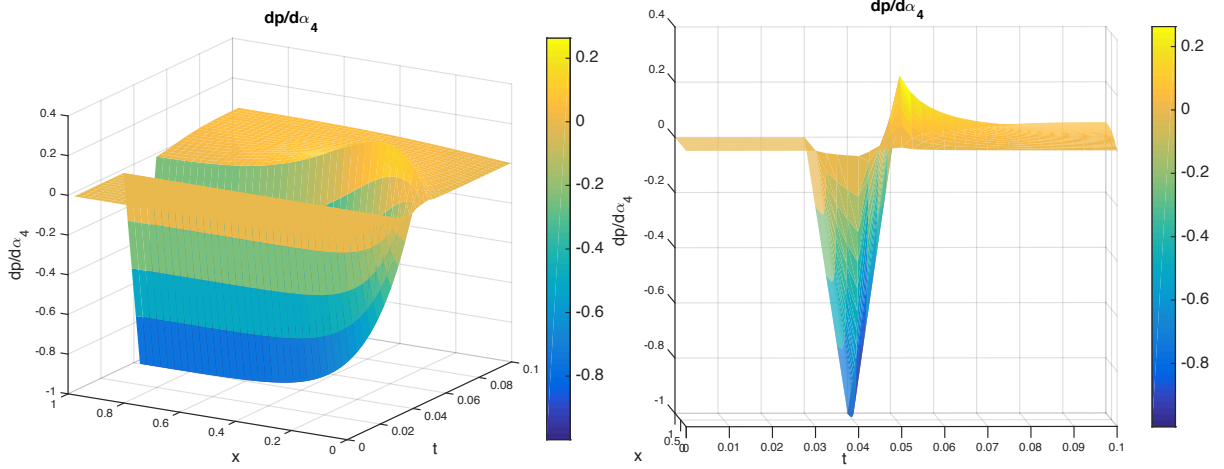


Figure 1.15 Sensitivity function of fluid pressure p with respect to boundary stress g_{3h} in the direction ϕ_4 when $\delta = 0$. Note, the two figures give different angles of view of the sensitivity.

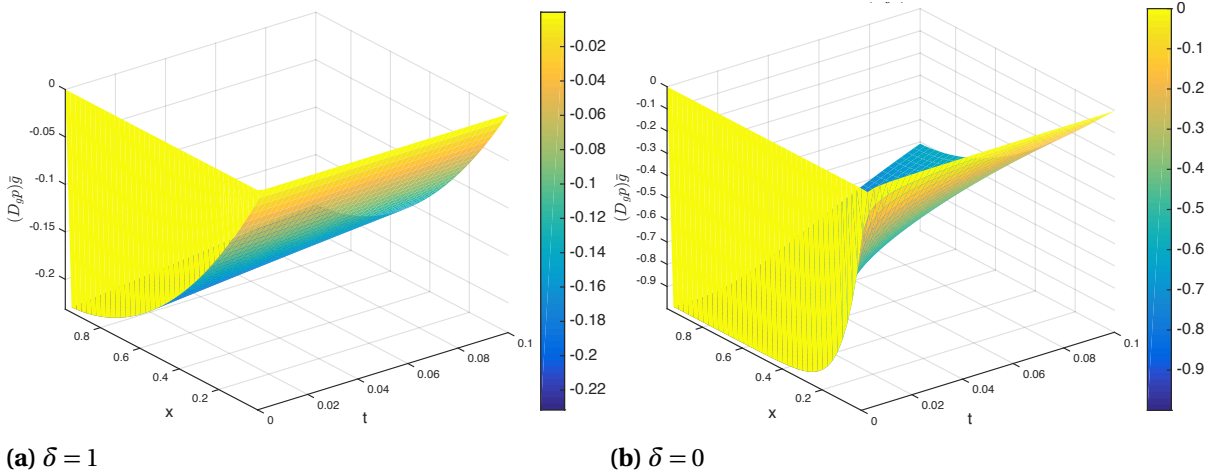


Figure 1.16 Sensitivity functions of fluid pressure p with respect to boundary stress g_{3h} in the direction $\bar{g} = \sum_{i=0}^{10} \phi_i$ when $\delta = 1$ (left) and $\delta = 0$ (right).

from the part of the boundary where the data g_{3h} is applied. In comparison, for $\delta = 0$, the solution is affected by the boundary datum g_{3h} throughout the entire domain. For $\delta = 1$, we see that the sensitivities $\frac{\partial u}{\partial a_i}$ stay similar for $t \geq t_i$, whereas for $\delta = 0$, the sensitivities drops shortly after $t = t_i$. This could indicate the effect of the term $\frac{\partial u}{\partial t}$ in equation (1.24) is dominant in the case $\delta = 1$.

Comparing Fig. 1.8 - Fig. 1.10, Fig. 1.14 - Fig. 1.16, and Fig. 1.20 - Fig. 1.22, we can see that the Darcy velocity v is the most sensitive to the boundary data g_{3h} . In the visco-elastic case, the magnitude of $\frac{\partial v}{\partial g_{3h}}$ is the highest among all of the sensitivities. Moreover, the sensitivity is one order of magnitude higher in the case of $\delta = 0$, and two sharp peaks appear around the time at which the direction is given.

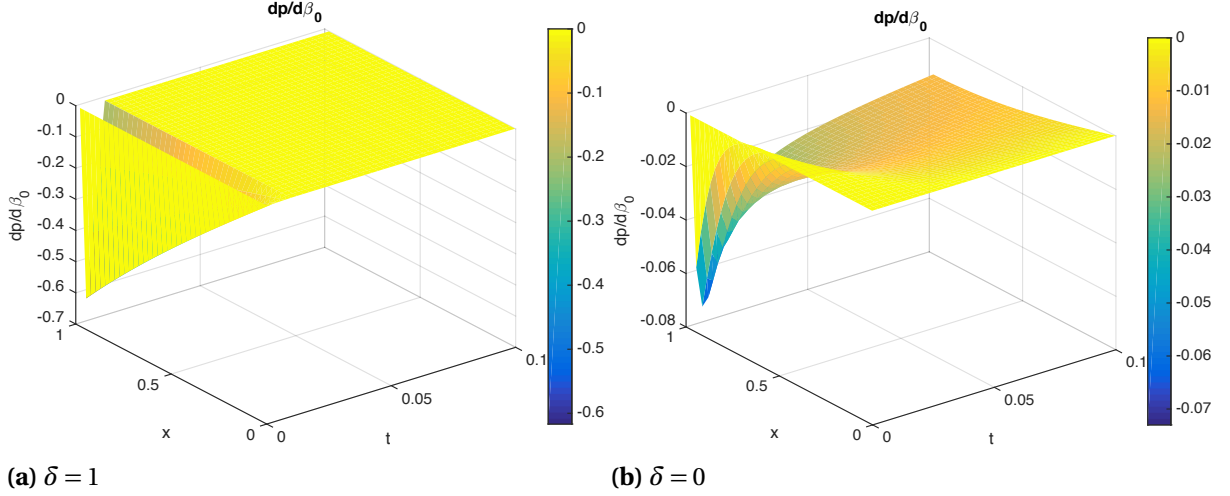


Figure 1.17 Sensitivity functions of fluid pressure p with respect to boundary source ψ_{3h} in the direction ϕ_0 when $\delta = 1$ (left) and $\delta = 0$ (right).

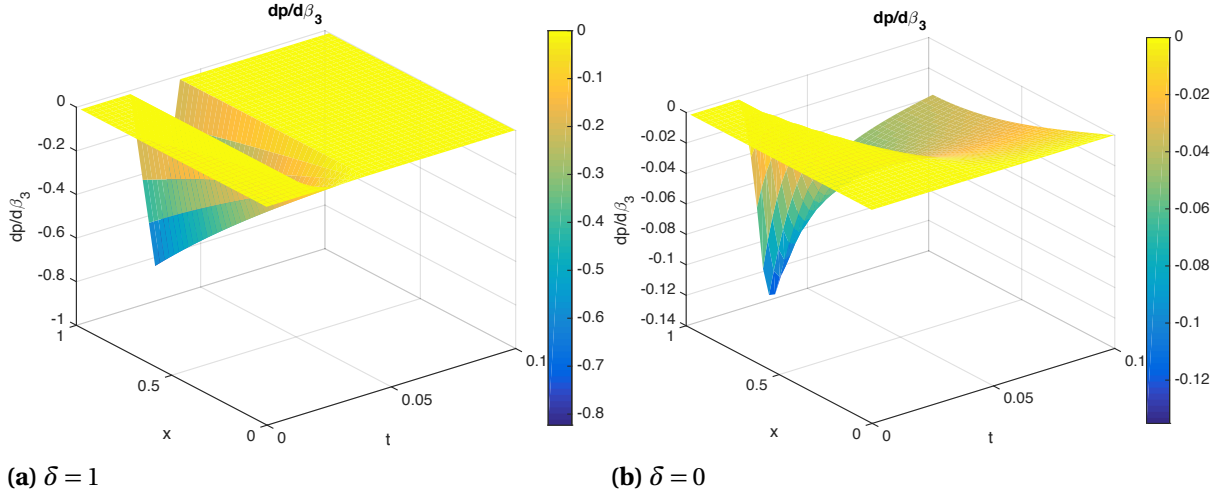


Figure 1.18 Sensitivity functions of fluid pressure p with respect to boundary source ψ_{3h} in the direction ϕ_3 when $\delta = 1$ (left) and $\delta = 0$ (right).

We also notice that in both elastic and visco-elastic cases, the sensitivity of the discharge velocity with respect to g_{3h} , which is applied at $x = 1$, increases towards the left end point, $x = 0$, of the domain. This is due to the fact that at $x = 1$, $v \cdot n = \psi_3$ and ψ_3 is not dependent on g_3 . This results in $\frac{\partial v}{\partial g_3} \cdot n = 0$ at $x = 1$. The magnitude of $\frac{\partial v}{\partial g_3}$ increases as we go farther away from $x = 1$, and ultimately reaches its maximum at $x = 0$, as there is no condition imposed on v at this boundary point.

Overall, we see that u is the least sensitive to both g_{3h} and ψ_{3h} and v is the most sensitive. We also note that the behavior of the sensitivities with respect to g_{3h} when we vary δ between 1 and 0 are more consistent and more drastic than the sensitivities with respect to ψ_{3h} .

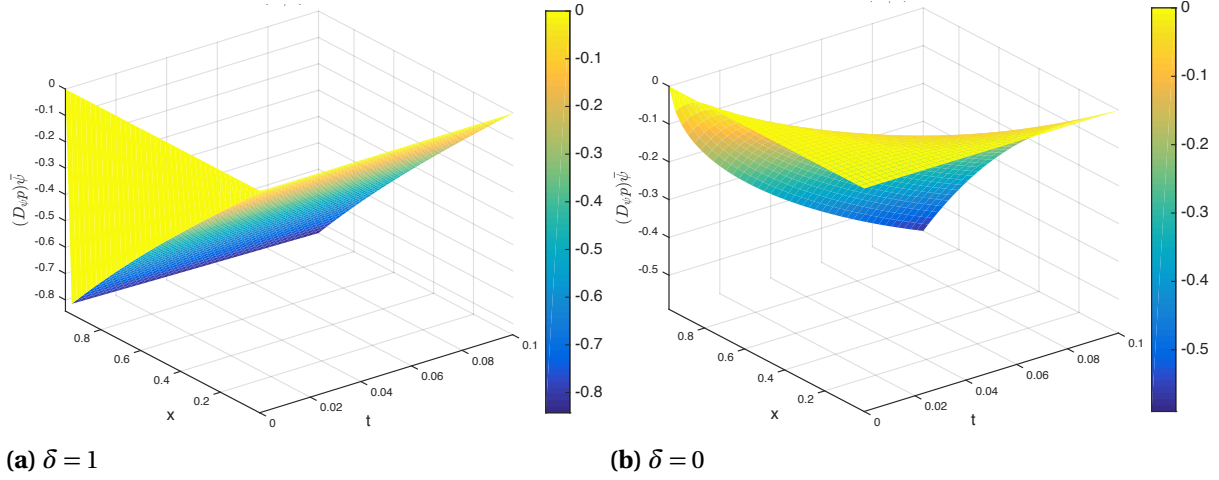


Figure 1.19 Sensitivity functions of fluid pressure p with respect to boundary stress ψ_{3h} in the direction $\bar{\psi} = \sum_{i=0}^{10} \phi_i$ when $\delta = 1$ (left) and $\delta = 0$ (right).

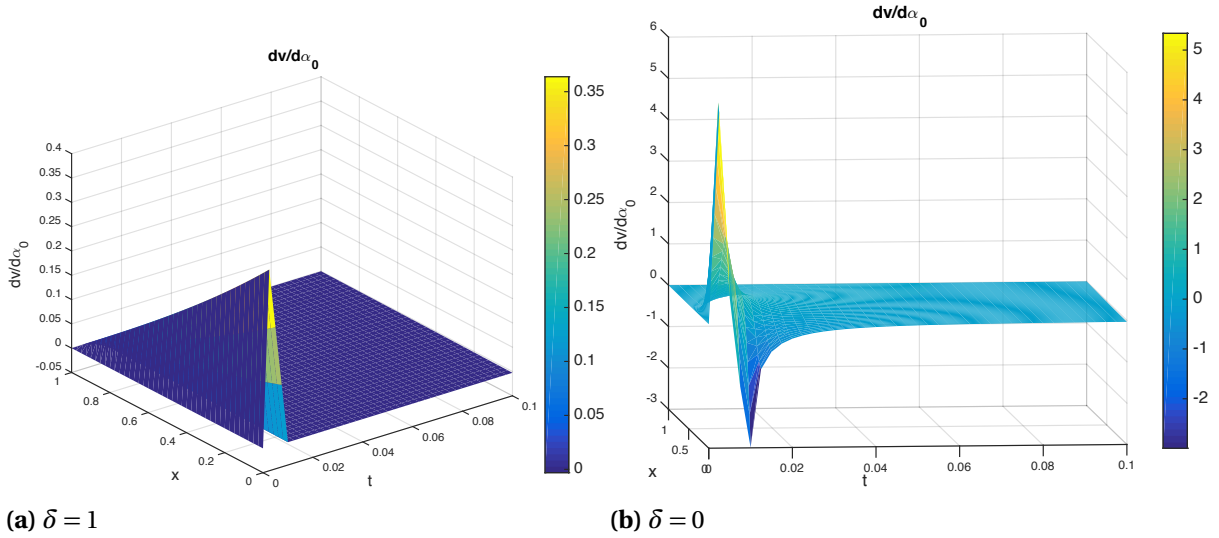


Figure 1.20 Sensitivity functions of discharge velocity v with respect to boundary stress g_{3h} in the direction ϕ_0 when $\delta = 1$ (left) and $\delta = 0$ (right).

1.4.1.4 Dynamical Model with Variable Permeability - Case 4

Consider the system given in Eq. 1.38 in the space-time domain $(x_0, x_f) \times (0, T) = (-1, 1) \times (0, 2)$, so that $L = 2\text{cm}$ and $T = 2\text{s}$. The boundary conditions are given by

$$\begin{cases} u = p = 0, & x_0 = -1, \\ \sigma n = g_4(t), \quad v n = \psi_4(t), & x_f = 1. \end{cases} \quad (1.138)$$

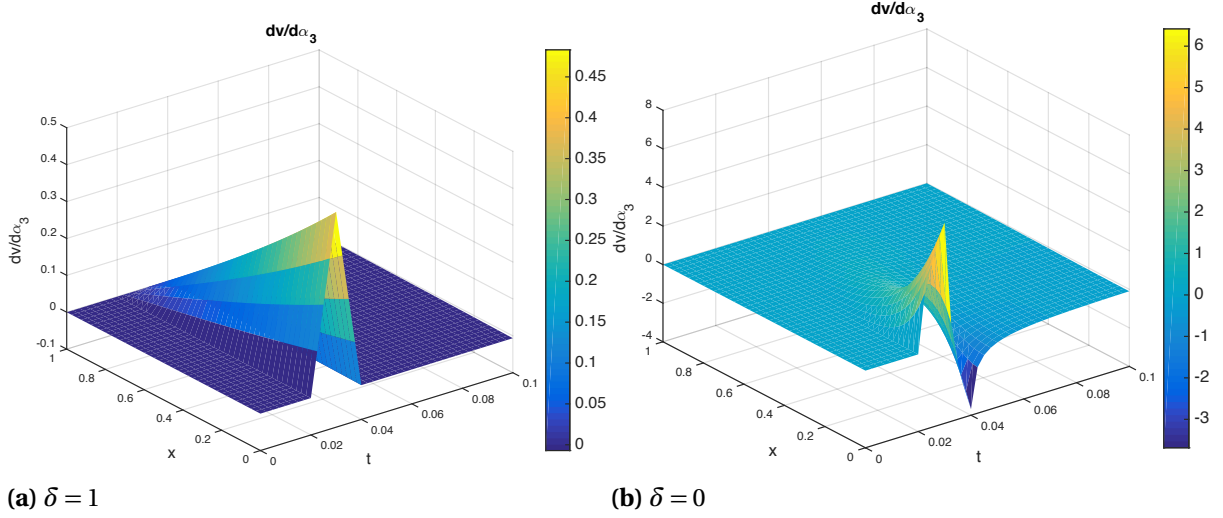


Figure 1.21 Sensitivity functions of discharge velocity v with respect to boundary stress g_{3h} in the direction ϕ_3 when $\delta = 1$ (left) and $\delta = 0$ (right).

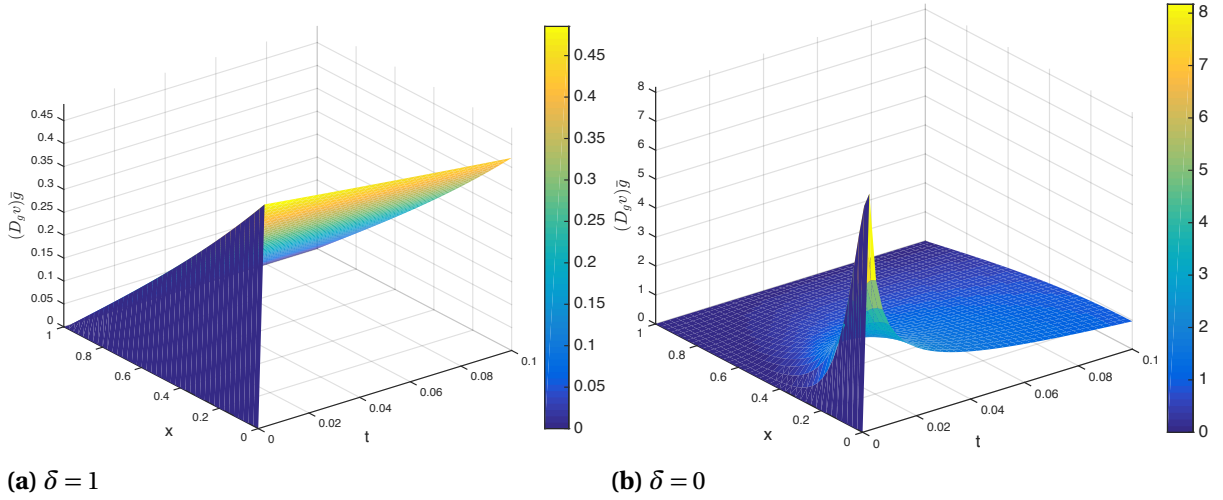


Figure 1.22 Sensitivity functions of discharge velocity v with respect to boundary stress g_{3h} in the direction $\tilde{g} = \sum_{i=0}^{10} \phi_i$ when $\delta = 1$ (left) and $\delta = 0$ (right).

Porosity and permeability are nonlinear functions of the solution, just as in Case 2. The porosity ϕ varies with the derivative of the displacement within the range $[\Phi_{\min}, \Phi_{\max}]$, where $0 < \Phi_{\min} < \Phi_{\max} < 1$, in such a way that the permeability k , expressed by the nonlinear relation of Carman-Kozeny Eq. 1.12, satisfies the following lower and upper bounds [48]:

$$0 < k_{\text{ref}} \frac{\Phi_{\min}^3}{(1 - \Phi_{\min})^2} \leq k(\phi) \leq k_{\text{ref}} \frac{\Phi_{\max}^3}{(1 - \Phi_{\max})^2}.$$

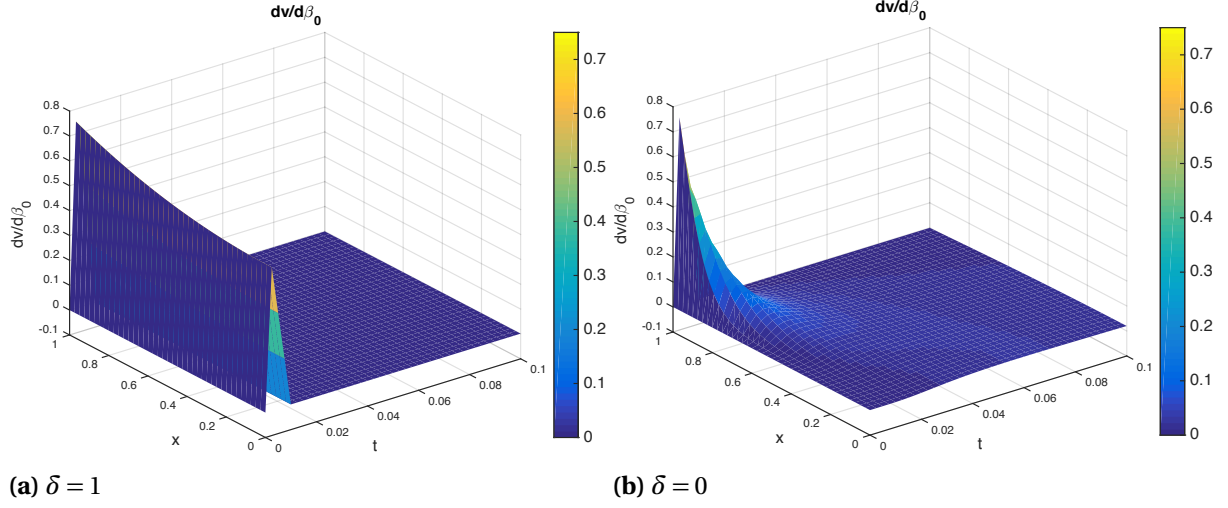


Figure 1.23 Sensitivity functions of discharge velocity v with respect to boundary source ψ_{3h} in the direction ϕ_0 when $\delta = 1$ (left) and $\delta = 0$ (right).

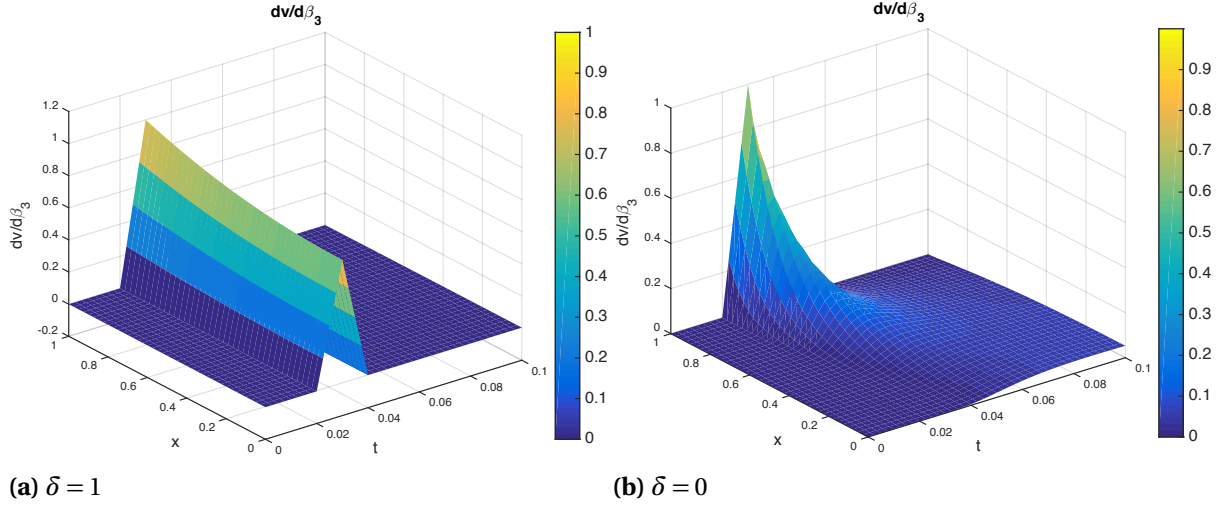


Figure 1.24 Sensitivity functions of discharge velocity v with respect to boundary source ψ_{3h} in the direction ϕ_3 when $\delta = 1$ (left) and $\delta = 0$ (right).

We set the following parameters,

$$\Phi_{\min} = 0.125, \quad \Phi_{\max} = 0.875, \quad \text{and } k_{\text{ref}} = 1 \text{ cm}^3 \text{ s g}^{-1}.$$

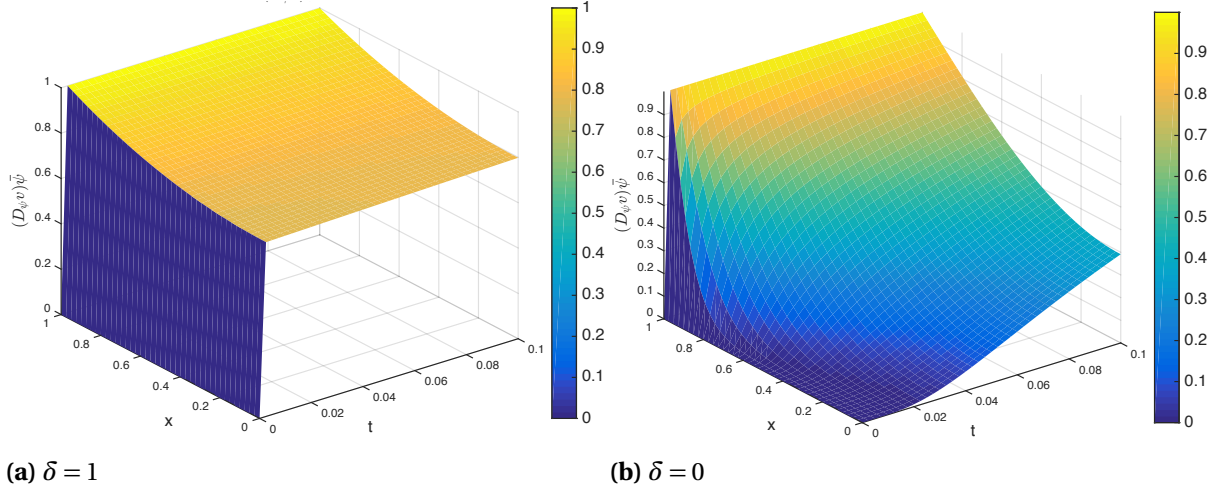


Figure 1.25 Sensitivity functions of discharge velocity v with respect to boundary stress ψ_{3h} in the direction $\bar{\psi} = \sum_{i=0}^{10} \phi_i$ when $\delta = 1$ (left) and $\delta = 0$ (right).

The volumetric and boundary source terms are time-dependent and are given by:

$$\begin{aligned}
 F_4(x, t) &= -[U_{ref} \chi''(x)(H_A \tau(t) + \delta H_V \tau'(t)) - P_{ref} \tau(t) \chi'(x)], \\
 S_4(x, t) &= U_{ref} \chi'(x) \tau'(t) - P_{ref} k_{ref} \chi''(x) \tau(t) \Theta(x, t) - k_{ref} P_{ref} U_{ref} \chi'(x) \chi''(x) \tau^2(t) \Xi(x, t), \\
 g_4(t) &= U_{ref} \chi'(x_{end})(H_A \tau(t) + \delta H_V \tau'(t)) - P_{ref} \tau(t) \chi(x_{end}), \\
 \psi_4(t) &= -k_{ref} P_{ref} \Theta(x_{end}) \chi'(x_{end}) \tau(t),
 \end{aligned}$$

where

$$\begin{aligned}
 \chi(x) &= \sin(\omega_x x), \quad \tau(t) = \sin(\omega_t t), \quad \Phi(x, t) = \phi_0 + U_{ref} \chi'(x) \tau(t), \\
 \Theta(x, t) &= \frac{\Phi^3(x, t)}{[1 - \Phi(x, t)]^2}, \quad \Xi(x, t) = \frac{\Phi^2(x, t)[3 - \Phi(x, t)]}{[1 - \Phi(x, t)]^3},
 \end{aligned}$$

with $\omega_t = 2\pi/T$, and all the other parameter values the same as those given in Case 3.

For the visco-elastic case $\delta = 1$, the problem admits the following exact solution [39]:

$$\begin{aligned}
 u(x, t) &= U_{ref} \chi(x) \tau(t), \\
 p(x, t) &= P_{ref} \chi(x) \tau(t), \\
 \sigma(x, t) &= U_{ref} \chi'(x)(H_A \tau(t) + \delta H_V \tau'(t)) - P_{ref} \chi(x) \tau(t), \\
 v(x, t) &= -P_{ref} k_{ref} \Theta(x, t) \chi'(x) \tau(t), \\
 \wp(x, t) &= -\lambda_e U_{ref} \chi'(x) \tau(t).
 \end{aligned}$$

Again, since the boundary sources g_4 and ψ_4 are time dependent, we approximate these func-

tions using linear splines as described in Section 1.3.1:

$$g_4(t) \approx g_{4h} = \sum_{i=0}^{N_g} \alpha_i \phi_i(t), \quad \psi_4(t) \approx \psi_{4h} = \sum_{i=0}^{N_\psi} \beta_i \tilde{\phi}_i(t),$$

with $N_g = 10$ and $N_\psi = 12$ where $\alpha_i = g_4(t_i)$ and $\beta_i = \psi_4(\tilde{t}_i)$ (see Figure 1.26).

In the figures below, we display the graphs of the directional derivatives first in the case of directions taken as particular splines, like ϕ_i and $\tilde{\phi}_i$, and then for specific linear combinations of the splines, like $w_h = \sum_{i=0}^{N_g} \phi_i$ and $\tilde{w}_h = \sum_{i=0}^{N_\psi} \tilde{\phi}_i$. For all the sensitivities, we include both visco-elastic and purely elastic cases, and compare the results.

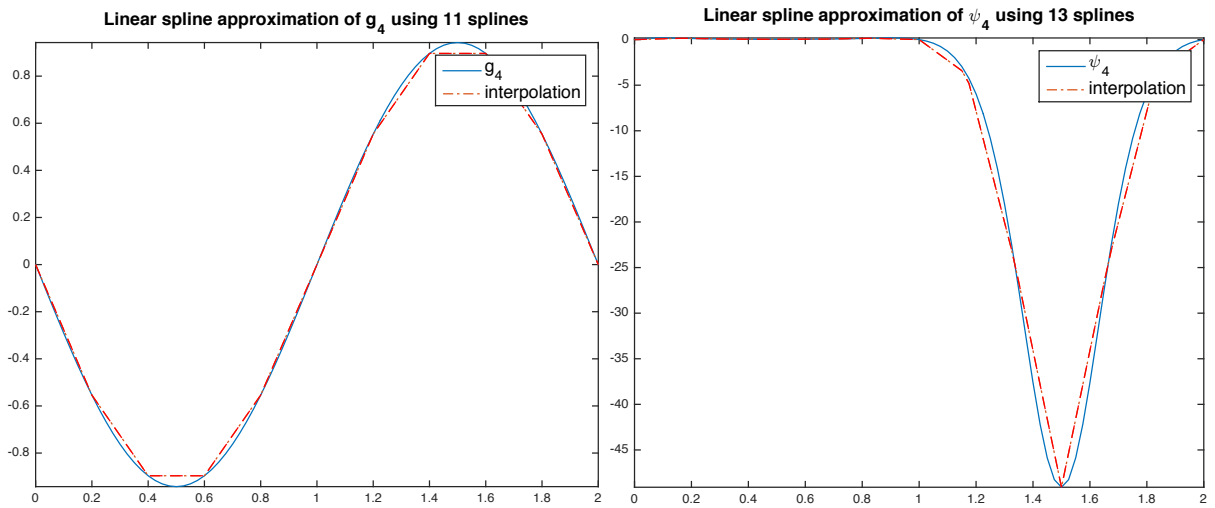


Figure 1.26 Linear spline approximations of g_4 and ψ_4 .

Observations In Fig. 1.27-Fig. 1.32, we see that unlike the sensitivities in the case of constant permeability, here u appears to be more sensitive to ψ_{4h} than g_{4h} . While there does not appear to be a large difference in magnitude of the sensitivity of u with respect to g_{4h} when $\delta = 0$ and $\delta = 1$ when taken in the direction ϕ_3 (see Fig. 1.28), we note that when the sensitivity is taken in the direction ϕ_0 (see Fig. 1.27) and $\bar{g} = \sum_{i=0}^{N_g} \phi_i$ (see Fig. 1.29), we see large differences of either three or two orders of magnitude. We also see that the sensitivity of u with respect to ψ_{4h} is at least one order of magnitude larger when $\delta = 0$ than when $\delta = 1$.

Further, when $\delta = 0$, the sensitivity of u with respect to ψ_{4h} is much more irregular than when $\delta = 1$. This behavior was seen in the sensitivities of u with respect to ψ_{4h} in the direction of each of the splines ϕ_i , $i = 0, \dots, N_\psi$. On the other hand, the sensitivities of u with respect to g_{4h} are

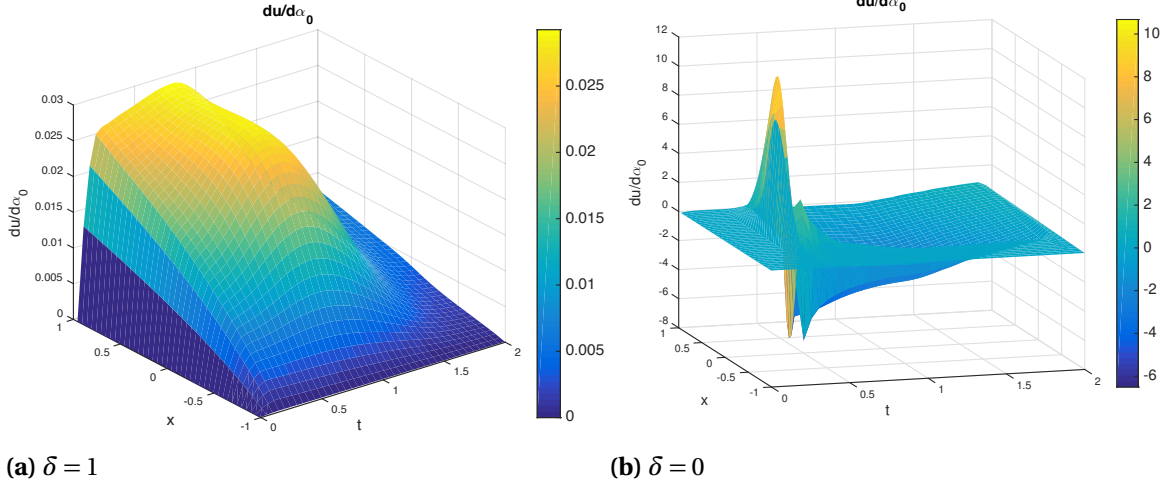


Figure 1.27 Sensitivity functions of solid displacement u with respect to boundary stress g_{4h} in the direction ϕ_0 when $\delta = 1$ (left) and $\delta = 0$ (right).

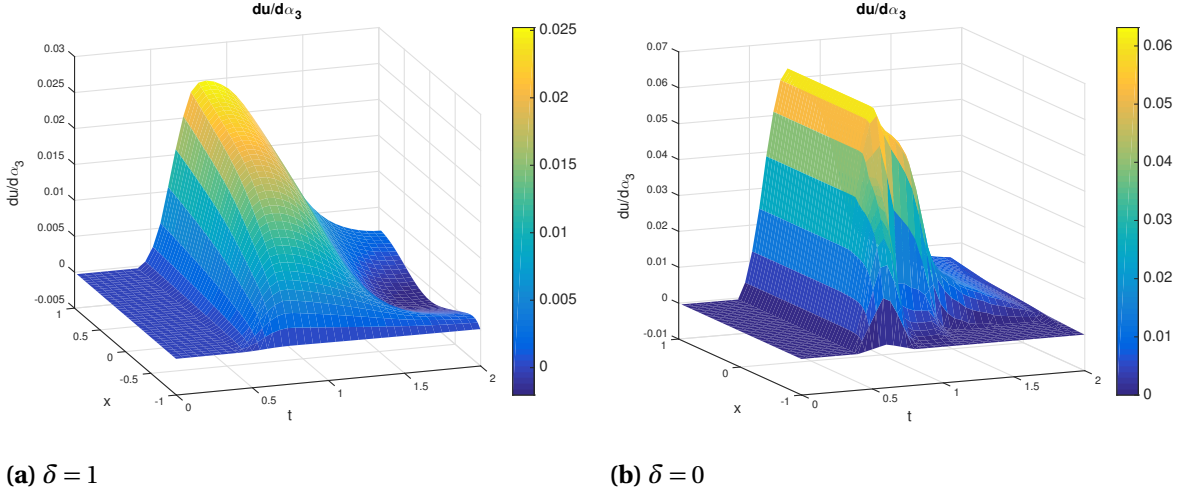


Figure 1.28 Sensitivity functions of solid displacement u with respect to boundary stress g_{4h} in the direction ϕ_3 when $\delta = 1$ (left) and $\delta = 0$ (right).

irregular in the direction of some of the earlier splines (i.e. $j < 3$), but smooth out for directions ϕ_j , $j = 3 \dots, N_g$.

In Fig. 1.33-Fig. 1.38, we see that overall, p appears to be more sensitive to ψ_{4h} than to g_{4h} and both $\frac{\partial p}{\partial g_{4h}}$ and $\frac{\partial p}{\partial \psi_{4h}}$ are at least one order of magnitude larger when $\delta = 0$ than when $\delta = 1$. When $\delta = 0$, the sensitivities of p with respect to g_{4h} is somewhat irregular when taken in the directions ϕ_j , $j \leq 7$, however they smooth out for $j = 7, \dots, N_g$ (not shown here). In contrast, the sensitivities of p with respect to ψ_{4h} are irregular in the directions of each spline and for both $\delta = 0, 1$.

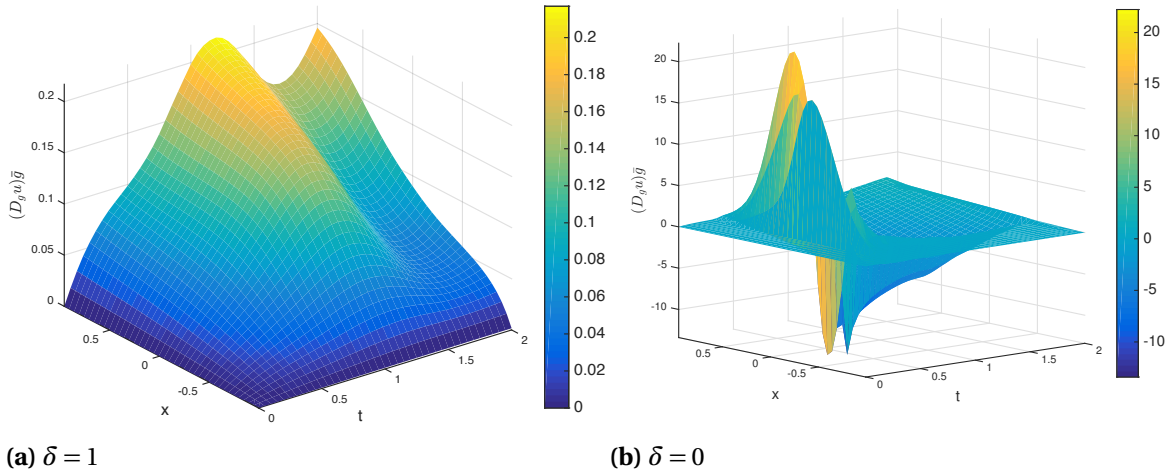


Figure 1.29 Sensitivity functions of solid displacement u with respect to boundary stress g_{4h} in the direction $\vec{g} = \sum_{i=0}^{N_g} \phi_i$ when $\delta = 1$ (left) and $\delta = 0$ (right).

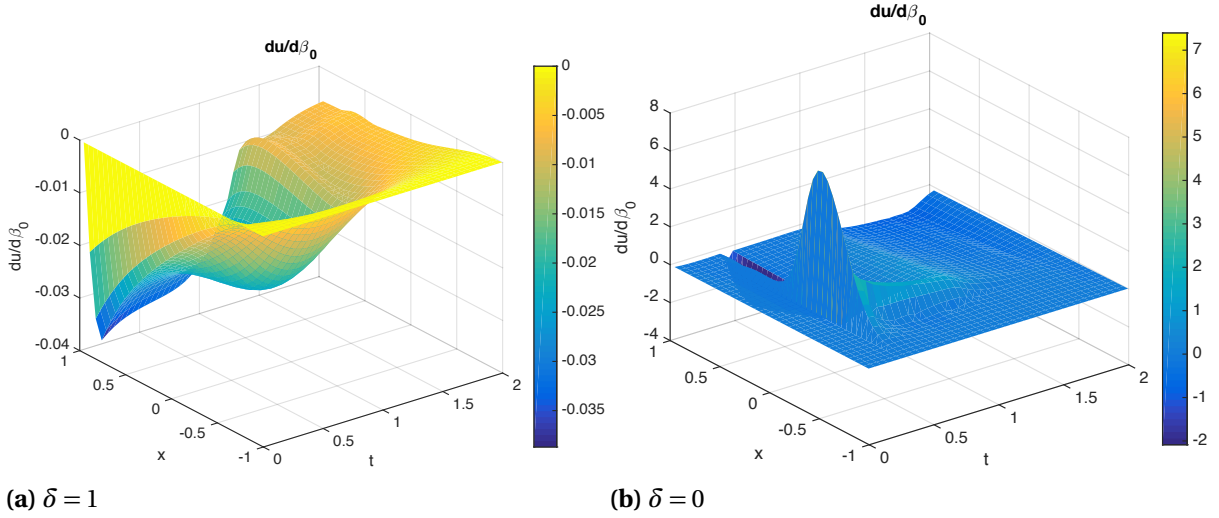


Figure 1.30 Sensitivity functions of solid displacement u with respect to boundary source ψ_{4h} in the direction $\hat{\phi}_0$ when $\delta = 1$ (left) and $\delta = 0$ (right).

Regarding the sensitivities of the solid displacement u and fluid pressure p with respect to g_{4h} , we see from Fig. 1.27-Fig. 1.29 and Fig. 1.33-Fig. 1.35 that the magnitude of the sensitivities is higher (up to 3 times in order of magnitude in the case of α_0) in the elastic case than in the visco-elastic case. The difference decreases for subsequent α_i 's.

Moreover, in the visco-elastic case, the sensitivity of u and p with respect to the boundary datum g_{4h} in the specific directions of the splines decreases as we get farther away from the boundary $x = 1$, where the datum acts. In comparison, the solid displacement and fluid pressure seem to be equally

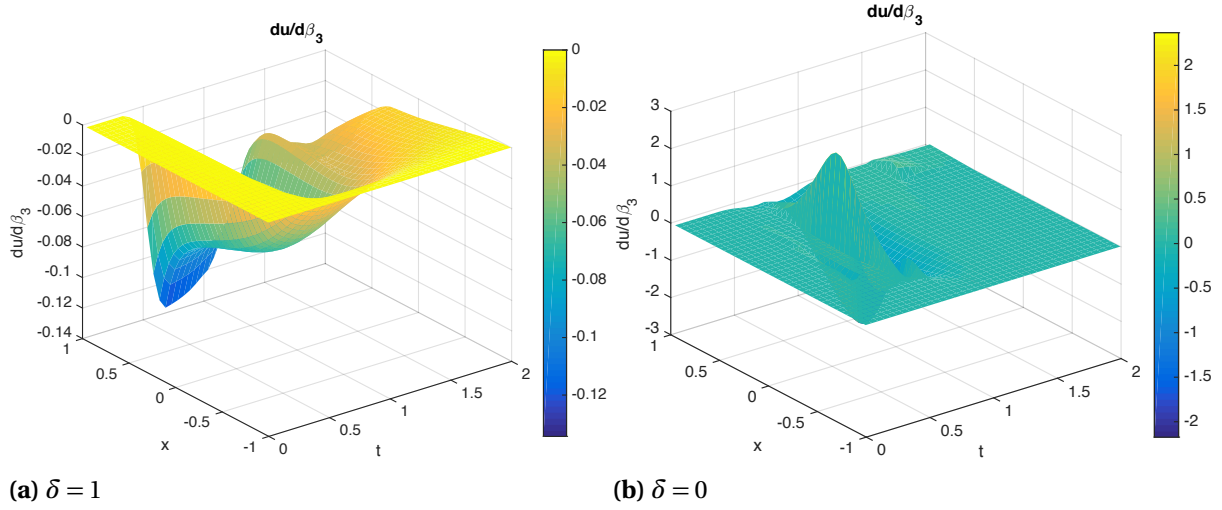


Figure 1.31 Sensitivity functions of solid displacement u with respect to boundary source ψ_{4h} in the direction $\tilde{\phi}_3$ when $\delta = 1$ (left) and $\delta = 0$ (right).

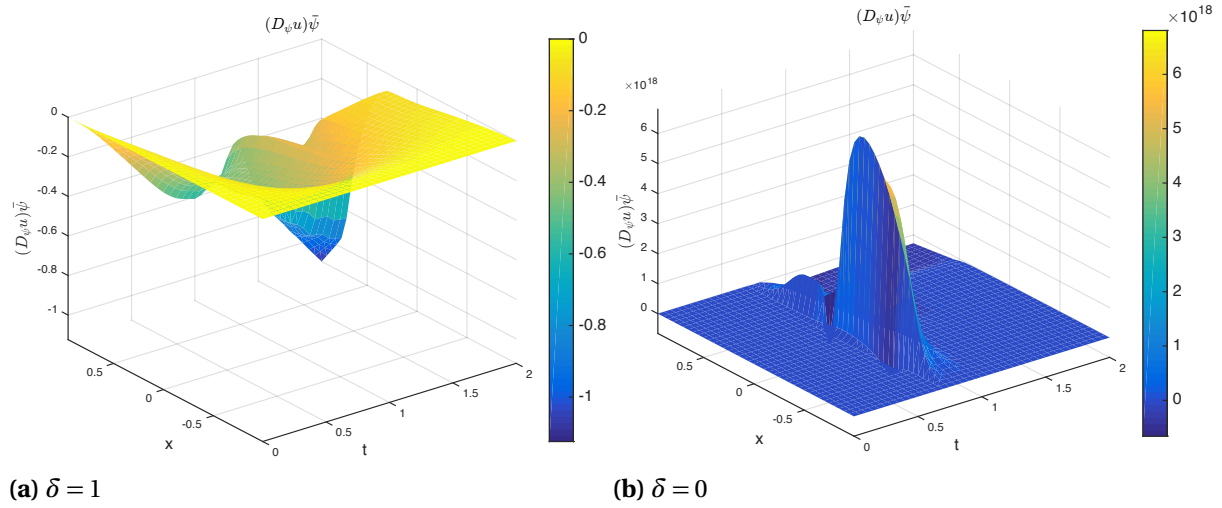
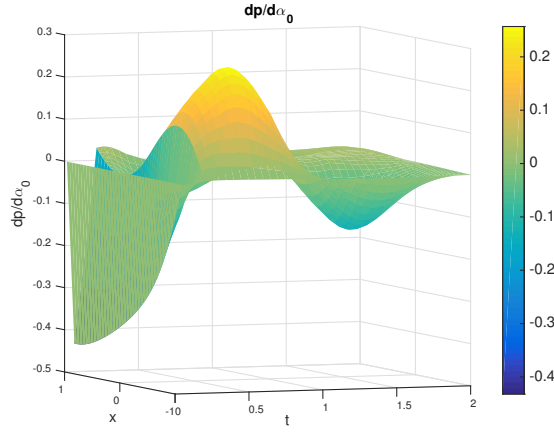


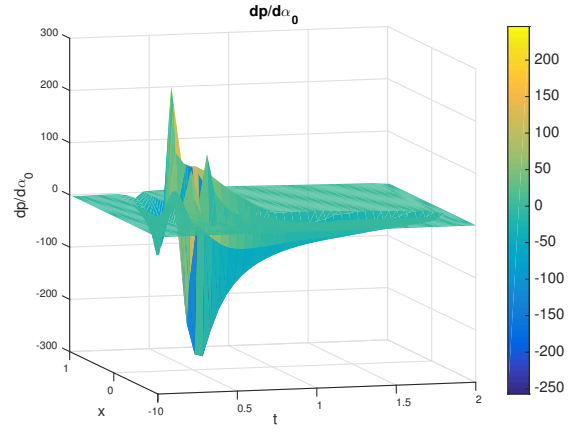
Figure 1.32 Sensitivity functions of solid displacement u with respect to boundary source ψ_{4h} in the direction $\tilde{\psi} = \sum_{i=0}^{N_{\psi}} \tilde{\phi}_i$ when $\delta = 1$ (left) and $\delta = 0$ (right).

sensitive to the boundary source g_{4h} throughout the space domain in the purely elastic case. This is similar to Case 3, where the same behaviour was observed between the elastic and visco-elastic cases. However, this is not the case for the sensitivity in the direction \bar{g} , where the influence of the boundary is seen throughout the space-time domain. It can be observed though that in the visco-elastic case, the sensitivity surface is much smoother than in the elastic counterpart.

It is interesting to see the difference in behaviors of the sensitivities of the solid displacement and fluid pressure with respect to the boundary traction g_{4h} in comparison to Case 3, where the

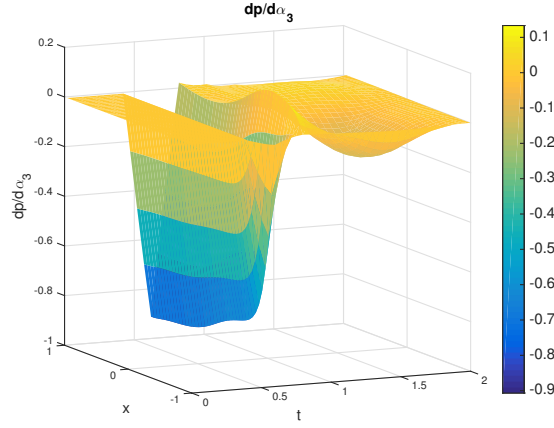


(a) $\delta = 1$

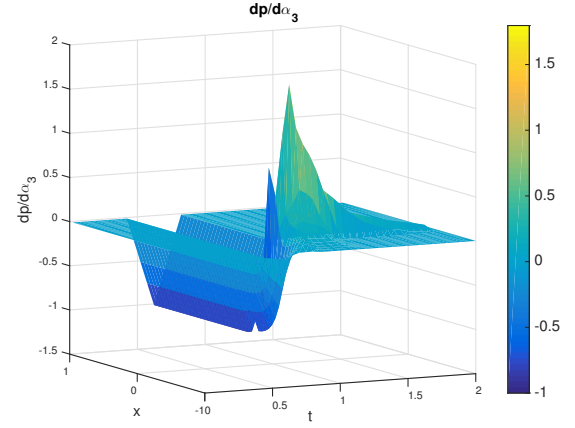


(b) $\delta = 0$

Figure 1.33 Sensitivity functions of pressure p with respect to boundary stress g_{4h} in the direction ϕ_0 when $\delta = 1$ (left) and $\delta = 0$ (right).



(a) $\delta = 1$

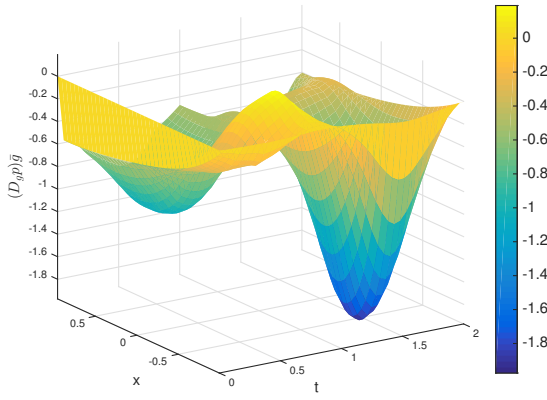


(b) $\delta = 0$

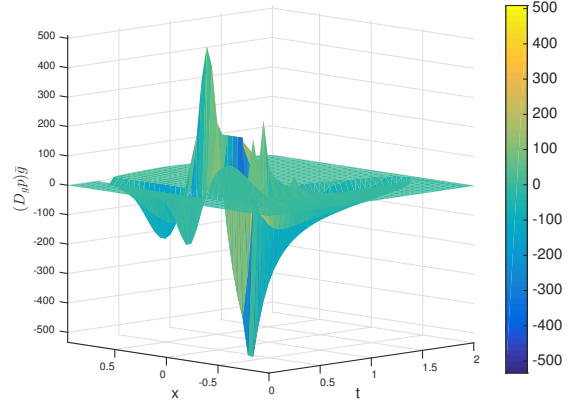
Figure 1.34 Sensitivity functions of pressure p with respect to boundary stress g_{4h} in the direction ϕ_3 when $\delta = 1$ (left) and $\delta = 0$ (right).

permeability is assumed to be constant. The surfaces associated with the sensitivities in this case are much more complex, with sharp peaks (present in the $\delta = 0$ scenario), and a non-zero presence almost throughout the space-time domain.

In Fig. 1.39-Fig. 1.44, we again see that v appears to be more sensitive to ψ_{4h} than it is to g_{4h} . Similarly to the sensitivity of u with respect to g_{4h} , there does not appear to be a large difference in magnitude of the sensitivity of v_{4h} with respect to g when $\delta = 0$ and $\delta = 1$ when taken in the direction ϕ_3 (see Fig. 1.40). However, when the sensitivity is taken in the direction ϕ_0 (see Fig. 1.39)

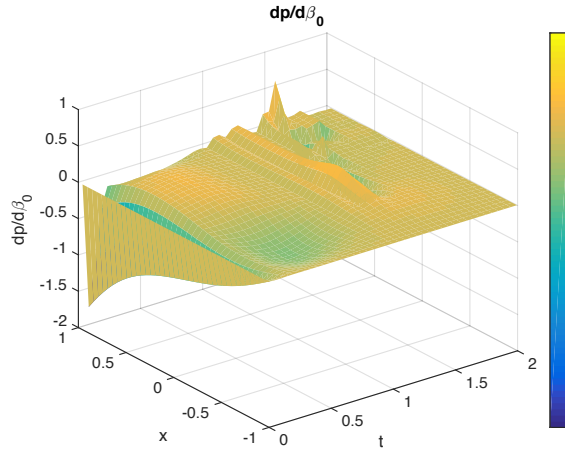


(a) $\delta = 1$

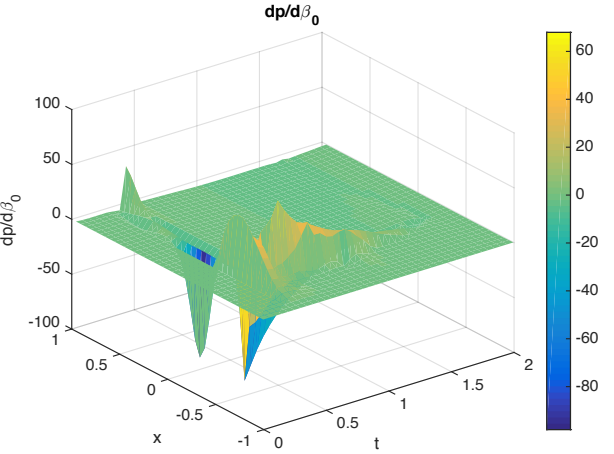


(b) $\delta = 0$

Figure 1.35 Sensitivity functions of fluid pressure p with respect to boundary stress g_{4h} in the direction $\bar{g} = \sum_{i=0}^{N_g} \phi_i$ when $\delta = 1$ (left) and $\delta = 0$ (right).



(a) $\delta = 1$



(b) $\delta = 0$

Figure 1.36 Sensitivity functions of fluid pressure p with respect to boundary source ψ_{4h} in the direction $\bar{\phi}_0$ when $\delta = 1$ (left) and $\delta = 0$ (right).

and $\bar{g} = \sum_{i=0}^{N_g} \phi_i$ (see Fig. 1.41), there is a difference of at least three orders of magnitude. We also see a drastic difference in magnitude of the sensitivities of v with respect to ψ_{4h} for the viscoelastic case versus the purely elastic case.

In regards to the sensitivity of the discharge velocity v with respect to the boundary traction g_{4h} , we see from Fig. 1.39-Fig. 1.41 that the discharge velocity, among the three state variables, is the most sensitive to the boundary datum g_{4h} . This could explain why the fluid energy (which is dependent on the discharge velocity and the permeability) seems to become unbounded when

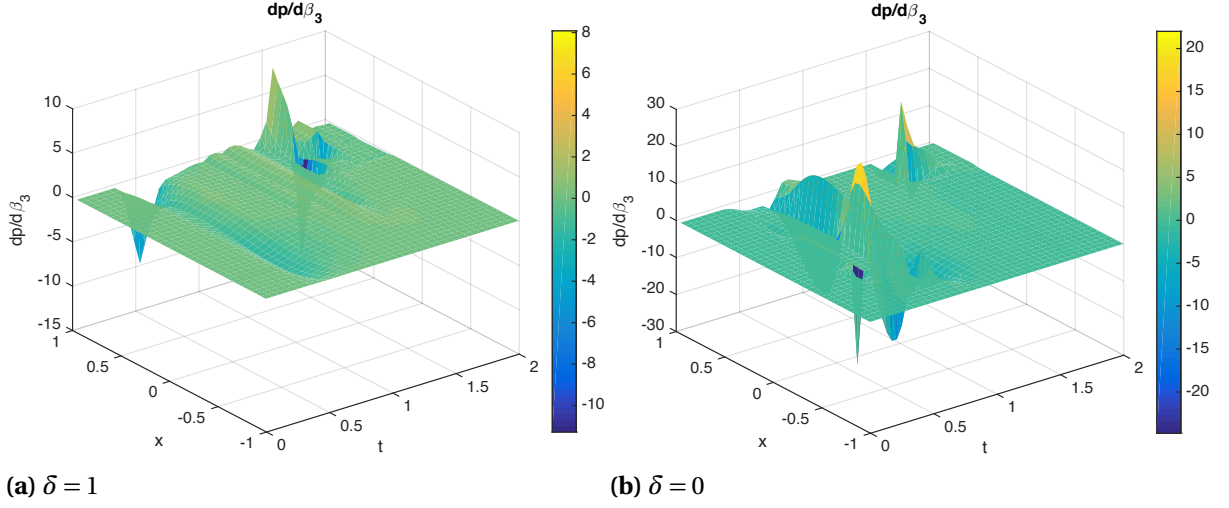


Figure 1.37 Sensitivity functions of fluid pressure p with respect to boundary source ψ_{4h} in the direction $\tilde{\phi}_3$ when $\delta = 1$ (left) and $\delta = 0$ (right).

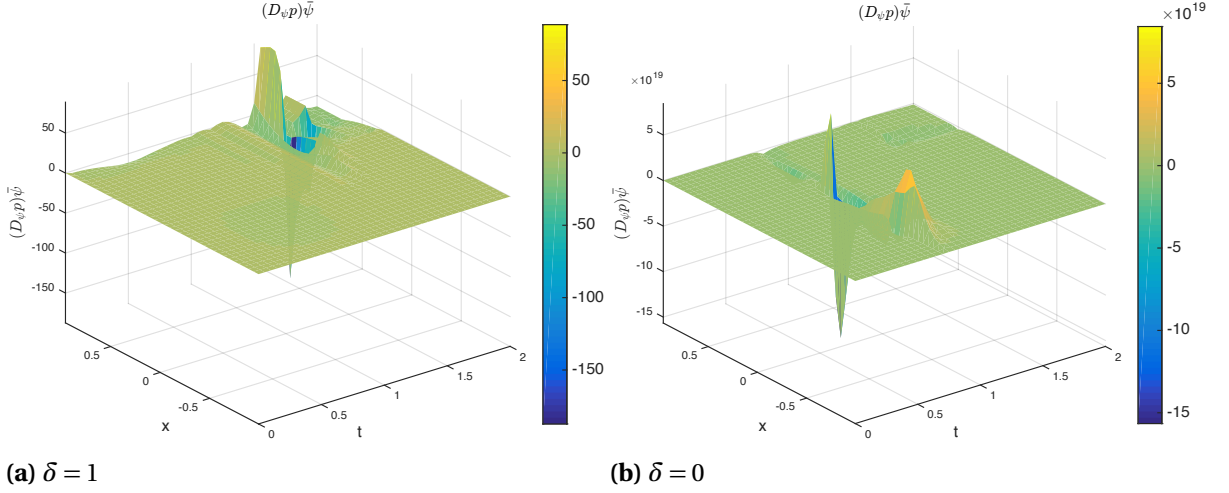
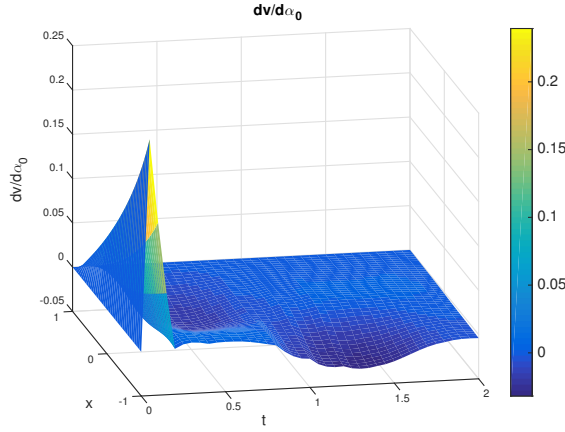


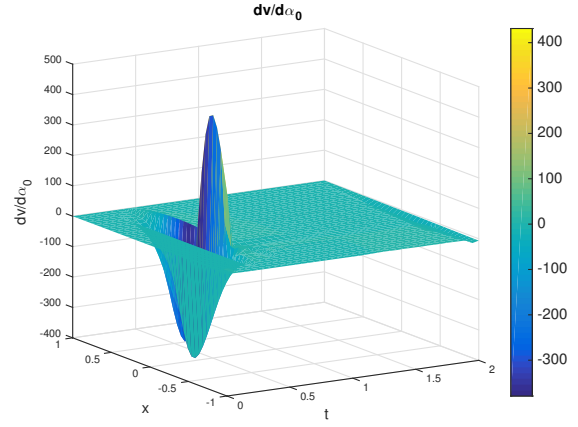
Figure 1.38 Sensitivity functions of fluid pressure p with respect to boundary source ψ_{4h} in the direction $\tilde{\psi} = \sum_{i=0}^{N_\psi} \tilde{\phi}_i$ when $\delta = 1$ (left) and $\delta = 0$ (right).

the data loses smoothness in time [39]. We also see that the surfaces associated with the discharge velocity sensitivities with respect to g_{4h} are less smooth and much sharper in this case than in Case 3 (where permeability is constant).

In comparison to the solid displacement and fluid pressure sensitivities with respect to g_{4h} , the sensitivity of the discharge velocity with respect to the boundary data g_{4h} seems to increase towards the left end point $x = -1$ of the domain in both the elastic and visco-elastic cases. This was explained when first observed in Case 3.

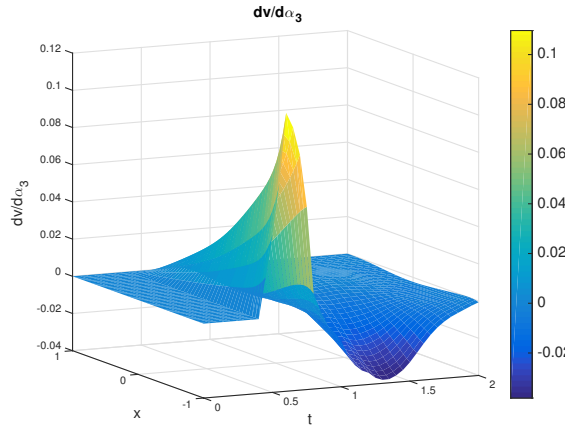


(a) $\delta = 1$

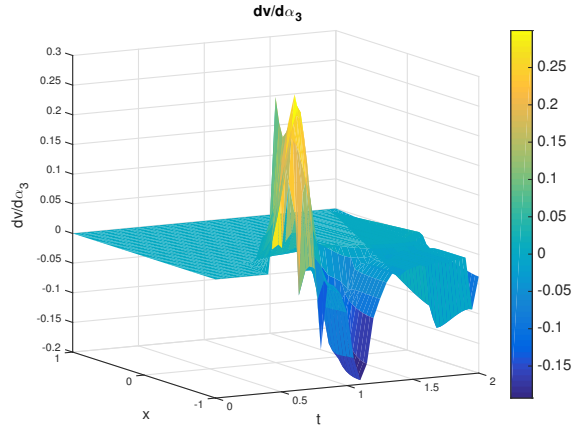


(b) $\delta = 0$

Figure 1.39 Sensitivity functions of discharge velocity ν with respect to boundary stress g_{4h} in the direction ϕ_0 when $\delta = 1$ (left) and $\delta = 0$ (right).



(a) $\delta = 1$



(b) $\delta = 0$

Figure 1.40 Sensitivity functions of discharge velocity ν with respect to boundary stress g_{4h} in the direction ϕ_3 when $\delta = 1$ (left) and $\delta = 0$ (right).

Here we also include the solution graphs for Case 4 in Fig. 1.45-Fig. 1.47. Note, the values u and p are given at the midpoints of the partition subintervals (x_i, x_{i+1}) of (x_0, x_f) .

1.4.1.5 Irregular Boundary Data - Case 5

In [39], the following example is used to study how time regularity in the boundary source term influences the solid displacement and fluid pressure in the presence and absence of viscosity. Let us consider again the system given in Eq. 1.38 in the space-time domain $(x_0, x_f) \times (0, T) = (-1, 1) \times (0, 2)$,

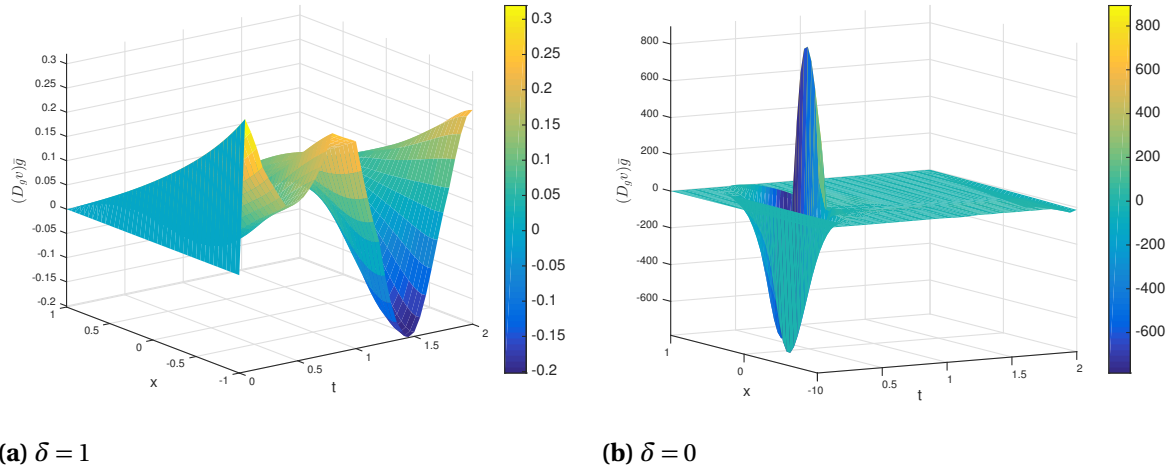


Figure 1.41 Sensitivity functions of discharge velocity v with respect to boundary stress g_{4h} in the direction $\tilde{g} = \sum_{i=0}^{N_g} \phi_i$ when $\delta = 1$ (left) and $\delta = 0$ (right).

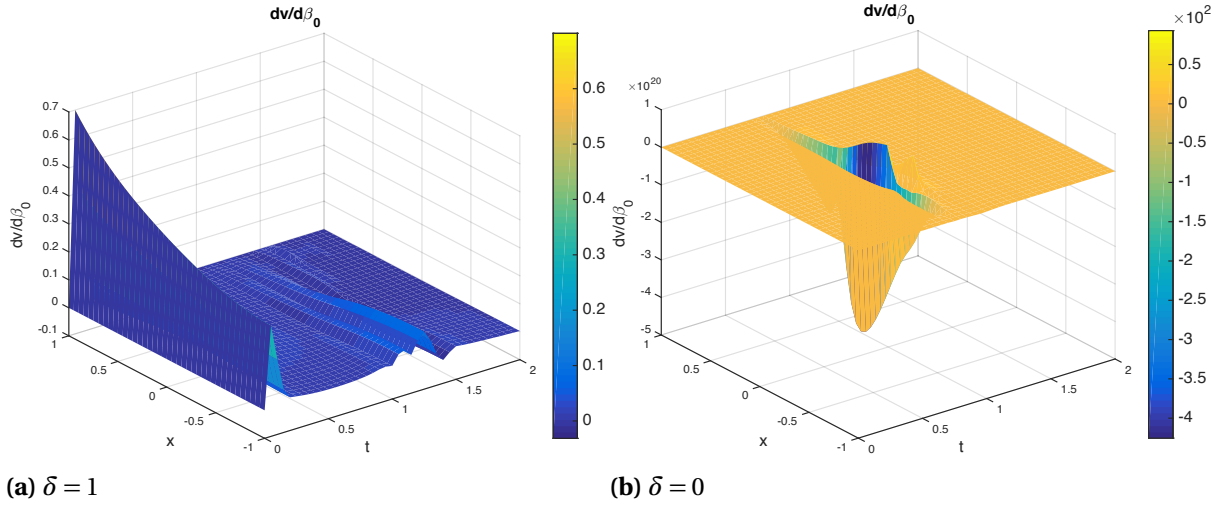


Figure 1.42 Sensitivity functions of discharge velocity v with respect to boundary source ψ_{4h} in the direction $\tilde{\phi}_0$ when $\delta = 1$ (left) and $\delta = 0$ (right).

so that $L = 2$ cm and $T = 2$ s. To help us see the effect better, we study the problem in the absence of volumetric sources of linear momentum and mass:

$$F_5(x, t) = S_5(x, t) = 0, \quad (1.139)$$

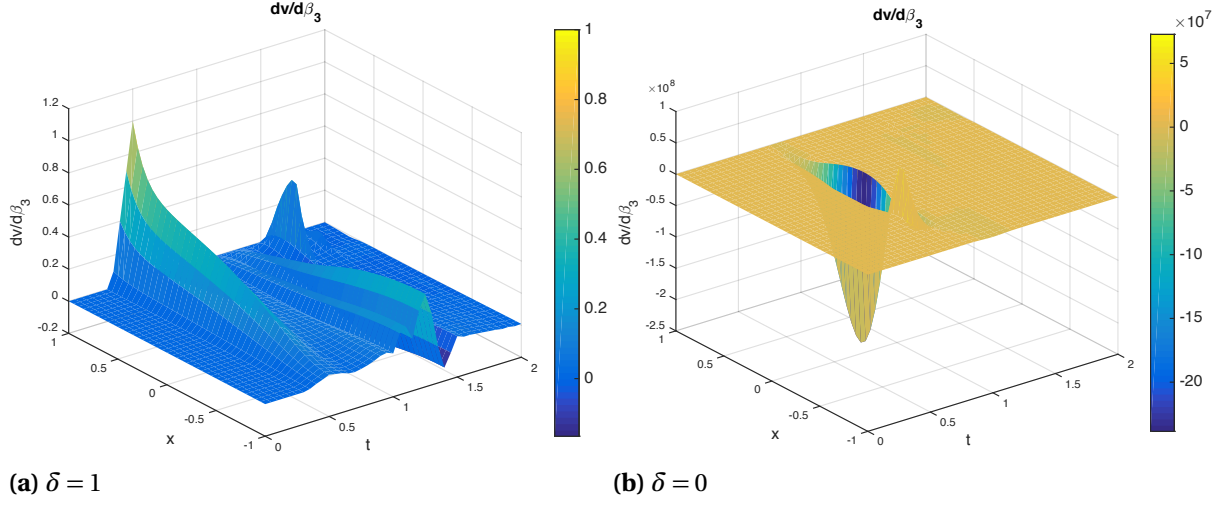


Figure 1.43 Sensitivity functions of discharge velocity v with respect to boundary source ψ_{4h} in the direction $\hat{\phi}_3$ when $\delta = 1$ (left) and $\delta = 0$ (right).

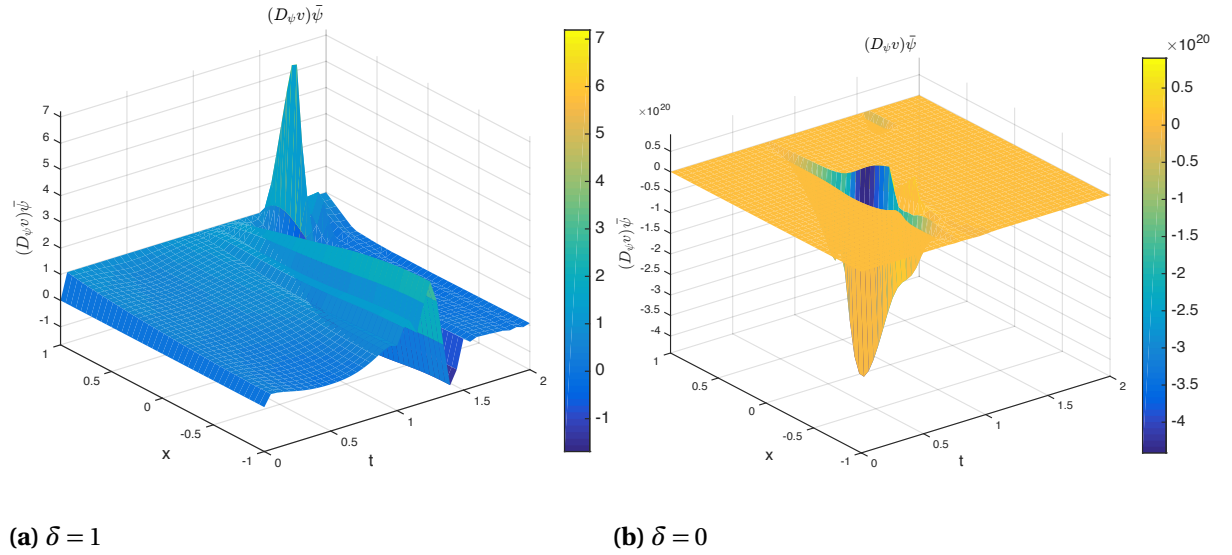


Figure 1.44 Sensitivity functions of discharge velocity v with respect to boundary source ψ_{4h} in the direction $\tilde{\psi} = \sum_{i=0}^{N_{\psi}} \tilde{\phi}_i$ when $\delta = 1$ (left) and $\delta = 0$ (right).

with boundary conditions given by

$$\begin{cases} u = p = 0, & x_0 = -1, \\ v n = 0, \sigma n = c_g \mathcal{G}_q(t, ; t_a, t_b), & x_f = 1, \end{cases} \quad (1.140)$$

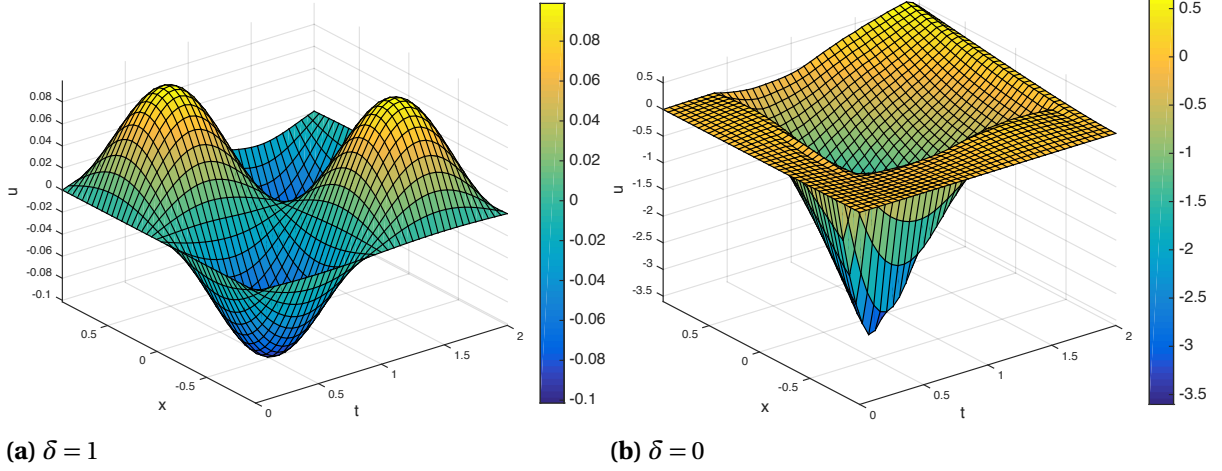


Figure 1.45 Solution functions of solid displacement u when $\delta = 1$ (left) and $\delta = 0$ (right).

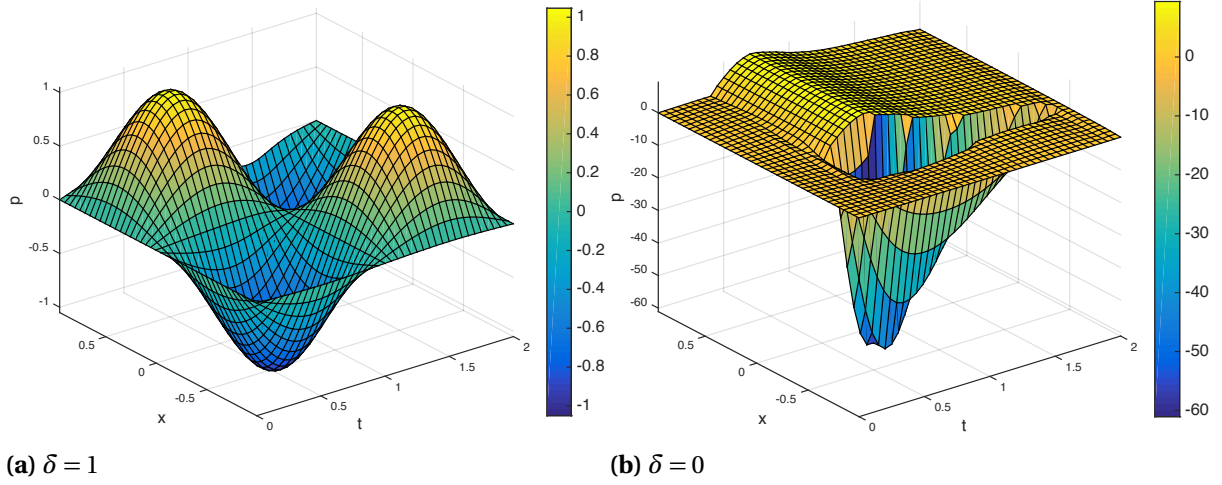


Figure 1.46 Solution functions of fluid pressure p when $\delta = 1$ (left) and $\delta = 0$ (right).

where

$$\mathcal{G}_q(t; t_a, t_b) = \frac{1}{2} [\tanh(q(t - t_a)) - \tanh(q(t - t_b))], \quad (1.141)$$

$$t_a = 1 - T/8, \quad t_b = 1 + T/8, \quad c_g = 0.01 \text{ dynecm}^{-2}.$$

We will consider both $g_5^{100} = \mathcal{G}_{100}(t; t_a, t_b)$ and $g_5^\infty = \mathcal{G}_\infty(t; t_a, t_b)$. In both cases, we approximate g_5^q using linear splines as described in Section 1.3.1 (see Fig. 1.48). Namely,

$$g_5^q(t) \approx g_{5h}^q = \sum_{i=0}^{20} \alpha_i \phi_i.$$

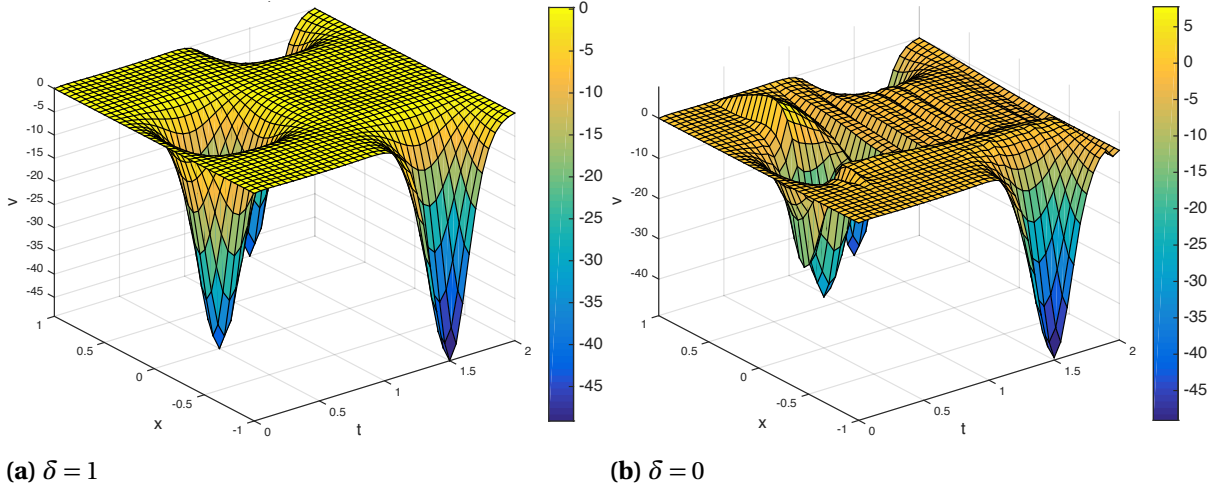


Figure 1.47 Solution functions of discharge velocity v when $\delta = 1$ (left) and $\delta = 0$ (right).

Note that we have set $\psi = 0$ in this case in order to better examine the effect of the boundary traction g_5^q . So, we do not consider sensitivities with respect to ψ in this case. The results are shown in Fig. 1.49 through Fig. 1.63.

Remark 1.4.2 *The spline approximation to the step function g_5^∞ does not appear to be significantly different enough from the spline approximation to g_5^{100} to have a noticeable effect on the computations.*

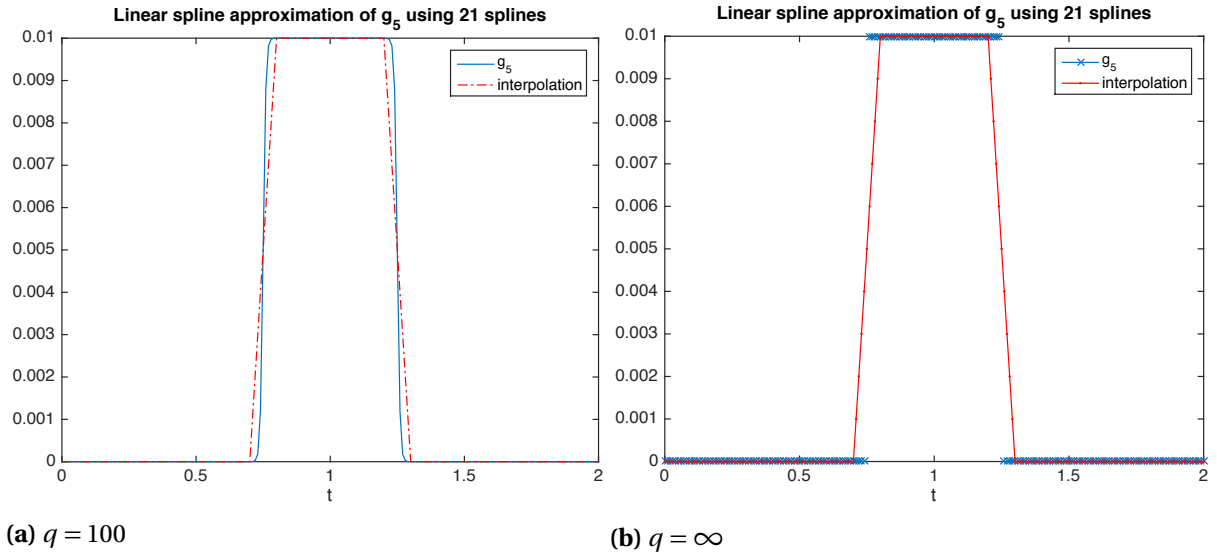


Figure 1.48 Linear spline approximations of g_5^q for $q = 100$ (left) and $q = \infty$ (right).

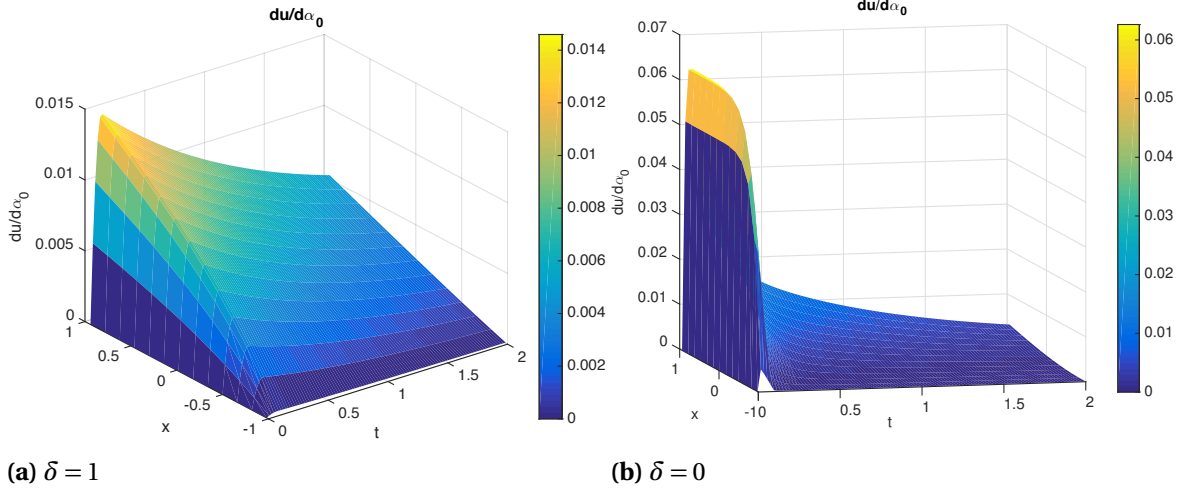


Figure 1.49 Sensitivity functions of solid displacement u with respect to boundary stress g_{5h}^{100} in the direction ϕ_0 when $\delta = 1$ (left) and $\delta = 0$ (right).

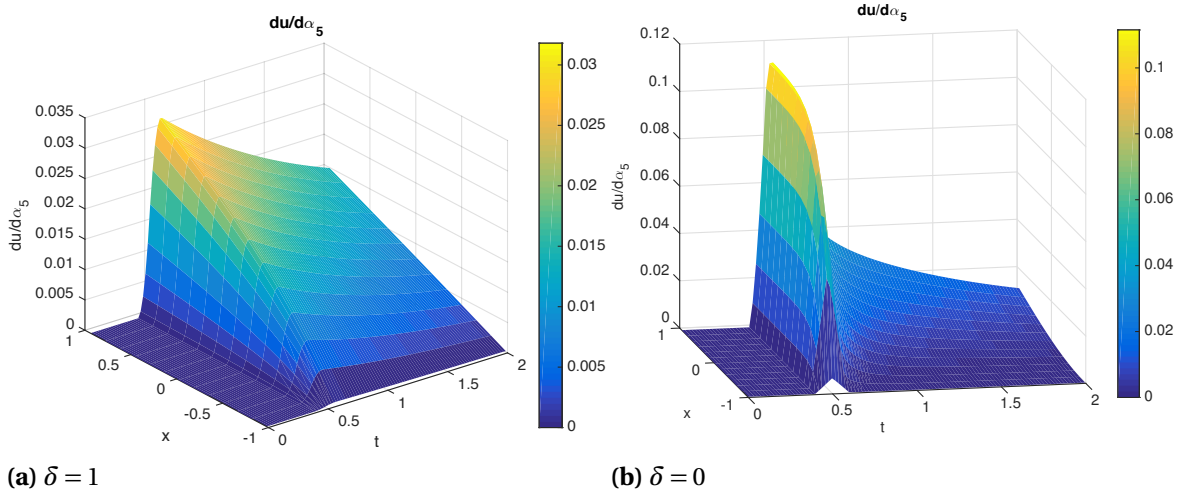


Figure 1.50 Sensitivity functions of solid displacement u with respect to boundary stress g_{5h}^{100} in the direction ϕ_5 when $\delta = 1$ (left) and $\delta = 0$ (right).

Observations From Figures 1.49-1.63 we again see that the magnitude of the sensitivities is bigger for the case when $\delta = 0$ than when $\delta = 1$. This suggests that the purely elastic model is more sensitive to the boundary traction than the visco-elastic model. We also note that in the elastic case $\delta = 0$, the effect of the boundary data on the solutions (u, p) is quite significant throughout the

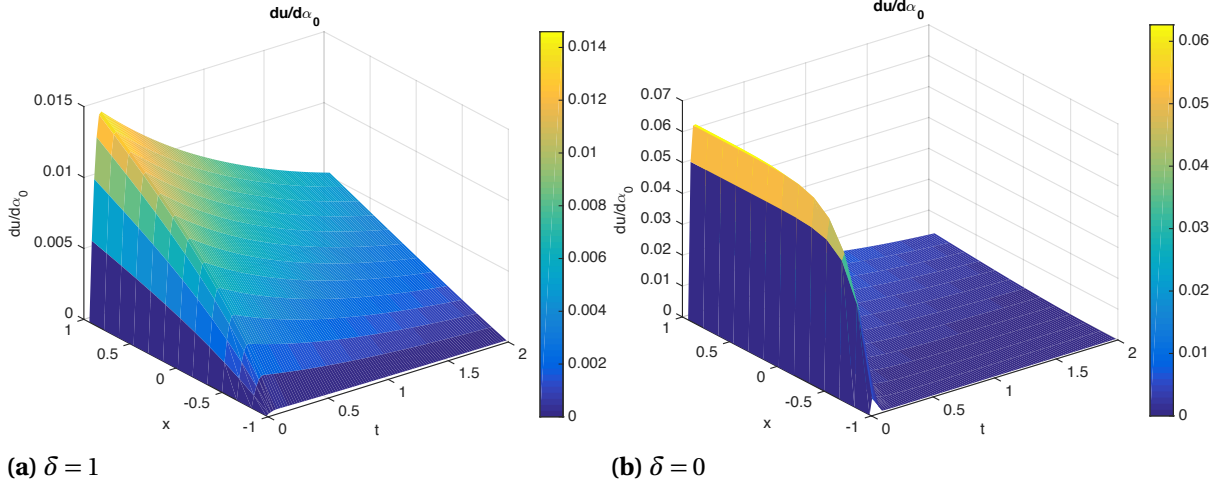


Figure 1.51 Sensitivity functions of solid displacement u with respect to boundary stress g_{5h}^{∞} in the direction ϕ_0 when $\delta = 1$ (left) and $\delta = 0$ (right).

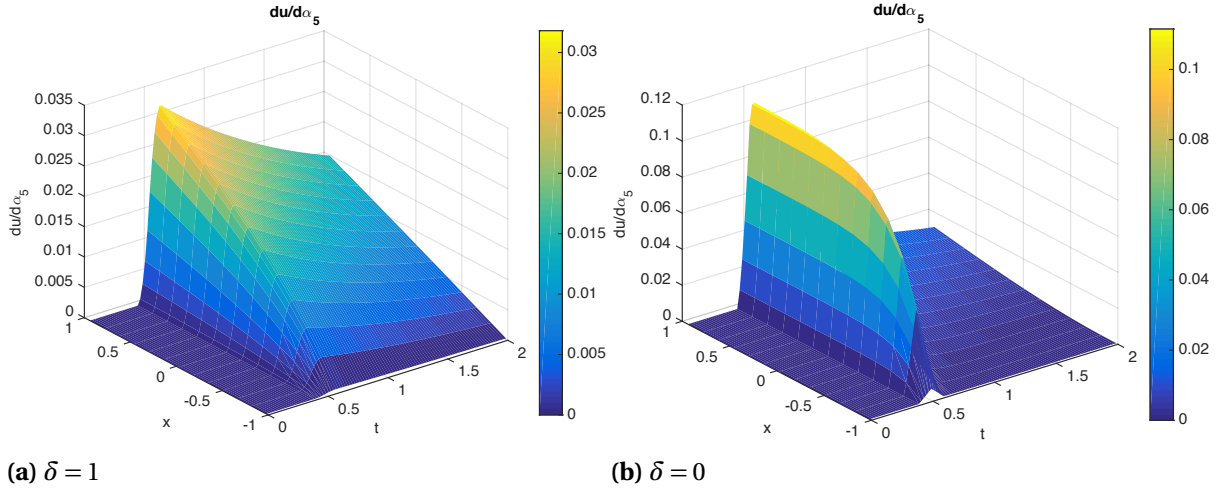


Figure 1.52 Sensitivity functions of solid displacement u with respect to boundary stress g_{5h}^{∞} in the direction ϕ_5 when $\delta = 1$ (left) and $\delta = 0$ (right).

domain. In comparison, the boundary effects on (u, p) diminish as we go farther from the boundary for the case when $\delta = 1$. The opposite is true of the sensitivities of v .

We also observe that the sensitivity graphs appear to be similar to those in Case 3, where the permeability is constant. Here, even though the permeability is nonlinear, the system is driven only by the boundary stress data g_5^q . In comparison, the sensitivities with respect to the boundary traction in the previous case (Case 4) are quite different, and this could be explained by the system's complexity due to the interaction between the nonlinear permeability k , body force F , and net volumetric fluid production rate S .

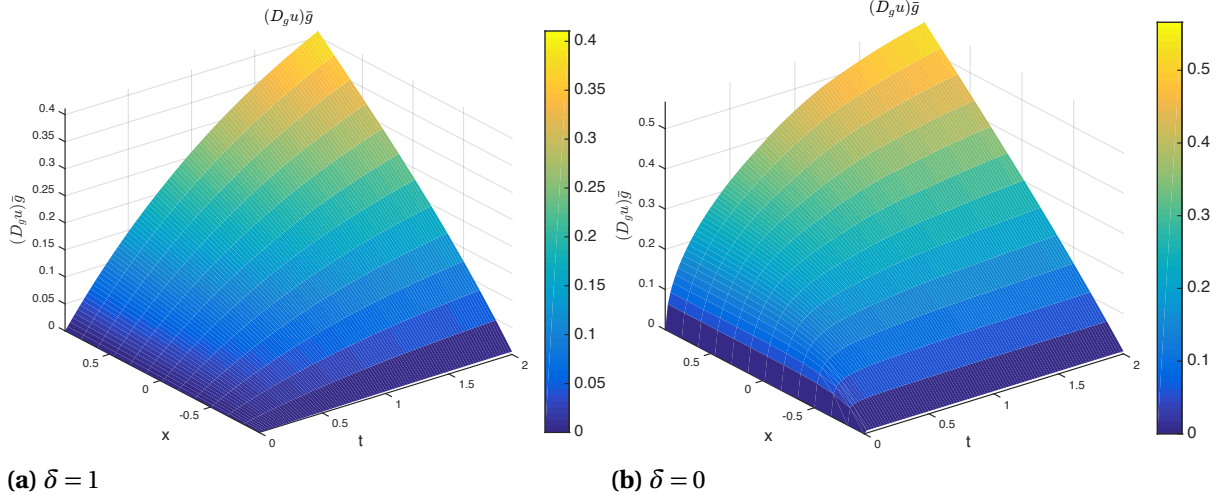


Figure 1.53 Sensitivity functions of solid displacement u with respect to boundary stress g_5^∞ in the direction $\bar{g} = \sum_{i=0}^{20} \phi_i$ when $\delta = 1$ (left) and $\delta = 0$ (right).

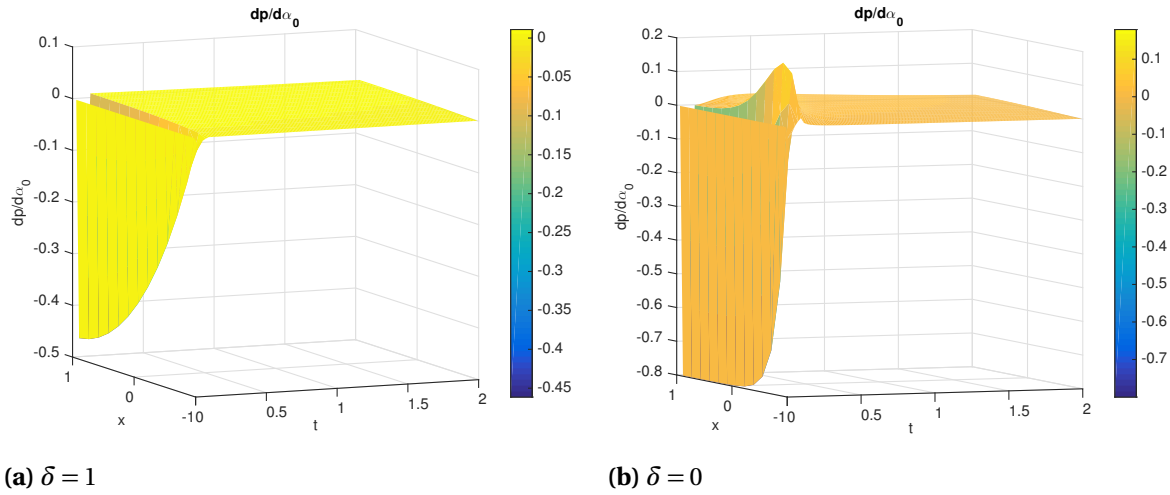


Figure 1.54 Sensitivity functions of fluid pressure p with respect to boundary stress g_{5h}^{100} in the direction ϕ_0 when $\delta = 1$ (left) and $\delta = 0$ (right).

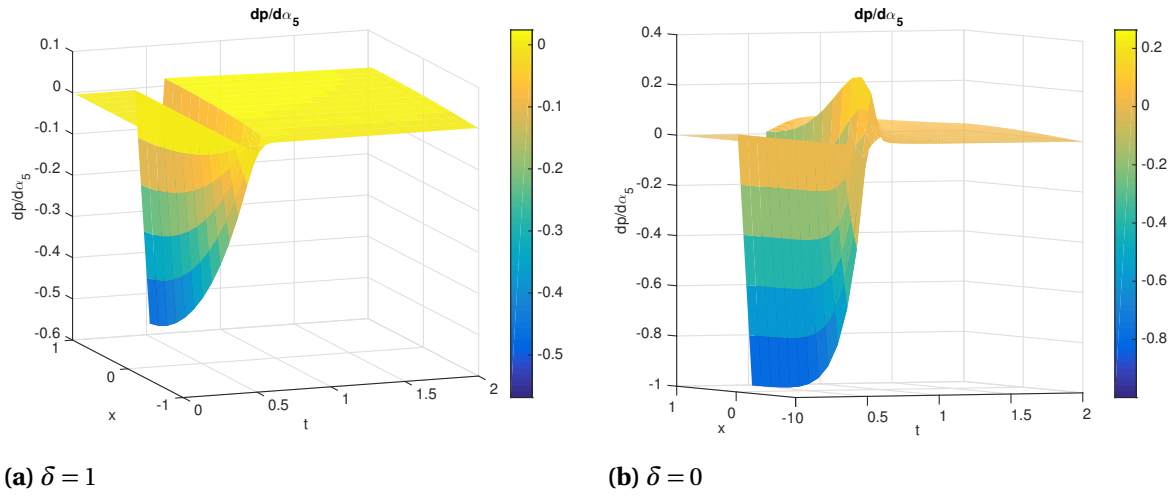


Figure 1.55 Sensitivity functions of fluid pressure p with respect to boundary stress g_{5h}^{100} in the direction ϕ_5 when $\delta = 1$ (left) and $\delta = 0$ (right).

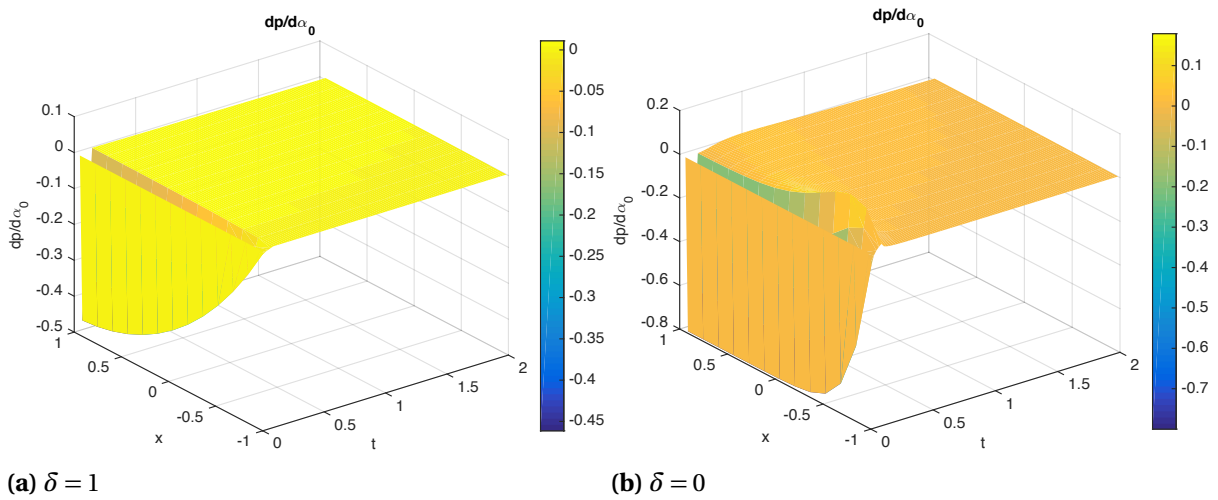


Figure 1.56 Sensitivity functions of fluid pressure p with respect to boundary stress g_{5h}^{∞} in the direction ϕ_0 when $\delta = 1$ (left) and $\delta = 0$ (right).

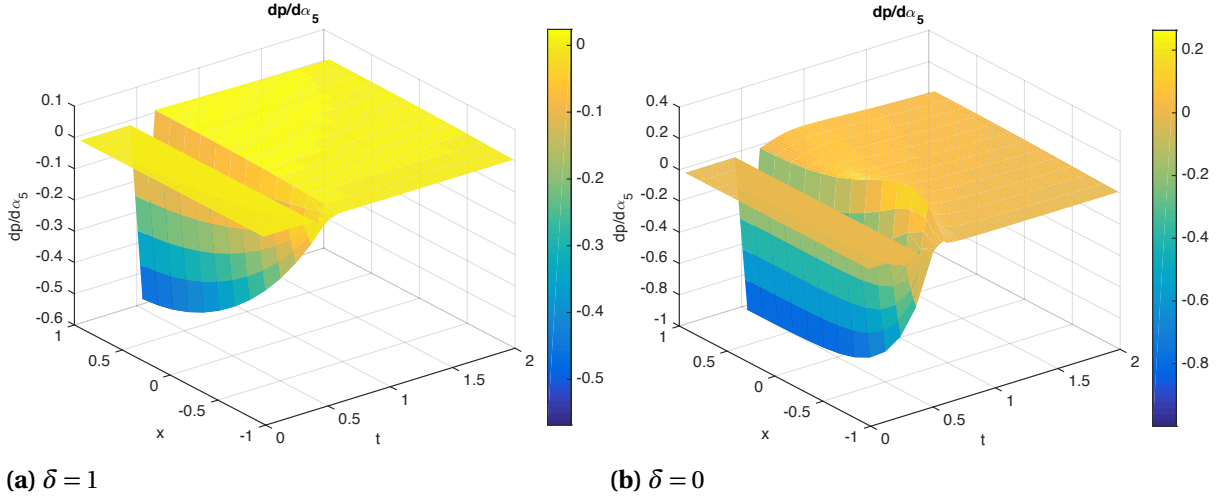


Figure 1.57 Sensitivity functions of fluid pressure p with respect to boundary stress g_{5h}^{∞} in the direction ϕ_5 when $\delta = 1$ (left) and $\delta = 0$ (right).

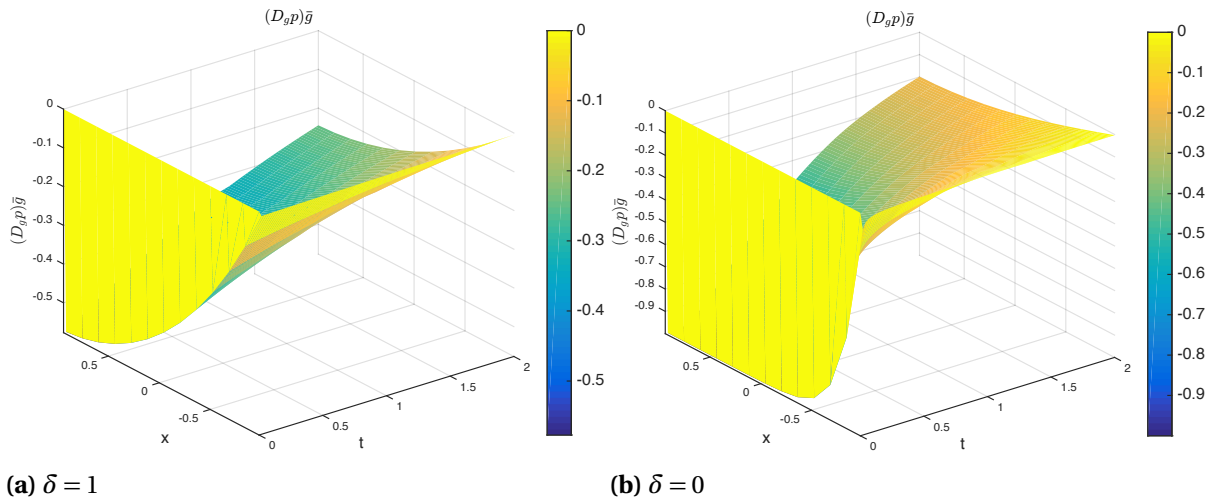


Figure 1.58 Sensitivity functions of fluid pressure p with respect to boundary stress g_5^{∞} in the direction $\bar{g} = \sum_{i=0}^{20} \phi_i$ when $\delta = 1$ (left) and $\delta = 0$ (right).

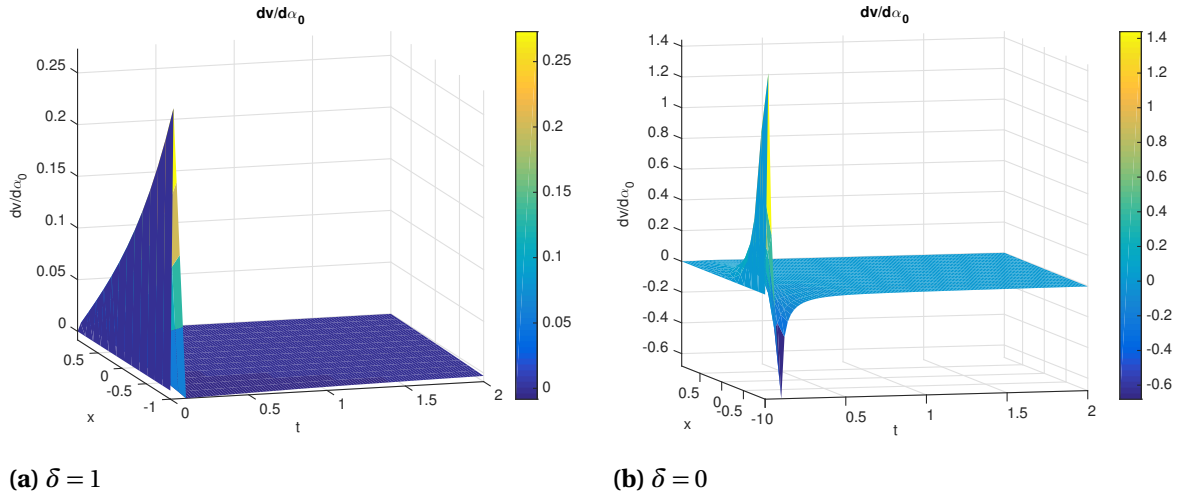


Figure 1.59 Sensitivity functions of discharge velocity v with respect to boundary stress g_{5h}^{100} in the direction ϕ_0 when $\delta = 1$ (left) and $\delta = 0$ (right).

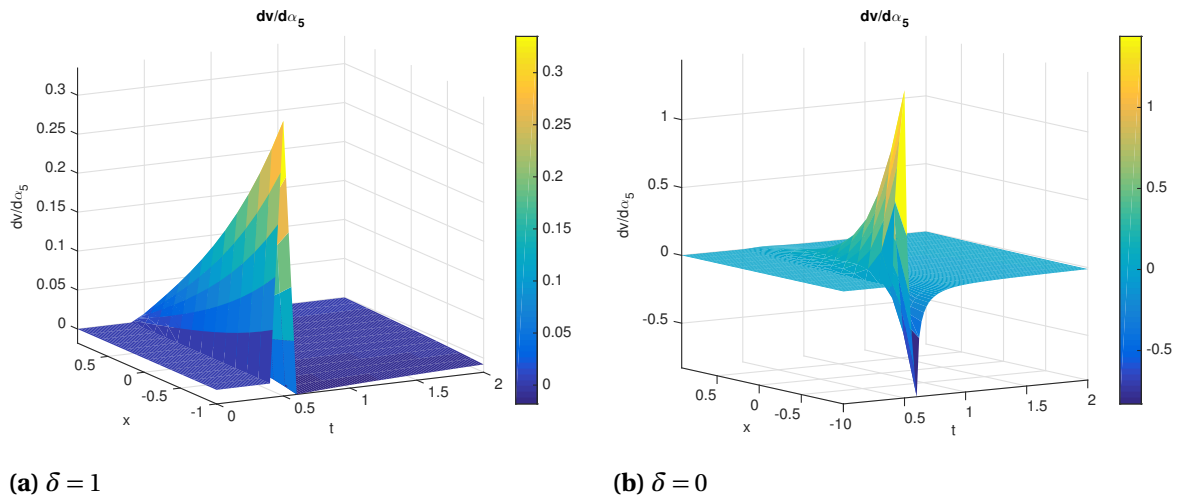


Figure 1.60 Sensitivity functions of discharge velocity v with respect to boundary stress g_{5h}^{100} in the direction ϕ_5 when $\delta = 1$ (left) and $\delta = 0$ (right).

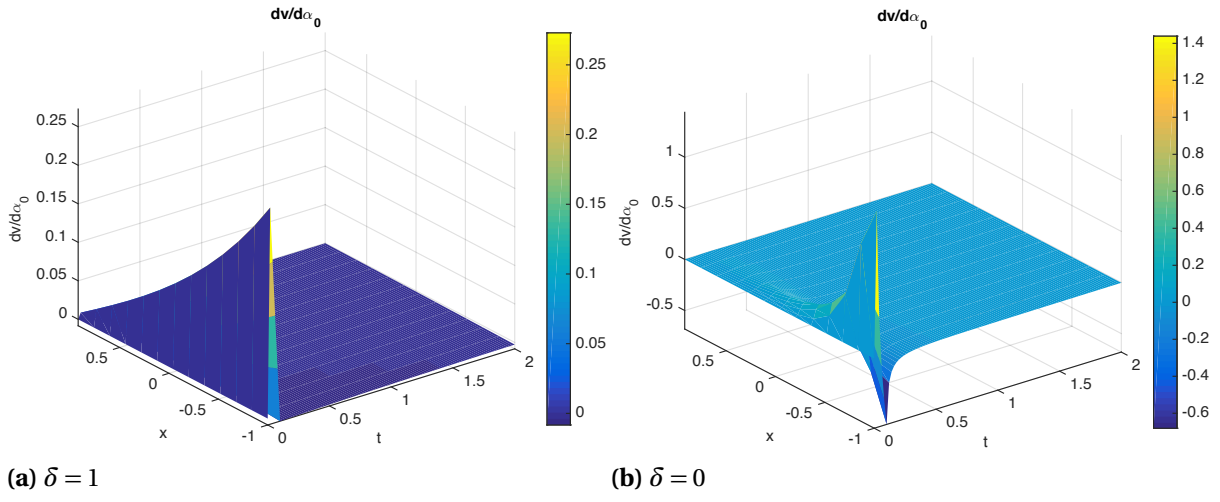


Figure 1.61 Sensitivity functions of discharge velocity v with respect to boundary stress g_{5h}^{∞} in the direction ϕ_0 when $\delta = 1$ (left) and $\delta = 0$ (right).

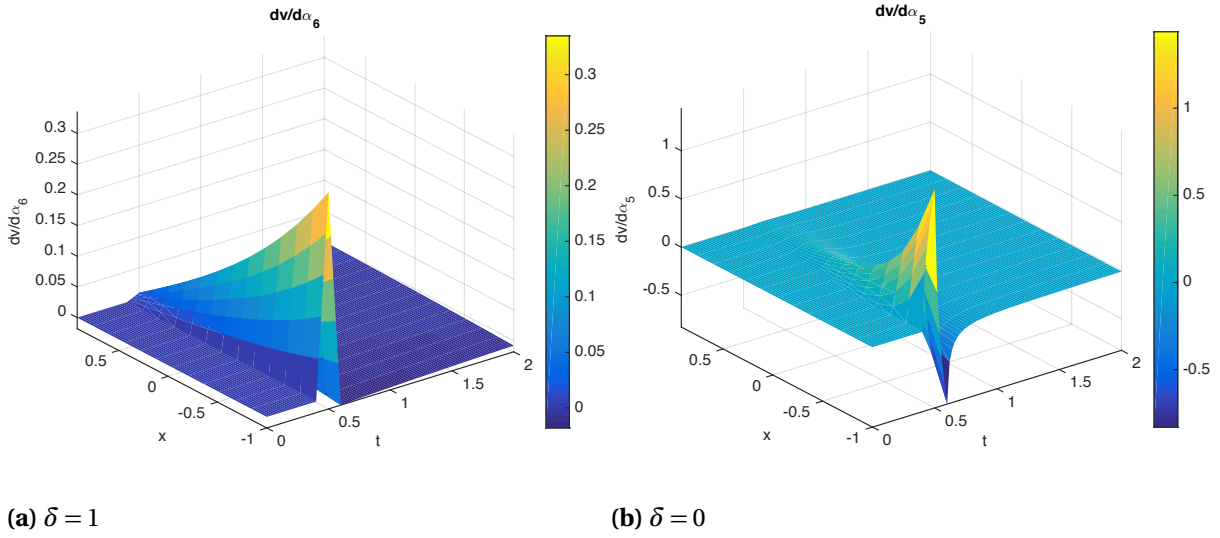


Figure 1.62 Sensitivity functions of discharge velocity v with respect to boundary stress g_{5h}^{∞} in the direction ϕ_5 when $\delta = 1$ (left) and $\delta = 0$ (right).

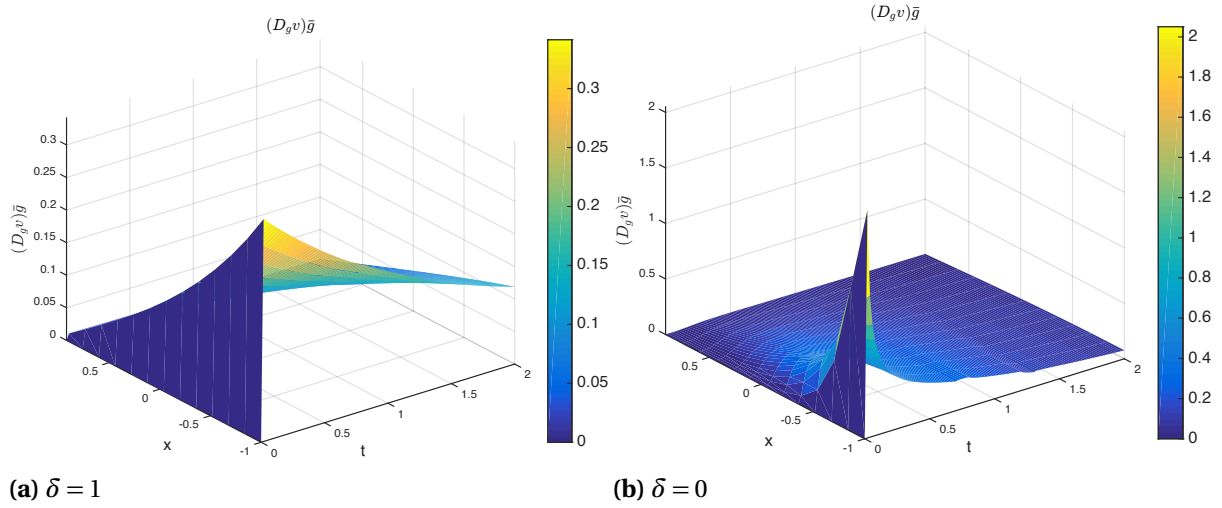


Figure 1.63 Sensitivity functions of discharge velocity v with respect to boundary stress g_5^∞ in the direction $\bar{g} = \sum_{i=0}^{20} \phi_i$ when $\delta = 1$ (left) and $\delta = 0$ (right).

1.4.2 Varying Structural Viscosity

In all of the previous examples, we can see that states (u, p, v) are more sensitive to the boundary traction in the purely elastic case $\delta = 0$ in comparison to the visco-elastic scenario $\delta = 1$. In this section, we further investigate the importance of the viscosity parameter by considering a variety of values for δ , and studying the effect of the boundary stress g on the solid displacement, fluid pressure, and discharge velocity in all these cases. We focus on two main ranges for δ : $0 \leq \delta \leq 1$ vs. $1 \leq \delta \leq 2$. In these computations, we use the same set up as in Case 4, now with constant boundary function $g_4 = 1$.

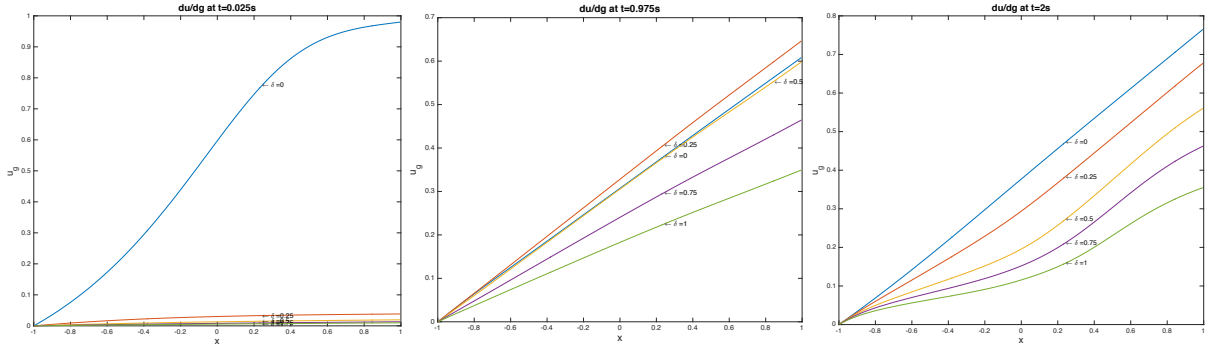


Figure 1.64 Sensitivity of u to boundary traction g for various values of $0 \leq \delta \leq 1$.

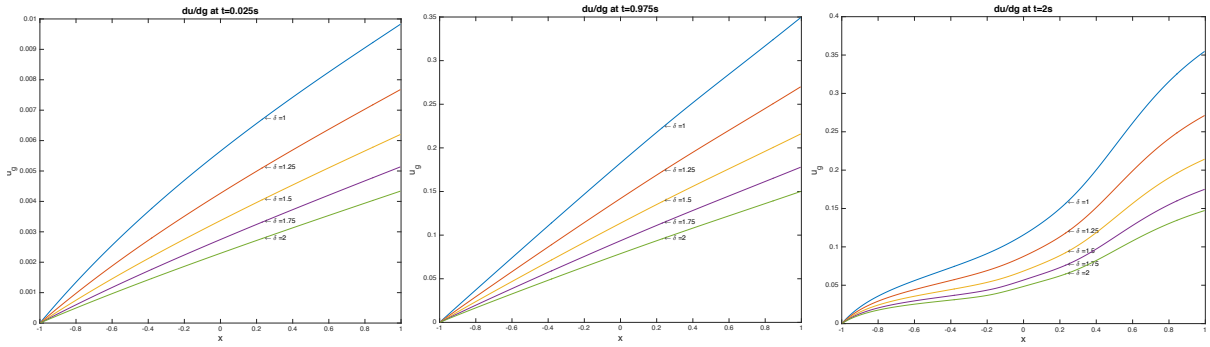


Figure 1.65 Sensitivity of u to boundary traction g for various values of $1 \leq \delta \leq 2$.

First we discuss the behaviors of the sensitivities of the solid displacement u with respect to the boundary datum g , shown in Fig. 1.64 and Fig. 1.65. For $0 \leq \delta \leq 1$, we can see that the sensitivities of the elastic displacement with respect to g do not follow a “prescribed” pattern, as we have two

different scenarios at the three times chosen. At times $t = 0.025$ and $t = 2$, we note that the solid displacement is more sensitive for $\delta = 0$ and there is clear pattern: the more visco-elasticity (i.e., the bigger the δ), the less sensitive the solid displacement is to g . At time $t = 0.975$, the sensitivity of the solid displacement is two to three times smaller for values of δ close to 1 compared to values of δ close to 0. However, it can also be observed that the sensitivity for $\delta = 0.25$ is slightly bigger than the one computed for $\delta = 0$ through the space domain. This could suggest that there is a range of small values of δ around 0 for which the sensitivity of the solid displacement stays within the same range as the one in the case of $\delta = 0$.

In comparison, for $1 \leq \delta \leq 2$, the graphs for the sensitivities of solid displacement show a solid trend for all the times considered: the larger the value of δ , the smaller the sensitivity. This suggests that the value $\delta = 1$ may be a “safe value” in terms of assuring that the sensitivity of the solid displacement will continue to decrease as δ increases above 1.

Comparing Fig. 1.64 and Fig. 1.65, we note that the magnitudes of the sensitivities are smaller for $1 \leq \delta \leq 2$ compared to $0 \leq \delta \leq 1$, which agrees with what we observed in the previous investigations (Case 1 - Case 5).

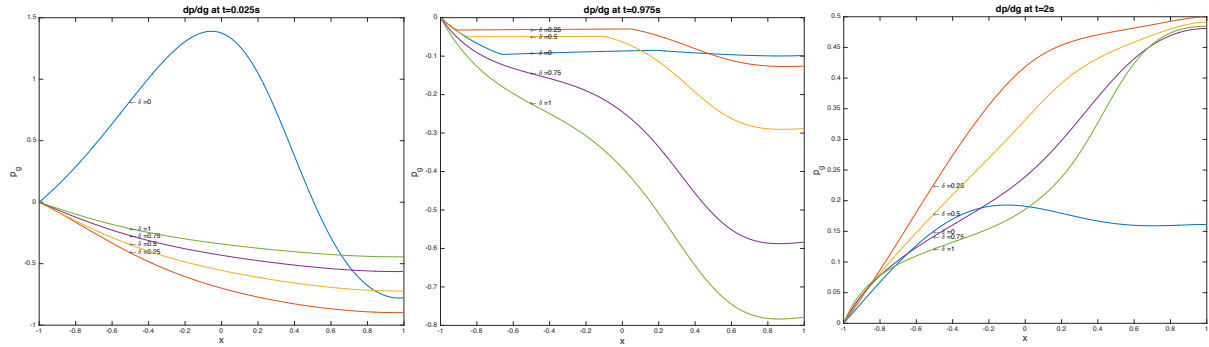


Figure 1.66 Sensitivity of p to boundary traction g for various values of $0 \leq \delta \leq 1$.

Regarding the sensitivities of the fluid pressure to the boundary datum g (Fig. 1.66 and Fig. 1.67), when $0 \leq \delta \leq 1$, the behavior of the sensitivities is “complex”. The various curves are intersecting with each other, hinting that different parts of the domain would have a different sensitivity to the data depending on the level of viscoelasticity. Thus, the choice of δ would affect differently various regions within the domain. Even in the case of $1 \leq \delta \leq 2$, the graphs do not show any pattern: at $t = 0.025$, the magnitude of the sensitivities decreases as δ gets larger, at $t = 0.975$, the behavior is quite the opposite, with the magnitude of the sensitivities increasing as δ gets larger, and at $t = 2$ the graphs of the sensitivities intersect and reverse their order in magnitude at around $x = -0.65$.

The sensitivities of the discharge velocity with respect to the boundary datum g show a clear

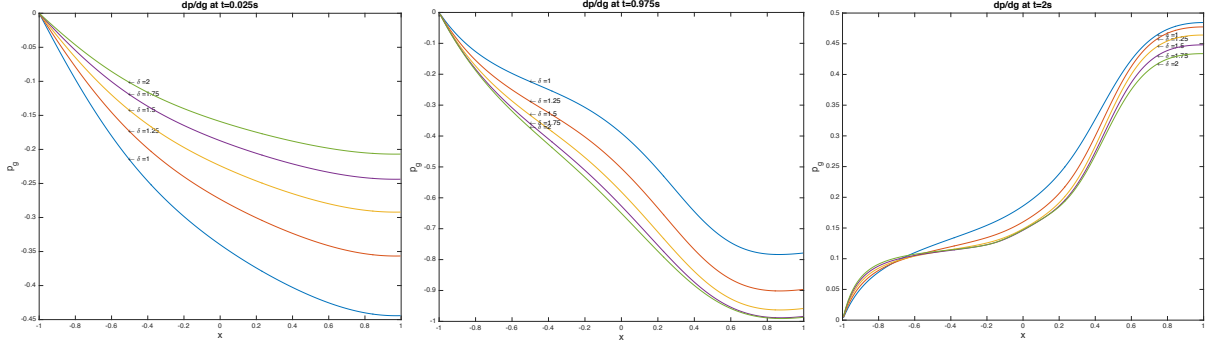


Figure 1.67 Sensitivity of p to boundary traction g for various values of $1 \leq \delta \leq 2$.

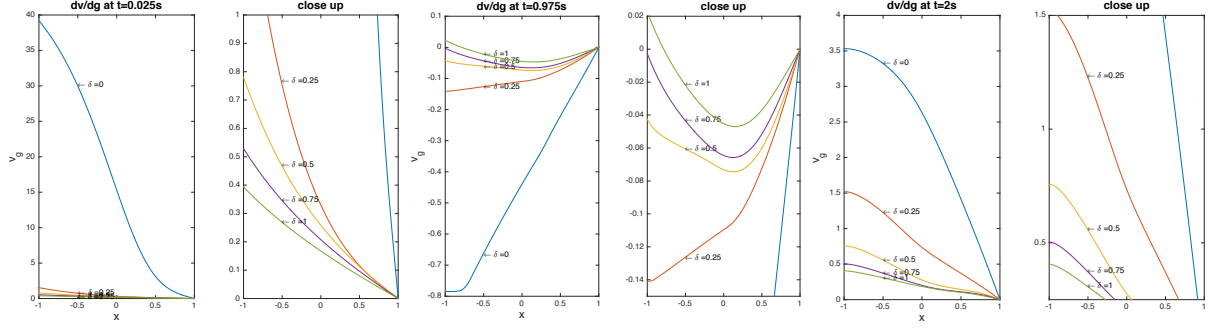


Figure 1.68 Sensitivity of v to boundary traction g for various values of $0 \leq \delta \leq 1$.

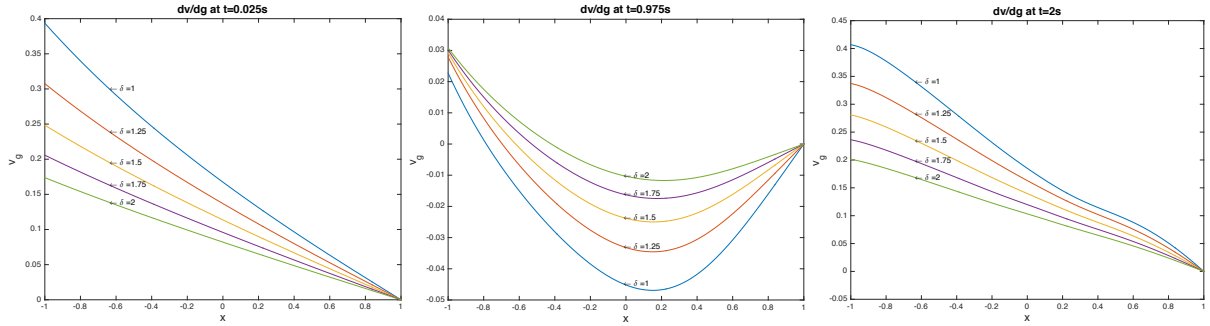


Figure 1.69 Sensitivity of v to boundary traction g for various values of $1 \leq \delta \leq 2$.

“order” in magnitudes at most of the times considered (see Fig. 1.68 and Fig. 1.69). For both $0 \leq \delta \leq 1$ and $1 \leq \delta \leq 2$, the sensitivity increases as δ gets smaller. There is one exception at time $t = 0.975$, in the case of $1 \leq \delta \leq 2$: the boundary source g is applied at $x = 1$, and around in the interval $x \in [-1, -0.4]$, the sensitivities lose the expected “ordering”, as their magnitudes fluctuate close to 0.

It is also interesting to see the big difference in the magnitudes of the sensitivities between $\delta = 0$ and values of δ close to 2. This again suggests that the discharge velocity becomes heavily sensitive to the boundary data of traction when visco-elasticity is not present in the system.

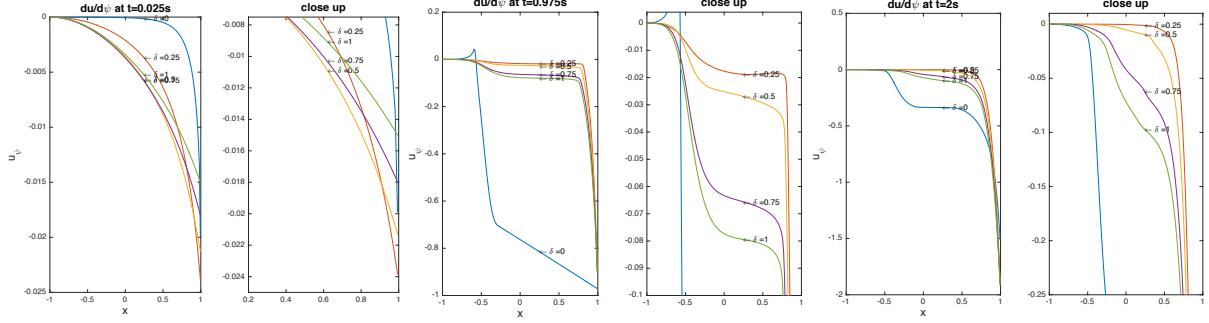


Figure 1.70 Sensitivity of u to ψ for various values of $0 \leq \delta \leq 1$.

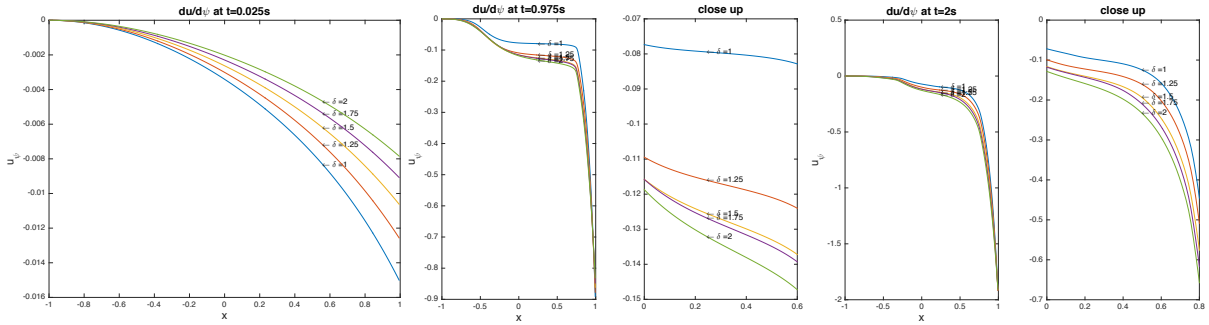


Figure 1.71 Sensitivity of u to ψ for various values of $1 \leq \delta \leq 2$.

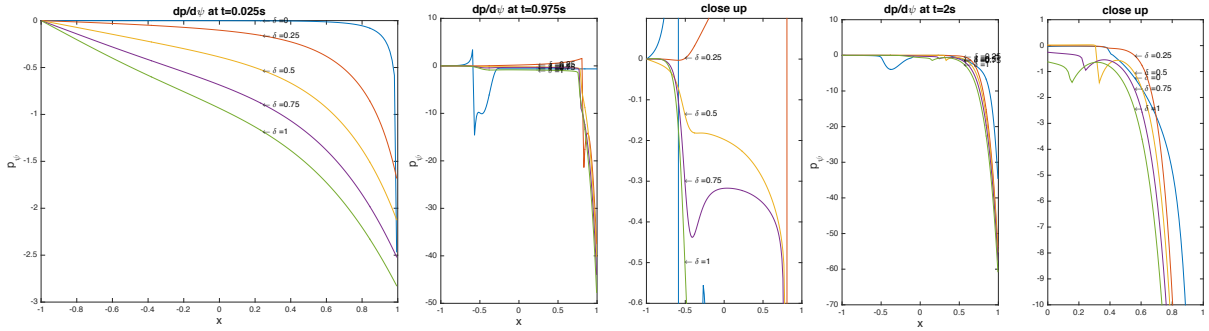


Figure 1.72 Sensitivity of p to ψ for various values of $0 \leq \delta \leq 1$.

As can be seen from Fig. 1.70-Fig. 1.75, the sensitivities of the states with respect to ψ don't show a clear pattern as δ changes. This is true for both scenarios $0 \leq \delta \leq 1$ and $1 \leq \delta \leq 2$.

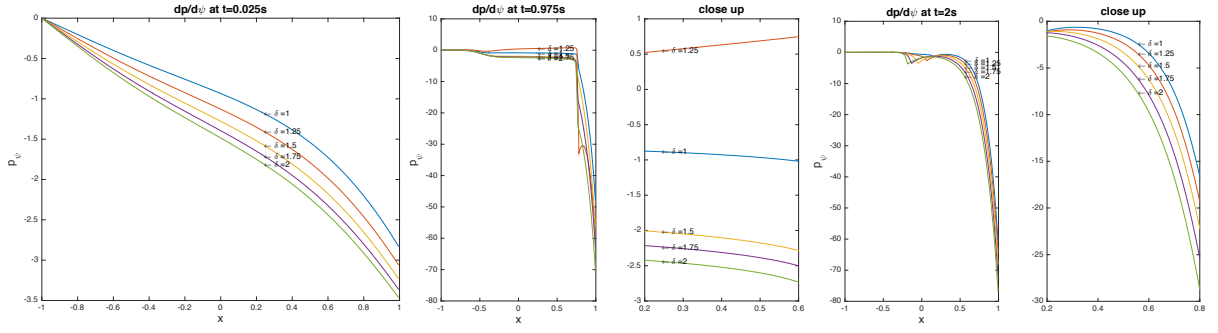


Figure 1.73 Sensitivity of p to ψ for various values of $1 \leq \delta \leq 2$.

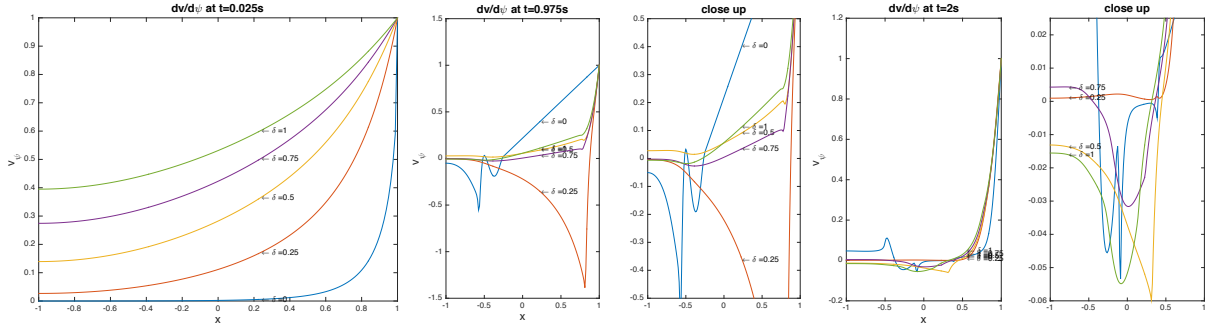


Figure 1.74 Sensitivity of ν to ψ for various values of $0 \leq \delta \leq 1$.

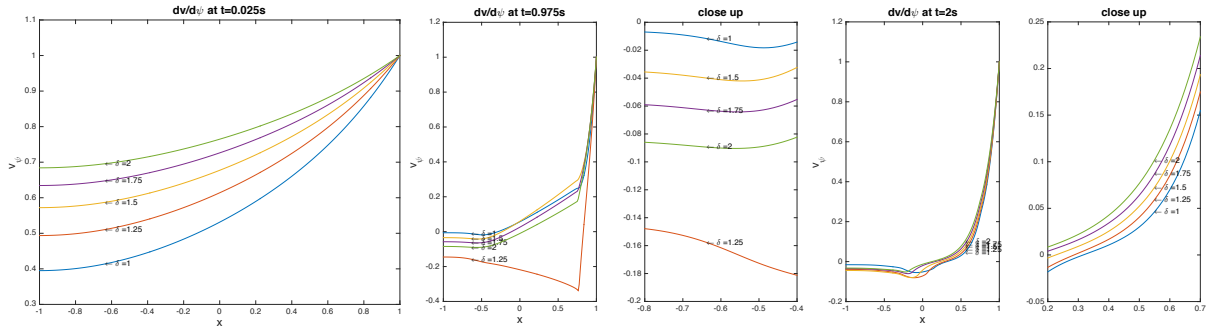


Figure 1.75 Sensitivity of ν to ψ for various values of $1 \leq \delta \leq 2$.

1.5 Dimensional Analysis

The numerical results presented in Section 1.4 show that the solution (solid displacement, fluid pressure and discharge velocity) is more sensitive to boundary traction in the elastic case than in the visco-elastic scenario. However, we do not see a direct correlation between the sensitivities and the viscous effects present in the solid component as was expected. In Section 1.4.2, we show that the sensitivities are not monotonic with respect to the amount of structural viscosity included and rather exhibit complex behavior in space and time. This result prompts the need for dimensional analysis, where relevant physical and geometrical parameters of the problem are combined in dimensionless numbers that can be used to establish some equivalences between behaviors of apparently different systems [186].

In [186], a dimensional analysis of the system is provided. Moreover, the response of deformable porous media with incompressible constituents to external applied loads (either step or trapezoidal pulses) and the role that the structural viscosity plays in this response were analyzed for the 1-D prototype. The authors showed that the fluid velocity within the medium could increase tremendously (even up to infinity), should the external applied load experience sudden changes in time and the structural viscoelasticity be too small. The authors also identify some dimensionless parameters that could be used in the design of structural properties and experimental conditions in order to maintain the fluid velocity within the medium below a desired threshold, and implicitly prevent potential damage to the material (which could be, for example, a biological tissue).

Here, we complement the results given above in Section 1.4 as well as those from [186] by numerically investigating the sensitivities of the 1-D dimensionless poro-visco-elastic solutions to applied boundary loads and their dependence on the dimensionless parameters identified in [186]. Due to the complex behavior the sensitivities exhibit in space and time as functions of δ , we conclude that δ may not be a good control parameter for the system. For this reason, we here present a sensitivity analysis on a dimensionless version of the model given in Eq. 1.38, which may highlight more clearly which physical and geometrical parameters of the problem will act as good control parameters.

1.5.1 Confined Compression

Confined compression is one of a number of mechanical testing regimes that are used to characterize properties of biological tissues. Being able to establish the compressive, tensile, bending, shear, or elastic and viscous properties of tissues is an important step in understanding the mechanics of the tissue. This is necessary in order to engineer materials that can act as tissue substitutes in order to replace and restore damaged tissues [83].

In confined compression, the biological material is placed in a confining chamber with the

bottom fixed (see Fig. 1.76). A permeable piston applies a compressive load at the top of the chamber while allowing the fluid in the tissue to exude unimpeded so that the tissue can be compressed. Due to the confinement, deformation occurs only in the longitudinal (x) direction and there is minimal lateral flow.

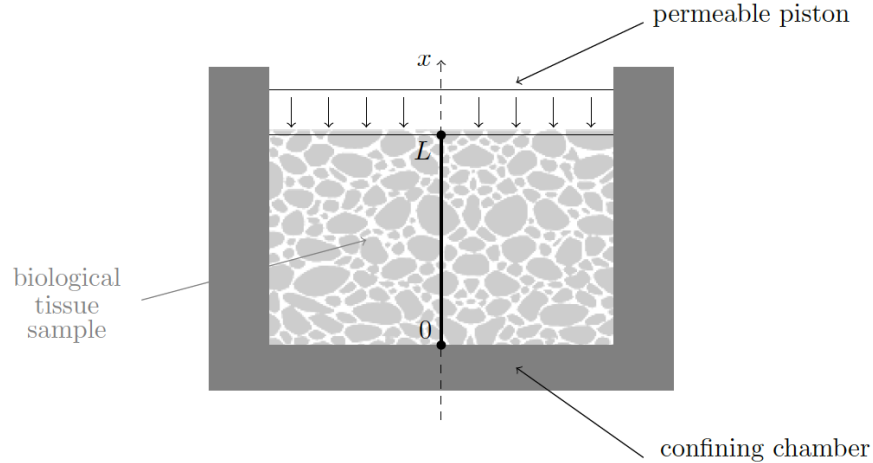


Figure 1.76 Schematic of confined compression as presented in [186].

One of the tests done using confined compression are creep tests. In these tests, the tissue is put under a constant load for a period of time before suddenly removing the load. The response of the tissue is measured through the strain of the material as a function of time. Utilizing these results along with mathematical models that can recreate such results allows one to quantify the elastic and viscous properties of the tissue [142]. In poro-visco-elastic materials, creep tests have shown that materials that have more viscoelastic effects take longer to reach equilibrium after the applied load [127]. The phenomena of fluid load support has also been observed [173]. This phenomena describes the pressurization of the fluid in the initial phases of loading in order to support up to 90% of the load. Over time, the load is transferred entirely to the strain and the pressures subsides. When this occurs, the tissue reaches its equilibrium deformation.

In the rest of this section, we will put ourselves in the framework of a confined compression creep test. Our simulation results correspond closely with those observed in these tests on poro-visco-elastic materials, thus acting as validation for our model.

1.5.2 Dimensionless Model

We again consider the 1-D poro-visco-elastic model presented in Section 1.2.1.2. Along with the assumptions of small deformations, full saturation of the mixture, incompressibility of the mixture constituents, and negligible inertia, we now also assume zero volumetric sources of linear momentum and fluid mass. This results in the homogeneous system

$$\left\{ \begin{array}{ll} \frac{\partial \sigma}{\partial x} = 0, & \text{in } (0, L) \times (0, T), \\ \frac{\partial \zeta}{\partial t} + \frac{\partial v}{\partial x} = 0, & \text{in } (0, L) \times (0, T), \\ u(0, t) = 0, & t \in (0, T), \\ v(0, t) = 0, & t \in (0, T), \\ \sigma(L, t) = -P(t), & t \in (0, T), \\ p(L, t) = 0, & t \in (0, T), \\ u(x, 0) = 0, & x \in (0, L). \end{array} \right. \quad (1.142)$$

We note that the boundary conditions here correspond with the setup in a confined compression creep test and that we have replaced g from early sections with $-P$ to represent the applied load. Though permeability often depends nonlinearly on the dilation of the solid in biological applications, we will assume here that the permeability $k = k_0$ is constant. This is an assumption made in [186] where the dimensionless model is presented, and was needed in order to solve the system analytically and determine appropriate characteristic (or scaling) values. Thus, the discharge velocity is now given by

$$v = -k_0 \frac{\partial p}{\partial x}. \quad (1.143)$$

Following [186], we define the dimensionless (or scaled) variables to be

$$\hat{x} = \frac{x}{[x]}, \quad \hat{t} = \frac{t}{[t]}, \quad \hat{P} = \frac{P}{[P]}, \quad \hat{\sigma} = \frac{\sigma}{[\sigma]}, \quad \hat{u} = \frac{u}{[u]}, \quad \hat{v} = \frac{v}{[v]}, \quad \hat{p} = \frac{p}{[p]}.$$

The bracket notation used above denotes the characteristic value for the respective variable. We note that the choice of characteristic values is not trivial and, in general, characteristic values are not unique. In this work, we select the characteristic values found in [186], which are given by

$$[x] = L, \quad [t] = \frac{L^2}{k_0(\lambda_e + 2\mu_e)}, \quad [P] = P_{ref}, \quad [\sigma] = P_{ref},$$

$$[u] = \frac{P_{ref}L}{\lambda_e + 2\mu_e}, \quad [v] = \frac{k_0 P_{ref}}{L}, \quad [p] = P_{ref},$$

where P_{ref} is a reference value, for example the mean value of the given function $P(t)$.

For $\hat{T} = \frac{T}{[t]}$, the dimensionless system is then given by

$$\begin{cases} \frac{\partial \hat{\sigma}}{\partial \hat{x}} = 0, & \text{in } (0, 1) \times (0, \hat{T}), \\ \frac{\partial^2 \hat{u}}{\partial \hat{t} \partial \hat{x}} + \frac{\partial \hat{v}}{\partial \hat{x}} = 0, & \text{in } (0, 1) \times (0, \hat{T}), \\ \hat{u}(0, \hat{t}) = 0, & \hat{t} \in (0, \hat{T}), \\ \hat{v}(0, \hat{t}) = 0, & \hat{t} \in (0, \hat{T}), \\ \hat{\sigma}(1, \hat{t}) = -\hat{P}(\hat{t}), & \hat{t} \in (0, \hat{T}), \\ \hat{p}(1, \hat{t}) = 0, & \hat{t} \in (0, \hat{T}), \\ \hat{u}(\hat{x}, 0) = 0, & \hat{x} \in (0, 1), \end{cases} \quad (1.144)$$

with constitutive equations

$$\hat{\sigma} = \frac{\partial \hat{u}}{\partial \hat{x}} + \hat{\eta} \frac{\partial^2 \hat{u}}{\partial \hat{t} \partial \hat{x}} - \hat{p}, \quad (1.145)$$

$$\hat{v} = -\frac{\partial \hat{p}}{\partial \hat{x}}. \quad (1.146)$$

The parameter $\hat{\eta}$ in (1.145), given by

$$\hat{\eta} = \frac{K_0}{L^2} \delta(\lambda_v + 2\mu_v), \quad (1.147)$$

is the analog to the viscoelastic parameter δ used above (and in [16, 18, 39]). Note that if $\delta = 0$, which corresponds to the poro-elastic case, then we also have $\hat{\eta} = 0$.

The solution to the dimensionless system was found in [186] to be

$$\hat{u}(\hat{x}, \hat{t}) = -2 \sum_{n=0}^{\infty} \frac{(-1)^n y_n(\hat{x})}{1 + \hat{\eta} \hat{\lambda}_n} \exp\left(-\frac{\hat{\lambda}_n}{1 + \hat{\eta} \hat{\lambda}_n} \hat{t}\right) * \hat{P}(\hat{t}), \quad (1.148)$$

$$\hat{p}(\hat{x}, \hat{t}) = 2 \sum_{n=0}^{\infty} \frac{(-1)^n y'_n(\hat{x})}{\sqrt{\hat{\lambda}_n}(1 + \hat{\eta} \hat{\lambda}_n)} \left[\hat{P}(\hat{t}) - \frac{\hat{\lambda}_n}{1 + \hat{\eta} \hat{\lambda}_n} \exp\left(-\frac{\hat{\lambda}_n}{1 + \hat{\eta} \hat{\lambda}_n} \hat{t}\right) * \hat{P}(\hat{t}) \right], \quad (1.149)$$

$$\hat{v}(\hat{x}, \hat{t}) = 2 \sum_{n=0}^{\infty} \frac{(-1)^n y_n(\hat{x})}{1 + \hat{\eta} \hat{\lambda}_n} \left[\hat{P}(\hat{t}) - \frac{\hat{\lambda}_n}{1 + \hat{\eta} \hat{\lambda}_n} \exp\left(-\frac{\hat{\lambda}_n}{1 + \hat{\eta} \hat{\lambda}_n} \hat{t}\right) * \hat{P}(\hat{t}) \right], \quad (1.150)$$

$$\hat{\sigma}(\hat{x}, \hat{t}) = -\hat{P}(\hat{t}), \quad (1.151)$$

where $'$ denotes ordinary differentiation, $*$ denotes convolution, and, for $n = 0, 1, \dots$,

$$\hat{\lambda}_n = \frac{(2n+1)^2 \pi^2}{4}, \quad (1.152)$$

$$y_n(\hat{x}) = \sin\left(\sqrt{\hat{\lambda}_n} \hat{x}\right). \quad (1.153)$$

1.5.3 Numerical Procedure

In this case, since the series solution is known and the system is linear, we can compute series representations of the sensitivities analytically. However, if we allow permeability to be nonlinear (which is the next step in this analysis), we will need to use computational methods in order to obtain approximate sensitivities.

The system was solved numerically using the approach outlined in Section 1.2.3. The resulting solution was validated against the series approximations (1.148)-(1.150). The norm used to measure the difference of the approximated solution with the series approximation is given by

$$\|w\|_Q := \sup_{t \in [0, \hat{T}]} \|w(t)\|_{L^2(0,1)} \quad (1.154)$$

for any function $w(x, t)$. Using this norm, we found that our algorithm consistently gives solutions within 10^{-5} of the series approximation. Sensitivities were again computed using the complex step method and were validated using series approximations to the sensitivities (which were obtained using (1.148)-(1.150)). This suggests that the complex step method may be an appropriate method for computing sensitivities in the case of nonlinear permeability. Thus, this work both studies the sensitivity of the system in the case of constant permeability and provides evidence for the use of the complex step method when the permeability is a nonlinear function of dilation.

1.5.4 Selected Results

In this section, we look at the sensitivities of \hat{u} , \hat{p} , and \hat{v} with respect to \hat{P} in the direction \bar{P} of the linear splines shown in Figure 1.77. In particular, we display here the sensitivities of \hat{u} in the direction of $\bar{P} = s_2$ (Figure 1.77, middle panel) and the sensitivities of \hat{p} , \hat{v} in the direction $\bar{P} = s_1$ (Figure 1.77, left panel). We note that the behaviors shown and discussed here are typical of the sensitivities for the other splines as well. Understanding the behavior of the sensitivities in the direction of these splines unveils how the sensitivities will behave in any direction that can be accurately approximated by linear splines.

General Comments. We note the following common trend: the sensitivity curves (for all three variables \hat{u} , \hat{p} and \hat{v}) appear to follow similar behaviors regardless of the value of $\hat{\eta}$, except for

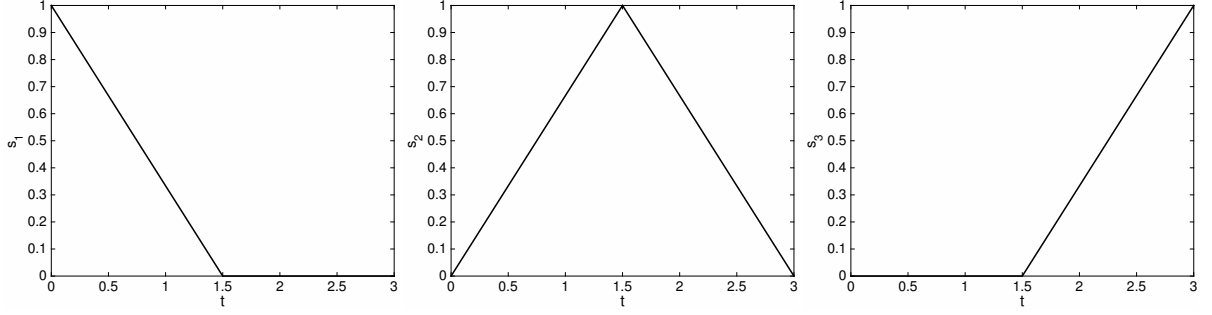


Figure 1.77 Linear splines

times that are close to a discontinuity in the direction \bar{P} (here, at $\hat{t} = 0$). Away from times near a discontinuity, the two main differences (with respect to $\hat{\eta}$) between the sensitivity curves appear to be their maximum magnitude and the rate at which they react to changes in the slope of \bar{P} . For the magnitudes of the sensitivities, we do see that the maximum is monotonic with respect to $\hat{\eta}$, with smaller values of $\hat{\eta}$ resulting in larger maximum magnitudes. This monotonicity in magnitudes, however, is not true over all time and space. Rather, we see that for smaller values of $\hat{\eta}$, the sensitivities tend to react more quickly to changes in the slope of \bar{P} which causes the sensitivities for different values of $\hat{\eta}$ to “cross over” each other. In fact, it appears that there is a “lag” in the sensitivities for larger values of $\hat{\eta}$ which visually manifests itself in the appearance of the sensitivity curves for smaller values of $\hat{\eta}$ “leading” the sensitivity curves for larger values of $\hat{\eta}$ in monotonic order.

On the other hand, near times where \bar{P} has a discontinuity, the sensitivities show drastically different behavior depending upon whether $\hat{\eta} = 0$ or $\hat{\eta} > 0$. This is particularly true for the sensitivities of \hat{p} and \hat{v} when $\hat{\eta} = 0$, which show discontinuities and blow up (respectively) near the boundary $\hat{x} = 1$ where the boundary traction is imposed. This is discussed in more detail below.

Sensitivity of the solid displacement \hat{u} . Fig. 1.78 shows the sensitivities of \hat{u} in the direction $\bar{P} = s_2$ at some conveniently selected times \hat{t} , for various values of $\hat{\eta} \in [0, 1]$. We chose these particular snapshots to include specific times when the slope of \bar{P} is constant (either positive or negative), as well as changing, and show the behavior of the sensitivities in those scenarios. In general, we found that the magnitude of the sensitivity of \hat{u} with respect to \hat{P} depends mostly upon the magnitude of \bar{P} . While \bar{P} is increasing away from zero, we see the magnitudes of the sensitivities of \hat{u} increasing as well. Similarly, when \bar{P} starts decreasing back to zero, we see the magnitudes of the sensitivities of \hat{u} decrease as well, though there is a slight lag in their response which is proportional to the value of $\hat{\eta}$.

Note that the bottom right panel of Fig. 1.78 shows the crossing over of the sensitivities due to the change in slope of \bar{P} from positive to negative. This is due to a lag in the reaction of the sensitivities to this change of slope (which occurs at $\hat{t} = 1.5$). To illustrate this lag further, we plot

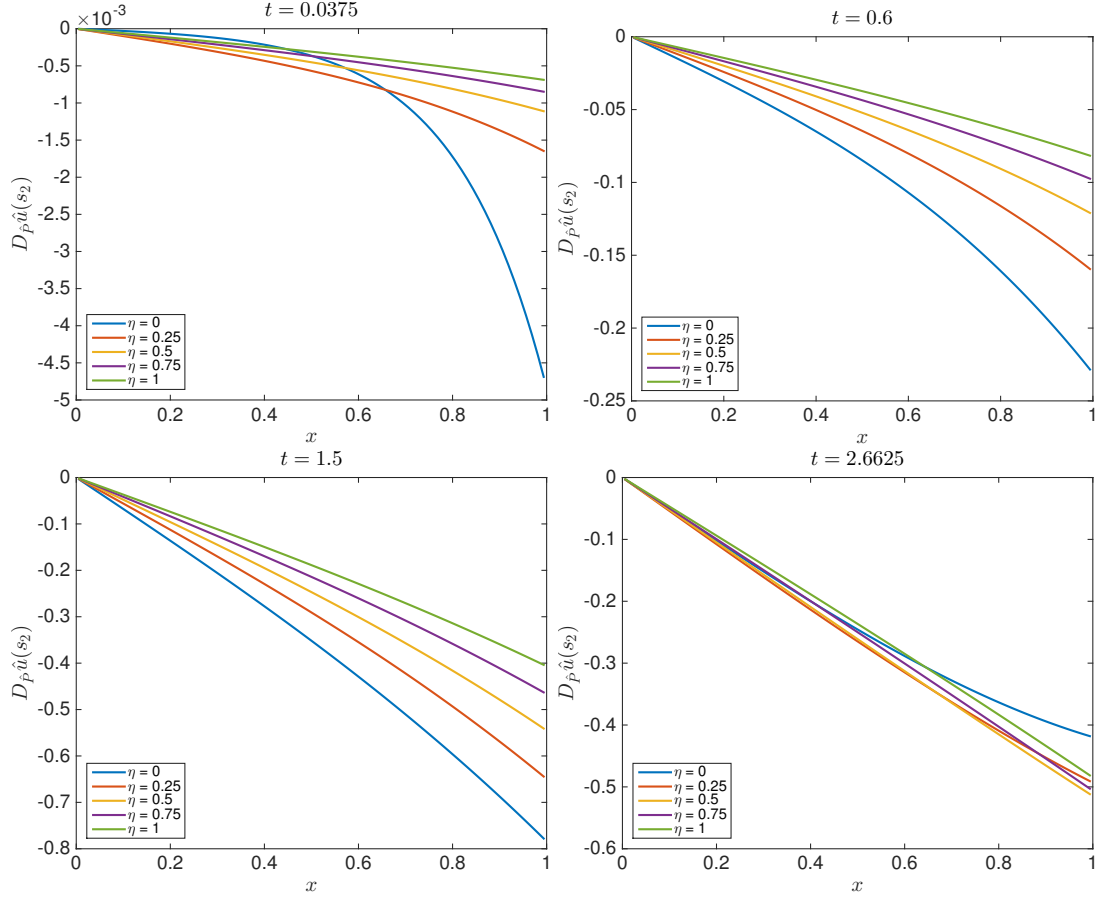


Figure 1.78 Sensitivity of \hat{u} to \hat{P} in direction $s_2(t)$ for $0 \leq \eta \leq 1$

the maximum value of the magnitude of the sensitivity of \hat{u} in the direction s_2 against the time at which it occurs in Fig. 1.79a. Here, we see that smaller values of $\hat{\eta}$ indeed lead to sensitivities with larger magnitudes, which are obtained in shorter time spans. This corresponds to the lag we see in Figure 1.78 in sensitivities with larger $\hat{\eta}$ values.

Sensitivity of the pressure \hat{p} . In Figure 1.80, we show the sensitivities of \hat{p} in the direction $\bar{P} = s_1$ for various values of $\hat{\eta} \in [0, 1]$. Overall, we see that \hat{p} is most sensitive when the direction \bar{P} has nonzero slope. When \bar{P} is constant, the sensitivities of \hat{p} collapse to 0. Overall, it appears that, for the most part, when the slope of \bar{P} is nonzero we have larger sensitivities for smaller values of $\hat{\eta}$. When the slope of \bar{P} is zero, the sensitivities for smaller values of $\hat{\eta}$ collapse more quickly causing the sensitivity curves for various values of $\hat{\eta}$ to cross over each other similar to the sensitivities of \hat{u} .

Interestingly, while we do see that the sensitivities of \hat{p} for larger values of $\hat{\eta}$ react more slowly to changes in the direction \bar{P} , the time at which the sensitivities attain their maximum is the same for

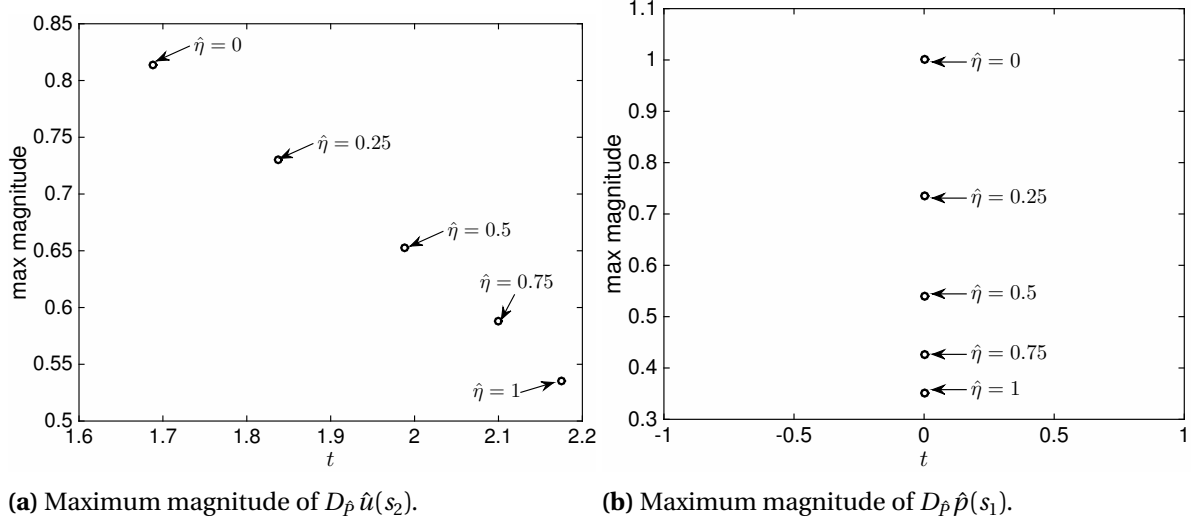


Figure 1.79 Maximum magnitude of sensitivities and the time at which it occurs for each value of $\hat{\eta}$ considered.

all $\hat{\eta}$ (see Figure 1.79b). This indicates that, unlike the sensitivities of the solid displacement \hat{u} , the sensitivities of \hat{p} are not exhibiting a true lag in reaction time. Rather, the response of the sensitivities of \hat{p} to a change in \bar{P} is simply smaller for larger $\hat{\eta}$. To investigate this further, we computed the time derivative of the sensitivities using a central finite difference. Figure 1.81 shows the results at $\hat{x} = 0$ for \hat{p} (left panel) and at $\hat{x} = 1$ for \hat{v} (right panel). Note that the value of \hat{x} was chosen to correspond with where we see the largest changes in the magnitude of these sensitivities. These plots show that the sensitivities do appear to respond at the same time, however the response when $\hat{\eta} = 0$ is much larger than the rest and in general smaller $\hat{\eta}$ corresponds to a larger response.

Sensitivity of the velocity \hat{v} . Figure 1.82 shows the sensitivities of \hat{v} in the direction $\bar{P} = s_1$ for various values of $\hat{\eta} \in [0, 1]$. In general, we see that the sensitivities of \hat{v} are similar to the sensitivities of \hat{p} in that they are most sensitive when the slope of \bar{P} is nonzero and collapse when the slope of \bar{P} is zero. We also see here that the sensitivities attain their maximum magnitude at the same time and that that magnitude is larger for smaller values of $\hat{\eta}$.

Sensitivity at time of discontinuity in \bar{P} ($\hat{t} = 0$). When $\hat{\eta} = 0$ and \hat{t} is close to 0 (where \bar{P} experiences a discontinuity) the sensitivities can display some complex and irregular behavior. The behavior here is of particular interest since, as is noted in [186], the discharge velocity experiences blow up in the purely elastic case of $\hat{\eta} = 0$ when \hat{P} has a jump. Here, we see that at $\hat{t} = 0$ and for $\hat{\eta} = 0$ the sensitivity of \hat{p} experiences a discontinuity at $\hat{x} = 1$ (note the boundary condition on \hat{p} at $\hat{x} = 1$ is a homogeneous Dirichlet condition) and the sensitivity of \hat{v} blows up at $\hat{x} = 1$. These sensitivities

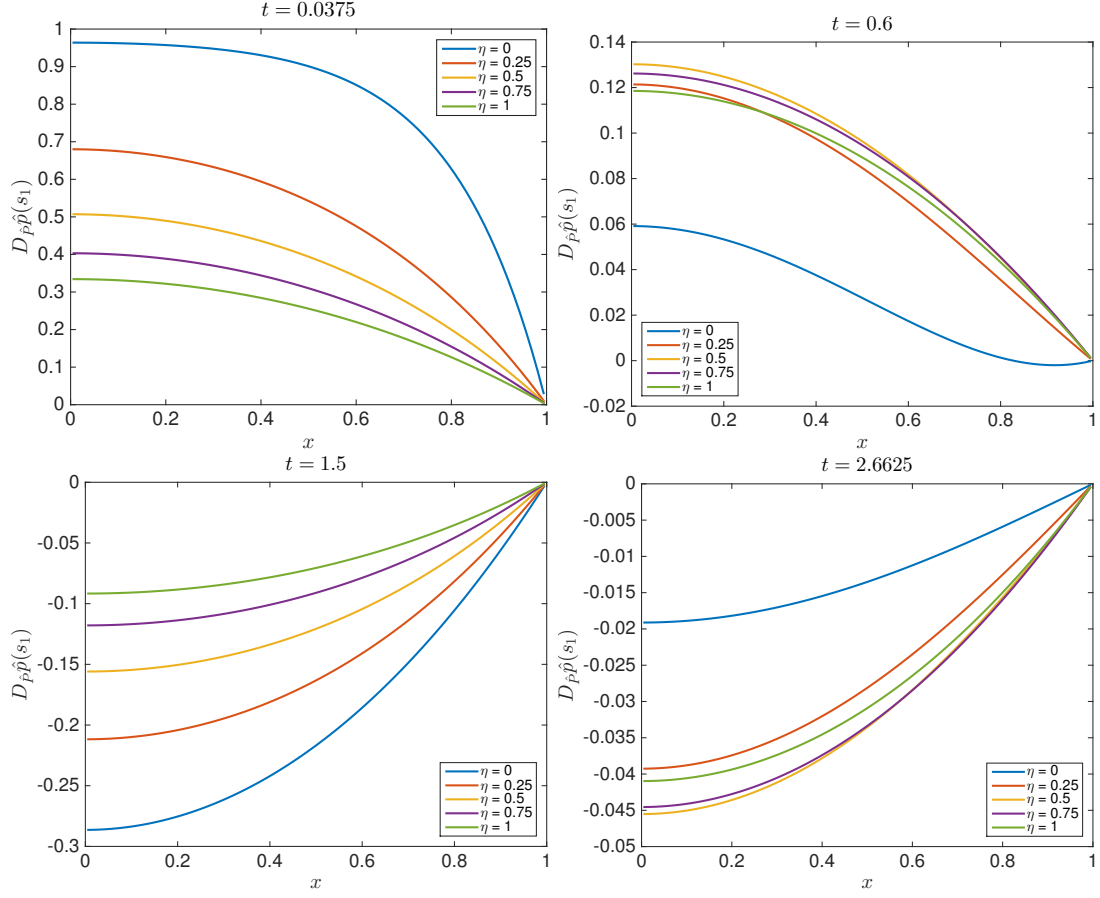


Figure 1.80 Sensitivity of \hat{p} to \hat{P} in direction $s_1(t)$ for $0 \leq \eta \leq 1$.

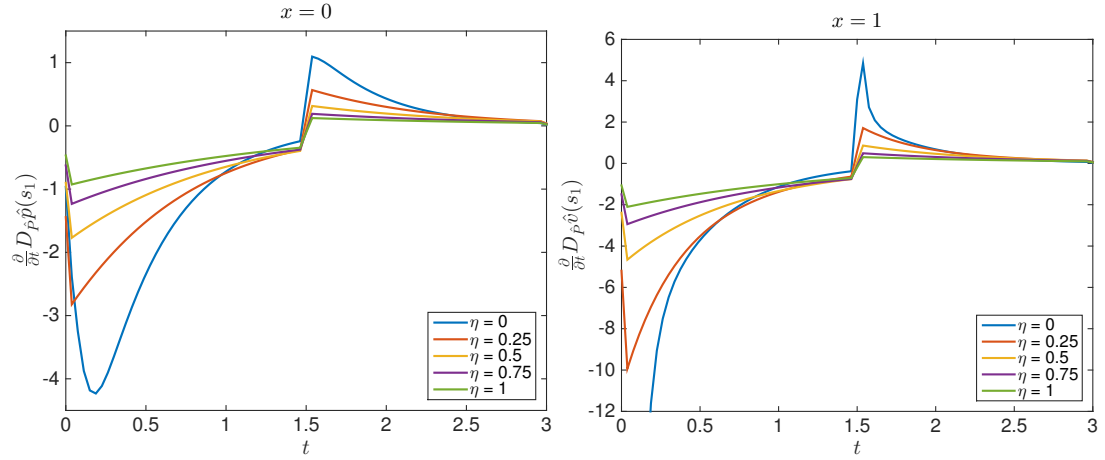


Figure 1.81 Time derivative of sensitivity of \hat{p} (left panel) and \hat{v} (right panel) in direction s_1 .

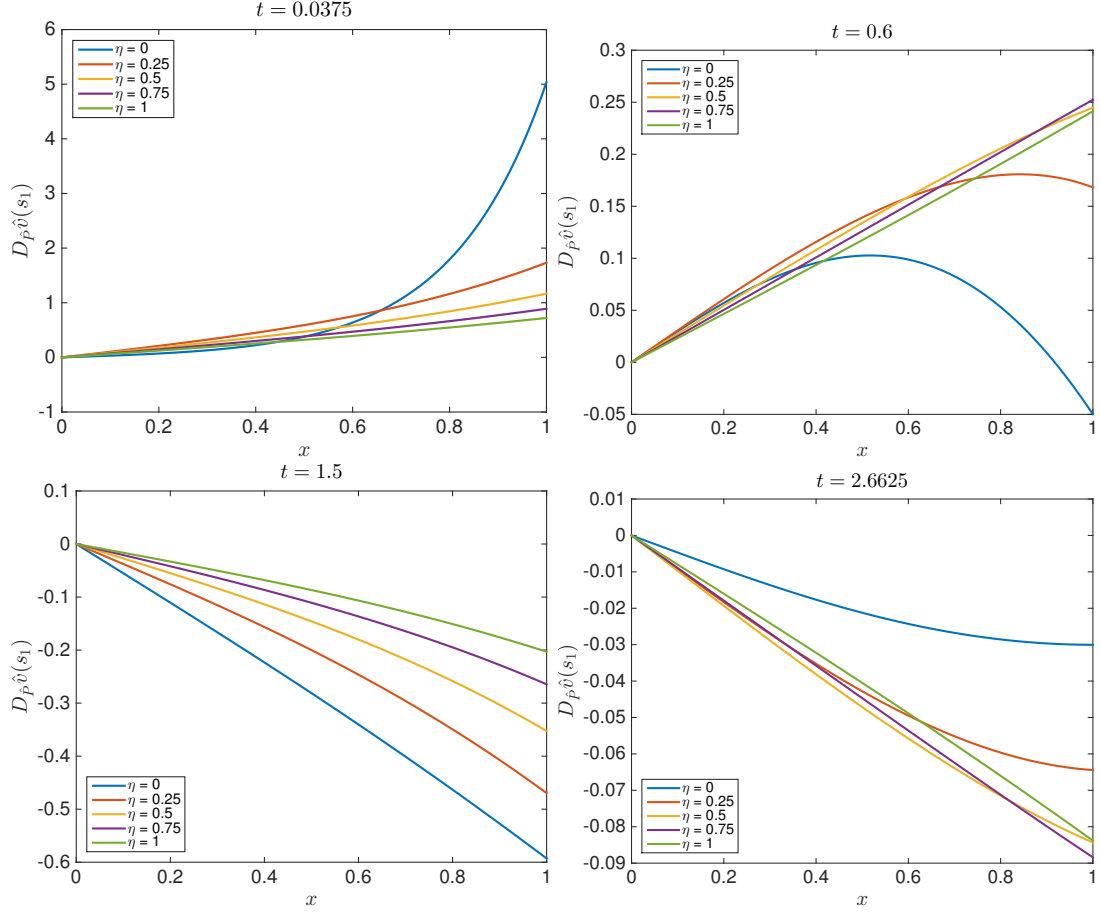


Figure 1.82 Sensitivity of \hat{v} to \hat{P} in direction $s_1(t)$ for $0 \leq \eta \leq 1$.

are shown in Figure 1.83. Note that the log of the sensitivity of \hat{v} (right panel) is shown to better illustrate the blow up.

1.6 Conclusions and Future Work

All our numerical results show that the solution (u, p, v) is more sensitive to the boundary traction g in the elastic case than in the visco-elastic scenario. This could explain why the theoretical results provided in [39] (and presented in Section 1.2.2) require the boundary source to have higher time regularity in order to obtain the solution (u, p) in L^2 in space and time, and with appropriate energy estimate in terms of data, in the purely elastic case.

The effects of the boundary source g are most significant for the discharge velocity v , especially in the purely elastic ($\delta = 0$) case. This is very important, as the numerical investigation in [39] hinted that the fluid energy (which is dependent on the discharge velocity) becomes unbounded as

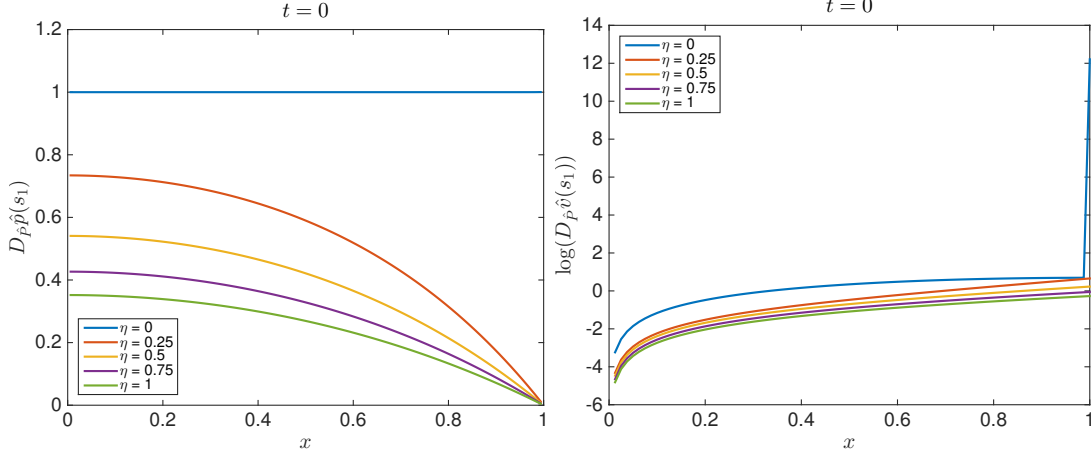


Figure 1.83 Sensitivity of \hat{p} (left panel) and log of sensitivity of \hat{v} (right panel) with respect to \hat{P} in direction s_1 at time $t = 0$.

the boundary source of traction g loses H^1 -smoothness in time, and visco-elasticity is no longer present.

While our results consistently show that the solution (u, p, v) is more sensitive to the boundary traction g in the elastic case than in the visco-elastic scenario, we do not observe such consistent results for the sensitivities with respect to boundary datum ψ . The solid displacement u , fluid pressure p , and discharge velocity v are all more sensitive to ψ in the purely elastic case, in the case of nonlinear permeability that is dependent on dilation. For constant permeability, the elastic displacement is again more sensitive to ψ when $\delta = 0$. However, the fluid pressure appears to be more sensitive to ψ in the visco-elastic case ($\delta = 1$) than in the purely elastic one. Further, the magnitudes of the sensitivities of the discharge velocity with respect to ψ are about the same in both scenarios.

When we compare the sensitivities of each variable to the two boundary terms g and ψ , the difference in magnitude depends on the specific variable when permeability is constant [17]. However, in the case when permeability is nonlinearly dependent on dilation, all of the variables (u, p, v) are consistently more sensitive to ψ than they are to g , regardless of the presence or absence of visco-elasticity in the system. This implies that, according to this preliminary analysis, while the theoretical results in [39] focus on g and F , ψ should not be disregarded from the control point of view.

However, we would like to point out that apart from the presence/absence of viscosity and nonlinearity of permeability, the sensitivity results were also dependent on other characteristics of the problem, such as the volumetric body force F and net volumetric fluid production rate S . This suggests that further investigation may be necessary to make definitive conclusions about the

effects of the boundary sources g and ψ .

Due to the consistency of our results for the sensitivities with respect to g , we believe that g could be an important control parameter in future control and optimization problems governed by poro-visco-elastic models. Specifically, we conclude that g would be an effective control for the fluid velocity and fluid pressure. The solid displacement u , on the other hand, appears to be the least sensitive to changes in g and ψ ; this motivates one to look for other ways to control the solid displacement, such as by acting on the material elastic and viscoelastic properties. In addition, these findings also show that small changes in the solid displacement may actually correspond to big changes in fluid velocity and pressure, thereby suggesting that monitoring the sole solid displacement might not be indicative of the fluid-dynamical state inside the medium.

Another important observation is that the areas within the domain exhibiting highest sensitivity to data differ from case to case depending on whether volumetric sources of mass and momentum are present and on whether the permeability depends on dilation. This finding suggests that each case should be studied in detail, should the control problem be of interest in a specific application under particular conditions.

A similar remark should be made for the influence of the viscoelastic parameter δ . Even though, in general, lower sensitivities are associated with higher values of δ , the results reported in Section 1.4.2 exhibit complex behaviors in space and time depending on the range of δ . This might be due to the fact that viscoelasticity introduces a time delay between stress and strain within the material, thereby strongly affecting the dynamic behavior of the system in time and space. To further understand this issue, we performed a sensitivity analysis on a dimensionless version of the problem.

Our results from the sensitivity analysis on the dimensionless problem consistently show that the maximum magnitude of the sensitivities (for all three dimensionless variables \hat{u} , \hat{p} and \hat{v}) is largest when $\hat{\eta} = \frac{k_0}{L^2} \delta (\lambda_v + 2\mu_v) = 0$ and gets smaller monotonically with respect to $\hat{\eta}$. However, the magnitudes of the sensitivities were not always monotonic with respect to $\hat{\eta}$ and this is due to the response of the sensitivities to changes in the slope of the direction \bar{P} also being dependent upon $\hat{\eta}$. In general, we found that the sensitivities of the solid displacement experience a lag to changes in the slope of \bar{P} if $\hat{\eta} > 0$ with larger values of $\hat{\eta}$ corresponding to longer lag times. On the other hand, while the sensitivities of the fluid pressure and discharge velocity did not experience any lags in time, their responses to changes in the slope of \bar{P} were markedly smaller for larger values of $\hat{\eta}$.

These results correspond closely with results typically observed in creep tests for poro-visco-elastic materials. The lag in the solid displacement due to the inclusion of structural viscosity is indicative of the increase in time that it takes for the solid to reach an equilibrium after an applied load [127]. The sharp increase in the sensitivity of the fluid pressure when the slope of the direction \bar{P} changes is itself consistent with the phenomena of fluid load support in the early time response of confined compression creep tests [173]. Further, the sensitivities of the fluid pressure collapse to zero around times where the sensitivities of the solid displacement are experiencing negligible

change in time. This indicates moments at which the load has been fully transferred to the strain and the solid has reached an equilibrium which is consistent with experimental results [173].

While the magnitudes of the sensitivities were not monotonic with respect to $\hat{\eta}$, we were still able to observe a correlation between the value of $\hat{\eta}$ and the extent and speed at which the sensitivities responded to changes in the direction \bar{P} as well as the maximum magnitude they obtained. For these reasons, we do believe $\hat{\eta}$ will work better as a control parameter than the measure of structural viscosity δ . This is due to the complex behavior the sensitivities with respect to boundary traction displayed depending upon the range of δ . Interestingly, while $\hat{\eta}$ does itself contain δ , it is also dependent upon the length L of the domain and the permeability k_0 . Here, we have only considered constant permeability, however the dependence of $\hat{\eta}$ upon k_0 suggests that taking the permeability k to be nonlinear (which is often more physically relevant) may result in interesting behaviors. Considering the case of nonlinear permeability k is currently a work in progress.

Finally, our analysis shows which directions \bar{P} will result in the most significant changes in \hat{u} , \hat{p} , and \hat{v} . In particular, we can increase the sensitivity for \hat{u} by keeping the direction \bar{P} nonzero and not changing the sign of its slope. On the other hand, \hat{p} and \hat{v} are most sensitive to directions \bar{P} that are always changing. This tells us that while the solid displacement will remain sensitive to a load as long as it is being applied, the fluid pressure and discharge velocity lose sensitivity over time unless the force of the load itself is being changed.

CHAPTER

2

ZONATED MODELS FOR THE LIVER MICROSTRUCTURE WITH APPLICATIONS IN NON-ALCOHOLIC FATTY LIVER DISEASE

Non-alcoholic fatty liver disease (NAFLD) is the most common cause of chronic liver disease and can lead to cirrhosis and liver cancer. Precipitated by the build up of extra fat in the liver not caused by alcohol, it is still not understood why steatosis occurs where it does in the liver microstructure in NAFLD. It is likely, however, that the location of steatosis is due, at least in part, to metabolic zonation (heterogeneity among liver cells in function and enzyme expression). Recently, there has been an influx of computational and mathematical models in order to investigate the relationship between metabolic zonation and steatosis in NAFLD. Of interest among these models are “compartments-in-series” models. These compartmental models include the spatial distribution of metabolite concentrations via series of compartments that are connected through some representation of blood flow. Here, we analyze one such model, looking at how the number of compartments as well as inclusion of dispersion in the flow affect simulation results.

2.1 Non-alcoholic Fatty Liver Disease

Non-alcoholic fatty liver disease (NAFLD) encompasses a spectrum of liver disease that begins as noninflammatory build-up of extra fat in liver cells (steatosis), can progress to non-alcoholic steatohepatitis (NASH) which is the occurrence of inflammation and liver damage in addition to the steatosis, and can eventually lead to cirrhosis [8, 14, 87]. Globally, an estimated 11-46% of people suffer from NAFLD [8, 14, 81]. Approximately 25-40% of patients with NAFLD will progress to NASH [14] with 40-50% of patients developing fibrosis and 20% developing cirrhosis [10]. The increasing prevalence of NAFLD has been linked to the rise of obesity [10] and is strongly associated with insulin resistance and type 2 diabetes mellitus [10, 14, 81, 87]. Considered the hepatic manifestation of metabolic syndrome [14, 42, 87], NAFLD is currently the most common cause of chronic liver disease [8, 14] with NASH currently the second leading cause of cirrhosis in adults waiting for liver transplants in the United States [8, 81, 84] and expected to become the first leading cause by 2030 [8, 10]. It has also been suggested that a recent increase in the prevalence of hepatocellular carcinoma is caused by NAFLD [8, 184].

As the prevalence of NAFLD continues to increase, the cause and pathogenesis of the disease remains an area of intensive study. Though our understanding of this disease has progressed substantially and continues to grow, there is much still to uncover. The pathogenesis of NAFLD is multifactorial and extremely complex, comprised of both environmental and genetic factors though the specific contributions of these are not yet known [8]. Further, though the metabolic processes involved in steatosis have been investigated for decades, there is still much unknown about why lipids accumulate where they do in the liver.

In the continuing investigation of this disease, mathematical and computational models will serve an important role as they give us the ability to explore the complex relationships between various components in a low cost setting. In this paper, we will look at a model of the liver metabolism and examine certain aspects of it in order to inform future development of such models.

2.2 Liver Biology

The liver is the main metabolic organ in the human body and, as such, plays a central role in the regulation of key metabolites including glucose and free fatty acid (FFA). Most of the metabolic processes that occur in the liver take place in the hepatocyte, the main cell type of the liver. These hepatocytes are tightly organized into tessellating columns embedded into liver lobules which make up each of the four lobes of the liver. The lobules have hexagonal cross sections, each corner of which harbors a portal triad which is comprised of a bile duct, hepatic artery (which supplies the hepatocytes with oxygenated blood), and a portal vein (which supplies the hepatocytes with nutrient filled blood). The blood exits the lobule through the central vein which is located at the center of the

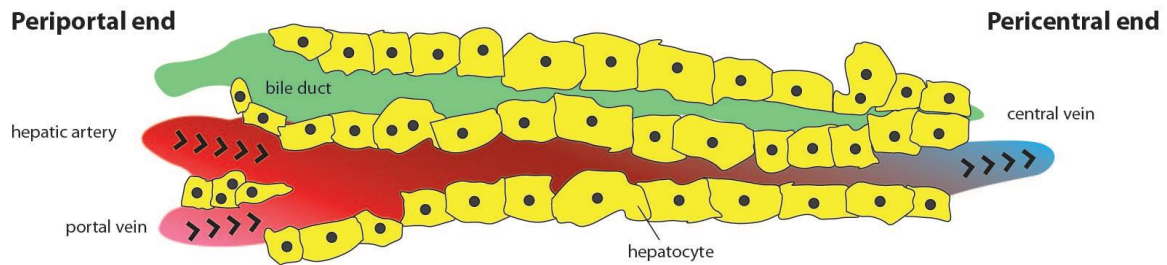


Figure 2.1 Portal axis of a liver sinusoid.

hexagonal structures. Numerous capillaries, called sinusoids, connect the periportal blood vessels of the portal triad with the central vein (see Fig. 2.1). These sinusoids are surrounded by the columns of hepatocytes and are the mechanism through which the hepatocytes have access to the blood provided by the portal triad.

2.2.1 Zonation

Hepatocytes vary in enzyme expression and function depending upon where they lie along the sinusoid, a phenomena called zonation [80, 101–103, 106–108]. This heterogeneity among hepatocytes is, at least in part, the result of differing concentrations of metabolites and signaling molecules along the sinusoid. For example, as blood flows through the sinusoid, oxygen diffuses and is taken up into the hepatocytes resulting in higher levels of oxygen on the periportal end of the sinusoid (near the portal triad) and lower levels of oxygen on the pericentral end of the sinusoid (near the central vein). This oxygen gradient was discovered decades ago and has long since been considered a significant driving force of zonation [35, 104, 105, 110–112, 192]. Some studies have also indicated that the hormones insulin and glucagon play an important role in the regulation of zoned gene expression [103, 106, 151]. More recently, other signaling pathways have also been proposed and studied as potential mechanisms for zonation [55, 89, 183].

2.2.2 Zonated steatosis

Metabolic zonation is not the only form of heterogeneity seen across the sinusoid. Most liver diseases show a varying amount of damage across the liver microstructure [103]. In NAFLD, studies have shown that, for adult patients, steatosis is typically most severe in pericentral cells [2, 43, 44, 51, 89, 195]. However not all patients show such an aberrant accumulation of lipids on a particular part of the sinusoid [44, 51]. Further, steatosis in pediatric patients with NAFLD tends to occur most severely in periportal cells [195]. The cause of this “zonated steatosis” in NAFLD is still not fully understood,

however the heterogeneity of hepatocytes likely results in certain liver cells being more vulnerable to lipid build up than others [11]. Further, in patients who have progressed to NASH, inflammation and fibrosis tends to be most severe on the pericentral end of the sinusoid [1, 43, 51, 89].

Although it is well known that lipids tend to accumulate heterogeneously across the sinusoid (both in NAFLD and in other liver diseases), the effect of metabolic zonation on such zoned steatosis has received limited attention experimentally. To great extent, this is because investigating changes in individual regions of the sinusoid is extremely time consuming and complex [11]. Computational models of liver metabolism that are spatially distributed give us the ability to explore relationships between metabolic zonation and zoned steatosis without the high cost of experimentation. Since NAFLD is induced by a change in metabolism, that is, the build up of lipids in the liver, it is tangible that metabolic zonation plays a major role in the pathology of this disease. Thus, the development of computational models of liver metabolism that include the spatial effects of zonation are of utmost importance in the continuing effort to understand and find treatment for NAFLD.

2.3 Mathematical models

Computational models have been used previously to study the effect of zonation on detoxification processes such as the detoxification of ammonia [140], xenobiotics [169], and drugs [144, 156], as well as more generally in pharmacokinetics [7, 143]. However, few models currently exist that explicitly consider the heterogeneous expression of enzymes which defines metabolic zonation.

Existing mechanistic models of liver metabolism that include spatial distribution can be roughly divided into two categories depending on the types of equations used: those which use partial differential equations (PDEs) and those which use ordinary differential equations (ODEs). As will be shown later on, models from different categories may not always be as different from each other as may appear at first glance. The PDE models can further be divided into models derived using the theory of porous media and models that utilize advection or advection-dispersion equations.

The advantages of deriving a system using the theory of porous media is in the ability to more accurately describe the process of blood perfusion through the liver lobule. This is of particular interest since steatosis can affect hepatic hemodynamics [71, 126, 135, 174]. In a series of publications [157–159], Ricken et al. develop a multi scale approach that does just this, coupling the blood perfusion through the liver lobule with a description of hepatic cell metabolism. While metabolic zonation is not explicitly included, they are still able to simulate some zoned steatosis.

Models using advection or advection-dispersion equations to represent the blood flow in the liver have been around for decades finding applications in many areas such as hepatic elimination, drug clearance, and capillary tissue exchange [31, 32, 63, 143, 160]. These models have generally been referred to as parallel-tube and distributed models (advective flow) [31, 32, 75] and dispersion

models (advective-dispersive flow) [161]. Similar models to the dispersion model have been used in the past decade to study aspects of hepatic metabolism as well [46, 52]. In 2006, Chalhoub et al. [52] used advection-dispersion-reaction equations to represent the concentrations of metabolites in the sinusoid, coupled through metabolic transport to mass-balance equations for the metabolites in the tissue. Enzymatic zonation is included for central carbohydrate pathways, but not for lipid metabolism. In 2008, Calvetti et al. [46] used a model similar to the one given in [52] to illustrate how one may embed such a model of cellular liver metabolism into a Bayesian framework for parameter estimation purposes. However, zonation is excluded from the model and the system is only considered at steady state. Use of these types of PDEs to model the liver microstructure has appeared to lag in the past decade as compartmental models have started to show prevalence. An explanation for this may be due to the appearance of these PDEs as being more difficult to use in comparison to compartmental models which are composed of ODEs [7, 82].

Compartmental models for the liver that include spatial distribution were originally inspired by “tanks-in-series” models from chemical engineering [82] and can be considered “compartments-in-series” models. These models are comprised of systems of ODEs derived by considering a series of compartments that are connected together, typically through blood flow. While early models of this type had each compartment represent both blood and tissue [82] so that there is only a single series of compartments, modern models tend to separate blood and tissue into different compartments with a transport between them [10, 11, 34, 140, 165]. These models have a series of hepatic blood compartments that are connected through blood flow along with a series of tissue compartments which are only connected to their corresponding hepatic blood compartment (i.e., there is no explicit connection between tissue compartments). These models often treat the series of compartments as being lined up along the portocentral axis of the liver sinusoid, and as such treat this as the repeating unit of the liver (rather than the hepatocyte). Recently, compartmental models that include spatial distribution have been applied more specifically to hepatic metabolism.

Schleicher et al. [165] used a three compartment model to simulate hepatic lipid metabolism. The hepatic blood flow is a basic advective flow that transports concentrations of metabolites in the hepatic blood from the periportal to the pericentral end of the sinusoid. This three compartment model is used to look at how the plasma oxygen gradient, plasma FA gradient, as well as the process for FA uptake affect the zonation of steatosis under a high-fat diet. Despite the fact that zonated enzyme expressions are not included in this model, model simulations do show a zonated steatosis.

A much more complex compartmental model was used by Berndt et al. [34] to study glucose metabolism and how it is affected by zonated enzyme expressions, metabolite and hormone gradients in the sinusoid, and blood perfusion. This model includes the blood in the sinusoid, accompanying space of Disse, as well as the adjacent layers of hepatocytes allowing the authors to take into account both morphological and systemic parameters. Each component (sinusoid, space of Disse, and hepatocytes) is partitioned into 20–25 compartments and flow is modeled in both the

sinusoid and the space of Disse as an advective-dispersive flow.

Among the most advanced compartmental models for liver metabolism is the one presented by Ashworth et al. in [10, 11]. This 8 compartment model does not include any morphology like the model in [34], however it does include a rather detailed representation of glucose, lipid, and energy metabolism including zoned enzyme expressions and metabolite and hormone gradients in the hepatic blood. The blood flow through the sinusoid is given by a simple advective flow from the periportal to the pericentral end of the sinusoid. This model was used to investigate causes of pericentral cell susceptibility to steatosis in NAFLD, especially in the case of insulin resistance. A distinctive aspect of this model is the inclusion of an extra compartment that holds a simplified representation of metabolism in the rest of the body including hormone release by the pancreas. This extra “body” compartment acts as an input into the first hepatic blood compartment of the series of compartments and takes the output of the final hepatic blood compartment to update its own concentrations, thus creating a type of feedback into the system.

As NAFLD becomes more and more prevalent, the ability to perform accurate *in silico* experiments is an integral part of uncovering important mechanisms and targets for these conditions. Compartments-in-series models are an attractive tool that allow one to investigate how metabolic zonation, hepatic blood gradients of metabolites and hormones, and even blood perfusion, affect liver metabolism at various levels of complexity. In particular, these models boast the ability to investigate various aspects of liver metabolism with sharp detail while keeping computational times reasonable. However, one may question if the simplification to a number of compartments rather than a continuum may result in the loss of information or misrepresentation of results. In what follows, we will examine a model similar to the one presented in [10, 11] in order to begin attempting to answer this question. The two main goals of the current work are (i) to investigate the effect that the number of compartments has on model simulations and (ii) to investigate the effect of dispersion on the system.

In what follows, we will present the models of the liver microstructure under consideration. Our models closely resembles that of [10, 11], with the main differences being how concentrations in the systemic blood (i.e., the blood/plasma in the body excluding the liver) are modeled as well as how we view the equations in the hepatic blood. We model the concentrations of a number of metabolites, hormones, and oxygen in the liver sinusoid. Equations are separated into those for the hepatocytes (referred to as hepatic equations), those for the hepatic blood (i.e., blood/plasma in the sinusoid), and those for the systemic blood (i.e., blood/plasma in the rest of the body). While oxygen, hormones, and metabolites are all modeled in the hepatic and systemic blood, only metabolites are modeled in the hepatocyte. However, the concentration of hormones and oxygen in the hepatic blood do affect the metabolic processes that occur in the hepatocyte. A full list of all the molecule concentrations modeled is included in Table 2.1 along with what kinds of equations they have and their abbreviated variable name that will be used to denote them throughout this chapter. Fig. 2.2

gives a schematic of the general structure of the models in consideration. We will use the following notation convention: variables in the hepatocyte will have a subscript H , variables in the hepatic blood will have a subscript HB , and variables in the systemic blood will have a subscript SB . The only exception to this will be molecules whose concentrations are only modeled in the hepatocyte (see the third column of Table 2.1) which will not have any subscript.

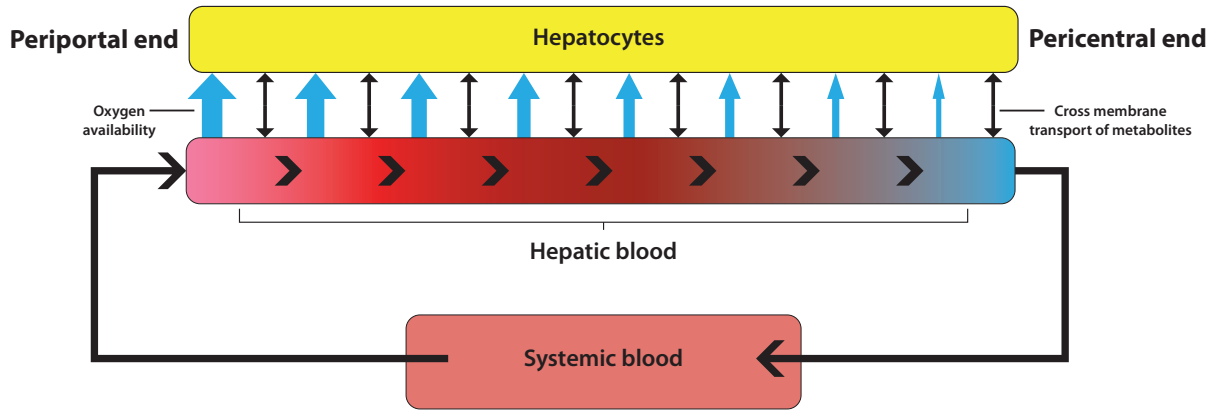


Figure 2.2 Schematic illustrating general structure of the models in consideration.

Table 2.1 All molecules represented in the model with their abbreviated variable name. H denotes hepatic, HB denotes hepatic blood, SB denotes systemic blood.

Eq. in H, HB, SB		Eq. in HB, SB		Eq. in H	
Glucose	gC	Insulin	Ins	Glycogen	G
Triglycerides	TG	Glucagon	GL	Glucose-6-phosphate	$g6p$
Fatty acids	FA	Oxygen	Oxy	Glycerol-3-phosphate	$g3p$
Glycerol	gly			Acetyl-CoA	$aCoA$
Lactate	Lac			Inorganic phosphate	P
				Guanosine Tri-phosphate	gtp
				Guanosine Di-phosphate	gdp
				Uridine Tri-phosphate	utp
				Uridine Di-phosphate	udp
				Adenosine Tri-phosphate	atp
				Adenosine Di-phosphate	adp
				Adenosine Mono-phosphate	amp

2.3.1 Compartments-in-series model

The compartments-in-series model can be seen as many two-compartment models lined up next to each other and connected via the blood flow through the hepatic blood compartments. Let n be the number of hepatic compartments in use. Then, there are $8(n + 1)$ equations in the hepatic and systemic blood compartments and $17n$ in the hepatic compartments, resulting in a total of $17n + 8(n + 1) = 25n + 8$ equations in this discrete model. Fig. 2.3 illustrates the structure of the compartment-in-series model with $n = 8$ hepatic compartments.

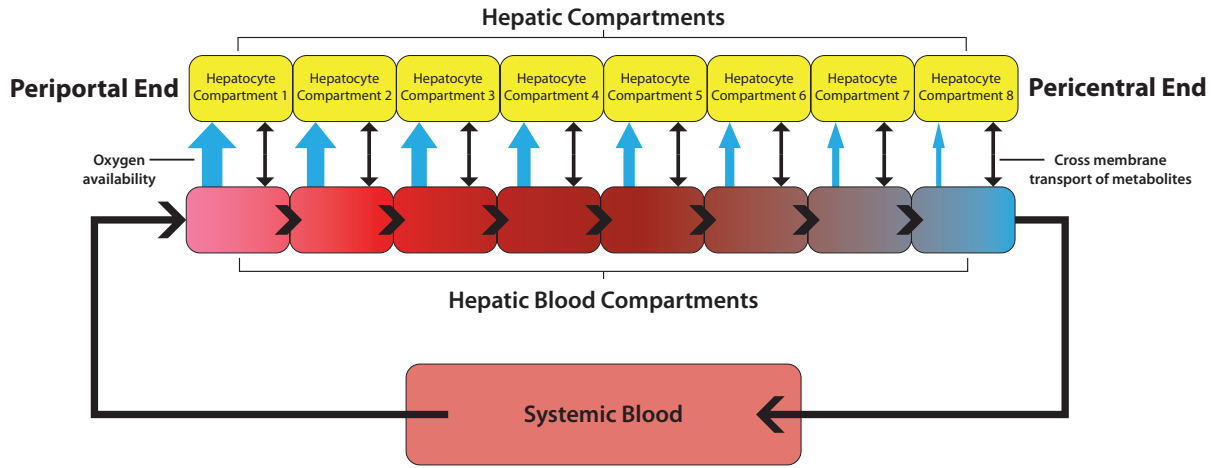


Figure 2.3 Schematic of compartments-in-series model.

2.3.1.1 Hepatic compartments

In the model presented in [10, 11], the rate of hepatic metabolic processes are modeled through the use of Hill functions. Rather than modeling every individual enzyme, sections of metabolic pathways are often modeled by a single function, thus depending upon a number of intermediate enzymes rather than a single one. Each substrate and allosteric activator/inhibitor is represented by a Hill function and the rate of the process is calculated to be the product of these Hill functions. Hormonal regulation of metabolic processes is modeled differently depending upon the strength and speed with which the hormone is known to act on the process. The hepatic metabolic processes included in the model are given in Appendix A along with the function for the rate of that process. Every hepatic compartment has the same processes modeled in it, however the rate of these processes vary due to zonation. An explanation for how zonation is included in the model is given below in Section 2.3.1.1.2. The hepatic equations are given in Appendix B.1.

2.3.1.1.1 Transports

The transport of metabolites between plasma and hepatocyte are modeled similarly to the metabolic processes within the hepatic compartment. For uni-directional transports, the rate is calculated using a Hill function where the plasma molecule is treated as the substrate and the hepatic molecule as the product. For bi-directional transports, the rate is calculated by a “Hill-like” function that depends on the difference in concentration of the molecule between the plasma and hepatocyte. The rates of transport of metabolites between plasma and hepatocyte are given below.

Glycerol transport. The glycerol transport is just a simple bi-directional transport:

$$\mathcal{T}_i^{gly} = \frac{v^{gly}([gly]_{HB,i} - [gly]_i)}{K_M^{gly} + [gly]_{HB,i} + [gly]_i}. \quad (2.1)$$

Triglyceride transport. The triglyceride transport is made up of both a bi-directional and a uni-directional transport. The uni-directional transport represents the release of VLDL (very large density lipids) from the liver into the plasma. The full transport then is given by

$$\mathcal{T}_i^{TG} = -\frac{v^{VLDL}[TG_H]_i}{K_M^{VLDL} + [TG_H]_i} + \frac{v^{TG}([TG_{HB}]_i - \frac{[TG_H]_i}{TG_{ref}})}{K_M^{TG} + [TG_{HB}]_i + \frac{[TG_H]_i}{TG_{ref}}}, \quad (2.2)$$

where TG_{ref} is used to ensure the bi-directional component does not give a constant output from the hepatocyte (i.e. always < 0).

Fatty acid transport. The regulation of fatty acid (FA) transport and uptake into the liver is a complex and often debated topic [130]. There is strong evidence for protein-mediated FA uptake with a number of membrane proteins being implicated [4, 130]. In particular, in the liver such proteins include fatty acid translocase FAT/CD36 [45, 130, 133], liver fatty acid binding protein LFABP [139, 155], and fatty acid transport proteins, specifically FATP2, FATP3, and FATP5 [4, 37, 38, 66, 67, 72, 130, 134]. Passive diffusion also contributes to hepatic FA uptake, however this process is minimal in comparison to facilitated uptake [130].

In [10, 11], the FFA transport is composed of a uni-directional, insulin dependent term and a bi-directional, insulin independent term. We omit the insulin dependent term here as, under physiological conditions, the hepatic FA transporters that appear to be the major players in hepatic FA uptake (LFABP, FATP2, FATP3, and FATP5) [4, 38, 139] are not known to be regulated by insulin. The greatest evidence for insulin regulated hepatic FA uptake is in FAT/CD36 mediated FA uptake.

FAT/CD36 is a fatty acid transporter that is regulated by muscle contraction and/or insulin and is an important protein implicated in FA uptake by skeletal muscle cells, cardiomyocytes, and

adipocytes [45]. Under physiological conditions, FAT/CD36 is weakly expressed in hepatocytes suggesting FA uptake is largely FAT/CD36 independent [45]. However, there is evidence that hepatic mRNA and protein levels of FAT/CD36 at the plasma membrane of hepatocytes increases in patients with NAFLD [45, 130, 133].

Of the FATP family of transporters, the only one known to be regulated by insulin is FATP1 [4]. While FATP1 does have some expression in the liver, this transport is more significant for skeletal muscle, heart, and adipose tissue [4, 38]. In fact, studies have shown that while mice lacking FATP1 show a decrease in insulin-stimulated long chain FA uptake in adipocytes and skeletal muscle, they actually have an increase in long chain FA uptake in the liver [193].

The fatty acid transport is a simple bi-directional transport that encompasses both transport due to diffusion and facilitated transport:

$$\mathcal{T}_i^{FA} = \frac{v^{FA}([FA_{HB}]_i - [FA_H]_i)}{K_M^{FA} + [FA_{HB}]_i + [FA_H]_i}. \quad (2.3)$$

Glucose transport. The glucose transport modeled here is GLUT2. This transport has both a uni and a bi-directional component where the uni-directional component represents pumping glucose into the hepatocyte and the bi-directional term represents the glucose diffusing into the hepatocyte. The transport is given by

$$\mathcal{T}_i^{gC} = \frac{v^{gC_{pump}}[gC_{HB}]_i}{K_M^{gC_{pump}} + [gC_{HB}]_i} + \frac{v^{gC_{diff}}([gC_{HB}]_i - [gC_H]_i)}{K_M^{gC_{diff}} + [gC_{HB}]_i + [gC_H]_i}. \quad (2.4)$$

Lactate transport. The lactate transport is just a simple bi-directional transport:

$$\mathcal{T}_i^{Lac} = \frac{v^{Lac}([Lac_{HB}]_i - [Lac_H]_i)}{K_M^{Lac} + [Lac_{HB}]_i + [Lac_H]_i}. \quad (2.5)$$

2.3.1.1.2 Zonation

We follow the process outlined in [10] to include zonation of enzyme expressions in the model. Specifically, zonation of the enzyme expressions are modeled through the metabolic processes (pathways) they are involved in by utilizing information about the enzymes involved in the process as well as the location of the hepatocyte along the sinusoid. Each hepatic compartment is assigned a value $z_i \in [-1, 1]$ (roughly) depending upon the concentration of oxygen in the corresponding hepatic blood compartment. Specifically,

$$z_i = \begin{cases} \tanh\left(\frac{[Ox y_{HB}]_i - 46.5}{12}\right) & \text{if } [Ox y_{HB}]_i > 46.5 \text{ mmHg} \\ 2 \tanh\left(\frac{[Ox y_{HB}]_i - 46.5}{24}\right) & \text{if } [Ox y_{HB}]_i \leq 46.5 \text{ mmHg} \end{cases}. \quad (2.6)$$

Note that periportal oxygen concentrations should be approximately 65-75 mmHg and pericentral oxygen concentrations should be approximately 30-35 mmHg so that a positive z_i value indicates the hepatic compartment is on the periportal end of the sinusoid, while a negative z_i value indicates the hepatic compartment is on the pericentral end.

Each metabolic process M is also assigned a zonation constant $k_M \in (-1, 1)$ that depends upon the experimentally measured ratio of the enzyme expression in periportal cells to pericentral cells. Specifically, if $k_{pp} : 1$ is this ratio, then

$$k_M = 1 - \frac{2k_{pp}}{|k_{pp}| + 1}. \quad (2.7)$$

The rate constant for the metabolic process in hepatic compartment i is then calculated as

$$v_i^M = (1 + z_i k_M) v_b^M, \quad (2.8)$$

where v_b^M is the base-value for the rate constant of metabolic process M .

The zonation constants for the compartments are also used to include how reception of hormones change across the sinusoid. However, instead of setting v_i^M to a base rate constant for a process, it is used to scale the concentration of the hormone in the metabolic process it is regulating (i.e. $v_i^{Ins}[Ins_{HB}]_i$ is used in regulation rather than $[Ins_{HB}]_i$).

2.3.1.2 Hepatic blood compartments

In the hepatic blood compartments, the equations for the concentrations of metabolites all have the same form which depends on the concentration in the previous compartment. For $i = 1, \dots, n$, if $[C_{HB}]_i$ is the concentration of metabolite C in hepatic blood compartment i , then

$$\frac{d[C_{HB}]_i}{dt} = v_{bf}([C_{HB}]_{i-1} - [C_{HB}]_i) - \gamma_H \mathcal{T}_i^C, \quad (2.9)$$

where $v_{bf} = 0.15n$ is the rate of blood flow, γ_H is the ratio of hepatic to hepatic blood volume, and \mathcal{T}_i^C is the rate of transport of metabolite C between hepatic blood compartment i and hepatic compartment i . We also set $[C_{HB}]_0 = [C_{SB}]$, the concentration of metabolite C in the systemic blood compartment. Note that the value 0.15 in the rate of blood flow in the hepatic blood compartment was chosen in order to make a circuit of blood flow last approximately 5 minutes [10].

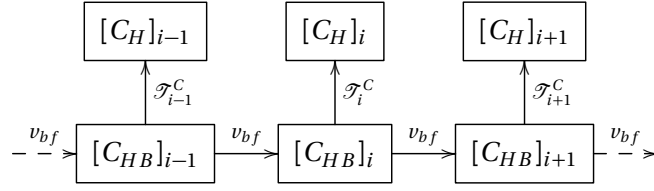


Figure 2.4 Schematic of metabolite concentration in hepatic blood for compartments-in-series liver microstructure model.

Oxygen and the hormones insulin and glucagon also have equations in the hepatic blood compartments. The concentration of oxygen in the hepatic blood compartments promotes all zonated expressions, while the concentrations of hormones act as regulators of the metabolic processes in the hepatic compartments. All three of these variables are modeled with a constant rate of degradation as the hormone travels through the sinusoid in order to simulate the oxygen and hormone gradients that occur across the sinusoid. In particular, the equation for oxygen is set such that the concentration of oxygen is approximately 65mmHg in the first (periportal) hepatic blood compartment and 35mmHg in the blood in the last (pericentral) hepatic blood compartment [10]. The hepatic blood equations are given in Appendix B.1.

2.3.1.3 Systemic blood compartment

The blood flow in the systemic blood compartment is treated similarly to the blood flow in the hepatic blood compartments. If $[C_{HB}]_n$ is the concentration of metabolite C in the final compartment of the hepatic blood, and $[C_{SB}]$ is the concentration in the systemic blood, then

$$\frac{d[C_{SB}]}{dt} = \frac{Q_H}{\gamma_B}([C_{HB}]_n - [C_{SB}]) + \mathcal{S}, \quad (2.10)$$

where γ_B is the ratio between the volume of systemic blood to the volume of hepatic blood, and \mathcal{S} represents the rates of the metabolic processes included in the model from the rest of the body.

It is in the representation and inclusion of metabolic processes in the systemic blood (referred to as the body compartment in [10, 11]) that the model presented here truly differs from the model in [10, 11]. These changes were made in order to improve biological detail as well as to simplify the equations here. Since the main focus of this model is on liver metabolism, we aim to leave these equations as simple as possible while keeping the concentrations at realistic levels. The main issue we came across was that the meal inputs were too significant of a driver of the system and resulted in metabolite concentrations falling too quickly in the absence of these inputs. To address this, we adjust the equations for the concentrations of metabolites and hormones in the systemic blood. A summary of the most significant changes is given below. Plots showing selected metabolite

and hormone levels in the systemic blood before and after these changes are given in Fig. 2.5. The systemic blood equations are given in Appendix B.1.

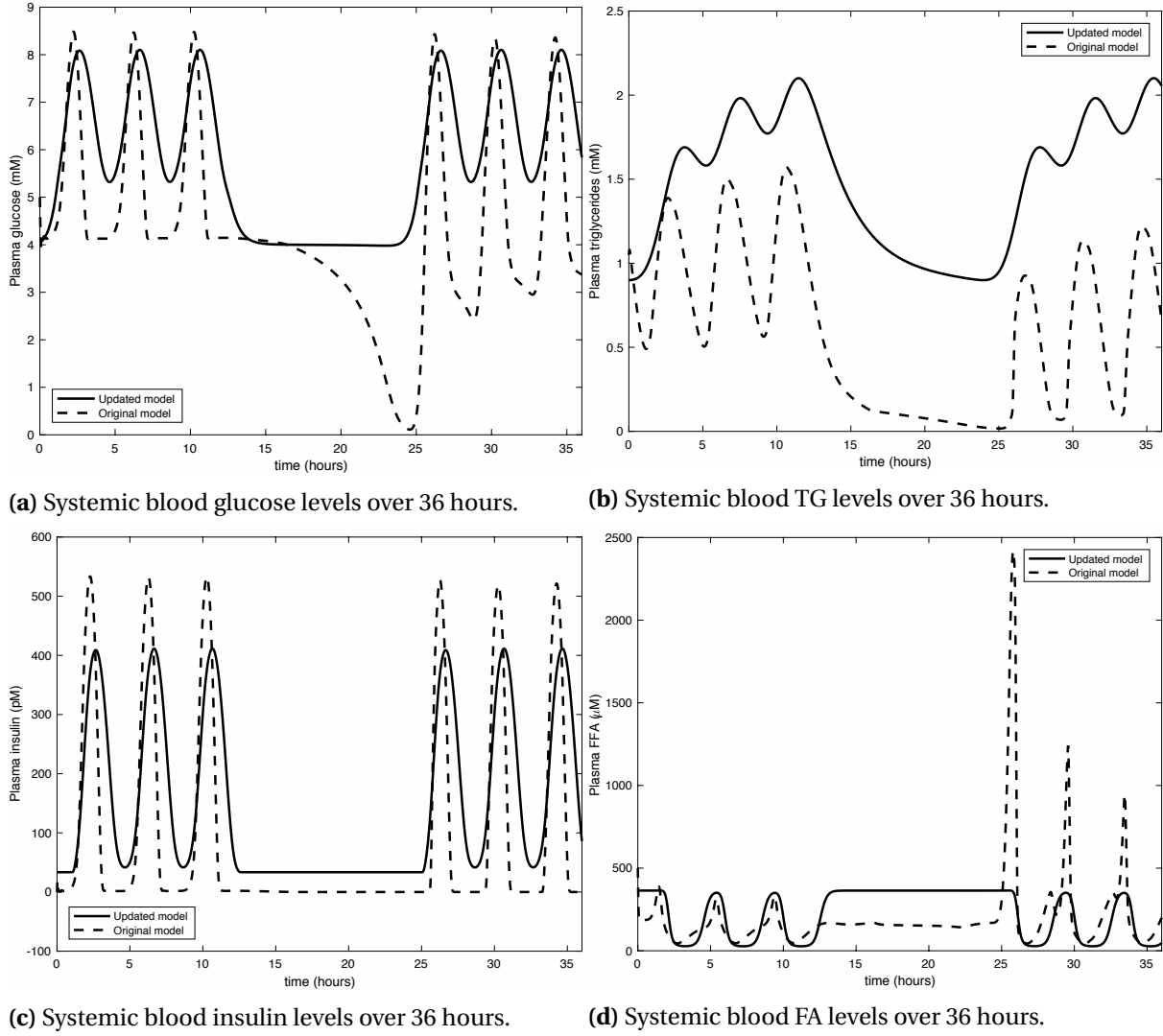


Figure 2.5 Concentrations in systemic blood before and after model changes.

2.3.1.3.1 Glucose uptake in body

In the original model, glucose uptake in the body (excluding the liver) is represented by a function \mathcal{J}_{gCup} dependent on plasma glucose level alone. This function takes the form of a simple Hill

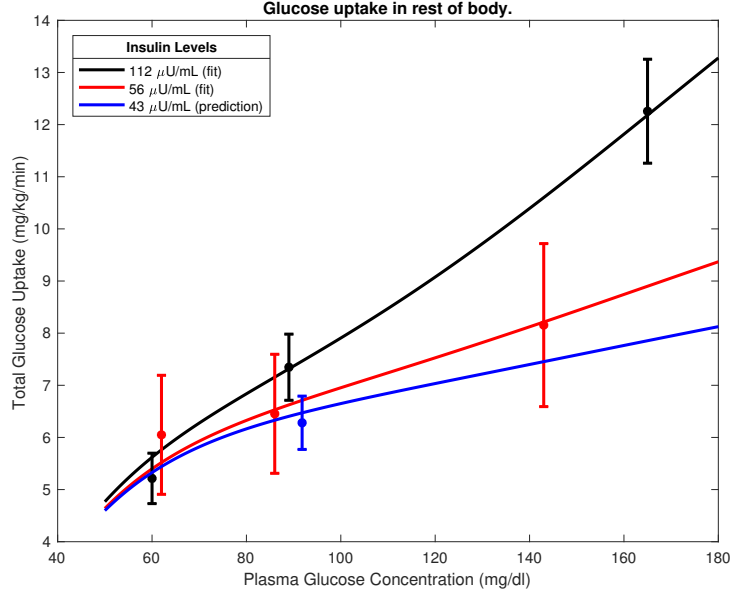


Figure 2.6 Data fit and model predictions for glucose uptake in rest of body.

function given by

$$\tilde{\mathcal{J}}_{gCup} = \frac{v[gC_{SB}]}{K_M + [gC_{SB}]} \quad (2.11)$$

While there is insulin independent glucose uptake in the body such as in the brain, the uptake of glucose in other tissues (such as muscle and adipose) does depend upon insulin [49, 170]. For this reason, we formulated a second term for the rate of insulin dependent glucose uptake in the body using Hill functions. Our resulting function for the rate of glucose uptake in the rest of the body is given by

$$\mathcal{J}_{gCup} = \frac{v_1[gC_{SB}]^{n_1}}{K_{M_1}^{n_1} + [gC_{SB}]^{n_1}} + v_2 \left(\frac{[Ins_{SB}]^{n_I}}{K_{M_I}^{n_I} + [Ins_{SB}]^{n_I}} \right) \left(\frac{[gC_{SB}]^{n_2}}{K_{M_2}^{n_2} + [gC_{SB}]^{n_2}} \right). \quad (2.12)$$

The parameters for this function were estimated using a weighted least squares scheme with data from [61] and predictions were tested using data from [182] (see Figure 2.6). Finally, to get \mathcal{J}_{gCup} in terms of the correct units for our model, we divide the rate by the volume of distribution of glucose, estimated to be 14L.

We note that the data used to estimate the parameters for \mathcal{J}_{gCup} are extremely sparse and as such identifiability is nearly impossible to obtain from this data set alone. However, in this work we prioritize biological detail over identifiability concepts and as such assume our parameter estimates are sufficient with low confidence.

2.3.1.3.2 Lipolysis in adipose tissue

Lipolysis is the breakdown of fats by hydrolysis to release fatty acids. Specifically, lipolysis breaks down a triglyceride into one glycerol molecule and three fatty acids. With no adipose compartment in the model, there is also no triglyceride storage in adipose tissue. In [10], plasma triglycerides are treated as adipose triglycerides for lipolysis in adipose tissue. To account for the fact that the size of the plasma triglyceride pool is much smaller than those stored in adipose tissue, rate constants that had a slow dependence upon plasma glucagon and insulin concentration were used. In our simulations, however, this adjustment to the rate constants did not prevent the plasma triglyceride pool from emptying during fasting periods (i.e., periods without meal inputs). To alleviate this, we take the rate of lipolysis in adipose tissue to be driven by insulin action alone. Fig. 2.7 gives schematic representations of how lipolysis in adipose tissue is represented in the model from [10] (Fig. 2.7a) and in the model given here (Fig. 2.7b).

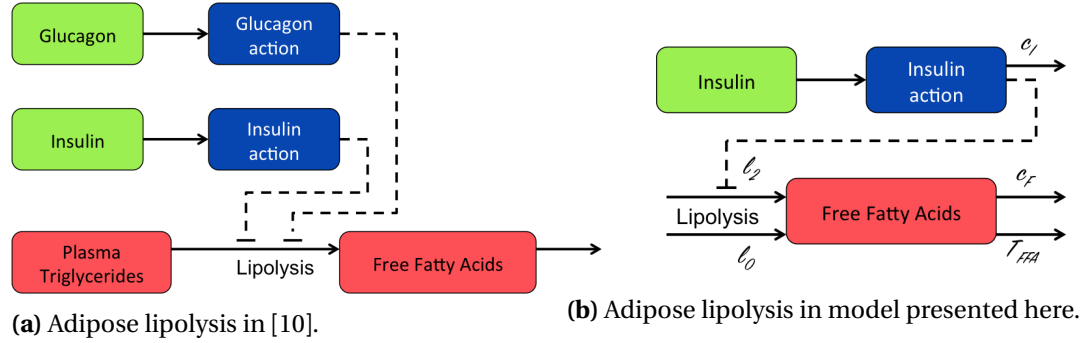


Figure 2.7 Schematics of how adipose lipolysis is modeled.

Following the work of Periwal et al. [121, 145], we model the rate of lipolysis in adipose tissue with the following system

$$\frac{d[FA_{SB}]}{dt} = L(I_A) - c_f[FA_{SB}], \quad (2.13a)$$

$$\frac{dI_A}{dt} = c_I([In_{SB}] - I_A - I_b), \quad (2.13b)$$

$$L(I_A) = l_0 + \frac{l_2}{1 + (I_A/I_{A2})^{\alpha_{AdLip}}}, \quad (2.13c)$$

where I_A is insulin action with initial condition $I_A(0) = 0$ and $L = \mathcal{S}_{AdLip}$ is the rate of lipolysis. We also have I_{bA} which is related to the basal insulin level (though not the basal insulin level itself), a basal lipolysis rate l_0 , the maximal insulin dependent lipolysis rate l_2 , a rate constant for insulin

dependent lipolysis I_{A2} , a Hill constant modulating free fatty acid lipolysis α_{AdLip} , and the clearance of fatty acid to the body c_f . This model was fit using data from [121] as well as mean parameter estimates and standard deviations provided therein as initial guesses and weights in a weighted least squares formulation. Fig. 2.8 shows the fit to the FFA data where the model (2.13) was driven by insulin data.

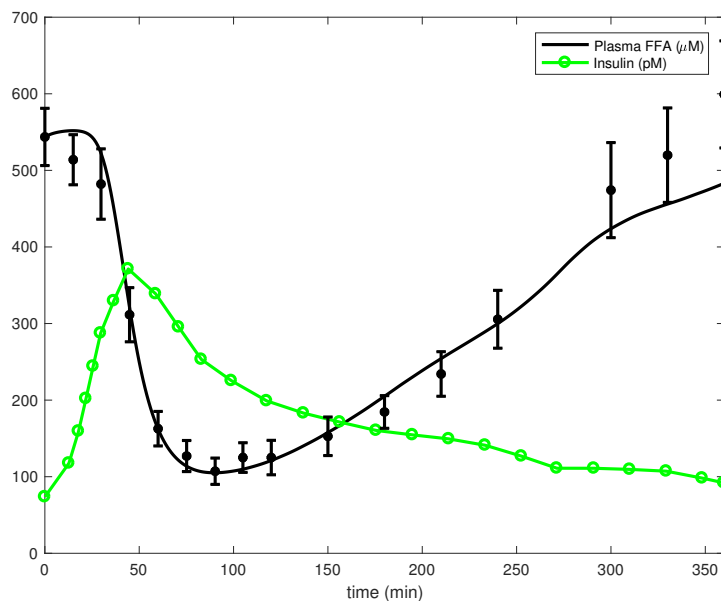


Figure 2.8 Data fit to reduced fatty acid model with adipose lipolysis Eq. 2.13.

Once the parameters for (2.13) were estimated, parameters for the fatty acid transport as well as the clearance of fatty acids c_f were then adjusted so that approximately 30% of FFA being cleared to the body is transported to the liver. This amount is based on the percentage of palmitate cleared by the liver as indicated by data in [85].

2.3.1.3.3 Meal inputs

In [10], the meal inputs are given by a high-powered sine function (i.e., $v_{in} \sin^6(2\pi t / (2 \text{ hours}))$) for some constant v_{in}). This representation for meal input causes sharp peaks with steep slopes in plasma glucose concentrations as well as other concentrations dependent on glucose (such as insulin). However, data shows [56, 59, 64] that the effect of meal ingestion upon concentrations of plasma metabolites should not give such a steep slope of decrease. These sharp peaks are largely due to the dynamics of the high-powered sine function which itself exhibits sharp peaks. Thus, to reduce the slopes of the peaks in plasma glucose concentration (and other plasma metabolites), we

represent the meal inputs using the solution to a basic differential equation (DE) that simulates the passage of food through the body (see Figure 2.9).

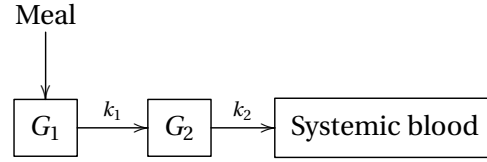


Figure 2.9 Schematic of meal input DE.

The DE used to simulate meal ingestion is a two-compartment model where each compartment represents part of the gut and is given by

$$\begin{cases} \frac{dG_1}{dt} = -k_1 G_1 + \alpha_{meal} G_{in} f_s, & G_1(0) = \alpha G_{in}, \\ \frac{dG_2}{dt} = k_1 G_1 - k_2 G_2, & G_2(0) = 0. \end{cases} \quad (2.14)$$

The rate of change in plasma glucose from the ingestion of meals is then given by $\mathcal{S}_{meal} = k_2 G_2$. The source function, f_s is a Gaussian centered at two hours after the beginning of the meal. The meal cycle is: meals occur every 4 hours for 12 hours, then no meals for 12 hours (to simulate rest).

2.3.2 Advection-Reaction (AR) Version

The AR version of the model is actually equivalent to the compartments-in-series model as $n \rightarrow \infty$. Here, we will briefly describe how the form of this model differs from the compartments-in-series model.

2.3.2.1 Hepatocytes

The metabolic processes in the hepatocytes as well as the transports between hepatocytes and hepatic blood are modeled in the same way as they are described above in Section 2.3.1.1. The only difference being that now the hepatic and hepatic blood concentrations are taken to be spatially, rather than compartmentally, dependent (i.e., $[C_*] = [C_*](x, t)$). Further, rather than having compartment dependent zonation constants z_i , we will use the spatially dependent function z_x given by

$$z_x = \begin{cases} \tanh\left(\frac{[Ox y_{HB}] - 46.5}{12}\right), & \text{if } [Ox y_{HB}] > 46.5 \text{ mmHg}, \\ 2 \tanh\left(\frac{[Ox y_{HB}] - 46.5}{24}\right), & \text{if } [Ox y_{HB}] \leq 46.5 \text{ mmHg}, \end{cases} \quad (2.15)$$

Table 2.2 Transports between hepatocytes (H) and hepatic blood (HB) in AR and ADR systems.

Transport	Rate
Glycerol	$\mathcal{T}^{gly} = \frac{v^{gly}([gly_{HB}] - [gly_H])}{K_M^{gly} + [gly_{HB}] + [gly_H]}$
Triglyceride	$\mathcal{T}^{TG} = -\frac{v^{VLDL}[TG_H]}{K_M^{VLDL} + [TG_H]} + \frac{v^{TG}([TG_{HB}] - \frac{[TG_H]}{TG_{ref}})}{K_M^{TG} + [TG_{HB}] + \frac{[TG_H]}{TG_{ref}}}$
Fatty acid	$\mathcal{T}^{FA} = \frac{v^{FA}([FA_{HB}] - [FA_H])}{K_M^{FA} + [FA_{HB}] + [FA_H]}$
Glucose (GLUT2)	$\mathcal{T}^{gC} = \frac{v^{gCump}[gC_{HB}]}{K_M^{gCump} + [gC_{HB}]} + \frac{v^{gCdiff}([gC_{HB}] - [gC_H])}{K_M^{gCdiff} + [gC_{HB}] + [gC_H]}$
Lactate	$\mathcal{T}^{Lac} = \frac{v^{Lac}([Lac_{HB}] - [Lac_H])}{K_M^{Lac} + [Lac_{HB}] + [Lac_H]}$

for $[Ox y_{HB}] = [Ox y_{HB}](x, t)$. Then, for metabolic process M , the rate constant is now given as the spatially dependent function

$$v_x^M = (1 + z_x k_M) v_b^M, \quad (2.16)$$

where v_b^M is the base-value rate constant of the metabolic process M and k_M is as given above in Eq. 2.7. The rates of the metabolic processes used in this model are given in Appendix A, the rates of the transports are given in Table 2.2, and the hepatic equations for this version of the model are given in Appendix B.2.

2.3.2.2 Hepatic blood

In the compartments-in-series model, the hepatocytes around the sinusoid and the blood flowing through the sinusoid are partitioned into compartments depending upon where they lie on the sinusoid (see Fig. 2.3). In this view, one might think of the model as multiple two compartment models that are connected by the blood flow through the hepatic blood compartments. As shown above in Section 2.3.1.2, the blood flow is modeled through a basic rate-in minus rate-out term. That is, supposing we've partitioned the hepatic blood into n compartments, if $[C_{HB}]_i$ is the concentration of metabolite C in hepatic blood compartment i , then the equation for $[C_{HB}]_i$ is given by

$$\frac{d[C_{HB}]_i}{dt} = v_{bf}([C_{HB}]_{i-1} - [C_{HB}]_i) - \gamma_H \mathcal{T}_i^C,$$

for $i = 1, \dots, n$. Here, γ_H is the ratio of hepatic to hepatic blood volume and \mathcal{T}_i^C is the rate of transport of metabolite C between hepatic blood compartment i and hepatic compartment i . The rate of blood flow v_{bf} is given by

$$v_{bf} = Q_H n \quad (2.17)$$

per second, where $Q_H = 0.15$. Note then that we have

$$\frac{d[C_{HB}]_i}{dt} = \frac{Q_H}{1/n}([C_{HB}]_{i-1} - [C_{HB}]_i) - \gamma_H \mathcal{T}_i^C, \quad (2.18)$$

and observe that

$$\frac{\partial[C_{HB}]_i}{\partial x} \approx \frac{Q_H}{1/n}([C_{HB}]_{i-1} - [C_{HB}]_i), \quad (2.19)$$

for $i = 1, \dots, n$, is the first order upwind advection discretization on a uniform mesh. Thus, while the model in Section 2.3.1 can be considered a compartments-in-series model comprised solely of ODE's, one can also view it as an advection-reaction equation strongly coupled to mass-balance equations describing the concentrations of metabolites in the liver cells (see Figure 2.2). That is, we allow $[C_{HB}]$ and $[C_H]$ to be spatially dependent and write

$$\frac{\partial[C_{HB}]}{\partial t} = Q_H \frac{\partial[C_{HB}]}{\partial x} - \gamma_H \mathcal{T}^C([C_{HB}], [C_H]). \quad (2.20)$$

Note that Q_H is in units $\frac{1}{\text{second}}$. That is, this advection equation is dimensionless in the axial direction. This implies that we can assume our “sinusoid” length is $L_{sca} = 1$. These hepatic blood equations are given in Appendix B.2.

2.3.2.3 Systemic blood

The equations for concentrations in the systemic blood remain effectively the same with the only difference being how concentrations in the hepatic blood come into the equation. Since the concentrations in hepatic blood are now considered to be spatially, rather than compartmentally dependent, we replace the n^{th} compartment concentration with the concentration at the out-flow boundary of the hepatic blood. That is,

$$\frac{d[C_{SB}]}{dt} = \frac{Q_H}{\gamma_B}([C_{HB}](1, t) - [C_{SB}](t)) + \mathcal{S}, \quad (2.21)$$

where γ_B is the ratio between the volume of systemic blood to the volume of hepatic blood, and \mathcal{S} represents the metabolic processes included in the model from the rest of the body. The interpretation of the role these equations play in the system, however, does change. Since the hepatic blood equations are now given by a system of PDEs on a bounded domain, boundary conditions are required. The concentrations of metabolites in the systemic blood (found by solving the systemic blood equations) then actually become Dirichlet conditions on the in-flow boundary of the hepatic

blood. Thus, the dynamics of the concentration of metabolite C in the hepatic blood is given by

$$\frac{\partial [C_{HB}]}{\partial t} = Q_H \frac{\partial [C_{HB}]}{\partial x} - \gamma_H \mathcal{T}^C([C_{HB}], [C_H]), \quad 0 < x < 1, t > 0, \quad (2.22)$$

$$[C_{HB}](0, t) = [C_{SB}](t), \quad t > 0, \quad (2.23)$$

$$[C_{HB}](x, 0) = f_{HB}, \quad 0 < x < 1, \quad (2.24)$$

where f_{HB} represents the initial distribution of the concentration of metabolite C in the hepatic blood. In order to solve Eq. 2.21 for $[C_{SB}]$, we can assign the initial condition $[C_{SB}](0) = f_{SB}$. The systemic blood equations are given in Appendix B.2.

2.3.3 Advection-Reaction-Dispersion (ADR) Version

While advection-reaction equations such as those given above in Section 2.3.2 are good models for simple flows, the actual dynamics of blood flow through a capillary are much more complex than just a pure advective flow. Here, we include the effect of the dispersion that occurs due to the flow by modeling the blood flow using Taylor's axial dispersion model [74]. This model has been used previously for blood flow through the liver sinusoid in other works such as [46, 52]. Here, we add a dispersion term to the AR model of Section 2.3.2 in order to get an advection-dispersion-reaction (ADR) system in order to compare the two and thus *determine whether or not a dispersion term makes a significant difference for the model presented here (one of the goals of this work)*. Note that the hepatic and systemic blood equations for this system are the same as those for the AR system, thus we omit the description of them here.

The addition of a dispersion term, and thus the addition of a second spatial derivative, requires boundary conditions at both the periportal (in-flow boundary) and pericentral (out-flow boundary) ends of the sinusoid in order to remain well-posed (in contrast, the AR equation only requires boundary conditions at one end). To accommodate this, we assign homogeneous Neumann conditions at the pericentral end (out-flow boundary) to indicate that the concentration of the metabolite leaving the sinusoid is the same as the concentration entering the systemic blood. The concentration of metabolite C in the hepatic blood is now given by

$$\frac{\partial [C_{HB}]}{\partial t} = Q_H \frac{\partial [C_{HB}]}{\partial x} - D_C \frac{\partial^2 [C_{HB}]}{\partial x^2} - \gamma_H \mathcal{T}^C([C_{HB}], [C_H]), \quad 0 < x < 1, t > 0, \quad (2.25)$$

$$[C_{HB}](0, t) = [C_{SB}](t), \quad t > 0, \quad (2.26)$$

$$\frac{\partial [C_{HB}]}{\partial x}(1, t) = 0, \quad t > 0, \quad (2.27)$$

$$[C_{HB}](x, 0) = f_{HB}, \quad 0 < x < 1, \quad (2.28)$$

where D_C is the dispersion coefficient of metabolite C in blood and everything else is defined as in

Section 2.3.2 (including the equation for $[C_{SB}]$).

Determining the appropriate values for D_C is nontrivial due to the fact that Q_H is dimensionless in the axial direction. This implies that we need D_C to be dimensionless in the axial direction as well. The difficulty here is the requirement to keep things scaled appropriately with respect to the biology without knowing the scaling factor used to render the AR equations dimensionless. In order to determine an appropriate scaling factor, we must look more closely at the role of v_{bf} in the compartments-in-series model.

If n is the number of compartments the hepatic blood has been separated into, then

$$v_{bf} = \frac{\text{rate of blood flow in the liver}}{\text{volume of blood compartment}}. \quad (2.29)$$

In general, the rate of blood flow in the liver is given by the volume of blood in the liver divided by the time it takes the blood to go through the liver. Since the volume of a blood compartment should be the volume of blood in the liver divided by n (the number of compartments), we get that

$$v_{bf} = \frac{n}{\text{time it takes blood to go through the liver}}. \quad (2.30)$$

Thus, from (2.17), we have that, under this scaling, the time it takes blood to go through the liver is $\frac{1}{Q_H}$ seconds.

In order to have an unscaled advection equation, we would need to know the velocity of the blood in the liver. Let v be this velocity. Then

$$v = \frac{\text{distance traveled through liver}}{\text{time it takes blood to go through the liver}} = \frac{L}{1/Q_H} \quad (2.31)$$

or

$$v = Q_H L. \quad (2.32)$$

Now, while our model is of the liver microstructure (that is, of a liver sinusoid and the surrounding cells), the concentrations of metabolites our model gives is actually representative of the accumulation from all sinusoids in the liver. On the other hand, in [52], the authors model the production from a single sinusoid using Taylor's axial dispersion and using physical measurements for the length of the sinusoid, velocity of blood, etc. Assuming then that our model gives us the concentration from a single sinusoid times the number of sinusoids in the liver, one can obtain that we should have $v = v_{sin}$ and $D_C^s = D_C^{sin}$ where v_{sin} and D_C^{sin} are the velocity of blood and dispersion coefficient in a single sinusoid respectively and D_C^s is the unscaled dispersion coefficient for our model. In [52] $L_{sin} = 1\text{mm}$ is used as the length of the sinusoid and $\tau = 5.4$ seconds is assumed to

be the time it takes blood to get through a sinusoid. Thus, we can calculate

$$L = \frac{v}{Q_H} = \frac{L_{sin}}{Q_H \tau} = 1.23 \text{mm}. \quad (2.33)$$

Now that we have our scaling factor L , we can follow the process and use the values given in [52] to compute D_C^{\sin} and then divide by L^2 in order to obtain the scaled dispersion coefficient D_C that we will use in our simulations. That is, we use Renkin's equation [76]

$$D_C^i = 1.013 \times 10^{-4} \times (MW)^{-0.46} \frac{\text{cm}^2}{s} \quad (2.34)$$

to compute the diffusion coefficient D_C^i , where MW is the molecular weight of C . We then use Aris-Taylor's relation [74]

$$D_C^{\sin} = D_C^i + \frac{\left(\frac{v_{sin} d_s}{2}\right)^2}{48 D_C^i} \quad (2.35)$$

to calculate D_C^s (where d_s is the diameter of the sinusoid (given in [52])). Finally, we scale the dispersion coefficient to obtain

$$D_C = \frac{D_C^s}{L^2}. \quad (2.36)$$

2.4 Results

Discretization in space is carried out using a first-order upwind difference for the advection term and a second-order central difference for the dispersion term. The resulting ODE's are then solved using ode15s from the Matlab ODE suite.

2.4.1 Mesh Refinement

First, we look at how varying the mesh size $h = 1/n$ affects the numerical solutions of the AR version of the model (equivalently, seeing how varying the number of compartments n affects the compartments-in-series ODE model). Fig. 2.10 shows some of the metabolite levels at the time when the difference between the metabolite levels from the most coarse grid used ($n = 5$) and the most fine grid used ($n = 500$) is largest. While the change in the metabolite levels from varying n can be rather small in some cases (e.g. change in hepatic blood glucose levels only reaches 0.37–0.43% of the span of hepatic blood glucose levels), in other cases it is much larger as can be seen from Table 2.3 which gives the largest change seen in the metabolites due to varying n from 5 to 500 using 72 hour simulations. We note that since the span of the metabolite levels varies depending upon where the level is taken on the sinusoid, these changes were calculated separately for each spatial grid point on the coarse grid (in this case, $n = 5$) and the span given in Table 2.3 contains the largest

changes in the metabolite level at each coarse grid point.

Table 2.3 Change of metabolite levels in over x from refining the mesh from $n = 5$ to $n = 500$ (relative to overall range of metabolite level).

Variable	Largest change	Variable	Largest change	Variable	Largest change
gC_{HB}	0.37–0.43%	gC_H	1.01–2.73%	gdp	9.91–31.7%
TG_{HB}	0.91–0.92%	TG_H	2.91–61.5%	gtp	9.91–31.7%
FA_{HB}	6.94–7.00%	FA_H	8.07–28.5%	udp	3.87–10.9%
gly_{HB}	6.87–17.4%	gly_H	3.51–28.2%	utp	3.87–10.9%
Lac_{HB}	7.48–8.00%	Lac_H	7.12–17.1%	adp	15.4–54.7%
Oxy_{HB}	16.0–80.6%	G	4.57–42.2%	atp	11.1–26.2%
GL_{HB}	6.43–9.94%	$g6p$	3.47–36.9%	amp	10.5–26.1%
Ins_{HB}	5.87–14.9%	$g3p$	9.94–35.8%	P	8.57–61.4%
				$aCoA$	10.9–38.0%

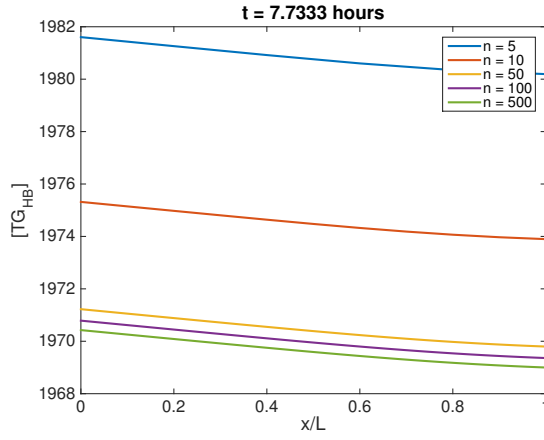
The differences seen due to the mesh size (or number of compartments) can be explained by the addition of numerical dispersion in the hepatic blood equations through the first-order upwind advection discretization. It can be shown that, while the first-order upwind scheme is first-order accurate to the advection equation

$$u_t + a u_x = 0, \quad (2.37)$$

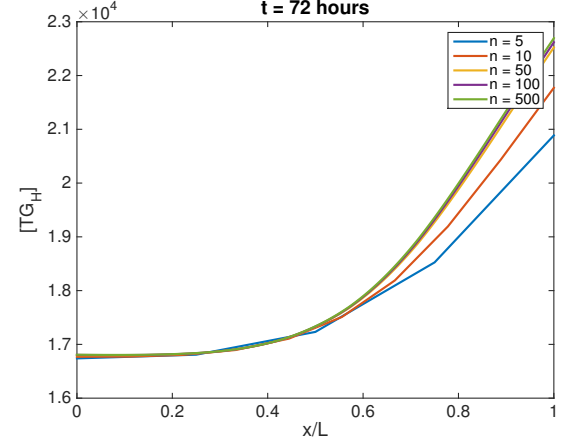
it is actually second-order accurate to the modified advection-dispersion equation

$$\tilde{u}_t + a \tilde{u}_x = \frac{1}{2} a h \tilde{u}_{xx}, \quad (2.38)$$

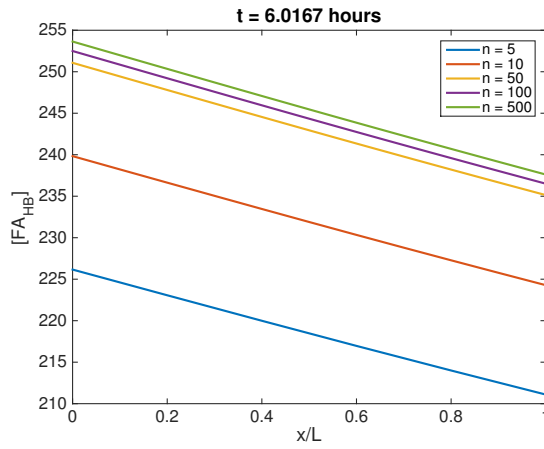
where a is the advection coefficient and h the mesh size [95]. Thus, the amount of numerical dispersion being introduced in the numerical solution is directly related to the mesh size (or number of compartments). We see further that the change in the hepatic blood metabolite levels also has a strong affect on the hepatic metabolite levels seen through the large changes seen in these levels (Table 2.3, two middle and two right columns). This is likely due to the strength of the coupling between these sets of equations. We also note that, regardless of the addition of numerical dispersion, it appears that if the mesh size h is not sufficiently small (or number of compartments n sufficiently large), then interesting spatial dynamics of the levels in the hepatocytes may be lost as can be seen by Fig. 2.10e and Fig. 2.10f.



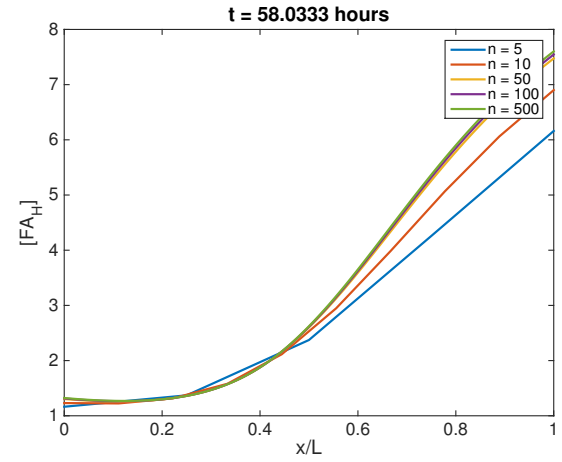
(a) Hepatic blood TG levels at 7.73 hours.



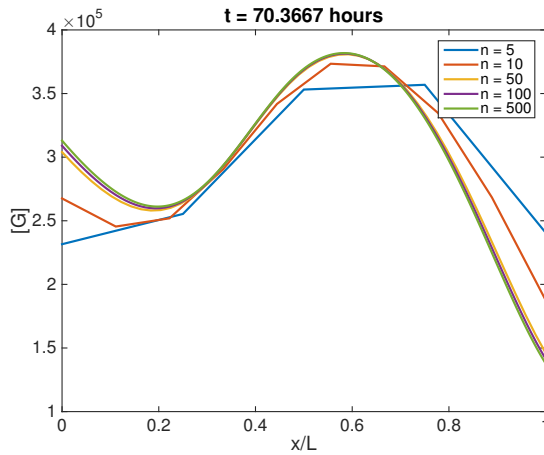
(b) Hepatic TG levels at 72 hours.



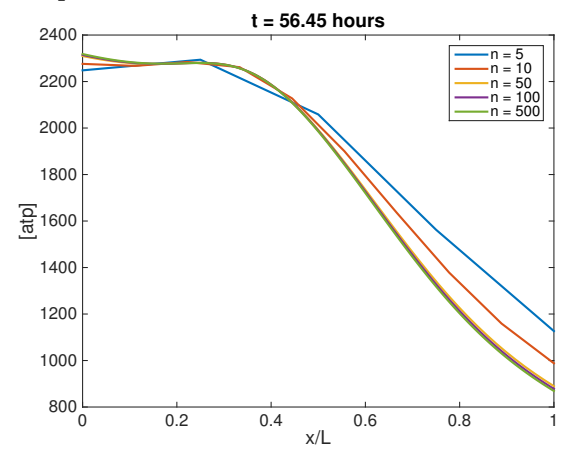
(c) Hepatic blood FA levels at 6.02 hours.



(d) Hepatic FA levels at 58.03 hours.



(e) Glycogen levels at 70.37 hours.



(f) Atp levels at 56.45 hours.

Figure 2.10 Metabolite levels for various mesh sizes across the sinusoid at time of largest difference between $h = 1/5$ and $h = 1/500$ (72 hour simulations).

2.4.2 Comparison of AR and ADR

We also want to investigate how the intentional inclusion of dispersion affects the system. That is, we wish to compare the AR simulation results with the ADR simulation results. In an attempt to limit the effect of numerical dispersion from the advection term while keeping computation time fairly short, we use $n = 50$ compartments (or a mesh size of $h = 1/50$). From Fig. 2.10 it appears that most of the metabolite levels start to converge around $n = 50$. Further, Table 2.4 shows that the changes in all metabolite levels between $n = 50$ and $n = 500$ is less than 10% of the span of the metabolite.

Table 2.4 Change of metabolite levels over x from refining the mesh from $n = 50$ to $n = 500$ (relative to overall range of metabolite level).

Variable	Largest change	Variable	Largest change	Variable	Largest change
gC_{HB}	0.0342–0.0386%	gC_H	0.052–0.38%	gdp	0.82–3.10%
TG_{HB}	0.0832–0.0835%	TG_H	0.21–5.88%	gtp	0.82–3.10%
FA_{HB}	0.65–0.66%	FA_H	0.58–2.76%	udp	0.18–1.16%
gly_{HB}	0.63–1.69%	gly_H	0.30–3.29%	utp	0.18–1.16%
Lac_{HB}	0.59–0.68%	Lac_H	0.62–1.74%	adp	1.42–4.39%
Ox_{yHB}	1.48–7.76%	G	0.065–4.21%	atp	0.69–2.42%
GL_{HB}	0.60–0.93%	$g6p$	0.32–7.11%	amp	0.70–2.41%
Ins_{HB}	0.53–1.37%	$g3p$	0.83–3.63%	P	0.70–5.81%
				$aCoA$	0.57–3.80%

Fig. 2.11 depicts the metabolite levels across the sinusoid at the time for which the solutions to the AR and ADR versions of the model have the largest difference for each particular metabolite (as measured by the discrete 2 norm). As can be seen from Fig. 2.11, there does not appear to be a significant difference between the solutions from the AR and ADR versions of the model. Further the differences are small in comparison to the span of the metabolite levels over time as can be seen from Table 2.5. This indicates that the addition of dispersion may not have a significant effect on the metabolite levels. However, we note that the presence of numerical dispersion could be muffling the effect of the actual dispersion. In fact, in these simulations the numerical dispersion is on the order of 10^{-3} while the actual dispersion is only on the order of 10^{-4} . Thus, though the actual dispersion does not have much of an effect in these numerical simulations, other discretizations could unveil the dispersion to have a larger effect than seen here.

Lastly, under this discretization, it appears that including the dispersion term increases computation time exponentially. Simulations were run using various mesh sizes (from $h = 1/5$ to $h = 1/50$) and computation times were recorded. Figure 2.12 illustrates the ADR computation times as a function of the AR computation times. The Matlab function `lsqcurvefit` was used to fit an exponential

Table 2.5 Change of metabolite levels over x between AR and ADR simulation (relative to overall range of AR simulation metabolite level).

Variable	Largest change	Variable	Largest change	Variable	Largest change
gC_{HB}	0.434–0.527%	gC_H	0.438–0.520%	gdp	0.279–1.557%
TG_{HB}	0.135–0.136%	TG_H	0.251–0.656%	gtp	0.279–1.557%
FA_{HB}	0.7698–0.723%	FA_H	0.360–0.976%	udp	1.27–1.49%
gly_{HB}	0.705–1.37%	gly_H	0.763–1.72%	utp	1.27–1.49%
Lac_{HB}	1.35–2.10%	Lac_H	1.10–1.90%	adp	0.325–1.52%
Ox_{HB}	0.505e-4–3.82e-4%	G	0.719–0.940%	atp	0.380–1.27%
GL_{HB}	0.258–0.493%	$g6p$	0.375–0.670%	amp	0.358–1.26%
Ins_{HB}	0.761–0.765%	$g3p$	0.535–1.63%	P	0.153–0.579%
				$aCoA$	0.338–0.979%

to this data and, at least empirically, appears to capture the trend quite well. The fit exponential is given by

$$t_{ADR} = 0.1720e^{0.3119t_{AR}} \quad (2.39)$$

where t_{ADR} and t_{AR} are computation times for the ADR and AR systems respectively.

2.5 Conclusions and Future Work

In this work, we investigated the effect the number of compartments used in a model of the liver microstructure similar to the one presented in [10, 11] has on the simulated concentrations as well as how including dispersion affects the system. The model of the liver microstructure from [10, 11] was adjusted in order to keep metabolic levels realistic when the system is not being driven by meal inputs. This adjustment included, most influentially, the addition of insulin dependent glucose uptake in the body excluding the liver, the rate of lipolysis in adipose tissue depending solely upon insulin action, and the representation of meal inputs as the solution to a two-compartment model of ingestion in the gut. We note that the compartment-in-series model presented in Section 2.3.1 is equivalent to the system presented in Section 2.3.2 when the hepatic blood equations have been spatially discretized using an upwind forward difference and a mesh size of $h = 1/n$ (corresponding to n compartments). The system presented in Section 2.3.2 uses advection-reaction equations to give the dynamics of concentrations in the hepatic blood, coupled to mass-balance equations that provide dynamics for the concentrations in the hepatic tissue presented. The in-flow boundary condition for the hepatic blood equations is given by the solution to an ODE that yields a basic representation of metabolism in the rest of the body which depends upon the out-flow concentrations, hence creating a feedback loop.

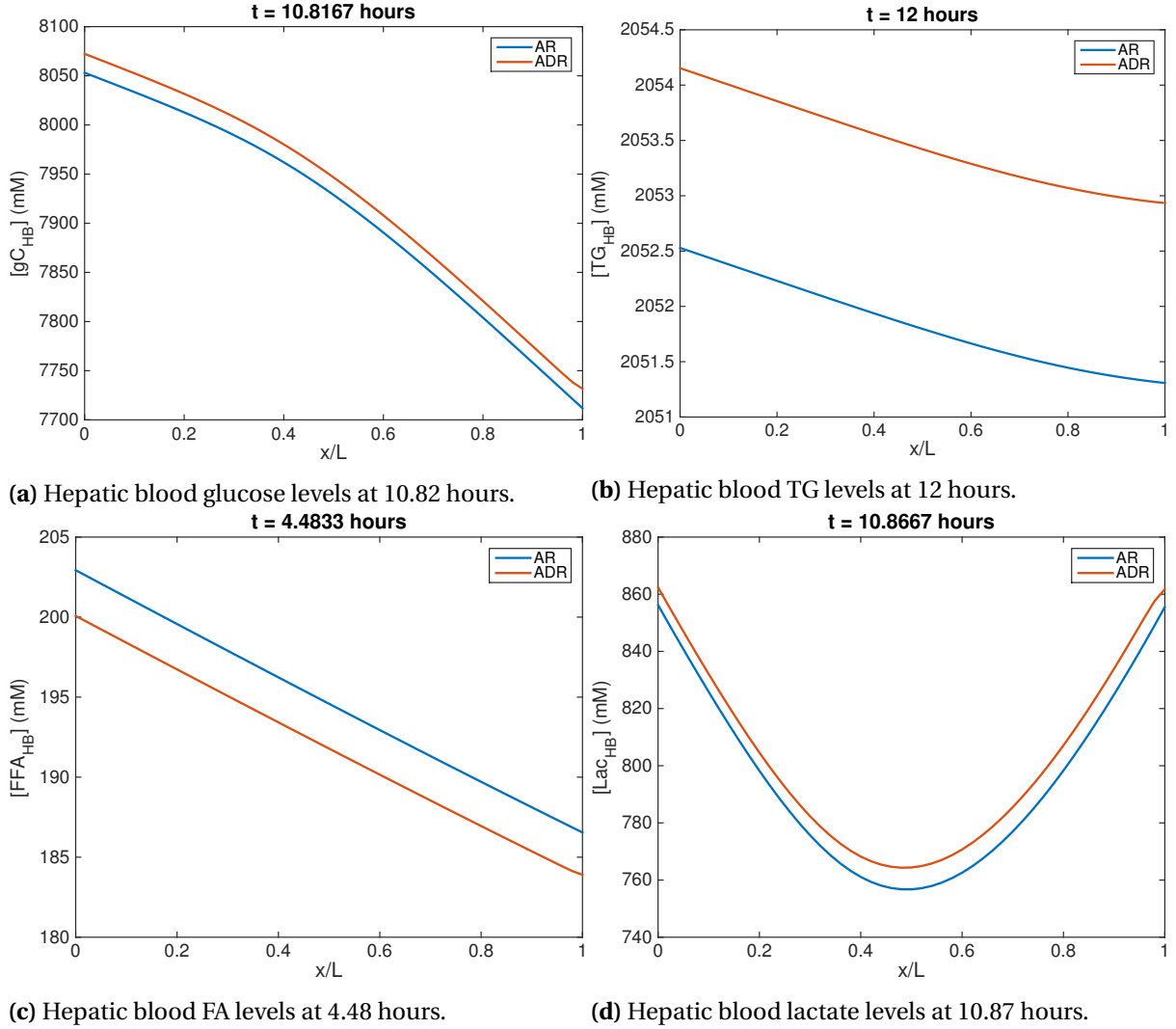


Figure 2.11 Metabolite levels for AR and ADR versions of the model across the sinusoid at time of largest difference (24 hour simulations).

Numerical simulations were carried out using the upwind forward difference discretization for the advection term in order to investigate how changing the number of compartments n affects the compartments-in-series model. We find that the value of n does have a large affect on the simulated concentrations, as can be seen from Table 2.3. One of the advantages of viewing this system as a PDE as opposed to a compartments-in-series ODE is the ability to analyze the numerical simulations in terms of spatial discretization. Indeed, by analyzing the modified equation (2.38) we see that numerical dispersion has been introduced into the solution, the amount of which has an inverse relationship with the number of compartments n . Interestingly, we find that the value of n has, in many cases, an even larger affect on the hepatic concentrations than on the hepatic blood

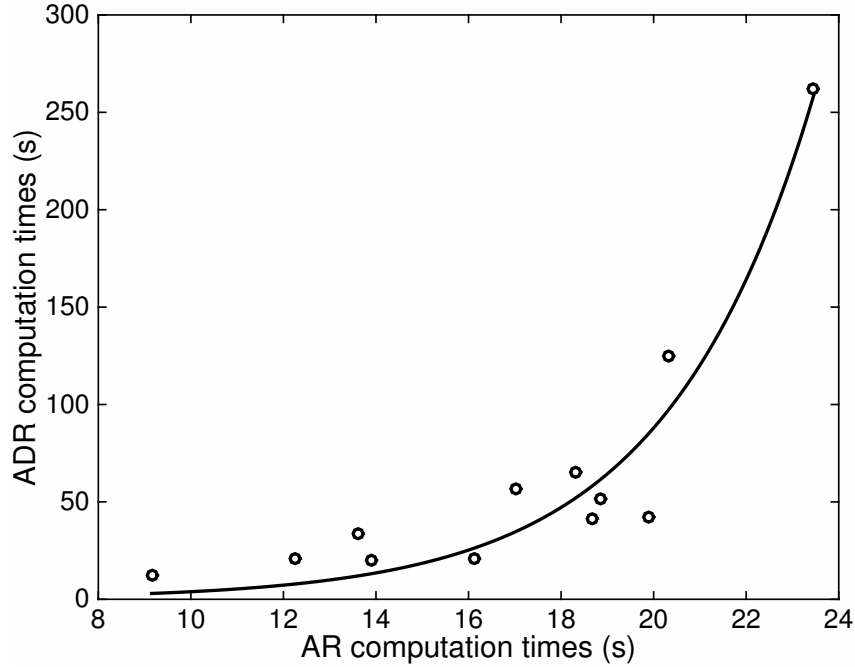


Figure 2.12 Computational times of ADR against AR with exponential fit.

concentrations. This seems counter intuitive as there is no spatial discretization in the equations for hepatic concentrations, thus no numerical dispersion is directly introduced to these concentrations. Thus, the numerical dispersion can only affect these concentrations indirectly through the coupling of the hepatic blood to the hepatic equations. This, then, is a testament to the strength of the coupling in the system, both between hepatic and hepatic blood variables as well as between the hepatic variables themselves since not all hepatic equations are directly coupled to a hepatic blood equation.

We also address how intentionally included dispersion affects the system. This is of interest because it is biologically more accurate and has been included in other models of the liver microstructure. Most notably, Berndt et al. [34] include a dispersive effect in the blood flow of their compartments-in-series model. When looked at closely, one sees that this dispersion is in fact modeled through a second-order central finite difference discretization for a standard dispersion term (that is, a discretization for $\frac{\partial^2}{\partial x^2}$). We use the same discretization in our simulations here and find that the inclusion of dispersion does not appear to have a significant affect on our system (see Table 2.5). Further, the addition of dispersion appears to increase computation time exponentially. Thus, we conclude that for models discretized in this way, it is more efficient to use just the AR version over the ADR version. However, we note that the numerical dispersion is dominating the actual dispersion, and is thus likely muting the effect of the actual dispersion. If we consider the system as a PDE system, then we can utilize more accurate spatial discretizations in order to better

analyze the effect of dispersion. Advection-dispersion equations are known to be difficult to solve numerically and every discretization has its pros and cons [95]. However, because of this there is a wide breadth of research on how to solve these systems numerically, and as such there is an abundance of existing algorithms one could utilize. Unfortunately, the size of the system considered here along with the stiffness and strong coupling of the system make other discretizations difficult to implement and computationally costly. Because of this, we recommend testing other discretizations on a smaller system that has the same form as the one considered here. This preliminary study on a smaller system will lend valuable insights into what numerical scheme will be most effective for systems of this type.

In the past, arguments have been made for compartments-in-series models over PDE models for hepatic elimination often citing the mathematical simplicity of ODEs compared to PDEs [7, 82]. However, many of these compartments-in-series models are equivalent to a spatially discretized PDE, especially in how they've been used thus far to model liver metabolism. Thus, considering these models strictly as ODEs is potentially limiting the information and insights these systems may be able to give us. In particular, if our goal is to understand why and how certain spatially dependent processes occur, such as metabolic zonation and the phenomena of zoned steatosis in liver disease, then it makes sense to consider systems of PDEs which give us more options when it comes to discretizing spatially in numerical schemes. Further, PDEs lends themselves more appropriately in this problem to theoretical analyses that can unveil properties of the system such as the functional framework and stability. Compartments-in-series models are very useful computational tools and considering these systems from the perspective of a PDE does not diminish that. Rather, it provides more options and tools with which to analyze the system, both numerically and theoretically.

Future work for this problem then includes an in depth study of a “toy version” of the PDE systems where we limit the number of variables (and hence the size of the system) but maintain the nonlinearities, coupling, stiffness, and overall structure. A numerical analysis on this toy model including the investigation of numerous solution algorithms will inform future attempts to numerically analyze larger systems of this form. Theoretical analyses on the toy model can be done to investigate the functional framework needed in order to guarantee the existence and uniqueness of solutions. A stability analysis on the system would also be of interest to further elucidate the behavior of the system, especially pertaining to the effect of the feedback from the systemic blood equations. Lastly, checking the positivity of the system is an important step to verifying its biological relevance. This theoretical analysis could potentially be expanded and applied to larger systems at a later time as well.

BIBLIOGRAPHY

- [1] Abdelmalek, M.F., Diehl, A.M. (2007). Nonalcoholic fatty liver disease as a complication of insulin resistance. *Med. Clin. North Am.* 91(6): 1125–1149. doi: 10.1016/j.mcna.2007.06.001
- [2] Adams, L.A., Angulo, P., Lindor, K.D. (2005). Nonalcoholic fatty liver disease. *CMAJ* 172: 899–905. doi.org/10.1503/cmaj.045232
- [3] Agnifili, L., Mastropasqua, R., Frezzotti, P., Fasanella, V., Motolese, I., Pedrotti, E., Di Iorio, A., Mattei, P.A., Motolese, E., Mastropasqua, L. (2015). Circadian intraocular pressure patterns in healthy subjects, primary open angle and normal tension glaucoma patients with a contact lens sensor. *Acta. Ophthalmol.* 93: e14–e21. doi: 10.1111/aos.12408
- [4] Anderson, C.M., Stahl, A. (2013). SLC27 fatty acid transport proteins. *Mol. Aspects Med.* 34(2-3): 516–528. doi.org/10.1016/j.mam.2012.07.010
- [5] Anderson, W.K., Nielsen, E.J. (2001). Sensitivity analysis for Navier-Stokes equations on unstructured meshes using complex variables. *AIAA J.* 39(1): 56–63. doi.org/10.2514/2.1270
- [6] Anderson, W.K., Nielsen, E.J., Whitfield, D.L. (1998). *Multidisciplinary sensitivity derivatives using complex variables* (Technical Report MSSU-COE-ERC-98-08). Engineering Research Center Report, Mississippi State University, Starkville, MS.
- [7] Anissimov, Y.G., Roberts, M.S. (2002). A compartmental model of hepatic disposition kinetics: 1. Model development and application to linear kinetics. *J. Pharmacokinet. Pharmacodyn.* 29(2): 131–156. doi.org/10.1023/A:10197036
- [8] Arab, J.P., Arrese, M., Trauner, M. (2018). Recent insights into the pathogenesis of nonalcoholic fatty liver disease. *Annu. Rev. Pathol. Mech. Dis.* 13: 321–350. doi.org/10.1146/annurev-pathol-020117-043617
- [9] Araujo, R.P., McElwain, D.L.S. (2005). A mixture theory for the genesis of residual stresses in growing tissues I: a general formulation. *SIAM J. Appl. Math.* 65(4):1261–1284. doi.org/10.1137/040607113
- [10] Ashworth, W.B., Davis, N.A., Bogle, I.D.L. (2016). A computational model of hepatic energy metabolism: understanding zoned damage and steatosis in NAFLD. *PLoS Comput. Biol.* 12(9): e1005105. doi.org/10.1371/journal.pcbi.1005105
- [11] Ashworth, W.B., Perez-Galvan, C., Davies, N.A., Bogle, I.D.L. (2016). Liver function as an engineering system. *AIChE J.* 62(9): 3285–3297. doi.org/10.1002/aic.15292
- [12] Asrani, S., Zeimer, R., Wilensky, J., Gieser, D., Vitale, S., Lindenmuth, K. (2000). Large diurnal fluctuations in intraocular pressure are an independent risk factor in patients with glaucoma. *J. Glaucoma* 9(2): 134–142. doi.org/10.1097/00061198-200004000-00002
- [13] Baker-Schena, L., *Update on 24-hour IOP monitoring*, Eynet Magazine, Jan. 2017.

- [14] Banini, B.A., Sanyal, A.J. (2016). Nonalcoholic fatty liver disease: epidemiology, pathogenesis, natural history, diagnosis, and current treatment options. *Clin. Med. Insights Ther.* 8: 75–84. doi.org/10.4137/CMT.S18885
- [15] Banks, H.T., Baraldi, R., Cross, K., Flores, K., McChesney, C., Poag, L., Thorpe, E. (2015). Uncertainty quantification in modeling HIV viral mechanics. *Math. Biosci. Engr.* 12: 937–964. doi.org/10.3934/mbe.2015.12.937
- [16] Banks, H.T., Bekele-Maxwell, K., Bociu, L., Noorman, M., Guidoboni, G. (2017). Sensitivity analysis in poro-elastic and poro-visco-elastic models with respect to boundary data, *Quart. Apply. Math.* 75: 697–735. doi.org/10.1090/qam/1475
- [17] Banks, H.T., Bekele-Maxwell, K., Bociu, L., Noorman, M., Guidoboni, G. (2017). *Sensitivity analysis in poro-elastic and poro-visco-elastic models* (Technical Report CRSC-TR17-01). Center for Research in Scientific Computation, North Carolina State University, Raleigh, NC.
- [18] Banks, H.T., Bekele-Maxwell, K., Bociu, L., Noorman, M., Guidoboni, G. (2018). Local sensitivity via the complex-step derivative approximation for 1-D poro-elastic and poro-visco-elastic models, *Math. Control Relat. E*, accepted.
- [19] Banks, H.T., Bekele-Maxwell, K., Bociu, L., Noorman, M., Tillman, K. (2015). The complex-step method for sensitivity analysis of non-smooth problems arising in biology. *Eurasian J. Math. Comput. Appl.* 3: 15–68.
- [20] Banks, H.T., Bekele-Maxwell, K., Bociu, L., Wang, C. (2016). Sensitivity via the complex-step method for delay differential equations with non-smooth initial data. *Quart. Appl. Math.* doi: 10.1090/qam/1458
- [21] Banks, H.T., Cintron-Arias, A., Capaldi, A., Lloyd, A.L. (2009). A sensitivity matrix based methodology for inverse problem formulation. *J. Inverse and Ill-posed Problems* 17: 545–564.
- [22] Banks, H.T., Cintron-Arias, A., Kappel, F., (2013). Parameter selection methods in inverse problem formulation. In J.J. Batzel, M. Bachar, F. Kappel (Eds.), *Mathematical Modeling and Validation in Physiology: Application to the Cardiovascular and Respiratory Systems* (pp. 43–73). Berlin, Germany: Springer-Verlag.
- [23] Banks, H.T., Dediu, S., Ernstberger, S.E. (2006). Sensitivity functions and their uses in inverse problems. *J. Inverse Ill-pos. P* 15: 683–708. doi.org/10.1515/jiip.2007.038
- [24] Banks, H.T., Doumic, M., Kruse, C., Prigent, S., Rezaei, H., (2015). Information content in data sets for a nucleated-polymerization model. *J. Biol. Dyn.* doi.org/10.1080/17513758.2015.1050465
- [25] Banks, H.T., Hu, S., Thompson, W.C. (2014). *Modeling and Inverse Problems in the Presence of Uncertainty*. Boca Raton, FL: Chapman & Hall/CRC Press.
- [26] Banks, H.T., Rehm, K.L. (2014). Experimental design for vector output systems. *Inverse Probl. Sci. Eng.* 22: 557–590. doi.org/10.1080/17415977.2013.797973

- [27] Banks, H.T., Rhem, K.L. (2014). Parameter estimation in distributed systems: optimal design. *Eurasian J. Math. Comput. Appl.* 2: 70–79.
- [28] Banks, H.T., Tran, H.T. (2000). *Mathematical and Experimental Modeling of Physical and Biological Processes*. Boca Raton, FL: CRC Press.
- [29] Barkana, Y., Anis, S., Liebmann, J., Tello, C., Ritch, R. (2006). Clinical utility of intraocular pressure monitoring outside of normal office hours in patients with glaucoma. *Arch. Ophthalmol.* 124: 793–797. doi.org/10.1001/archophth.124.6.793
- [30] Baskaran, M., Raman, K., Ramani, K.K., Roy, J., Vijaya, L., Badrinath, S.S. (2006). Intraocular pressure changes and ocular biometry during Sirsasana (headstand posture) in yoga practitioners. *Ophthalmol.* 113(8): 1327–1332. doi: 10.1016/j.ophtha.2006.02.063
- [31] Bass, L., Keiding, S., Winkler, K., Tygstrup, N. (1976). Enzymatic elimination of substrates flowing through the intact liver. *J. Theor. Biol.* 61: 393–409. doi.org/10.1016/0022-5193(76)90026-6
- [32] Bass, L., Robinson, P., Bracken, A.J. (1978). Hepatic elimination of flowing substrates: the distributed model. *J. Theor. Biol.* 72: 161–184. doi.org/10.1016/0022-5193(78)90023-1
- [33] Behie, G.A., Settari, A., Walters, D.A. (2001). Use of coupled reservoir and geomechanical modeling for integrated reservoir analysis and management. *J. Can. Petrol. Technol.* 40(12). doi.org/10.2118/01-12-04
- [34] Berndt, N., Horger, M.S., Bulik, S., Holzhütter, H.-G. (2018). A multiscale modelling approach to assess the impact of metabolic zonation and microperfusion on the hepatic carbohydrate metabolism. *PLoS Comput. Biol.* 14(2): e1006005. doi.org/10.1371/journal.pcbi.1006005
- [35] Bhatia, S.N., Toner, M., Foy, B.D., Rotem, A., O’Neil, K.M., Tompkins, R.G., Yarmush, M.L. (1996). Zonal liver cell heterogeneity: effects of oxygen on metabolic functions of hepatocytes. *J. Cell. Eng.* 1: 125–135.
- [36] M.A. Biot, M.A. (1941). General theory of three-dimensional consolidation. *J. Appl. Phys.* 12(2): 155–164. doi.org/10.1063/1.1712886
- [37] Black, P.N., Ahowesso, C., Montefusco, D., Saini, N., DiRusso, C.C. (2016). Fatty acid transport proteins: targeting FATP2 as a gatekeeper involved in the transport of exogenous fatty acids. *Medchemcomm* 7(4): 612–622. doi.org/10.1039/C6MD00043F
- [38] Black, P.N., Sandoval, A., Arias-Barrau, E., DiRusso, C.C. (2009). Targeting the fatty acid transport proteins (FATP) to understand the mechanisms linking fatty acid transport to metabolism. *Immunol. Endocr. Metab. Agents Med. Chem.* 9(1): 11–17. doi.org/10.2174/187152209788009850
- [39] Bociu, L., Guidoboni, G., Sacco, R., Webster, J. (2016). Analysis of nonlinear poro-elastic and poro-viscoelastic models. *Arch. Ration. Mech. Anal.* 222: 1445–1519. doi.org/10.1007/s0020
- [40] Brody, S., Erb, C., Veit, R., Rau, H. (1999). Intraocular pressure changes: the influence of psychological stress and the Valsalva maneuver. *Biol. Psychol.* 51(1): 43–57. doi.org/10.1016/S0301-0511(99)00012-5

- [41] Bruno, M.S. (2002). Geomechanical analysis and decision analysis for mitigating compaction related casing damage. *SPE Drill. Completion* 17(3). doi.org/10.2118/79519-PA
- [42] Brunt, E.M. (2010). Pathology of nonalcoholic fatty liver disease. *Nat. Rev. Gastroenterol. Hepatol.* 7: 195–203. doi.org/10.1038/nrgastro.2010.21
- [43] Brunt, E.M. (2007). Pathology of fatty liver disease. *Mod. Pathol.* 20(1 Suppl): S40–S48. doi.org/10.1038/modpathol.3800680
- [44] Brunt, E.M., Janney, C.G., Di Bisceglie, A.M., Neuschwander-Tetri, B.A., Bacon, B.R. (1999). Nonalcoholic steatohepatitis: a proposal for grading and staging the histological lesions. *Am. J. Gastroenterol.* 94: 2467–2474. doi: 10.1111/j.1572-0241.1999.01377.x
- [45] Buqué, X., Cano, A., Miquilena-Colina, M.E., García-Monzón, C., Ochoa, B., Aspichueta, P. (2012). High insulin levels are required for FAT/CD36 plasma membrane translocation and enhanced fatty acid uptake in obese Zucker rat hepatocytes. *Am. J. Physiol. Endocrinol. Metab.* 303: E504–E514. doi.org/10.1152/ajpendo.00653.2011
- [46] Calvetti, D., Kuceyeski, A., Somersalo, E. (2008). Sampling-based analysis of a spatially distributed model for liver metabolism at steady state. *Multiscale Model. Simul.* 7(1): 407–431. doi.org/10.1137/070682824
- [47] Cao, Y., Chen, S., Meir, A.J. (2013). Analysis and numerical approximations of equations of nonlinear poroelasticity. *Discrete Cont. Dyn.-B* 18(5): 1253–1273. doi.org/10.3934/dcdsb.2013.18.1253
- [48] Cao, Y., Chen, S., Meir, A.J. (2014). Quasilinear Poroelasticity: Analysis and Hybrid Finite Element Approximation. *Num. Meth. PDE* doi: 10.1002/num.21940.
- [49] Cartee, G.D. (2015). Mechanisms for greater insulin-stimulated glucose uptake in normal and insulin-resistant skeletal muscle after acute exercise. *Am. J. Physiol. Endocrinol. Metab.* 309(12): E949–E959. doi.org/10.1152/ajpendo.00416.2015
- [50] Causin, P., Guidoboni, G., Harris, A., Prada, D., Sacco, R., Terragni, S. (2014). A poroelastic model for the perfusion of the lamina cribrosa in the optic nerve head. *Math. Biosci.* 257: 33–41. doi.org/10.1016/j.mbs.2014.08.002
- [51] Chalasani, N., Wilson, L., Kleiner, D.E., Cummings, O.W., Brunt, E.M., Ůnalp A (2008). Relationship of steatosis grade and zonal location to histological features of steatohepatitis in adult patients with non-alcoholic fatty liver disease. *J. Hepatol.* 48: 829–834. doi.org/10.1016/j.jhep.2008.01.016
- [52] Chalhoub, E., Xie, L., Balasubramanian, V., Kim, J., Belovich, J. (2007). A distributed model of carbohydrate transport and metabolism in the liver during rest and high-intensity exercise. *Ann. Biomed. Eng.* 35(3): 474–491. doi.org/10.1007/s10439-006-9217-2
- [53] Chapelle, D., Sainte-Marie, J., Gerbeau, J.-F., Vignon-Clementel, I. (2010). A poroelastic model valid in large strains with applications to perfusion in cardiac modeling. *Comput. Mech.* 46(1): 91–101. doi.org/10.1007/s00466-009-0452-x

- [54] Chrysostomou, V., Trounce, I.A., Crowston, J.G. (2010). Mechanisms of retinal ganglion cell injury in aging and glaucoma. *Ophthalmic. Res.* 44: 173–178. doi.org/10.1159/000316478
- [55] Colletti, M., Cicchini, C., Conigliaro, A., Santangelo, L., Alonzi, T., Pasquini, E., Tripodi, M., Amicone, L. (2009). Convergence of Wnt signaling on the HNF4 α -driven transcription in controlling liver zonation. *Gastroenterology* 137(2): 660–672. doi.org/10.1053/j.gastro.2009.05.038
- [56] Coppack, S.W., Fisher, R.M., Gibbons, G.F., Humphreys, S.M., McDonough, M.J., Potts, J.L., Frayn, K.N. (1990). Postprandial substrate deposition in human forearm and adipose tissues in vivo. *Clin. Sci. (Lond.)* 79(4): 339–348. doi.org/10.1042/cs0790339
- [57] Coussy, O. (2004). *Poromechanics*. Hoboken, NJ: John Wiley & Sons.
- [58] Cowin, S.C. (1999). Bone poroelasticity. *J. Biomech.* 32(3): 217–238. doi.org/10.1016/S0021-9290(98)00161-4
- [59] Daly, M.E., Vale, C., Walker, M., Littlefield, A., Alberti, K.G., Mathers, J.C. (1998). Acute effects of insulin sensitivity and diurnal metabolic profiles of a high-sucrose compared with a high-starch diet. *Am. J. Clin. Nutr.* 67(6): 1186–1196. doi.org/10.1093/ajcn/67.6.1186
- [60] Davidian, M., Giltinan, D.M. (1995). *Nonlinear Models for Repeated Measurement Data*. London, England: Chapman & Hall.
- [61] DeFronzo, R.A., Ferrannini, E. (1982). Influence of plasma glucose and insulin concentration on plasma glucose clearance in man. *Diabetes* 31(8): 683–688. doi.org/10.2337/diab.31.8.683
- [62] Detournay, E., Cheng, A.H.-D. (1988). Poroelastic response of a borehole in non-hydrostatic stress field. *Int. J. Rock Mech. Min. Sci.* 25: 171–182. doi.org/10.1016/0148-9062(88)92299-1
- [63] Deussen, A., Bassingthwaighe, J.B. (1996). Modeling [¹⁵O] oxygen tracer data for estimating oxygen consumption. *Am. J. Physiol.* 270(3 Pt 2): H1115–H1130. doi.org/10.1152/ajpheart.1996.270.3.H1115
- [64] Dimitriadis, G., Mitrou, P., Lambadiari, V., Boutati, E., Maratou, E., Koukkou, E., Tzanela, M., Thallasinos, N., Raptis, S.A. (2006). Glucose and lipid fluxes in the adipose tissue after meal ingestion in hyperthyroidism. *J. Clin. Endocrinol. Metab.* 91(3): 1112–1118. doi.org/10.1210/jc.2005-0960
- [65] DiSilvestro, M.R., Suh, J.-K.F. (2002). Biphasic poroviscoelastic characteristics of proteoglycan-depleted articular cartilage: simulation of degeneration, *Ann. Biomed. Eng.* 30: 792–800. https://doi.org/10.1114/1.1496088
- [66] Doege, H., Baillie, R.A., Ortegon, A.M., Tsang, B., Wu, Q., Punreddy, S., Hirsch, D., Watson, N., Gimeno, R., Stahl, A. (2006). Targeted deletion of FATP5 reveals multiple functions in liver metabolism: alterations in hepatic lipid homeostasis. *Gastroenterology* 130: 1245–1258. doi.org/10.1053/j.gastro.2006.02.006
- [67] Doege, H., Grimm, D., Falcon, A., Tsang, B., Storm, T.A., Xu, H., Ortegon, A.M., Kazantzis, M., Kay, M.A., Stahl, A. (2008). Silencing of hepatic fatty acid transporter protein 5 *in vivo* reverses diet-induced non-alcoholic fatty liver disease and improves hyperglycemia. *J. Biol. Chem.* 283(32): 22186–22192. doi.org/10.1074/jbc.M803510200

- [68] Downs, J.C., Suh, J.K., Thomas, K.A., Bellezza, A.J., Hart, R.T., Burgoyne, C.F. (2005). Viscoelastic material properties of the peripapillary sclera in normal and early-glaucoma monkey eyes. *Invest. Ophthalmol. Vis. Sci.* 46(2): 540–546. doi.org/10.1167/iovs.04-0114
- [69] Dusseault, M.B., Bruno, M.S., Barrera, J. (2001). Casing shear: Causes, cases, cures. *SPE Drill. Completion* 16(2). doi.org/10.2118/72060-PA
- [70] Elkington, A.R., Inman, C.B.E., Steart, P.V., Weller, R.O. (1990). The structure of the lamina cribrosa of the human eye: an immunocytochemical and electron microscopical study. *Eye* 4: 42–57. doi.org/10.1038/eye.1990.5
- [71] Erdogmus, B., Tamer, A., Buyukkaya, R., Yazici, B., Buyukkaya, A., Korkut, E., Alcelik, A., Korkmaz, U. (2008). Portal vein hemodynamics in patients with non-alcoholic fatty liver disease. *Tohoku J. Exp. Med.* 215(1): 89–93. doi.org/10.1620/tjem.215.89
- [72] Falcon, A., Doege, H., Fluitt, A., Tsang, B., Watson, N., Kay, M.A., Stahl, A. (2010). FATP2 is a hepatic fatty acid transporter and peroxisomal very long-chain acyl-CoA synthetase. *Am. J. Physiol. Endocrinol. Metab.* 299: E384–E393. doi.org/10.1152/ajpendo.00226.2010
- [73] Fogagnolo, P., Nicola, O., Ferreras, A., Rossetti, L. (2009). The circadian curve of intraocular pressure: can we estimate its characteristics during office hours? *IOVS* 50(5): 2209–2215. doi.org/10.1167/iovs.08-2889
- [74] Fogler, S. (2001). *Elements of Chemical Reaction Engineering*, 3rd ed. Upper Saddle River, NJ: Prentice Hall.
- [75] Forker, E.L., Luxon, B. (1978). Hepatic transport kinetics and plasma disappearance curves: distributed modeling vs. conventional approach. *Am. J. Physiol.* 235: E648–E660. doi.org/10.1152/ajpendo.1978.235.6.E648
- [76] Fournier, R.L. (1998). *Basic Transport Phenomena in Biomedical Engineering*. New York, NY: Taylor & Francis.
- [77] Frijns, A.J.H. (2000). A four-component mixture theory applied to cartilaginous tissues: Numerical modelling and experiments. PhD dissertation. Eindhoven University of Technology, Eindhoven, Netherlands.
- [78] Gallant, A.R. (1987). *Nonlinear Statistical Models*. Hoboken, NJ: John Wiley & Sons.
- [79] Garagash, D., Detournay, E. (1997). An analysis of the influence of the pressurization rate on the borehole breakdown pressure. *Int. J. Solids Struct.* 34(24): 3099–3118. doi.org/10.1016/S0020-7683(96)00174-6
- [80] Gebhardt, R. (1992). Metabolic zonation of the liver: regulation and implications for liver function. *Pharmacol. Ther.* 53(3): 275–354. doi.org/10.1016/0163-7258(92)90055-5
- [81] Gong, Z., Tas, E., Yakar, S., Muzumdar, R. (2017). Hepatic lipid metabolism and non-alcoholic fatty liver disease in aging. *Mol. Cell. Endocrinol.* 455: 115–130. doi.org/10.1016/j.mce.2016.12.022

- [82] Gray, M.R., Tam, Y.K. (1987). The series-compartment model for hepatic elimination. *Drug Metab. Dispos.* 15(1): 27–31.
- [83] Griffin, M., Premakumar, Y., Seifalian, A., Butler, P.E., Szarko, M. (2016). Biomechanical characterization of human soft tissues using indentation and tensile testing. *J. Vis. Exp.* 118. doi:10.3791/54872
- [84] Haas, J.T., Francque, S., Staels, B. (2016). Pathophysiology and mechanisms of nonalcoholic fatty liver disease. *Annu. Rev. Physiol.* 78: 181–205. doi.org/10.1146/annurev-physiol-021115-105331
- [85] Hames, K.C., Vella, A., Kemp, B.J., Jensen, M.D. (2014). Free fatty acid uptake in humans with CD36 deficiency. *Diabetes* 63(11): 3606–3614. doi.org/10.2337/db14-0369
- [86] Hara T, Hara T, Tsuru T (2006). Increase of peak intraocular pressure during sleep in reproduced diurnal changes by posture. *Arch. Ophthalmol.* 124: 165–168. doi.org/10.1001/archopht.124.2.165
- [87] Hardy, T., Oakley, F., Anstee, Q.M., Day, C.P. (2016). Nonalcoholic fatty liver disease: pathogenesis and disease spectrum. *Annu. Rev. Pathol. Mech. Dis.* 11: 451–496. doi.org/10.1146/annurev-pathol-012615-044224
- [88] Hetherington, J., Sumner, T., Seymour, R.M., Li, L., Rey, M.V., Yamaji, S., Saffrey, P., Margoninski, O., Bogle, I.D.L., Finkelstein, A., Warner, A. (2011). A composite computational model of liver glucose homeostasis. I. Building the composite model. *J. R. Soc. Interface* 9(69): 689–700. doi.org/10.1098/rsif.2011.0141
- [89] Hijmans, B.S., Grefhorst, A., Oosterveer, M.H., Groen, A.K. (2014). Zonation of glucose and fatty acid metabolism in the liver: mechanism and metabolic consequences. *Biochimie* 96: 121–129. doi.org/10.1016/j.biochi.2013.06.007
- [90] Hsu, C.T., Cheng, P. (1990). Thermal dispersion in a porous medium. *Int. J. Heat Mass Tran.* 33(8): 1587–1597. doi.org/10.1016/0017-9310(90)90015-M
- [91] Huang, W., Fan, Q., Wang, W., Zhou, M., Laties, A.M., Zhang, X. (2013). Collagen: a potential factor involved in the pathogenesis of glaucoma. *Med. Sci. Monit. Basic Res.* 19: 237–240. doi: 10.12659/MSMBR.889061
- [92] Hudson, J., Stephansson, O., Andersson, J., Tsang, C.-F., Ling, L. (2001). Coupled T-H-M issues related to radioactive waste repository design and performance. *Int. J. Rock Mech. Min. Sci.* 38: 143–161. doi.org/10.1016/S1365-1609(00)00070-8
- [93] Hughes, E., Spry, P., Diamond, J. (2003). 24-hour monitoring of intraocular pressure in glaucoma management: a retrospective review. *J. Glaucoma* 12(3): 232–236. doi.org/10.1016/j.ajo.2003.10.008
- [94] Hughes, T.J.R. (2000). *The Finite Element Method: Linear Static and Dynamic Finite Element Analysis*. Mineola, NY: Dover Publications, Inc.
- [95] Hundsdorfer, W., Verwer, J.G. (2003). *Numerical Solution of Time-Dependent Advection-Diffusion-Reaction Equations*. Berlin, Germany: Springer.

- [96] Huyghe, J.M., Arts, T., van Campen, D.H., Reneman, R.S. (1992). Porous medium finite element model of the beating left ventricle. *Am. J. Physiol.* 262: 1256–1267. doi.org/10.1152/ajpheart.1992.262.4.H1256
- [97] Jasien, J.V., Jonas, J.B., de Moraes, C.G., Ritch, R. (2015). Intraocular pressure rise in subjects with and without glaucoma during four common yoga positions. *PLoS ONE* 10(12): e0144505. doi: 10.1371/journal.pone.0144505
- [98] Jonas, J.B., Aung, T., Bourne, R.R., Bron, A.M., Ritch, R., Panda-Jonas, S. (2017). Glaucoma. *Lancet* 390: 2083–2093. doi.org/10.1016/S0140-6736(17)31469-1
- [99] Jonas, J.B., Berenshtein, E., Holbach, L. (2003). Anatomic relationship between lamina cribrosa, intraocular space, and cerebrospinal fluid space. *IOVS* 44(12): 5189–5195. doi.org/10.1167/iovs.03-0174
- [100] Jorge, J., Ramoa-Marques, R., Lourenco, A., Silva, S., Nascimento, S., Queirós, A., Gonzalez-Méijome, J.M. (2010). IOP variations in the sitting and supine positions. *J. Glaucoma* 19: 609–612. doi.org/10.1097/IJG.0b013e3181ca7ca5
- [101] Jungermann, K. (1987). Metabolic zonation of liver parenchyma: significance for the regulation of glycogen metabolism, gluconeogenesis, and glycolysis. *Diabetes Metab. Rev.* 3(1): 269–293. doi.org/10.1002/dmr.5610030112
- [102] Jungermann, K., Katz, N. (1982). Functional hepatocellular heterogeneity. *Hepatology* 2(3): 385–395. doi.org/10.1002/hep.1840020316
- [103] Jungermann, K., Katz, N. (1989). Functional specialization of different hepatocyte populations. *Physiol. Rev.* 69(3): 708–764. doi.org/10.1152/physrev.1989.69.3.708
- [104] Jungermann, K., Kietzmann, T. (2000). Oxygen: modulator of metabolic zonation and disease of the liver. *Hepatology* 31(2): 255–260. doi.org/10.1002/hep.510310201
- [105] Jungermann, K., Kietzmann, T. (1997). Role of oxygen in the zonation of carbohydrate metabolism and gene expression in liver. *Kidney Int.* 51(2): 402–412. doi.org/10.1038/ki.1997.53
- [106] Jungermann, K., Kietzmann, T. (1996). Zonation of parenchymal and nonparenchymal metabolism in liver. *Annu. Rev. Nutr.* 16: 179–203. doi.org/10.1146/annurev.nu.16.070196.001143
- [107] Jungermann, K., Sasse, D. (1978). Heterogeneity of liver parenchymal cells. *Trends Biochem. Sci.* 3(3): P198–P202. doi.org/10.1016/S0968-0004(78)91764-4
- [108] Katz, N.R. (1992). Metabolic heterogeneity of hepatocytes across the liver acinus. *J. Nutr.* 122(3 Suppl): 843–849. doi.org/10.1093/jn/122.suppl_3.843
- [109] Khayyeri, H., Gustafsson, A., Heuwerker, A., Matikainen, M.K., Julkunen, P., Eliasson, P., Aspenberg, P., Isaksson, H. (2015). A Fibre-Reinforced Poroviscoelastic Model Accurately Describes the Biomechanical Behaviour of the Rat Achilles Tendon. *PLoS One* 10(6): e0126869. doi: 10.1371/journal.pone.0126869

- [110] Kietzmann, T. (2017). Metabolic zonation of the liver: the oxygen gradient revisited. *Redox Biol.* 11: 622–630. doi.org/10.1016/j.redox.2017.01.012
- [111] Kietzmann, T., Dimova, E.Y., Flügel, D., Scharf, J.G. (2006). Oxygen: modulator of physiological and pathophysiological processes in the liver. *Z. Gastroenterol.* 44(1): 67–76. doi.org/10.1055/s-2005-858987
- [112] Kietzmann, T., Jungermann, K. (1997). Modulation by oxygen of zonal gene expression in liver studied in primary rat hepatocyte cultures. *Cell. Biol. Toxicol.* 13(4-5): 243–255. doi.org/10.1023/A:1007427206391
- [113] Kim, J.-M., Parizek, R. (1997). Numerical simulation of the Noordbergum effect resulting from groundwater pumping in a layered aquifer system. *J. Hydrology* 202: 231–243. doi.org/10.1016/S0022-1694(97)00067-X
- [114] King, A., Azuara-Blanco, A., Tuulonen, A. (2013). Glaucoma. *BMJ* 346: f3518. doi: 10.1136/bmj.f3518
- [115] Klisch, S.M. (1999). Internally constrained mixtures of elastic continua. *Math. Mech. Solids* 4: 481–498. doi.org/10.1177/108128659900400405
- [116] Konstas, A.G.P., Quaranta, L., Bozkurt, B., Katsanos, A., Garcia-Feijoo, J., Rossetti, L., Shaarawy, T., Pfeiffer, N., Miglior, S. (2016). 24-h efficacy of glaucoma treatment options. *Adv. Ther.* 33: 481–517. doi: 10.1007/s12325-016-0302-0
- [117] Lai, W.M., Hou, J.S., Mow, V.C. (1991). A triphasic theory for the swelling and deformation behaviors of articular cartilage. *J. Biomech. Eng.* 113: 245–258. doi.org/10.1115/1.2894880
- [118] Langford, T., *Northwest Houston sinking faster than coastal areas*, Reporter-News.com, Aug. 28, 1997.
- [119] Leidl, M.C., Choi, C.J., Syed, Z.A., Melki, S.A. (2014). Intraocular pressure fluctuation and glaucoma progression: what do we know? *Br. J. Ophthalmol.* 98(10): 1315–1319. doi: 10.1136/bjophthalmol-2013-303980
- [120] Lemon, G., King, J.R., Byrne, H.M., Jensen, O.E., Shakesheff, K.M. (2006). Mathematical modelling of engineered tissue growth using a multiphase porous flow mixture theory. *J. Math. Biol.* 52: 571–594. doi.org/10.1007/s00285-005-0363-1
- [121] Li, Y., Chow, C.C., Courville, A.B., Sumner, A.D., Periwal, V. (2016). Modeling glucose and free fatty acid kinetics in glucose and meal tolerance test. *Theor. Biol. Med. Model.* 13(8). doi.org/10.1186/s12976-016-0036-3
- [122] Liu, J.H., Zhang, X., Kripke, D.F., Weinreb, R.N. (2003). Twenty-four-hour intraocular pressure pattern associated with early glaucomatous changes. *Invest. Ophthalmol. Vis. Sci.* 44(4): 1586–1590. doi.org/10.1167/iovs.02-0666
- [123] Lubick, N., *Modeling complex, multiphase porous media systems*, SIAM News, April 3, 2002.

- [124] Lyness, J.N. (1967). Numerical algorithms based on the theory of complex variable. *Proc. ACM 22nd Nat. Conf.* 4: 125–133. doi.org/10.1145/800196.805983
- [125] Lyness, J.N., Moler, C.B. (1967). Numerical differentiation of analytic functions. *SIAM J. Numer. Anal.* 4: 202–210. doi.org/10.1137/0704019
- [126] Magalotti, D., Marchesini, G., Ramilli, S., Berzigotti, A., Bianchi, G., Zoli, M. (2004). Splanchnic haemodynamics in non-alcoholic fatty liver disease: effect of a dietary/pharmacological treatment: a pilot study. *Dig. Liver Dis.* 36(6): 406–411. doi.org/10.1016/j.dld.2004.01.023
- [127] Mak, A.F. (1986). The apparent viscoelastic behavior of articular cartilage - the contributions from the intrinsic matrix viscoelasticity and interstitial fluid flows. *J. Biomech. Eng.* 108: 123–130. <https://doi.org/10.1115/1.3138591>
- [128] Martins, J.R.R.A., Kroo, I.M., Alonso, J.J. (2000). An automated method for sensitivity analysis using complex variables. *AIAA Paper* 2000-0689. doi.org/10.2514/6.2000-689
- [129] Martins, J.R.R.A., Sturdza, P., Alonso, J.J. (2003). The complex-step derivative approximation. *ACM T. Math. Software* 29(3): 245–262. doi.org/10.1145/838250.838251
- [130] Mashek, D.G. (2013). Hepatic fatty acid trafficking: multiple forks in the road. *Adv. Nut.* 4(6): 697–710. doi.org/10.3945/an.113.004648
- [131] McMonnies, C.W. (2014). An examination of the hypothesis that intraocular pressure elevation episodes can have prognostic significance in glaucoma suspects. *J. Optom.* 8: 223–231. doi: 10.1016/j.optom.2014.07.008
- [132] McMonnies, C.W. (2014). The significance of intraocular pressure elevation during sleep-related postures. *Clin. Exp. Optom.* 97: 221–224. doi: 10.1111/cxo.12108
- [133] Miquilena-Colina, M.E., Lima-Cabello, E., Sánchez-Campos, S., García-Mediavilla, M.V., Fernández-Bermejo, M., Lozano-Rodríguez, T., Vargas-Castrillón, J., Buqué, X., Ochoa, B., Aspichueta, P., González-Gallego, J., García-Monzón, C. (2011). Hepatic fatty acid translocase CD36 upregulation is associated with insulin resistance, hyperinsulinaemia and increased steatosis in non-alcoholic steatohepatitis and chronic hepatitis C. *Gut* 60: 1394–1402. doi.org/10.1136/gut.2010.222844
- [134] Mitsuyoshi, H., Yasui, K., Harano, Y., Endo, M., Tsuji, K., Minami, M., Itoh, Y., Okanou, T., Yoshikawa, T. (2009). Analysis of hepatic genes involved in the metabolism of fatty acids and iron in nonalcoholic fatty liver disease. *Hepatol. Res.* 39: 366–373. doi.org/10.1111/j.1872-034X.2008.00464.x
- [135] Mohammadi, A., Ghasemi-rad, M., Zahedi, H., Toldi, G., Alinia, T. (2011). Effect of severity of steatosis as assessed ultrasonographically on hepatic vascular indices in non-alcoholic fatty liver disease. *Med. Ultrason.* 13(3): 200–206.
- [136] Morgan, W.H., Yu, D.Y., Alder, V.A., Cringle, S.J., Cooper, R.L., House, P.H., Constable, I.J. (1998). The correlation between cerebrospinal fluid pressure and retrolaminar tissue pressure. *Invest. Ophthalmol. Vis. Sci.* 39(8): 1419–1428.

- [137] Mosaed, S., Liu, J.H.K., Weinreb, R.N. (2005). Correlation between office and peak nocturnal intraocular pressures in healthy subjects and glaucoma patients. *Ophthalmol.* 139: 320–324. doi.org/10.1016/j.ajo.2004.09.062
- [138] Mow, V.C., Kuei, S.C., Lai, W.M., Armstrong, C.G. (1980). Biphasic creep and stress relaxation of articular cartilage in compression: theory and experiments. *J. Biomech. Eng.* 102: 73–84. doi.org/10.1115/1.3138202
- [139] Newberry, E.P., Xie, Y., Kennedy, S., Han, X., Buhman, K.K., Luo, J., Gross, R.W., Davidson, N.O. (2003). Decreased hepatic triglyceride accumulation and altered fatty acid uptake in mice with deletion of the liver fatty acid-binding protein gene. *J. Biol. Chem.* 278(51): 51664–51672. doi.org/10.1074/jbc.M309377200
- [140] Ohno, H., Naito, Y., Nakajima, H., Tomita, M. (2008). Construction of a biological tissue model based on a single-cell model: a computer simulation at metabolic heterogeneity in the liver lobule. *Artif. Life* 14(1): 3–28. doi.org/10.1162/artl.2008.14.1.3
- [141] Owczarek, S. (2010). A Galerkin method for Biot consolidation model. *Math. Mech. Solids* 15: 42–56. doi.org/10.1177/1081286508090966
- [142] Özkaya, N., Nordin, M., Goldsheyder, D., Leger, D. (2012). Mechanical Properties of Biological Tissues. In: *Fundamentals of Biomechanics* (pp. 221–236). New York, NY: Springer.
- [143] Pang, K.S., Weiss, M., Macheras, P. (2007). Advanced pharmacokinetic models based on organ clearance, circulatory, and fractal concepts. *AAPS J.* 9(2): E268–E283. doi.org/10.1208/aapsj0902030
- [144] Park, S., Kim, S.H.J., Ropella, G.E.P., Roberts, M.S., Hunt, C.A. (2010). Tracing multiscale mechanisms of drug disposition in normal and diseased livers. *J. Pharmacol. Exp. Ther.* 334(1): 124–136. doi.org/10.1124/jpet.110.168526
- [145] Periwal, V., Chow, C.C., Bergman, R.N., Rick, M., Vega, G.L., Sumner, A.E. (2008). Evaluation of quantitative models of the effect of insulin on lipolysis and glucose disposal. *Am. J. Physiol. Regul. Integr. Comp. Physiol.* 295(4): R1089–R1096. doi.org/10.1152/ajpregu.90426.2008
- [146] Phillips, P.J., Wheeler, M.F. (2007). A coupling of mixed and continuous Galerkin finite-element methods for poroelasticity I: the continuous in time case. *Comput. Geosci.* 11(2): 131–144. doi.org/10.1007/s10596-007-9045-y
- [147] Phillips, P.J., Wheeler, M.F. (2007). A coupling of mixed and continuous Galerkin finite-element methods for poroelasticity II: the continuous in time case. *Comput. Geosci.* 11(2): 145–158. doi.org/10.1007/s10596-007-9044-z
- [148] Phillips, P.J., Wheeler, M.F. (2008). A coupling of mixed and continuous Galerkin finite-element methods for poroelasticity. *Comput. Geosci.* 12(4): 417–435. doi.org/10.1007/s10596-008-9082-1
- [149] Prada, D., Harris, A., Guidoboni, G., Sieksy, B., Huang, A.M., Arciero, J. (2016). Autoregulation and neurovascular coupling in the optic nerve head. *Surv. Ophthalmol.* 61: 164–186. doi.org/10.1016/j.survophthal.2015.10.004

- [150] Preziosi, L., Tosin, A. (2009). Multiphase modelling of tumour growth and extracellular matrix interaction: mathematical tools and applications. *J. Math. Biol.* 58: 625–656. doi.org/0.1007/s00285-008-0218-7
- [151] Probst, I., Schwartz, P., Jungermann, K. (1982). Induction in primary culture of ‘gluconeogenic’ and ‘glycolytic’ hepatocytes resembling periportal and perivenous cells. *Eur. J. Biochem.* 126(2): 271–278. doi.org/10.1111/j.1432-1033.1982.tb06775.x
- [152] Quigley, H.A. (2011). Glaucoma. *Lancet* 377: 1367–1377. doi: 10.1016/S0140-6736(10)61423-7
- [153] Raghunathan, S., Evans, D., Sparks, J.L. (2010). Poroviscoelastic modeling of liver biomechanical response in unconfined compression. *Ann. Biomed. Eng.* 38(5): 1789–1800. doi: 10.1007/s10439-010-9957-x
- [154] Rajapakse, R. (1993). Stress analysis of borehole in poroelastic medium. *J. Eng. Mech.-ASCE* 119(6): 1205–1227. doi.org/10.1061/(ASCE)0733-9399(1993)119:6(1205)
- [155] Rajaraman, G., Roberts, M.S., Hung, D., Wang, G.Q., Burczynski, F.J. (2005). Membrane binding proteins are the major determinants for the hepatocellular transmembrane flux of long-chain fatty acids bound to albumin. *Pharm. Res.* 22(11): 1793–1804. doi.org/10.1007/s11095-005-7248-2
- [156] Rezaia, V., Coombe, D., Tuszynski, J.A. (2016). A physiologically-based flow network model for hepatic drug elimination III: 2D/3D DLA lobule models. *Theor. Biol. Med. Model.* 13(9). doi.org/10.1186/s12976-016-0034-5
- [157] Ricken, T., Dahmen, U., Dirsch, O. (2010). A biphasic model for sinusoidal liver perfusion remodeling after outflow obstruction. *Biomech. Model. Mechanobiol.* 9: 435–450. doi.org/10.1007/s10237-009-0186-x
- [158] Ricken, T., Werner, D., Holzhütter, H.G., König, M., Dahmen, U., Dirsch, O. (2015). Modeling function-perfusion behavior in liver lobules including tissue, blood, glucose, lactate and glycogen by use of a coupled two-scale PDE-ODE approach. *Biomech. Model. Mechanobiol.* 14: 515–536. doi.org/10.1007/s10237-014-0619-z
- [159] Ricken, T., Waschinsky, N., Werner, D. (2018). Simulation of steatosis zonation in liver lobule—a continuummechanical bi-scale, tri-phasic, multi-component approach. In Wriggers, P., Lenarz, T., (Eds.) *Lecture Notes in Applied and Computational Mechanics*, Vol. 84. Cham, Switzerland: Springer.
- [160] Roberts, M.S., Rowland, M. (1986). Correlation between in-vitro microsomal enzyme activity and whole organ hepatic elimination kinetics: analysis with a dispersion model. *J. Pharm. Pharmacol.* 38: 177–181. doi.org/10.1111/j.2042-7158.1986.tb04540.x
- [161] Roberts, M.S., Rowland, M. (1985). Hepatic elimination–dispersion model. *J. Pharm. Sci.* 74(5): 585–587. doi.org/10.1002/jps.2600740522
- [162] Roose, T., Netti, P.A., Munn, L., Boucher, Y., Jain, R. (2003). Solid stress generated by spheroid growth estimated using a linear poroelastic model. *Microvasc. Res.* 66: 204–212. doi.org/10.1016/S0026-2862(03)00057-8

- [163] Rutqvist, J., Tsang, C.-F. (2003). Analysis of thermal-hydrologic-mechanical behavior near an emplacement drift at Yucca mountain. *J. Contam. Hydrol.* 62-63: 637–652. doi.org/10.1016/S0169-7722(02)00184-5
- [164] Sawaguchi, S., Yue, B.Y.J.T., Fukuchi, T., Abe, H., Suda, K., Kaiya, T., Iwata, K. (1999). Collagen fibrillar network in the optic nerve head of normal monkey eyes and monkey eyes with laser-induced glaucoma - a scanning electron microscopic study. *Curr. Eye Res.* 18(2): 143–149. doi: 10.1076/ceyr.18.2.143.5385
- [165] Schleicher, J., Dahmen, U., Guthke, R., Schuster, S. (2017). Zonation of hepatic fat accumulation: insights from mathematical modelling of nutrient gradients and fatty acid uptake. *J. R. Soc. Interface* 14: 20170443. doi.org/10.1098/rsif.2017.0443
- [166] Seber, G.A.F., Wild, C.J. (2003). *Nonlinear Regression*. Hoboken, NJ: John Wiley & Sons.
- [167] Settari, A., Walters, D.A. (2001). Advances in coupled geomechanical and reservoir modeling with applications to reservoir compaction. *SPE J.* 6(3): doi.org/10.2118/74142-PA
- [168] Setton, L.A., Zhu, W., Mow, V.C. (1993). The biphasic poroviscoelastic behavior of articular cartilage: role of the surface zone in governing the compressive behavior. *J. Biomech.* 26: 581–592. https://doi.org/10.1016/0021-9290(93)90019-B
- [169] Sheikh-Bahaei, S., Maher, J.J., Hunt, C.A. (2010). Computational experiments reveal plausible mechanisms for changing patterns of hepatic zonation of xenobiotic clearance and hepatotoxicity. *J. Theor. Biol.* 265(4): 718–733. doi.org/10.1016/j.jtbi.2010.06.011
- [170] Shi, J., Kandror, K.V. (2008). Study of glucose uptake in adipose cells. *Methods Mol. Biol.* 456: 307–315. doi.org/10.1007/978-1-59745-245-8_23
- [171] Showalter, R.E. (2000). Diffusion in poro-elastic media. *JMAA* 251: 310–340. doi.org/10.1006/jmaa.2000.7048
- [172] Smillie, A., Sobey, I., Molnar, Z. (2005). A hydro-elastic model of hydrocephalus. *J. Fluid Mech.* 539: 417–443. doi.org/10.1017/S0022112005005707
- [173] Soltz, M.A., Ateshian, G.A. (1998). Experimental verification and theoretical prediction of cartilage interstitial fluid pressurization at an impermeable contact interface in confined compression, *J. Biomech.* 31: 927–934. doi.org/10.1016/S0021-9290(98)00105-5
- [174] Soresi, M., Giannitrapani, L., Noto, D., Terranova, A., Campagna, M.E., Cefalú, A.B., Giammanco, A., Montalto, G. (2015). Effects of steatosis on hepatic hemodynamics in patients with metabolic syndrome. *Ultrasound Med. Biol.* 41(6): 1545-1552. doi.org/10.1016/j.ultrasmedbio.2015.01.020
- [175] Squire, W., Trapp, G. (1998). Using complex variables to estimate derivatives of real functions. *SIAM Rev.* 40(1): 110–112. doi.org/10.1137/S003614459631241X
- [176] Su, N., Showalter, R.E. (2001). Partially saturated flow in a poroelastic medium. *Discrete Cont. Dyn.-B* 1: 403–420. 10.3934/dcdsb.2001.1.403

- [177] Suh, J.-K., Bai, S. (1998). Finite element formulation of biphasic poroviscoelastic model for articular cartilage. *J. Biomech. Eng.* 120: 195–201. <https://doi.org/10.1115/1.2798302>
- [178] Susanna Jr, R., De Moraes, C.G., Cioffi, G.A., Ritch, R. (2015). Why do people (still) go blind from glaucoma? *Trans. Vis. Sci. Tech.* 4(2). doi.org/10.1167/tvst.4.2.1
- [179] Swan, C.C., Lakes, R.S., Brand, R.A., Stewart, K.J. Micromechanically based poroelastic modeling of fluid flow in haversian bone. *J. Biomech. Eng.* 125(1): 25–37. doi.org/10.1115/1.1535191
- [180] Tengroth, B., Ammitzboll, T. (1984). Changes in the content and composition of collagen in the glaucomatous eye - basis for a new hypothesis for the genesis of chronic open angle glaucoma - a preliminary report. *Acta. Ophthalmol.* 62(6): 999–1008. doi.org/10.1111/j.1755-3768.1984.tb08452.x
- [181] Terzaghi, K. (1925). Principle of soil mechanics. *Eng. News Record, A Series of Articles*.
- [182] Thorburn, A.W., Gumbiner, B., Bulacan, F., Wallace, P., Henry, R.R. (1990). Intracellular glucose oxidation and glycogen synthase activity are reduced in non-insulin-dependent (type II) diabetes independent of impaired glucose uptake. *J. Clin. Invest.* 85(2): 522–529. doi.org/10.1172/JCI114468
- [183] Torre, C., Perret, C., Colnot, S. (2010). Molecular determinants of liver zonation. *Prog. Mol. Biol. Transl. Sci.* 97: 127–150. doi.org/10.1016/B978-0-12-385233-5.00005-2
- [184] van Ginneken, V., de Vries, E., Verheij, E., van der Greef, J. (2017). Potential biomarkers for “fatty liver” (hepatic steatosis) and hepatocellular carcinoma (HCC) and an explanation of their pathogenesis. *Gastroenterol. Liver Clin. Med.* 1(1): 001.
- [185] Vera, J., Jiménez, R., García, J.A., Cárdenas, D. (2016). Intraocular pressure is sensitive to cumulative and instantaneous mental workload. *Appl. Ergon.* 60: 313–319. [doi:10.1016/j.apergo.2016.12.011](https://doi.org/10.1016/j.apergo.2016.12.011)
- [186] Verri, M., Guidoboni, G., Bociu, L., Sacco, R. (2018). The role of structural viscoelasticity in deformable porous media with incompressible constituents: applications in biomechanics. *Math. Biosci. Eng.* 15: 933–959. doi.org/10.3934/mbe.2018042
- [187] Vieira, G.M., Oliveira, H.B., de Andrade, D.T., Bottaro, M., Ritch, R. (2006). Intraocular pressure variation during weight lifting. *Arch. Ophthalmol.* 124: 1251–1254. doi.org/10.1001/archophth.124.9.1251
- [188] Wang, H.F. (2000). *Theory of Linear Poroelasticity with Applications to Geomechanics and Hydrogeology*. Princeton, NJ: Princeton University Press.
- [189] Wang, Y., Dusseault, M. (2003). A coupled conductive-convective thermo-poroelastic solution and implications for wellbore stability. *J. Petrol. Sci. Eng.* 38: 187–198. [doi.org/10.1016/S0920-4105\(03\)00032-9](https://doi.org/10.1016/S0920-4105(03)00032-9)
- [190] Weinreb, R.N., Aung, T., Medeiros, F.A. (2014). The pathophysiology and treatment of glaucoma: a review. *JAMA* 311(18): 1901–1911. [doi:10.1001/jama.2014.3192](https://doi.org/10.1001/jama.2014.3192)

- [191] Wilson, W., van Donkelaar, C.C., van Rietbergen, B., Huiskes, R. (2005). A fibril-reinforced poroviscoelastic swelling model for articular cartilage. *J. Biomech.* 38(6): 1195–1204. doi: 10.1016/j.jbiomech.2004.07.003
- [192] Wölflle, D., Jungermann, K. (1985). Long-term effects of physiological oxygen concentrations on glycolysis and gluconeogenesis in hepatocyte cultures. *Eur. J. Biochem.* 151(2): 299–303. doi.org/10.1111/j.1432-1033.1985.tb09100.x
- [193] Wu, Q., Ortegon, A.M., Tsang, B., Doege, H., Feingold, K.R., Stahl, A. (2006). FATP1 is an insulin-sensitive fatty acid transporter involved in diet-induced obesity. *Mol. Cell. Biol.* 26(9): 3455–3467. doi.org/10.1128/MCB.26.9.3455-3467.2006
- [194] Yang, Z., Smolinski, P. (2006). Dynamic finite element modeling of poroviscoelastic soft tissue. *Comput. Methods Biomech. Biomed. Engin.* 9(1): 7–16. doi: 10.1080/10255840500529540
- [195] Yeh, M.M., Brunt, E.M. (2014). Pathological features of fatty liver disease. *Gastroenterology* 147: 754–764. doi.org/10.1053/j.gastro.2014.07.056
- [196] Zenisek, A. (1984). The existence and uniqueness theorem in Biot’s consolidation theory. *Appl. Math.* 29: 194–211.

APPENDICES

APPENDIX

A

RATES OF METABOLIC PROCESSES FOR LIVER MODELS

The rates of metabolic processes assume the forms given in [10] which uses Hill functions to represent each substrate and allosteric activator/inhibitor. The way in which hormonal regulation is modeled is dependent upon the strength and speed with which the hormone is known to act on the process. These regulations will be dependent upon the hepatic blood concentration of the hormone at the same point as the hepatocyte along the sinusoid. Zonation is included through rate constants for the metabolic processes. A complete description of how zonation is included in the models is given in Section 2.3.1.1.2 for the compartments-in-series model and in Section 2.3.2.1 for the PDE models. Fig. A.1 gives a schematic of a hepatic compartment from the compartments-in-series model. This schematic shows in detail the metabolic processes that occur in each hepatic compartment, including where these processes are upregulated due to zonation via the color of the arrows indicating the process. Though this schematic is specifically of a hepatic compartment in the compartments-in-series model, it illustrates the metabolic processes being simulated in the hepatic equations for both the compartments-in-series model and the PDE models.

Below, we give the hepatic metabolic processes included in the model along with the function for the rate of the process. For each process (excluding transports and inorganic phosphate control), we include a table indicating the number and type of molecules used and synthesized in the process, as well as which molecules act as allosteric activators or inhibitors. We also include in this table

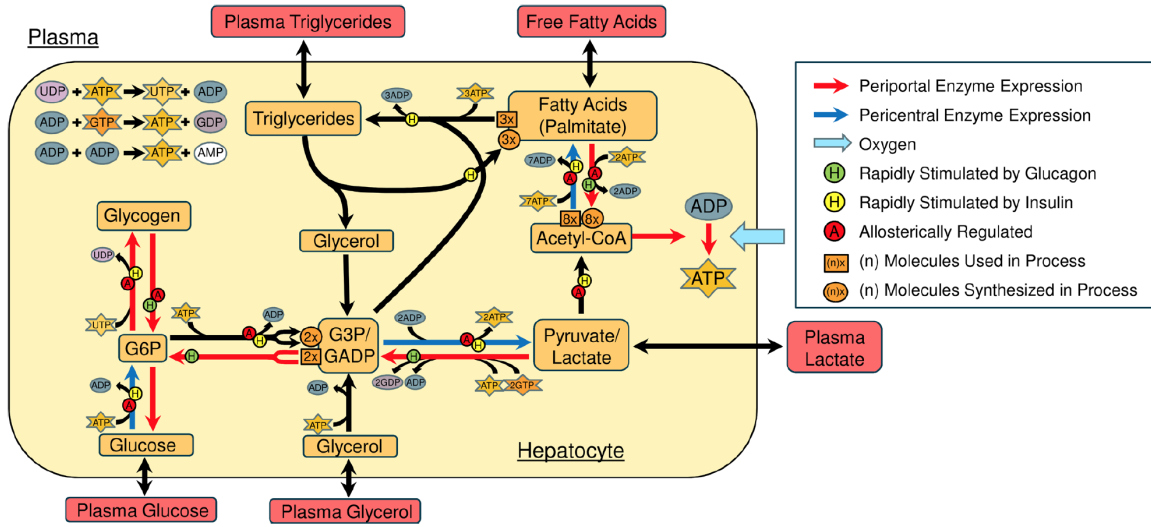


Figure A.1 Variables and conversions included in each hepatic compartment as depicted in [11].

whether any hormones stimulate or depress the process. We note that the supplementary material from [10] provides a thorough search of the literature for parameter values. Those values are utilized here unless otherwise specified.

A.1 Glucose Metabolism

Fig. A.2 gives a basic schematic of how glucose metabolism is simulated in the models.

- **GLUT2.** GLUT2 is a glucose transport that is described in Section 2.3.1.1.1 for the compartments-in-series model and in Table 2.2 for the PDE models. We take $v^{g_{diff}} = 500\mu\text{M}/s$ as opposed to $224\mu\text{M}/s$ which is reported in the supplementary material of [10]. Note that the value reported in the supplementary material of [10] was, according to the authors, found by fitting data of glucose levels to the system by eye.
- **Glucokinase (GK).** Converts glucose into glucose-6-phosphate using a phosphate from ATP. This enzyme is upregulated in pericentral cells. Table A.1 gives the roles of molecules in glucokinase.

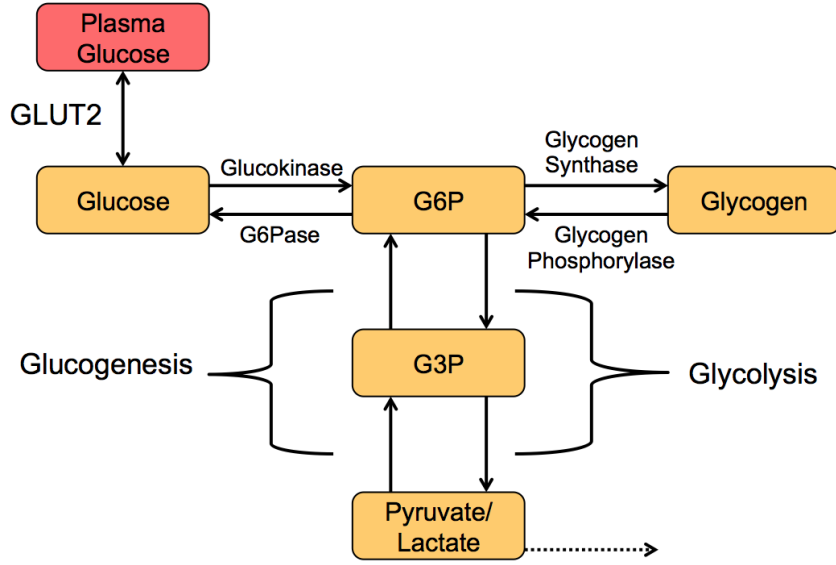


Figure A.2 Schematic of glucose metabolism.

Table A.1 Roles of molecules in Glucokinase (GK).

Molecules used in process	(#)	Molecules synthesized in process	(#)
Glucose (gC_H)	1	Glucose-6-phosphate ($g6p$)	1
Adenosine Tri-phosphate (atp)	1	Adenosine Di-phosphate (adp)	1
Inhibitors		Activators	
Glucose-6-phosphate ($g6p$)		Glucose (gC_H)	
Depressant		Stimulant	
N/A		N/A	

- Compartments-in-series model: for $i = 1, \dots, n$, the rate of glucokinase in hepatic compartment i is given by

$$\mathcal{R}_i^{GK} = v_i^{GK} \left(\frac{[gC_H]_i^{n_{GK}^{act}}}{(K_{GK}^{act})^{n_{GK}^{act}} + [gC_H]_i^{n_{GK}^{act}}} \right) \left(\frac{[gC_H]_i^{n_{GK}^{gC}}}{(K_{GK}^{gC})^{n_{GK}^{gC}} + [gC_H]_i^{n_{GK}^{gC}}} \right) \dots$$

$$\dots \left(\frac{[atp]_i}{K_{GK}^{atp} + [atp]_i} \right) \left(1 - \frac{[g6p]_i^{n_{GK}^{inh}}}{(K_{GK}^{inh})^{n_{GK}^{inh}} + [g6p]_i^{n_{GK}^{inh}}} \right). \quad (A.1)$$

- PDE models: the rate of glucokinase in the hepatocytes is given by

$$\mathcal{R}^{GK} = v_x^{GK} \left(\frac{[g C_H]^{n_{GK}^{act}}}{(K_{GK}^{act})^{n_{GK}^{act}} + [g C_H]^{n_{GK}^{act}}} \right) \left(\frac{[g C_H]^{n_{GK}^{gC}}}{(K_{GK}^{gC})^{n_{GK}^{gC}} + [g C_H]^{n_{GK}^{gC}}} \right) \dots \left(\frac{[atp]}{K_{GK}^{atp} + [atp]} \right) \left(1 - \frac{[g6p]^{n_{GK}^{inh}}}{(K_{GK}^{inh})^{n_{GK}^{inh}} + [g6p]^{n_{GK}^{inh}}} \right). \quad (A.2)$$

- **Glucose-6-phosphatase (G6Pase).** Glucose-6-phosphate is converted to glucose, releasing a phosphate. This enzyme is upregulated in the periportal cells. Table A.2 gives the roles of molecules in glucose-6-phosphatase.

Table A.2 Roles of molecules in Glucose-6-phosphatase (G6Pase).

Molecules used in process (#)	Molecules synthesized in process (#)
Glucose-6-Phosphate (g6p) 1	Glucose (g C _H) 1 Inorganic phosphate (P) 1
Inhibitors	Activators
none	none
Depressant	Stimulant
N/A	N/A

- Compartments-in-series model: for $i = 1, \dots, n$, the rate of glucose-6-phosphatase in hepatic compartment i is given by

$$\mathcal{R}_i^{G6Pase} = v_i^{G6Pase} \left(\frac{[g6p]_i}{K_{G6Pase}^{g6p} + [g6p]_i} \right). \quad (A.3)$$

- PDE models: the rate of glucose-6-phosphatase in the hepatocytes is given by

$$\mathcal{R}^{G6Pase} = v_x^{G6Pase} \left(\frac{[g6p]}{K_{G6Pase}^{g6p} + [g6p]} \right). \quad (A.4)$$

- **Glycogen Synthase (GS).** Glucose-6-phosphate extends a glycogen chain. This enzyme is upregulated in the periportal cells. Table A.3 gives the roles of molecules in glycogen synthase.

Table A.3 Roles of molecules in Glycogen Synthase (GS).

Molecules used in process	(#)	Molecules synthesized in process	(#)
Glucose-6-phosphate ($g6p$)	1	Glycogen (G)	1
Uridine Tri-phosphate (utp)	1	Uridine Di-phosphate (udp)	1
		Inorganic phosphate (P)	2
Inhibitors		Activators	
none		Glucose-6-phosphate ($g6p$)	
Depressant		Stimulant	
Glucagon (GL_{HB})		Insulin (Ins_{HB})	

- Compartments-in-series model: for $i = 1, \dots, n$, the rate of glycogen synthase in hepatic compartment i is given by

$$\mathcal{R}_i^{GS} = v_i^{GS} K_{max}^{GS} \left(\frac{[g6p]_i^{n_{GS}}}{(K_{GS}^{g6p})^{n_{GS}} + [g6p]_i^{n_{GS}}} \right) \left(\frac{[utp]_i}{K_{GS}^{utp} + [utp]_i} \right), \quad (A.5)$$

where hormonal regulation is given by

$$K_{max}^{GS} = \frac{v_i^{Ins}[Ins_{HB}]_i + K_I^{GS}}{v_i^{GL}[GL_{HB}]_i + K_G^{GS}}. \quad (A.6)$$

- PDE models: the rate of glycogen synthase in the hepatocytes is given by

$$\mathcal{R}^{GS} = v_x^{GS} K_{max}^{GS} \left(\frac{[g6p]^{n_{GS}}}{(K_{GS}^{g6p})^{n_{GS}} + [g6p]^{n_{GS}}} \right) \left(\frac{[utp]}{K_{GS}^{utp} + [utp]} \right), \quad (A.7)$$

where hormonal regulation is given by

$$K_{max}^{GS} = \frac{v_x^{Ins}[Ins_{HB}] + K_I^{GS}}{v_x^{GL}[GL_{HB}] + K_G^{GS}}. \quad (A.8)$$

- **Glycogen Phosphorylase (GP)**. Glycogen is depolymerised and converted to glucose-6-phosphate. Table A.4 gives the roles of molecules in glycogen synthase.

Table A.4 Roles of molecules in Glycogen Phosphorylase (GP).

Molecules used in process	(#)	Molecules synthesized in process	(#)
Glycogen (G)	1	Glucose-6-phosphate ($g6p$)	1
Inorganic phosphate (P)	1		
Inhibitors		Activators	
none		none	
Depressant		Stimulant	
Insulin (Ins_{HB})		Glucagon (GL_{HB})	

- Compartments-in-series model: for $i = 1, \dots, n$, the rate of glycogen phosphorylase in hepatic compartment i is given by

$$\mathcal{R}_i^{GP} = v^{GP} K_{max}^{GP} \left(\frac{[G]_i^{n_{GP}}}{(K_G^G)^{n_{GP}} + [G]_i^{n_{GP}}} \right) \left(\frac{[P]_i}{K_{GP}^P + [P]_i} \right), \quad (\text{A.9})$$

where hormonal regulation is given by

$$K_{max}^{GP} = \frac{v_i^{GL} [GL_{HB}]_i + K_G^{GP}}{v_i^{Ins} [Ins_{HB}]_i + K_I^{GP}}. \quad (\text{A.10})$$

- PDE models: the rate of glycogen phosphorylase in the hepatocytes is given by

$$\mathcal{R}^{GP} = v^{GP} K_{max}^{GP} \left(\frac{[G]^{n_{GP}}}{(K_G^G)^{n_{GP}} + [G]^{n_{GP}}} \right) \left(\frac{[P]}{K_{GP}^P + [P]} \right), \quad (\text{A.11})$$

where hormonal regulation is given by

$$K_{max}^{GP} = \frac{v_x^{GL} [GL_{HB}] + K_G^{GP}}{v_x^{Ins} [Ins_{HB}] + K_I^{GP}}. \quad (\text{A.12})$$

- **Glucogenesis part 1, phosphoenolpyruvate carboxykinase ($PEPCK$)**. Conversion of pyruvate (in the model, bunched together with lactate (Lac)) to glyceraldehyde-3-phosphate (in the model, bunched together with glycerol-3-phosphate ($g3p$)). This enzyme is upregulated in the periportal cells. Table A.5 gives the roles of molecules in glucogenesis part 1.

Table A.5 Roles of molecules in Glucogenesis part 1 (*PEPCK*).

Molecules used in process	(#)	Molecules synthesized in process	(#)
Lactate ($La c_H$)	1	Glycerol-3-phosphate ($g3p$)	1
Adenosine Tri-phosphate (atp)	2	Adenosine Di-phosphate (adp)	2
Guanosine Tri-phosphate (gtp)	1	Guanosine Di-phosphate (gdp)	1
		Inorganic phosphate (P)	2
Inhibitors		Activators	
none		none	
Depressant		Stimulant	
Insulin (Ins_{HB})		Glucagon (GL_{HB})	

- Compartments-in-series model: for $i = 1, \dots, n$, the rate of glucogenesis part 1 in hepatic compartment i is given by

$$\mathcal{R}_i^{PEPCK} = v_i^{PEPCK} K_{max}^{PEPCK} \left(\frac{[La c_H]_i}{K_{PEPCK}^{Lac} + [La c_H]_i} \right) \left(\frac{[atp]_i}{K_{PEPCK}^{atp} + [atp]_i} \right) \dots \left(\frac{[gtp]_i}{K_{PEPCK}^{gtp} + [gtp]_i} \right), \quad (A.13)$$

where hormonal regulation is given by

$$K_{max}^{PEPCK} = \frac{v_i^{GL}[GL_{HB}]_i + K_G^{PEPCK}}{v_i^{Ins}[Ins_{HB}]_i + K_I^{PEPCK}}. \quad (A.14)$$

- PDE models: the rate of glucogenesis part 1 in the hepatocytes is given by

$$\mathcal{R}_{PEPCK} = v_x^{PEPCK} K_{max}^{PEPCK} \left(\frac{[La c_{HB}]}{K_{PEPCK}^{Lac} + [La c_{HB}]} \right) \left(\frac{[atp]}{K_{PEPCK}^{atp} + [atp]} \right) \dots \left(\frac{[gtp]}{K_{PEPCK}^{gtp} + [gtp]} \right), \quad (A.15)$$

where hormonal regulation is given by

$$K_{max}^{PEPCK} = \frac{v_x^{GL}[GL_{HB}] + K_G^{PEPCK}}{v_x^{Ins}[Ins_{HB}] + K_I^{PEPCK}}. \quad (A.16)$$

- **Glucogenesis part 2, fructose biphosphatase (*FBP*)**. Conversion of 2 glyceraldehyde-3-phosphate

molecules to glucose-6-phosphate. This enzyme is upregulated in the periportal cells. Table A.6 gives the roles of molecules in glucogenesis part 2.

Table A.6 Roles of molecules in Glucogenesis part 2 (FBP).

Molecules used in process (#)	Molecules synthesized in process (#)
Glycerol-3-phosphate ($g3p$) 2	Glucose-6-phosphate ($g6p$) 1 Inorganic phosphate (P) 1
Inhibitors	Activators
none	none
Depressant	Stimulant
Insulin (Ins_{HB})	Glucagon (GL_{HB})

- Compartments-in-series model: for $i = 1, \dots, n$, the rate of glucogenesis part 2 in hepatic compartment i is given by

$$\mathcal{R}_i^{FBP} = v_i^{FBP} K_{max}^{FBP} \left(\frac{[g3p]_i}{K_{FBP}^{g3p} + [g3p]_i} \right), \quad (A.17)$$

where hormonal regulation is given by

$$K_{max}^{FBP} = \frac{v_i^{GL}[GL_{HB}]_i + K_G^{FBP}}{v_i^{Ins}[Ins_{HB}]_i + K_I^{FBP}}. \quad (A.18)$$

- PDE models: the rate of glucogenesis part 2 in the hepatocytes is given by

$$\mathcal{R}^{FBP} = v_x^{FBP} K_{max}^{FBP} \left(\frac{[g3p]}{K_{FBP}^{g3p} + [g3p]} \right), \quad (A.19)$$

where hormonal regulation is given by

$$K_{max}^{FBP} = \frac{v_x^{GL}[GL_{HB}] + K_G^{FBP}}{v_x^{Ins}[Ins_{HB}] + K_I^{FBP}}. \quad (A.20)$$

- **Glycolysis part 1, phosphofructokinase (PFK)**. Glucose-6-phosphate is broken down to two glyceraldehyde-3-phosphate molecules. Table A.7 gives the roles of molecules in glycolysis part 1.

Table A.7 Roles of molecules in Glycolysis part 1 (PFK).

Molecules used in process	(#)	Molecules synthesized in process	(#)
Glucose-6-phosphate ($g6p$)	1	Glycerol-3-phosphate ($g3p$)	2
Adenosine Tri-phosphate (atp)	1	Adenosine Di-phosphate (adp)	1
Inhibitors		Activators	
Adenosine Tri-phosphate (atp)		Adenosine Di-phosphate (adp)	
Glycerol-3-phosphate ($g3p$)			
Depressant		Stimulant	
Glucagon (GL_{HB})		Insulin (Ins_{HB})	

- Compartments-in-series model: for $i = 1, \dots, n$, the rate of glycolysis part 1 in hepatic compartment i is given by

$$\mathcal{R}_i^{PFK} = v^{PFK} K_{max}^{PFK} \left(\frac{[g6p]_i}{K_{PFK}^{g6p} + [g6p]_i} \right) \left(\frac{[atp]_i}{K_{PFK}^{atp} + [atp]_i} \right) \left(\frac{[adp]_i}{K_{PFK}^{adp} + [adp]_i} \right) \dots$$

$$\dots \left(1 - \beta_{PFK}^{atp} \frac{[atp]_i}{K_{PFK}^{inh1} + [atp]_i} \right) \left(1 - \beta_{PFK}^{g3p} \frac{[g3p]_i}{K_{PFK}^{inh2} + [g3p]_i} \right), \quad (A.21)$$

where hormonal regulation is given by

$$K_{max}^{PFK} = \frac{v_i^{Ins} [Ins_{HB}]_i + K_I^{PFK}}{v_i^{GL} [GL_{HB}]_i + K_G^{PFK}}. \quad (A.22)$$

- PDE models: the rate of glycolysis part 1 in the hepatocytes is given by

$$\mathcal{R}^{PFK} = v^{PFK} K_{max}^{FBP} \left(\frac{[g6p]}{K_{PFK}^{g6p} + [g6p]} \right) \left(\frac{[atp]}{K_{PFK}^{atp} + [atp]} \right) \left(\frac{[adp]}{K_{PFK}^{adp} + [adp]} \right) \dots$$

$$\dots \left(1 - \beta_{PFK}^{atp} \frac{[atp]}{K_{PFK}^{inh1} + [atp]} \right) \left(1 - \beta_{PFK}^{g3p} \frac{[g3p]}{K_{PFK}^{inh2} + [g3p]} \right), \quad (A.23)$$

where hormonal regulation is given by

$$K_{max}^{PFK} = \frac{v_x^{Ins} [Ins_{HB}] + K_I^{PFK}}{v_x^{GL} [GL_{HB}] + K_G^{PFK}}. \quad (A.24)$$

- **Glycolysis part 2, pyruvate kinase (PK).** Each glyceraldehyde-3-phosphate molecule is converted to pyruvate (and lactate). This enzyme is upregulated in the pericentral cells. Table A.8 gives the roles of molecules in glycolysis part 2.

Table A.8 Roles of molecules in Glycolysis part 2 (PK).

Molecules used in process	(#)	Molecules synthesized in process	(#)
Glycerol-3-phosphate ($g3p$)	1	Lactate ($La c_H$)	1
Adenosine Di-phosphate (adp)	3.25	Adenosine Tri-phosphate (atp)	3.25
Inorganic phosphate (P)	2.25		
Inhibitors		Activators	
Acetyl-CoA ($aCoA$)		none	
Depressant		Stimulant	
Glucagon (GL_{HB})		Insulin (Ins_{HB})	

- Compartments-in-series model: for $i = 1, \dots, n$, the rate of glycolysis part 2 in hepatic compartment i is given by

$$\mathcal{R}_i^{PK} = v_i^{PK} K_{max}^{PK} \left(\frac{[g3p]_i}{K_{PK}^{g3p} + [g3p]_i} \right) \left(\frac{[adp]_i}{K_{PK}^{adp} + [adp]_i} \right) \dots \left(1 - \beta_{aCoA} \frac{[aCoA]_i}{K_{PK}^{aCoA} + [aCoA]_i} \right), \quad (A.25)$$

where hormonal regulation is given by

$$K_{max}^{PK} = \frac{v_i^{Ins} [Ins_{HB}]_i + K_I^{PK}}{v_i^{GL} [GL_{HB}]_i + K_G^{PK}}. \quad (A.26)$$

- PDE models: the rate of glycolysis part 2 in the hepatocytes is given by

$$\mathcal{R}^{PK} = v_x^{PK} K_{max}^{PK} \left(\frac{[g3p]}{K_{PK}^{g3p} + [g3p]} \right) \left(\frac{[adp]}{K_{PK}^{adp} + [adp]} \right) \dots \left(1 - \beta_{PK}^{aCoA} \frac{[aCoA]}{K_{PK}^{aCoA} + [aCoA]} \right), \quad (A.27)$$

where hormonal regulation is given by

$$K_{max}^{PK} = \frac{v_x^{Ins} [Ins_{HB}] + K_I^{PK}}{v_x^{GL} [GL_{HB}] + K_G^{PK}}. \quad (A.28)$$

A.2 Lipid Metabolism

Fig. A.3 gives a basic schematic of how lipid metabolism is simulated in the models.

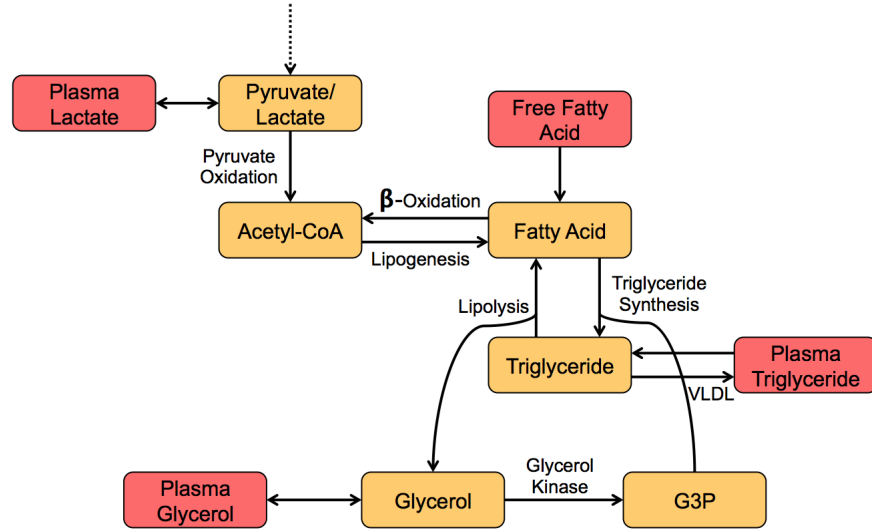


Figure A.3 Schematic of lipid metabolism.

- **Transports.** The lactate, glycerol, free fatty acid, and triglyceride transports are described in Section 2.3.1.1.1 for the compartments-in-series model and in Table 2.2 for the PDE models.
- **Pyruvate Oxidation (PDH).** The conversion of pyruvate to acetyl-CoA. Table A.9 gives the roles of molecules in pyruvate oxidation.

Table A.9 Roles of molecules in pyruvate oxidation (PDH).

Molecules used in process	(#)	Molecules synthesized in process	(#)
Lactate (La_{cH})	1	Acetyl-CoA ($aCoA$)	1
Adenosine Di-phosphate (adp)	2.5	Adenosine Tri-phosphate (atp)	2.5
Inorganic phosphate (P)	2.5		
Inhibitors		Activators	
Acetyl-CoA ($aCoA$)		none	
Depressant		Stimulant	
Glucagon (GL_{HB})		Insulin (In_{sHB})	

- Compartments-in-series model: for $i = 1, \dots, n$, the rate of pyruvate oxidation in hepatic

compartment i is given by

$$\mathcal{R}_i^{PDH} = v^{PDH} K_{max}^{PDH} \left(\frac{[Lac_H]_i}{K_{PDH}^{Lac} + [Lac_H]_i} \right) \left(1 - \frac{[aCoA]_i}{K_{PDH}^{aCoA} + [aCoA]_i} \right), \quad (A.29)$$

where hormonal regulation is given by

$$K_{max}^{PDH} = 1 + v_i^{Ins} \frac{[Ins_{HB}]_i}{Ins_{ref}^{PDH}} - v_i^{GL} \frac{[GL_{HB}]_i}{GL_{ref}^{PDH}}. \quad (A.30)$$

– PDE models: the rate of pyruvate oxidation in the hepatocytes is given by

$$\mathcal{R}^{PDH} = v^{PDH} K_{max}^{PDH} \left(\frac{[Lac_H]}{K_{PDH}^{Lac} + [Lac_H]} \right) \left(1 - \frac{[aCoA]}{K_{PDH}^{aCoA} + [aCoA]} \right), \quad (A.31)$$

where hormonal regulation is given by

$$K_{max}^{PDH} = 1 + v_x^{Ins} \frac{[Ins_{HB}]}{Ins_{ref}^{PDH}} - v_x^{GL} \frac{[GL_{HB}]}{GL_{ref}^{PDH}}. \quad (A.32)$$

- **β -Oxidation** (βoxi). Acetyl-CoA molecules are produced from the breakdown of fatty acids. The zonation of enzymes included in this process makes this process upregulated in the periportal cells. Table A.10 gives the roles of molecules in β -oxidation.

Table A.10 Roles of molecules in β -Oxidation (βoxi).

Molecules used in process	(#)	Molecules synthesized in process	(#)
Fatty acids (FA_H)	1	Acetyl-CoA ($aCoA$)	8
Adenosine Tri-phosphate (atp)	2	Adenosine Di-phosphate (adp)	1
		Adenosine Mono-phosphate (amp)	1
		Inorganic phosphate (P)	3
Inhibitors		Activators	
Acetyl-CoA ($aCoA$)		none	
Depressant		Stimulant	
Insulin (Ins_{HB})		Glucagon (GL_{HB})	

– Compartments-in-series model: for $i = 1, \dots, n$, the rate of β -oxidation in hepatic com-

partment i is given by

$$\mathcal{R}_i^{\beta oxi} = v_i^{\beta oxi} K_{max}^{\beta oxi} \left(\frac{[FA_H]_i}{K_{\beta oxi}^{FA} + [FA_H]_i} \right) \left(\frac{[atp]_i}{K_{\beta oxi}^{atp} + [atp]_i} \right) \dots \left(1 - \beta_{\beta oxi}^{aCoA} \frac{[aCoA]_i}{K_{\beta oxi}^{aCoA} + [aCoA]_i} \right), \quad (A.33)$$

where hormonal regulation is given by

$$K_{max}^{\beta oxi} = 1 - v_i^{Ins} \frac{[Ins_{HB}]_i}{Ins_{ref}^{\beta oxi}} + v_i^{GL} \frac{[GL_{HB}]_i}{GL_{ref}^{\beta oxi}}. \quad (A.34)$$

– PDE models: the rate of β -oxidation in the hepatocytes is given by

$$\mathcal{R}^{\beta oxi} = v_x^{\beta oxi} K_{max}^{\beta oxi} \left(\frac{[FA_H]}{K_{\beta oxi}^{FA} + [FA_H]} \right) \left(\frac{[atp]}{K_{\beta oxi}^{atp} + [atp]} \right) \dots \left(1 - \beta_{\beta oxi}^{aCoA} \frac{[aCoA]}{K_{\beta oxi}^{aCoA} + [aCoA]} \right), \quad (A.35)$$

where hormonal regulation is given by

$$K_{max}^{\beta oxi} = 1 - v_x^{Ins} \frac{[Ins_{HB}]}{Ins_{ref}^{\beta oxi}} + v_x^{GL} \frac{[GL_{HB}]}{GL_{ref}^{\beta oxi}}. \quad (A.36)$$

- **Lipogenesis** ($Lgen$). Acetyl-CoA molecules are converted to malonyl-CoA which, under fatty acid synthase, form a fatty acid chain. The zonation of enzymes included in this process makes this process upregulated in the pericentral cells. Table A.11 gives the roles of molecules in Lipogenesis.

Table A.11 Roles of molecules in Lipogenesis (L_{gen}).

Molecules used in process	(#)	Molecules synthesized in process	(#)
Acetyl-CoA ($aCoA$)	8	Free fatty acids (FA_H)	1
Adenosine Tri-phosphate (atp)	7	Adenosine Di-phosphate (adp)	7
		Inorganic phosphate (P)	7
Inhibitors		Activators	
Fatty acids (FA_H)		none	
Depressant		Stimulant	
Glucagon (GL_{HB})		Insulin (Ins_{HB})	

- Compartments-in-series model: for $i = 1, \dots, n$, the rate of lipogenesis in hepatic compartment i is given by

$$\mathcal{R}_i^{L_{gen}} = v_i^{L_{gen}} K_{max}^{L_{gen}} \left(\frac{[aCoA]_i}{K_{L_{gen}}^{aCoA} + [aCoA]_i} \right) \left(\frac{[atp]_i}{K_{L_{gen}}^{atp} + [atp]_i} \right) \dots \left(1 - \frac{[FA_H]_i}{K_{L_{gen}}^{FA} + [FA_H]_i} \right), \quad (A.37)$$

where hormonal regulation is given by

$$K_{max}^{L_{gen}} = 1 + v_i^{Ins} \frac{[Ins_{HB}]_i}{Ins_{ref}^{L_{gen}}} - v_i^{GL} \frac{[GL_{HB}]_i}{GL_{ref}^{L_{gen}}}. \quad (A.38)$$

- PDE models: the rate of lipogenesis in the hepatocytes is given by

$$\mathcal{R}^{L_{gen}} = v_x^{L_{gen}} K_{max}^{L_{gen}} \left(\frac{[aCoA]}{K_{L_{gen}}^{aCoA} + [aCoA]} \right) \left(\frac{[atp]}{K_{L_{gen}}^{atp} + [atp]} \right) \dots \left(1 - \frac{[FA_H]}{K_{L_{gen}}^{FA} + [FA_H]} \right), \quad (A.39)$$

where hormonal regulation is given by

$$K_{max}^{L_{gen}} = 1 + v_x^{Ins} \frac{[Ins_{HB}]}{Ins_{ref}^{L_{gen}}} - v_x^{GL} \frac{[GL_{HB}]}{GL_{ref}^{L_{gen}}}. \quad (A.40)$$

- **Lipolysis** (Lip). Triglycerides are broken down to three fatty acids and a glycerol molecule. Table A.12 gives the roles of molecules in Lipolysis.

Table A.12 Roles of molecules in Lipolysis (Lip).

Molecules used in process (#)	Molecules synthesized in process (#)
Triglycerides (TG_H) 1	Free fatty acids (FA_H) 3 Glycerol (gly_H) 1
Inhibitors	Activators
none	none
Depressant	Stimulant
Insulin (Ins_{HB})	Glucagon (GL_{HB})

- Compartments-in-series model: for $i = 1, \dots, n$, the rate of lipolysis in hepatic compartment i is given by

$$\mathcal{R}_i^{Lip} = v^{Lip} K_{max}^{Lip} \left(\frac{[TG_H]_i}{K_{Lip}^{TG} + [TG_H]_i} \right), \quad (A.41)$$

where hormonal regulation is given by

$$K_{max}^{Lip} = 1 - v_i^{Ins} \frac{[Ins_{HB}]_i}{Ins_{ref}^{Lip}} + v_i^{GL} \frac{[GL_{HB}]_i}{GL_{ref}^{Lip}}. \quad (A.42)$$

- PDE models: the rate of lipolysis in the hepatocytes is given by

$$\mathcal{R}^{Lip} = v^{Lip} K_{max}^{Lip} \left(\frac{[TG_H]}{K_{Lip}^{TG} + [TG_H]} \right), \quad (A.43)$$

where hormonal regulation is given by

$$K_{max}^{Lip} = 1 - v_x^{Ins} \frac{[Ins_{HB}]}{Ins_{ref}^{Lip}} + v_x^{GL} \frac{[GL_{HB}]}{GL_{ref}^{Lip}}. \quad (A.44)$$

- **Triglyceride Synthesis ($TSyn$)**. Fatty acids are joined with a coenzyme A (CoA) to form acyl-CoA and attach to a glycerol backbone derived from glycerol-3-phosphate to form triglycerides. Table A.13 gives the roles of molecules in triglyceride synthesis.

Table A.13 Roles of molecules in Triglyceride Synthesis ($TSyn$).

Molecules used in process	(#)	Molecules synthesized in process	(#)
Fatty acids (FA_H)	3	Triglycerides (TG_H)	1
Glycerol-3-phosphate ($g3p$)	1	Adenosine Mono-phosphate (amp)	3
Adenosine Tri-phosphate (atp)	3	Inorganic phosphate (P)	7
Inhibitors		Activators	
none		none	
Depressant		Stimulant	
Glucagon (GL_{HB})		Insulin (Ins_{HB})	

- Compartments-in-series model: for $i = 1, \dots, n$, the rate of triglyceride synthesis in hepatic compartment i is given by

$$\mathcal{R}_i^{TSyn} = v^{TSyn} K_{max}^{TSyn} \left(\frac{[FA_H]_i}{K_{TSyn}^{FA} + [FA_H]_i} \right) \left(\frac{[g3p]_i}{K_{TSyn}^{g3p} + [g3p]_i} \right), \quad (A.45)$$

where hormonal regulation is given by

$$K_{max}^{TSyn} = 1 + v_i^{Ins} \frac{[Ins_{HB}]_i}{Ins_{ref}^{TSyn}} - v_i^{GL} \frac{[GL_{HB}]_i}{GL_{ref}^{TSyn}}. \quad (A.46)$$

- PDE models: the rate of triglyceride synthesis in the hepatocytes is given by

$$\mathcal{R}^{TSyn} = v^{TSyn} K_{max}^{TSyn} \left(\frac{[FA_H]}{K_{TSyn}^{FA} + [FA_H]} \right) \left(\frac{[g3p]}{K_{TSyn}^{g3p} + [g3p]} \right), \quad (A.47)$$

where hormonal regulation is given by

$$K_{max}^{TSyn} = 1 + v_x^{Ins} \frac{[Ins_{HB}]}{Ins_{ref}^{TSyn}} - v_x^{GL} \frac{[GL_{HB}]}{GL_{ref}^{TSyn}}. \quad (A.48)$$

- **Glycerol Kinase ($Gl y K$)**. Glycerol is converted to glycerol-3-phosphate. Table A.14 gives the roles of molecules in glycerol kinase.

Table A.14 Roles of molecules in Glycerol Kinase ($GlyK$).

Molecules used in process	(#)	Molecules synthesized in process	(#)
Glycerol (gly_H)	1	Glycerol-3-phosphate ($g3p$)	1
Adenosine Tri-phosphate (atp)	1	Adenosine Di-phosphate (adp)	1
Inhibitors		Activators	
none		none	
Depressant		Stimulant	
N/A		N/A	

- Compartments-in-series model: for $i = 1, \dots, n$, the rate of glycerol kinase in hepatic compartment i is given by

$$\mathcal{R}_i^{GlyK} = v^{GlyK} \left(\frac{[gly_H]_i}{K_{GlyK}^{gly} + [gly_H]_i} \right) \left(\frac{[atp]_i}{K_{GlyK}^{atp} + [atp]_i} \right). \quad (A.49)$$

- PDE models: the rate of glycerol kinase in the hepatocytes is given by

$$\mathcal{R}^{GlyK} = v^{GlyK} \left(\frac{[gly_H]}{K_{GlyK}^{gly} + [gly_H]} \right) \left(\frac{[atp]}{K_{GlyK}^{atp} + [atp]} \right). \quad (A.50)$$

A.3 Energy Metabolism

- **Adenosine Tri-phosphate Synthesis (ATPS).** In the model, this synthesis of adenosine tri-phosphate takes the place of the citrate cycle and electron transport chain. For each acetyl-CoA molecule that enters the citrate cycle, 12 adenosine tri-phosphate molecules are produced from adenosine di-phosphate and inorganic phosphate. The zonation of enzymes included in this process makes this process upregulated in the periportal cells. Table A.15 gives the roles of molecules in adenosine tri-phosphate synthesis.

Table A.15 Roles of molecules in Adenosine Tri-phosphate Synthesis ($ATPS$).

Molecules used in process	(#)	Molecules synthesized in process	(#)
Acetyl-CoA ($aCoA$)	1	Adenosine Tri-phosphate (atp)	12
Adenosine Di-phosphate (adp)	12		
Inorganic phosphate (P)	12		
Inhibitors		Activators	
none		Oxygen (Oxy_{HB})	
Depressant		Stimulant	
N/A		N/A	

- Compartments-in-series model: for $i = 1, \dots, n$, the rate of adenosine tri-phosphate synthesis in hepatic compartment i is given by

$$\mathcal{R}_i^{ATPS} = v_i^{ATPS} \left(\frac{[aCoA]_i}{K_{ATPS}^{aCoA} + [aCoA]_i} \right) \left(\frac{[adp]_i}{K_{ATPS}^{adp} + [adp]_i} \right) \dots \left(\frac{[P]_i}{K_{ATPS}^P + [P]_i} \right) \left(\frac{[Oxy_{HB}]_i}{K_{ATPS}^{Oxy} + [Oxy_{HB}]_i} \right). \quad (A.51)$$

- PDE models: the rate of adenosine tri-phosphate synthesis in the hepatocytes is given by

$$\mathcal{R}^{ATPS} = v_x^{ATPS} \left(\frac{[aCoA]}{K_{ATPS}^{aCoA} + [aCoA]} \right) \left(\frac{[adp]}{K_{ATPS}^{adp} + [adp]} \right) \dots \left(\frac{[P]}{K_{ATPS}^P + [P]} \right) \left(\frac{[Oxy_{HB}]}{K_{ATPS}^{Oxy} + [Oxy_{HB}]} \right). \quad (A.52)$$

- **Nucleoside Diphosphate Kinases ($NDKU$ and $NDKG$).** Nucleoside diphosphate kinases mediate the exchange of phosphate groups between various nucleoside di- (and tri-) phosphates. Tables A.16 and A.17 gives the roles of molecules in the nucleoside diphosphate kinases.

Table A.16 Roles of molecules in Uridine Diphosphate Kinase (*NDKU*).

Molecules used in process	(#)	Molecules synthesized in process	(#)
Uridine Di-phosphate (<i>udp</i>)	1	Uridine Tri-phosphate (<i>utp</i>)	1
Adenosine Tri-phosphate (<i>atp</i>)	1	Adenosine Di-phosphate (<i>adp</i>)	1
Inhibitors		Activators	
none		none	
Depressant		Stimulant	
N/A		N/A	

Table A.17 Roles of molecules in Guanosine Diphosphate Kinase (*NDKG*).

Molecules used in process	(#)	Molecules synthesized in process	(#)
Guanosine Di-phosphate (<i>gdp</i>)	1	Guanosine Tri-phosphate (<i>gtp</i>)	1
Adenosine Tri-phosphate (<i>atp</i>)	1	Adenosine Di-phosphate (<i>adp</i>)	1
Inhibitors		Activators	
none		none	
Depressant		Stimulant	
N/A		N/A	

- Compartments-in-series model: for $i = 1, \dots, n$, the rate of nucleoside diphosphate kinases in hepatic compartment i are given by

$$\mathcal{R}_i^{NDKU} = v^{NDKU} \frac{[atp]_i [udp]_i}{(K_{NDKU}^{atp} + [atp]_i)(K_{NDKU}^{udp} + [udp]_i)} - v^{NDKU} \frac{[adp]_i [utp]_i}{(K_{NDKU}^{adp} + [adp]_i)(K_{NDKU}^{utp} + [utp]_i)}, \quad (\text{A.53})$$

$$\mathcal{R}_i^{NDKG} = v^{NDKG} \frac{[atp]_i [gdp]_i}{(K_{NDKG}^{atp} + [atp]_i)(K_{NDKG}^{gdp} + [gdp]_i)} - v^{NDKG} \frac{[adp]_i [gtp]_i}{(K_{NDKG}^{adp} + [adp]_i)(K_{NDKG}^{gtp} + [gtp]_i)}. \quad (\text{A.54})$$

- PDE models: the rate of nucleoside diphosphate kinases in the hepatocytes are given by

$$\mathcal{R}^{NDKU} = v^{NDKU} \frac{[atp][udp]}{(K_{NDKU}^{atp} + [atp])(K_{NDKU}^{udp} + [udp])} - v^{NDKU} \frac{[adp][utp]}{(K_{NDKU}^{adp} + [adp])(K_{NDKU}^{utp} + [utp])}, \quad (\text{A.55})$$

$$\mathcal{R}^{NDKG} = v^{NDKG} \frac{[atp][gdp]}{(K_{NDKG}^{atp} + [atp])(K_{NDKG}^{gdp} + [gdp])} - v^{NDKG} \frac{[adp][gtp]}{(K_{NDKG}^{adp} + [adp])(K_{NDKG}^{gtp} + [gtp])}. \quad (\text{A.56})$$

- **Adenosine Kinase (AK).** Adenosine kinase mediates the bi-directional transfer of a phosphate from adenosine tri-phosphate to adenosine mon-phosphate providing two adenosine di-phosphate molecules. Table A.18 gives the roles of molecules in adensoine kinase.

Table A.18 Roles of molecules in Adenosine Kinase (AK). Note: this is a bidirectional process.

Molecules used in process	(#)	Molecules synthesized in process	(#)
Adenosine Tri-phosphate (<i>atp</i>)	1	Adenosine Di-phosphate (<i>adp</i>)	2
Adenosine Mono-phosphate (<i>amp</i>)	1		
Inhibitors		Activators	
none		none	
Depressant		Stimulant	
N/A		N/A	

- Compartments-in-series model: for $i = 1, \dots, n$, the rate of adenosine kinase in hepatic compartment i is given by

$$\mathcal{R}_i^{AK} = v^{AK} \left(\frac{[atp]_i[amp]_i}{(K_{AK}^{atp} + [atp]_i)(K_{AK}^{amp} + [amp]_i)} - \frac{[adp]_i^2}{(K_{AK}^{adp})^2 + [adp]_i^2} \right). \quad (\text{A.57})$$

- PDE models: the rate of adenosine kinase in the hepatocytes is given by

$$\mathcal{R}^{AK} = v^{AK} \left(\frac{[atp][amp]}{(K_{AK}^{atp} + [atp])(K_{AK}^{amp} + [amp])} - \frac{[adp]^2}{(K_{AK}^{adp})^2 + [adp]^2} \right). \quad (\text{A.58})$$

- **Additional Adenosine Tri-phosphate Use ($ATPu$).** Adenosine Tri-phosphate is consumed by processes other than glucose and lipid metabolism in hepatocytes. In the model, a single equation allows for this clearance. Table A.19 gives the roles of molecules in additional adenosine triphosphate use.

Table A.19 Roles of molecules in Additional Adenosine Triphosphate Use ($ATPu$).

Molecules used in process	(#)	Molecules synthesized in process	(#)
Adenosine Tri-phosphate (atp)	1	Adenosine Di-phosphate (adp)	1
		Inorganic phosphate (P)	1
Inhibitors		Activators	
none		none	
Depressant		Stimulant	
N/A		N/A	

- Compartments-in-series model: for $i = 1, \dots, n$, the rate of this additional adenosine tri-phosphate use in hepatic compartment i is given by

$$\mathcal{R}_i^{ATPu} = v^{ATPu} \left(\frac{[atp]_i}{K_{ATPu}^{atp} + [atp]_i} \right). \quad (\text{A.59})$$

- PDE models: the rate of this additional adenosine tri-phosphate use in the hepatocytes is given by

$$\mathcal{R}^{ATPu} = v^{ATPu} \left(\frac{[atp]}{K_{ATPu}^{atp} + [atp]} \right). \quad (\text{A.60})$$

- **Control of Cellular Phosphate Levels ($PReg$).** This term was added to control the cytosolic phosphate concentration and is merely a clearance term for the inorganic phosphate equation.

- Compartments-in-series model: for $i = 1, \dots, n$, the rate of this control on cellular phosphate levels in hepatic compartment i is given by

$$\mathcal{R}_i^{PReg} = v^{PReg} ([P]_i - P_{ref}^{PReg}). \quad (\text{A.61})$$

- PDE models: the rate of this control on cellular phosphate levels in the hepatocytes is given by

$$\mathcal{R}^{PReg} = v^{PReg} ([P] - P_{ref}^{PReg}). \quad (\text{A.62})$$

APPENDIX

B

EQUATIONS FOR LIVER METABOLISM MODELS

B.1 Compartments-in-series model

The system of equations that defines the compartments-in-series model is given below. We note that this model is equivalent to the AR system after the advection term has been spatially discretized by the upwind forward difference with a mesh size of $1/n$. Appropriate initial conditions are assumed for all equations.

B.1.1 Hepatic equations

For $i = 1, \dots, n$, the hepatic compartment equations are given by

$$\frac{d[G]_i}{dt} = \mathcal{R}_i^{GS} - \mathcal{R}_i^{GP}, \quad (B.1)$$

$$\frac{d[g6p]_i}{dt} = \mathcal{R}_i^{GK} - \mathcal{R}_i^{G6Pase} - \mathcal{R}_i^{GS} + \mathcal{R}_i^{GP} + \frac{1}{2}\mathcal{R}_i^{FBP} - \mathcal{R}_i^{PFK}, \quad (B.2)$$

$$\frac{d[gC_H]_i}{dt} = -\mathcal{R}_i^{GK} + \mathcal{R}_i^{G6Pase} + \mathcal{T}_i^{gC}, \quad (B.3)$$

$$\frac{d[g3p]_i}{dt} = \mathcal{R}_i^{PEPCK} - \mathcal{R}_i^{FBP} + 2\mathcal{R}_i^{PFK} - \mathcal{R}_i^{PK} - \mathcal{R}_i^{TSyn} + \mathcal{R}_i^{GlyK}, \quad (B.4)$$

$$\frac{d[Lac_H]_i}{dt} = -\mathcal{R}_i^{PEPCK} + \mathcal{R}_i^{PK} - \mathcal{R}_i^{PDH} + \mathcal{T}_i^{Lac}, \quad (B.5)$$

$$\frac{d[aCoA]_i}{dt} = \mathcal{R}_i^{PDH} + 8\mathcal{R}_i^{\beta ox i} - \mathcal{R}_i^{Lgen} - \frac{1}{12}\mathcal{R}_i^{ATPS}, \quad (B.6)$$

$$\frac{d[FA_H]_i}{dt} = -\mathcal{R}_i^{\beta ox i} + \frac{1}{8}\mathcal{R}_i^{Lgen} + 3\mathcal{R}_i^{Lip} - 3\mathcal{R}_i^{TSyn} + \frac{1}{2}\mathcal{T}_i^{FA}, \quad (B.7)$$

$$\frac{d[TG_H]_i}{dt} = -\mathcal{R}_i^{Lip} + \mathcal{R}_i^{TSyn} + \mathcal{T}_i^{TG}, \quad (B.8)$$

$$\frac{d[gly_H]_i}{dt} = \mathcal{R}_i^{Lip} - \mathcal{R}_i^{GlyK} + \mathcal{T}_i^{gly}, \quad (B.9)$$

$$\frac{d[gt p]_i}{dt} = -\mathcal{R}_i^{PEPCK} + \mathcal{R}_i^{NDKG}, \quad (B.10)$$

$$\frac{d[gdp]_i}{dt} = \mathcal{R}_i^{PEPCK} - \mathcal{R}_i^{NDKG}, \quad (B.11)$$

$$\frac{d[ut p]_i}{dt} = -\mathcal{R}_i^{GS} + \mathcal{R}_i^{NDKU}, \quad (B.12)$$

$$\frac{d[udp]_i}{dt} = \mathcal{R}_i^{GS} - \mathcal{R}_i^{NDKU}, \quad (B.13)$$

$$\begin{aligned} \frac{d[P]_i}{dt} = & \mathcal{R}_i^{G6Pase} + 2\mathcal{R}_i^{GS} - \mathcal{R}_i^{GP} + 2\mathcal{R}_i^{PEPCK} + \frac{1}{2}\mathcal{R}_i^{FBP} - 2.25\mathcal{R}_i^{PK} - 2.5\mathcal{R}_i^{PDH} + \dots \\ & \dots + 3\mathcal{R}_i^{\beta ox i} + \frac{7}{8}\mathcal{R}_i^{Lgen} + 7\mathcal{R}_i^{TSyn} - \mathcal{R}_i^{ATPS} + \mathcal{R}_i^{ATPu} - \mathcal{R}_i^{PReg}, \end{aligned} \quad (B.14)$$

$$\begin{aligned} \frac{d[at p]_i}{dt} = & -\mathcal{R}_i^{GK} - 2\mathcal{R}_i^{PEPCK} - \mathcal{R}_i^{PFK} + 3.25\mathcal{R}_i^{PK} + 2.5\mathcal{R}_i^{PDH} - 2\mathcal{R}_i^{\beta ox i} - \frac{7}{8}\mathcal{R}_i^{Lgen} - \dots \\ & \dots - 3\mathcal{R}_i^{TSyn} - \mathcal{R}_i^{GlyK} + \mathcal{R}_i^{ATPS} - \mathcal{R}_i^{NDKU} - \mathcal{R}_i^{NDKG} - \mathcal{R}_i^{AK} - \mathcal{R}_i^{ATPu}, \end{aligned} \quad (B.15)$$

$$\begin{aligned} \frac{d[ad p]_i}{dt} = & \mathcal{R}_i^{GK} + 2\mathcal{R}_i^{PEPCK} + \mathcal{R}_i^{PFK} - 3.25\mathcal{R}_i^{PK} - 2.5\mathcal{R}_i^{PDH} + \mathcal{R}_i^{\beta ox i} + \frac{7}{8}\mathcal{R}_i^{Lgen} + \dots \\ & \dots + \mathcal{R}_i^{GlyK} - \mathcal{R}_i^{ATPS} + \mathcal{R}_i^{NDKU} + \mathcal{R}_i^{NDKG} + 2\mathcal{R}_i^{AK} + \mathcal{R}_i^{ATPu}, \end{aligned} \quad (B.16)$$

$$\frac{d[amp]_i}{dt} = \mathcal{R}_i^{\beta ox i} + 3\mathcal{R}_i^{TSyn} - \mathcal{R}_i^{AK}, \quad (B.17)$$

where the rates of all metabolic processes M , \mathcal{R}_i^M , are given in Appendix A, and the rate of transport for metabolite C , \mathcal{T}_i^C , is given in Section 2.3.1.1.1.

B.1.2 Systemic blood equations

The systemic blood equations are given by

$$\frac{d[gl y_{SB}]}{dt} = \frac{v_{bf}}{s}([gl y_{HB}]_n - [gl y_{SB}]) + \frac{1}{3}\mathcal{S}_{AdLip}, \quad (B.18)$$

$$\frac{d[TG_{SB}]}{dt} = \frac{v_{bf}}{s}([TG_{HB}]_n - [TG_{SB}]) + s_{TG}\mathcal{S}_{Meal} - \frac{\ln 2}{\lambda}[TG_{SB}], \quad (B.19)$$

$$\frac{d[FA_{SB}]}{dt} = \frac{v_{bf}}{s}([FA_{HB}]_n - [FA_{SB}]) + \mathcal{S}_{AdLip} - c_f[FA_{SB}], \quad (B.20)$$

$$\frac{d[gC_{SB}]}{dt} = \frac{v_{bf}}{s}([gC_{HB}]_n - [gC_{SB}]) + \mathcal{S}_{Meal} - \mathcal{S}_{gCup}, \quad (B.21)$$

$$\frac{d[Lac_{SB}]}{dt} = \frac{v_{bf}}{s}([Lac_{HB}]_n - [Lac_{SB}]), \quad (B.22)$$

$$\frac{d[Ins_{SB}]}{dt} = \frac{v_{bf}}{s}([Ins_{HB}]_n - [Ins_{SB}]) + \frac{1}{60r\tau_I}\mathcal{H}_I + b_{Ins}, \quad (B.23)$$

$$\frac{d[GL_{SB}]}{dt} = \frac{v_{bf}}{s}([GL_{HB}]_n - [GL_{SB}]) + \frac{1}{60r\tau_L}\mathcal{H}_L, \quad (B.24)$$

$$\frac{d[Ox y_{SB}]}{dt} = \frac{v_{bf}}{s}([Ox y_{HB}]_n - [Ox y_{SB}]) + c_{Oxy}, \quad (B.25)$$

where $s = 5n$ is the ratio between the volume of the systemic blood compartment to the volume of a hepatic compartment, $s_{TG} = 0.0145$ is a scaling factor on meal inputs to triglycerides, $\frac{\ln 2}{\lambda}$ is the half life of triglycerides with $\lambda = 4.5$ hours, $c_f = 0.0018$ is the rate of clearance of free fatty acids to the body (excluding the liver), $b_{Ins} = 0.0022$ is a constant source term for insulin (so that it doesn't drop to zero), and $c_{Oxy} = 1.35\text{mmHg/s}$ is a constant rate of oxygen input. The rates of insulin and glucagon release, $\frac{1}{60r\tau_I}\mathcal{H}_I$ and $\frac{1}{60r\tau_L}\mathcal{H}_G$, are based off of a model developed by Hetherington et al. [88] for which insulin and glucagon are only released when the concentration of glucose is either above or below a certain threshold. The functions \mathcal{H}_I and \mathcal{H}_G are Hill functions dependent upon the level of glucose, given by

$$\mathcal{H}_I = \frac{f_I([gC_{SB}])}{(K_M^{Ins})^{n_{Ins}} + f_I([gC_{SB}])}, \quad (B.26)$$

$$\mathcal{H}_G = \frac{f_G([gC_{SB}])}{(K_M^{GL})^{n_{GL}} + f_G([gC_{SB}])}, \quad (B.27)$$

where

$$f_I([g]C_{SB}) = \begin{cases} \ln\left(\frac{s_{blood}[g]C_{SB}}{I_{ref}^{gC}}\right), & \text{if } \frac{s_{blood}[g]C_{SB}}{I_{ref}^{gC}} \geq 1, \\ 0, & \text{otherwise,} \end{cases} \quad (\text{B.28})$$

$$f_G([g]C_{SB}) = \begin{cases} \ln\left(\frac{GL_{ref}^{gC}}{s_{blood}[g]C_{SB}}\right), & \text{if } \frac{GL_{ref}^{gC}}{s_{blood}[g]C_{SB}} \geq 1, \\ 0, & \text{otherwise,} \end{cases} \quad (\text{B.29})$$

where s_{blood} is a scaling factor. The parameters given in [10] are used with the exception of I_{ref}^{gC} and τ_I which were set to 2.5 and 0.03, respectively. The rates of glucose uptake \mathcal{S}_{gCup} , adipose lipolysis \mathcal{S}_{AdLip} , and meal inputs \mathcal{S}_{meal} are given in Sections 2.3.1.3.1 - 2.3.1.3.3 with parameter values given in Tables B.1, B.2, and B.3, respectively.

Table B.1 Parameter values for rate of glucose uptake in the body excluding the liver.

Parameter	Value	Parameter	Value	Parameter	Value
ν_1	42.953	K_{M_1}	2141	n_1	3
ν_2	151.49	K_{M_2}	12137	n_2	3
		K_{M_I}	1.894	n_I	3

Table B.2 Parameter values for rate of adipose lipolysis.

Parameter	Value	Parameter	Value	Parameter	Value
c_I	4.31e-4	l_0	0.125	I_b	5.95
α_{AdLip}	3.29	l_2	1.28	I_{A2}	16

Table B.3 Parameter values for rate of meal inputs.

Parameter	Value	Parameter	Value	Parameter	Value
k_1	3.7e-3	α_{meal}	32.7	σ^2	10^7
k_2	4.7e-4	G_{in}	0.507		

B.1.3 Hepatic blood equations

We will use the notational convention $[C_{HB}]_0 = [C_{SB}]$ for all molecules C modeled in the hepatic blood. For $i = 1, \dots, n$, the hepatic blood equations are given by

$$\frac{d[gl y_{HB}]_i}{dt} = v_{bf}([gl y_{HB}]_{i-1} - [gl y_{HB}]_i) - \gamma_H \mathcal{T}_i^{gl y}, \quad (\text{B.30})$$

$$\frac{d[TG_{HB}]_i}{dt} = v_{bf}([TG_{HB}]_{i-1} - [TG_{HB}]_i) - \gamma_H \mathcal{T}_i^{TG}, \quad (\text{B.31})$$

$$\frac{d[FA_{HB}]_i}{dt} = v_{bf}([FA_{HB}]_{i-1} - [FA_{HB}]_i) - \gamma_H \mathcal{T}_i^{FA}, \quad (\text{B.32})$$

$$\frac{d[gC_{HB}]_i}{dt} = v_{bf}([gC_{HB}]_{i-1} - [gC_{HB}]_i) - \gamma_H \mathcal{T}_i^{gC}, \quad (\text{B.33})$$

$$\frac{d[Lac_{HB}]_i}{dt} = v_{bf}([Lac_{HB}]_{i-1} - [Lac_{HB}]_i) - \gamma_H \mathcal{T}_i^{Lac}, \quad (\text{B.34})$$

$$\frac{d[Ins_{HB}]_i}{dt} = v_{bf}([Ins_{HB}]_{i-1} - [Ins_{HB}]_i) - k_{Ins}[Ins_{HB}]_i, \quad (\text{B.35})$$

$$\frac{d[GL_{HB}]_i}{dt} = v_{bf}([GL_{HB}]_{i-1} - [GL_{HB}]_i) - k_{GL}[GL_{HB}]_i, \quad (\text{B.36})$$

$$\frac{d[Ox y_{HB}]_i}{dt} = v_{bf}([Ox y_{HB}]_{i-1} - [Ox y_{HB}]_i) - k_{Oxy}[Ox y_{HB}]_i, \quad (\text{B.37})$$

where $v_{bf} = Q_H n = 0.15n$ is the rate of blood flow, $\gamma_H = 4$ is the ratio of hepatic to hepatic blood volume, \mathcal{T}_i^C is the rate of transport of metabolite C , given in Section 2.3.1.1.1, and $k_{Ins} = 0.1389$, $k_{GL} = 0.1543$, $k_{Oxy} = 0.141$ are constant rates of degradation.

B.2 PDE models

The PDE models follow a very similar form to the compartments-in-series model, with the exception of the hepatic blood equations. Since the AR and ADR system have the same hepatic and systemic blood equations, we present them together here. We keep the same definitions as those given above unless otherwise specified. Appropriate initial conditions are assumed for all equations.

B.2.1 Hepatic equations

We represent the dynamics of the metabolite concentrations in the hepatocytes through mass-balance equations given by

$$\frac{\partial[G]}{\partial t} = \mathcal{R}^{GS} - \mathcal{R}^{GP}, \quad (\text{B.38})$$

$$\frac{\partial[g6p]}{\partial t} = \mathcal{R}^{GK} - \mathcal{R}^{G6Pase} - \mathcal{R}^{GS} + \mathcal{R}^{GP} + \frac{1}{2}\mathcal{R}^{FBP} - \mathcal{R}^{PFK}, \quad (\text{B.39})$$

$$\frac{\partial[gC_H]}{\partial t} = -\mathcal{R}^{GK} + \mathcal{R}^{G6Pase} + \mathcal{T}^{gC}, \quad (\text{B.40})$$

$$\frac{\partial[g3p]}{\partial t} = \mathcal{R}^{PEPCK} - \mathcal{R}^{FBP} + 2\mathcal{R}^{PFK} - \mathcal{R}^{PK} - \mathcal{R}^{TSyn} + \mathcal{R}^{GlyK}, \quad (\text{B.41})$$

$$\frac{\partial[Lac_H]}{\partial t} = -\mathcal{R}^{PEPCK} + \mathcal{R}^{PK} - \mathcal{R}^{PDH} + \mathcal{T}^{Lac}, \quad (\text{B.42})$$

$$\frac{\partial[aCoA]}{\partial t} = \mathcal{R}^{PDH} + 8\mathcal{R}^{\beta_{oxi}} - \mathcal{R}^{Lgen} - \frac{1}{12}\mathcal{R}^{ATPS}, \quad (\text{B.43})$$

$$\frac{\partial[FA_H]}{\partial t} = -\mathcal{R}^{\beta_{oxi}} + \frac{1}{8}\mathcal{R}^{Lgen} + 3\mathcal{R}^{Lip} - 3\mathcal{R}^{TSyn} + \frac{1}{2}\mathcal{T}^{FA}, \quad (\text{B.44})$$

$$\frac{\partial[TG_H]}{\partial t} = -\mathcal{R}^{Lip} + \mathcal{R}^{TSyn} + \mathcal{T}^{TG}, \quad (\text{B.45})$$

$$\frac{\partial[gly_H]}{\partial t} = \mathcal{R}^{Lip} - \mathcal{R}^{GlyK} + \mathcal{T}^{gly}, \quad (\text{B.46})$$

$$\frac{\partial[gt p]}{\partial t} = -\mathcal{R}^{PEPCK} + \mathcal{R}^{NDKG}, \quad (\text{B.47})$$

$$\frac{\partial[gdp]}{\partial t} = \mathcal{R}^{PEPCK} - \mathcal{R}^{NDKG}, \quad (\text{B.48})$$

$$\frac{\partial[utp]}{\partial t} = -\mathcal{R}^{GS} + \mathcal{R}^{NDKU}, \quad (\text{B.49})$$

$$\frac{\partial[udp]}{\partial t} = \mathcal{R}^{GS} - \mathcal{R}^{NDKU}, \quad (\text{B.50})$$

$$\begin{aligned} \frac{\partial[P]}{\partial t} = & \mathcal{R}^{G6Pase} + 2\mathcal{R}^{GS} - \mathcal{R}^{GP} + 2\mathcal{R}^{PEPCK} + \frac{1}{2}\mathcal{R}^{FBP} - 2.25\mathcal{R}^{PK} - 2.5\mathcal{R}^{PDH} + \dots \\ & \dots + 3\mathcal{R}^{\beta_{oxi}} + \frac{7}{8}\mathcal{R}^{Lgen} + 7\mathcal{R}^{TSyn} - \mathcal{R}^{ATPS} + \mathcal{R}^{ATPu} - \mathcal{R}^{PReg}, \end{aligned} \quad (\text{B.51})$$

$$\begin{aligned} \frac{\partial[atp]}{\partial t} = & -\mathcal{R}^{GK} - 2\mathcal{R}^{PEPCK} - \mathcal{R}^{PFK} + 3.25\mathcal{R}^{PK} + 2.5\mathcal{R}^{PDH} - 2\mathcal{R}^{\beta_{oxi}} - \frac{7}{8}\mathcal{R}^{Lgen} - \dots \\ & \dots - 3\mathcal{R}^{TSyn} - \mathcal{R}^{GlyK} + \mathcal{R}^{ATPS} - \mathcal{R}^{NDKU} - \mathcal{R}^{NDKG} - \mathcal{R}^{AK} - \mathcal{R}^{ATPu}, \end{aligned} \quad (\text{B.52})$$

$$\begin{aligned} \frac{\partial[adp]}{\partial t} = & \mathcal{R}^{GK} + 2\mathcal{R}^{PEPCK} + \mathcal{R}^{PFK} - 3.25\mathcal{R}^{PK} - 2.5\mathcal{R}^{PDH} + \mathcal{R}^{\beta_{oxi}} + \frac{7}{8}\mathcal{R}^{Lgen} + \dots \\ & \dots + \mathcal{R}^{GlyK} - \mathcal{R}^{ATPS} + \mathcal{R}^{NDKU} + \mathcal{R}^{NDKG} + 2\mathcal{R}^{AK} + \mathcal{R}^{ATPu}, \end{aligned} \quad (\text{B.53})$$

$$\frac{\partial[amp]}{\partial t} = \mathcal{R}^{\beta_{oxi}} + 3\mathcal{R}^{TSyn} - \mathcal{R}^{AK}, \quad (\text{B.54})$$

where the rates of all metabolic processes M , \mathcal{R}^M , are given in Appendix A, and the rate of transport for metabolite C , \mathcal{T}^C , is given in Table 2.2. Note that these equations are now for partial derivatives with respect to t rather than ordinary derivatives with respect to t . This is because we are considering the concentration of each molecule along the sinusoid to be represented by a single function rather than a number of separate functions that are each in their own compartment. Note, however, that we still do not include any spatial dynamics in these equations.

B.2.2 Systemic blood equations

Unlike the hepatic equations, the systemic blood equations remain ordinary differential equations. Thus, this compartment is still assumed to be well-mixed. The systemic blood equations are given by

$$\frac{d[gl y_{SB}]}{dt} = \frac{v_{bf}}{s} ([gl y_{HB}](L, t) - [gl y_{SB}]) + \frac{1}{3} \mathcal{S}_{AdLip}, \quad (\text{B.55})$$

$$\frac{d[TG_{SB}]}{dt} = \frac{v_{bf}}{s} ([TG_{HB}](L, t) - [TG_{SB}]) + s_{TG} \mathcal{S}_{Meal} - \frac{\ln 2}{\lambda} [TG_{SB}], \quad (\text{B.56})$$

$$\frac{d[FA_{SB}]}{dt} = \frac{v_{bf}}{s} ([FA_{HB}](L, t) - [FA_{SB}]) + \mathcal{S}_{AdLip} - c_f [FA_{SB}], \quad (\text{B.57})$$

$$\frac{d[gC_{SB}]}{dt} = \frac{v_{bf}}{s} ([gC_{HB}](L, t) - [gC_{SB}]) + \mathcal{S}_{Meal} - \mathcal{S}_{gCup}, \quad (\text{B.58})$$

$$\frac{d[Lac_{SB}]}{dt} = \frac{v_{bf}}{s} ([Lac_{HB}](L, t) - [Lac_{SB}]), \quad (\text{B.59})$$

$$\frac{d[Ins_{SB}]}{dt} = \frac{v_{bf}}{s} ([Ins_{HB}](L, t) - [Ins_{SB}]) + \frac{1}{60r\tau_I} \mathcal{H}_I + b_{Ins}, \quad (\text{B.60})$$

$$\frac{d[GL_{SB}]}{dt} = \frac{v_{bf}}{s} ([GL_{HB}](L, t) - [GL_{SB}]) + \frac{1}{60r\tau_L} \mathcal{H}_L, \quad (\text{B.61})$$

$$\frac{d[Ox y_{SB}]}{dt} = \frac{v_{bf}}{s} ([Ox y_{HB}](L, t) - [Ox y_{SB}]) + c_{Oxy}. \quad (\text{B.62})$$

B.2.3 Hepatic blood equations

The hepatic blood equations is where the AR and ADR system vary due to the inclusion of dispersion. This dispersion takes form as a second spatial derivative in the equations, hence requiring boundary conditions at both the in-flow and the out-flow boundaries. The AR system on the other hand only requires a boundary condition on one boundary, here taken to be the in-flow boundary. For

notational convenience, we will denote

$$\mathbf{C}_{HB}(x, t) = \begin{bmatrix} [gly_{HB}](x, t) \\ [TG_{HB}](x, t) \\ [FA_{HB}](x, t) \\ [gC_{HB}](x, t) \\ [Lac_{HB}](x, t) \\ [Ins_{HB}](x, t) \\ [GL_{HB}](x, t) \\ [Oxy_{HB}](x, t) \end{bmatrix}, \quad \mathbf{C}_{SB}(t) = \begin{bmatrix} [gly_{SB}](t) \\ [TG_{SB}](t) \\ [FA_{SB}](t) \\ [gC_{SB}](t) \\ [Lac_{SB}](t) \\ [Ins_{SB}](t) \\ [GL_{SB}](t) \\ [Oxy_{SB}](t) \end{bmatrix}, \quad \mathcal{T}^C = \begin{bmatrix} \mathcal{T}^{gly} \\ \mathcal{T}^{TG} \\ \mathcal{T}^{FA} \\ \mathcal{T}^{gC} \\ \mathcal{T}^{Lac} \\ 0 \\ 0 \\ 0 \end{bmatrix}, \quad \mathbf{k} = \begin{bmatrix} 0 \\ 0 \\ 0 \\ 0 \\ 0 \\ k_{Ins} \\ k_{GL} \\ k_{Oxy} \end{bmatrix}.$$

B.2.3.1 AR system

We note that the AR system is equivalent to the compartments-in-series model if you take the number of compartments $n \rightarrow \infty$. Using the notation defined above, the hepatic blood equations are given by the advection-reaction system

$$\frac{\partial \mathbf{C}_{HB}}{\partial t} = Q_H \frac{\partial \mathbf{C}_{HB}}{\partial x} - \gamma_H \mathcal{T}^C - \mathbf{k} \odot \mathbf{C}_{HB}, \quad 0 < x < 1, t > 0, \quad (\text{B.63})$$

$$\mathbf{C}_{HB}(0, t) = \mathbf{C}_{SB}(t), \quad t > 0, \quad (\text{B.64})$$

$$\mathbf{C}_{HB}(x, 0) = \mathbf{f}_{HB}(x), \quad 0 < x < 1, \quad (\text{B.65})$$

for some appropriate initial conditions \mathbf{f}_{HB} . Here, \odot is taken to mean component wise multiplication and the derivative operators are also meant to be taken in a component wise sense.

B.2.3.2 ADR system

The ADR system represents the hepatic blood equations as advection-dispersion-reaction equations. The exception to this is the equations for hormones and oxygen which will remain advection-reaction equations. The hepatic blood equations are given by

$$\frac{\partial \mathbf{C}_{HB}}{\partial t} = Q_H \frac{\partial \mathbf{C}_{HB}}{\partial x} - \mathbf{D}_C \odot \frac{\partial^2 \mathbf{C}_{HB}}{\partial x^2} - \gamma_H \mathcal{T}^C - \mathbf{k} \odot \mathbf{C}_{HB}, \quad 0 < x < 1, t > 0, \quad (\text{B.66})$$

$$\mathbf{C}_{HB}(0, t) = \mathbf{C}_{SB}(t), \quad t > 0, \quad (\text{B.67})$$

$$\mathbf{C}_{HB}(x, 0) = \mathbf{f}_{HB}(x), \quad 0 < x < 1, \quad (\text{B.68})$$

where $\mathbf{D}_C = [D_{gly}, D_{TG}, D_{FA}, D_{gC}, D_{Lac}, 0, 0, 0]^T$ and for some appropriate initial conditions \mathbf{f}_{HB} . Again, \odot is taken to mean component wise multiplication and the derivative operators are also meant to be taken in a component wise sense.